# EMERGING METHODS IN NON-INVASIVE VASCULAR IMAGING

EDITED BY: Luca Biasiolli, Luca Saba, Steven Rogers and Venkatesh Mani
PUBLISHED IN: Frontiers in Cardiovascular Medicine

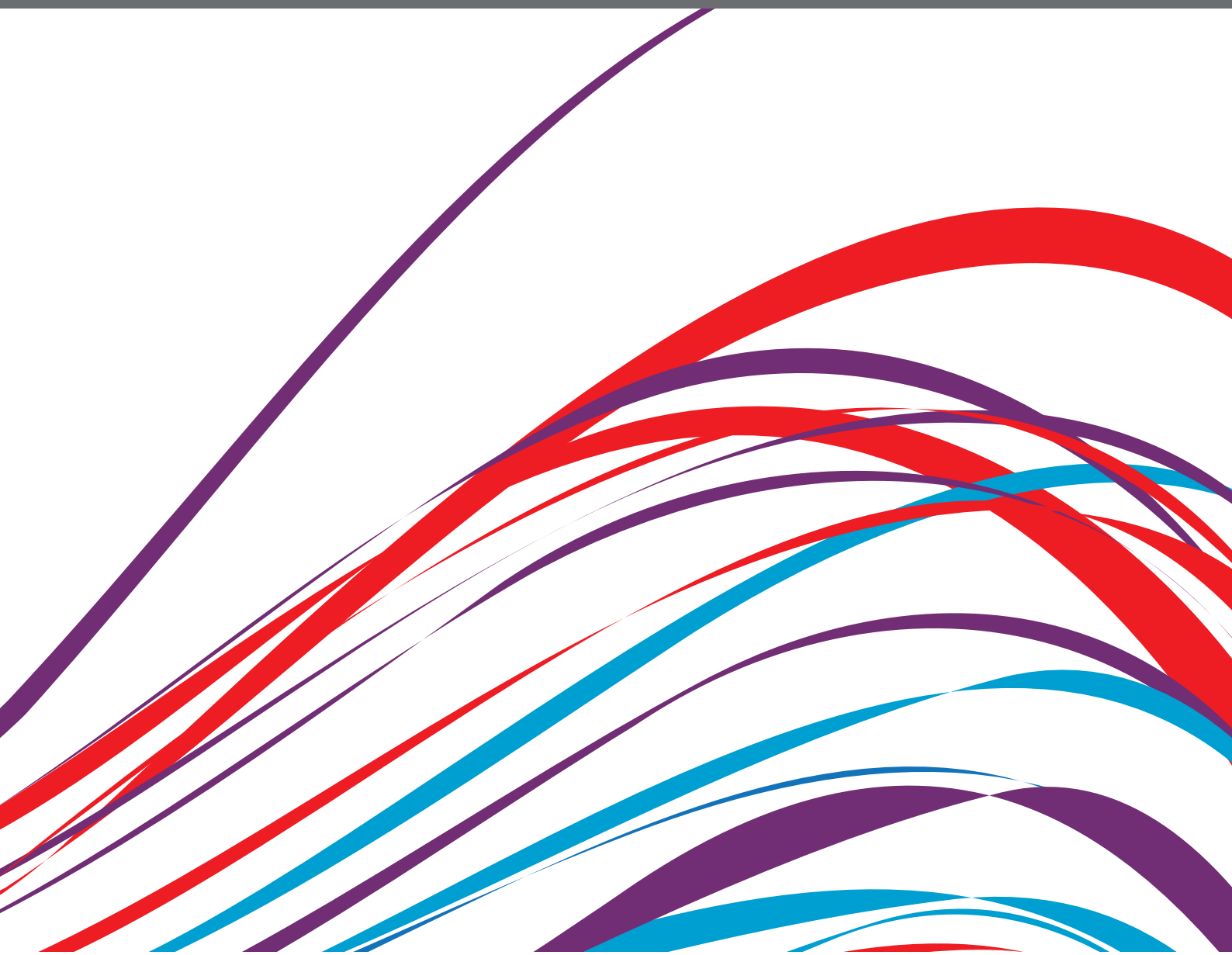

frontiers Research Topics

ISSN 1664-8714
ISBN 978-2-83250-862-6
DOI 10.3389/978-2-83250-862-6

## About Frontiers

Frontiers is more than just an open-access publisher of scholarly articles: it is a pioneering approach to the world of academia, radically improving the way scholarly research is managed. The grand vision of Frontiers is a world where all people have an equal opportunity to seek, share and generate knowledge. Frontiers provides immediate and permanent online open access to all its publications, but this alone is not enough to realize our grand goals.

## Frontiers Journal Series

The Frontiers Journal Series is a multi-tier and interdisciplinary set of open-access, online journals, promising a paradigm shift from the current review, selection and dissemination processes in academic publishing. All Frontiers journals are driven by researchers for researchers; therefore, they constitute a service to the scholarly community. At the same time, the Frontiers Journal Series operates on a revolutionary invention, the tiered publishing system, initially addressing specific communities of scholars, and gradually climbing up to broader public understanding, thus serving the interests of the lay society, too.

## Dedication to Quality

Each Frontiers article is a landmark of the highest quality, thanks to genuinely collaborative interactions between authors and review editors, who include some of the world's best academicians. Research must be certified by peers before entering a stream of knowledge that may eventually reach the public - and shape society; therefore, Frontiers only applies the most rigorous and unbiased reviews.
Frontiers revolutionizes research publishing by freely delivering the most outstanding research, evaluated with no bias from both the academic and social point of view. By applying the most advanced information technologies, Frontiers is catapulting scholarly publishing into a new generation.

## What are Frontiers Research Topics?

Frontiers Research Topics are very popular trademarks of the Frontiers Journals Series: they are collections of at least ten articles, all centered on a particular subject. With their unique mix of varied contributions from Original Research to Review Articles, Frontiers Research Topics unify the most influential researchers, the latest key findings and historical advances in a hot research area! Find out more on how to host your own Frontiers Research Topic or contribute to one as an author by contacting the Frontiers Editorial Office: frontiersin.org/about/contact

# EMERGING METHODS IN NON-INVASIVE VASCULAR IMAGING

Topic Editors:
**Luca Biasiolli,** University of Oxford, United Kingdom
**Luca Saba,** Azienda Ospedaliero-Universitaria Cagliari, Italy
**Steven Rogers,** The University of Manchester, United Kingdom
**Venkatesh Mani,** Integrated Research Facility, National Institute of Allergy and Infectious Diseases (NIH), United States

**Citation:** Biasiolli, L., Saba, L., Rogers, S., Mani, V., eds. (2022). Emerging Methods in Non-invasive Vascular Imaging. Lausanne: Frontiers Media SA. doi: 10.3389/978-2-83250-862-6

# Table of Contents

frontiers in Cardiovascular Medicine

ORIGINAL RESEARCH
published: 09 September 2021
doi: 10.3389/fcvm.2021.739332

# The Use of Pointwise Encoding Time Reduction With Radial Acquisition MRA to Assess Middle Cerebral Artery Stenosis Pre- and Post-stent Angioplasty: Comparison With 3D Time-of-Flight MRA and DSA

*Feifei Zhang[1†], Yuncai Ran[1*†], Ming Zhu[2], Xiaowen Lei[1], Junxia Niu[1], Xiao Wang[1], Yong Zhang[1], Shujian Li[1], Jinxia Zhu[3], Xuemei Gao[1*], Mahmud Mossa-Basha[4], Jingliang Cheng[1] and Chengcheng Zhu[4]*

[1] Department of Magnetic Resonance, The First Affiliated Hospital of Zhengzhou University, Zhengzhou, China, [2] Department of Intervention, The First Affiliated Hospital of Zhengzhou University, Zhengzhou, China, [3] MR Collaboration, Siemens Healthcare, Ltd., Beijing, China, [4] Department of Radiology, University of Washington, Seattle, WA, United States

OPEN ACCESS

**Edited by:**
Luca Saba,
Azienda Ospedaliero-Universitaria Cagliari, Italy

**Reviewed by:**
Ali Alaraj,
University of Illinois at Chicago, United States
Emilio Lozupone,
Ospedale Vito Fazzi, Italy

***Correspondence:**
Yuncai Ran
fccranyc@zzu.edu.cn
Xuemei Gao
Gaoxuemei1964@163.com

[†] These authors have contributed equally to this work and share first authorship

**Specialty section:**
This article was submitted to Cardiovascular Imaging, a section of the journal Frontiers in Cardiovascular Medicine

**Received:** 10 July 2021
**Accepted:** 18 August 2021
**Published:** 09 September 2021

**Citation:**
Zhang F, Ran Y, Zhu M, Lei X, Niu J, Wang X, Zhang Y, Li S, Zhu J, Gao X, Mossa-Basha M, Cheng J and Zhu C (2021) The Use of Pointwise Encoding Time Reduction With Radial Acquisition MRA to Assess Middle Cerebral Artery Stenosis Pre- and Post-stent Angioplasty: Comparison With 3D Time-of-Flight MRA and DSA. Front. Cardiovasc. Med. 8:739332. doi: 10.3389/fcvm.2021.739332

**Background and Purpose:** 3D pointwise encoding time reduction magnetic resonance angiography (PETRA-MRA) is a promising non-contrast magnetic resonance angiography (MRA) technique for intracranial stenosis assessment but it has not been adequately validated against digital subtraction angiography (DSA) relative to 3D-time-of-flight (3D-TOF) MRA. The aim of this study was to compare PETRA-MRA and 3D-TOF-MRA using DSA as the reference standard for intracranial stenosis assessment before and after angioplasty and stenting in patients with middle cerebral artery (MCA) stenosis.

**Materials and Methods:** Sixty-two patients with MCA stenosis (age 53 ± 12 years, 43 males) underwent MRA and DSA within a week for pre-intervention evaluation and 32 of them had intracranial angioplasty and stenting performed. The MRAs' image quality, flow visualization within the stents, and susceptibility artifact were graded on a 1–4 scale (1 = poor, 4 = excellent) independently by three radiologists. The degree of stenosis was measured by two radiologists independently on DSA and MRAs.

**Results:** There was an excellent inter-observer agreement for stenosis assessment on PETRA-MRA, 3D-TOF-MRA, and DSA (ICCs > 0.90). For pre-intervention evaluation, PETRA-MRA had better image quality than 3D-TOF-MRA (3.87 ± 0.34 vs. 3.38 ± 0.65, $P < 0.001$), and PETRA-MRA had better agreement with DSA for stenosis measurements compared to 3D-TOF-MRA ($r = 0.96$ vs. $r = 0.85$). For post-intervention evaluation, PETRA-MRA had better image quality than 3D-TOF-MRA for in-stent flow visualization and susceptibility artifacts (3.34 ± 0.60 vs. 1.50 ± 0.76, $P < 0.001$; 3.31 ± 0.64 vs. 1.41 ± 0.61, $P < 0.001$, respectively), and better agreement with DSA for stenosis measurements than 3D-TOF-MRA ($r = 0.90$ vs. $r = 0.26$). 3D-TOF-MRA significantly overestimated the stenosis post-stenting compared to DSA (84.9 ± 19.7 vs. 39.3 ± 13.6%, $p < 0.001$) while PETRA-MRA didn't (40.6 ± 13.7 vs. 39.3 ± 13.6%, $p = 0.18$).

**Conclusions:** PETRA-MRA is accurate and reproducible for quantifying MCA stenosis both pre- and post-stenting compared with DSA and performs better than 3D-TOF-MRA.

**Keywords: middle cerebral artery, pointwise encoding time reduction with radial acquisition, stent angioplasty, magnetic resonance imaging, digital subtraction angiography**

## INTRODUCTION

Ischemic stroke is one of the top sources of morbidity and mortality globally (1). Intracranial arterial stenosis is a major cause of ischemic stroke and the incidence of middle cerebral artery (MCA) stenosis in patients with stroke is 7.0–17.7% (2). The degree of stenosis is a critical factor for the management of stroke patients with MCA stenosis. Patients with high-grade stenosis (>70%) have a high risk of recurrent stroke and aggressive medical treatment or endovascular intervention is normally recommended for these patients (3). Digital subtraction angiography (DSA) is considered the gold standard for measuring stenosis, however, it is an invasive technique with radiation exposure, risk of stroke, and contrast-related complications (4). Other non-invasive techniques, including computed tomography angiography (CTA) and contrast, enhanced magnetic resonance angiography (CE-MRA), provide accurate stenosis measurements, but are limited due to radiation exposure and/or contrast-related complications (5, 6). Time-of-flight (TOF) is a non-contrast MRA technique that is commonly used for cerebral vascular imaging, but it has limited accuracy due to flow-related artifacts (7).

While the SAMMPRIS trial (8) showed intracranial stenting is not superior to medical therapy, the use of stenting for MCA stenosis remains controversial. The WEAVE trail (9) recently demonstrated the advantage of stenting over medical therapy in select patient populations. An accurate evaluation of stenosis is needed for appropriate patient selection for angioplasty and stenting (10, 11). Post-stenting arterial segment evaluation is also important considering the re-stenosis rate after stenting is 11.9–17.9% (12). This evaluation, however, is challenging for CTA, CE-MRA, and 3D-TOF-MRA due to beam hardening artifacts or magnetic susceptibility artifacts (13–15).

Pointwise Encoding Time Reduction with Radial Acquisition (PETRA) is a non-contrast MRA technique that uses Arterial Spin Labeling (ASL) and UTE techniques (16). The ultra-short TE of <100 μs significantly reduces susceptibility artifact (17). It has been successfully used for the evaluation of intracranial aneurysms after stent-assisted coil embolization (18–20) and the evaluation of other cerebral artery diseases (21, 22). Whether PETRA-MRA can be used as an alternative angiographic technique that approximates DSA performance has not been investigated. We hypothesize that PETRA-MRA can evaluate MCA stenosis more accurately than 3D-TOF-MRA when compared to DSA for both pre-intervention evaluation and post-intervention follow-up.

## MATERIALS AND METHODS

### Study Population

This study was approved by the local institutional review board, and informed consent was obtained from all participants. Written informed consent was obtained from the individuals for the publication of any potentially identifiable images or data included in this article. Patients who presented between October 2018 and August 2019 were recruited. The inclusion criteria were as follows: (1) patients with stroke or TIA attributing to MCA atherosclerotic stenosis; (2) over 18 years old; (3) underwent MRA that included PETRA-MRA and 3D-TOF-MRA; (4) underwent DSA, with the interval between the MRA and DSA being <1 week. Patients were excluded if they had any of the following conditions: (1) intracranial hemorrhage or non-atherosclerotic intracranial vasculopathy; (2) inadequate image quality; (3) no stenosis identified; (4) incomplete imaging dataset.

### Image Acquisition

Patients with MCA stenosis underwent 3D-TOF-MRA, PETRA-MRA, and DSA examinations within a week to identify patients that were suitable for intracranial angioplasty and stenting treatment. For patients who were selected for intervention, DSA was again performed immediately after the stent placement, and patients then underwent 3D-TOF-MRA and PETRA-MRA within a week of intervention.

### MRI Protocol

Both MRAs were performed on a 3-Tesla system (MAGNETOM Prisma, Siemens Healthcare, Erlangen, Germany) using a 64-channel head-neck coil.

The scan parameters for 3D-TOF-MRA were: TR/TE, 20/3.69 ms; flip angle, 18°; field of view (FOV), 200 × 160 $mm^2$; matrix, 320 × 256; slice thickness, 0.6 mm; voxel size, 0.6 × 0.6 × 0.6 $mm^3$; number of slab, 4; slices per slab, 44; acquisition time, 3 min 29 s. The scan parameters of PETRA-MRA were: TR/TE, 3.32/0.07 ms; flip angle, 3°; FOV, 300 × 300 mm; matrix, 320 × 320; radial spoke, 60,000; slice thickness, 0.9 mm; voxel size, 0.9 × 0.9 × 0.9 $mm^3$; number of slab, 1; slices per slab, 320; A control scan (bright blood) without the slice-slective saturation slab was first acquired with an acquisition time of 3 min and 29 s, and then a labeled scan (black blood) with a saturation band proximal to the imaging volume was acquired with an acquisition time of 5 min and 51 s. The final images were subtracted from the two datasets (Control-Label).

### Digital Subtraction Angiography

Patients underwent cerebral angiography examinations on a fixed digital angiographic system, FD 20 Artis (Phillips Healthcare,

Best, The Netherlands). All procedures were performed with local anesthesia. Femoral arterial access was used in all cases. DSA acquisition protocol was performed with Omnipaque 300 contrast injection (GE Healthcare, Waukesha, WI, USA), at a rate of 4 ml/s. During the 5-s acquisition after a delay of 1 s, a 200-degree rotation of the C-arm was performed to obtain 133 frames. Scan parameters were: FOV = 320 × 320 $mm^2$, matrix = 1,024 × 1,024. Four-vessel angiography was performed in all patients. Standard anteroposterior, oblique, and lateral views were obtained for all interrogated arteries.

## Image Analysis

The maximum intensity projection (MIP) of both MRA sequences were reconstructed by a neuroradiologist using a dedicated workstation. The MRA datasets were anonymized and placed in random order. Both the source images and MIPs were used for image evaluation. Three experienced radiologists (observer A, 8 years of experience; observer B, 5 years of experience; observer C, 5 years of experience) reviewed the image quality of the MRAs independently and blindly (for example, when evaluating PETRA-MRA, 3D-TOF-MRA images were not

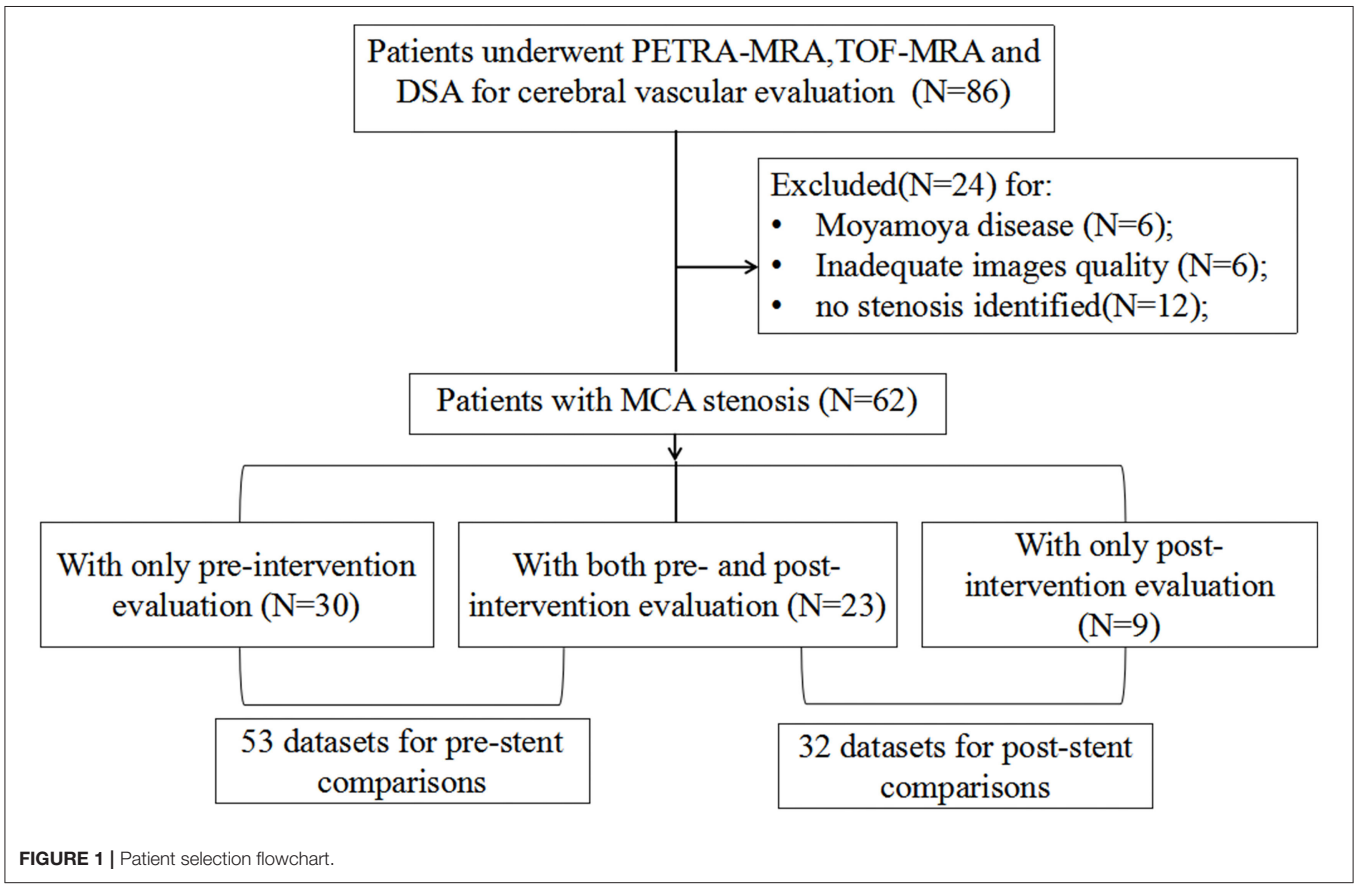


**FIGURE 1 |** Patient selection flowchart.

**TABLE 1 |** Comparison of PETRA-MRA/TOF-MRA and DSA in measurements of stenosis.

| | Mean ± SD | *CV* (%) | *p** | Bias | LOA | *r*# | *ICC* |
|---|---|---|---|---|---|---|---|
| **Stenosis (100%, Pre-operative)** | | | | | | | |
| DSA | 54.5 ± 25.8 | Reference | Reference | Reference | Reference | Reference | Reference |
| PETRA-MRA | 53.4 ± 27.2 | 4.6 | 0.10 | 1.1 | (−8.3, 10.5) | 0.96 | 0.98 |
| TOF-MRA | 62.0 ± 25.6 | 11.0 | <0.001 | −7.5 | (−29.0, 13.9) | 0.85 | 0.87 |
| **Stenosis (100%, Post-operative)** | | | | | | | |
| DSA | 39.3 ± 13.6 | Reference | Reference | Reference | Reference | Reference | Reference |
| PETRA-MRA | 40.6 ± 13.7 | 5.4 | 0.18 | −1.3 | (−11.9, 9.3) | 0.90 | 0.92 |
| TOF-MRA | 84.9 ± 19.7 | 20.9 | <0.001 | −45.6 | (−86.7, −4.6) | 0.26 | 0.05 |

**Comparison between MRA and DSA.*

*#Spearman correlation.*

*SD, standard deviation; CV, coefficient of variation; LOA, limit of the agreement; ICC, intra-class coefficient.*

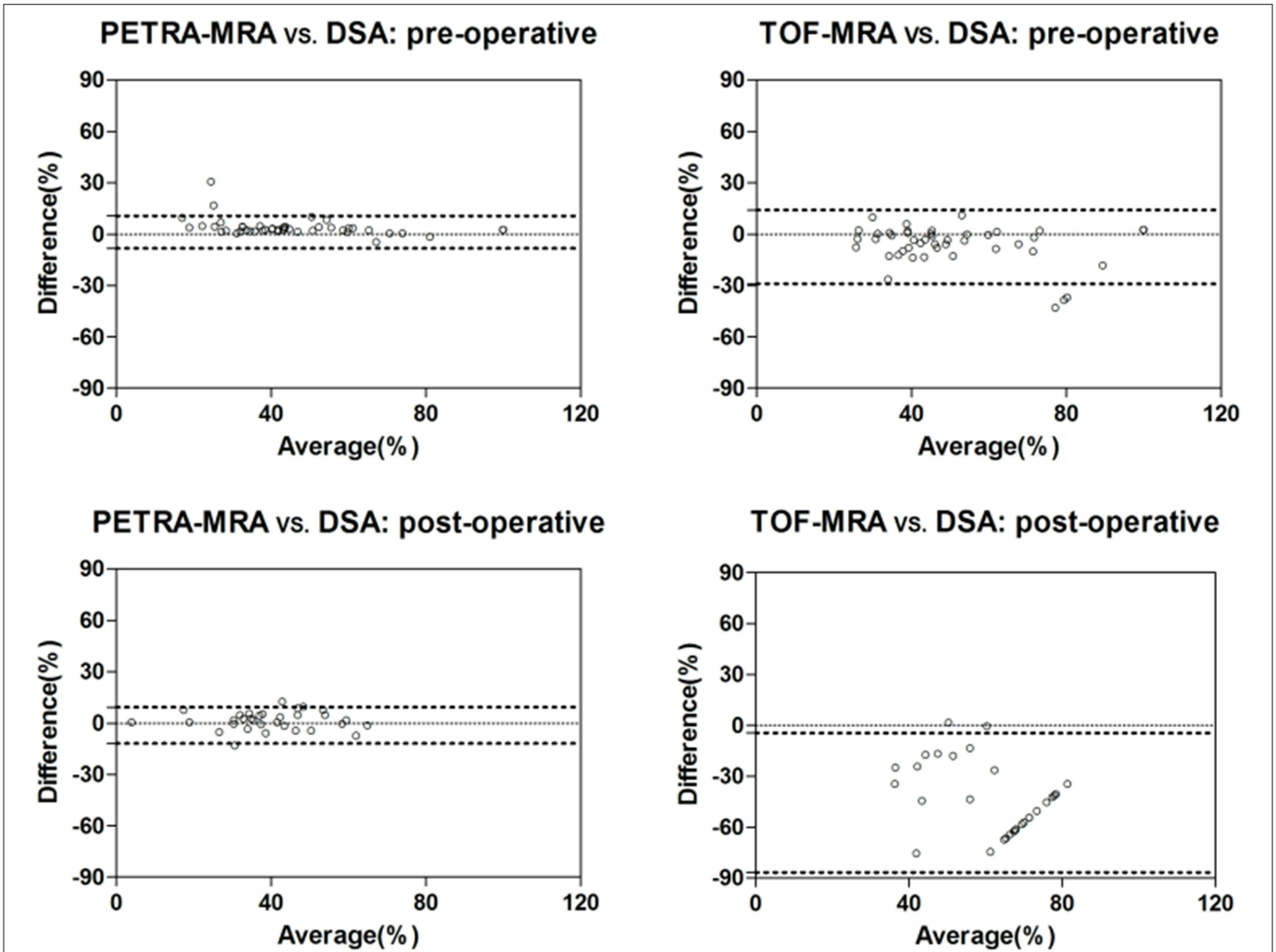


**FIGURE 2 |** Bland-Altman plots for the comparisons of stenosis measurements between PETRA-MRA/TOF-MRA and reference standard DSA.

present), and two experienced radiologists (observer A, 8 years of experience; observer B, 5 years of experience) measured the degree of stenosis on the MIPs of MRAs and DSA independently and blindly (without knowing the patients' clinical information, and when evaluating one imaging modality, without seeing other modality's images).

For pre-intervention MRAs, the overall image quality was reported using a previously defined four-point scale to determine signal homogeneity, lesion conspicuity, quality of venous signal suppression, and diagnostic confidence (21): 4 = excellent (excellent quality diagnostic information with detailed vascular architecture, no artifacts), 3 = good (good quality diagnostic information with adequate delineation of the vascular architecture, minimal artifacts), 2 = poor (poor quality diagnostic information with ordinary delineation of the vascular architecture, moderate artifacts), and 1 = not visible (almost no signal of the vascular architecture, severe artifacts).

After the intervention, two qualitative image scores were used to evaluate the susceptibility artifact and in-stent flow signal which were adopted from a previous publication (19). The ratings of susceptibility artifact intensity were determined using the following four-point scale: 4 = no susceptibility signal loss; 3 = minimal signal loss; 2 = moderate signal loss, which compromised image assessment; and 1 = severe signal loss, which prevented image assessment. The ratings of the in-stent flow signal were determined using the following four-point scale: 4 = excellent (excellent quality diagnostic information, nearly equal to that of DSA); 3 = good (good quality diagnostic information with minimal blurring or artifacts); 2 = poor (structures were slightly visible but with significant blurring or artifacts, not diagnostic); and 1 = arterial segments not visible (almost no signal).

The degree of stenosis was measured according to WASID criteria (23):

$$\text{Stenosis\%} = (1 - \text{d/D}) \times 100\%$$

the *d* is the diameter of the lumen at the most stenotic site, and the *D* is the diameter of the lumen at the proximal normal segment.

## Statistical Analyses

All statistical analyses were performed using SPSS 17.0 software or GraphPad Prism 5. Continuous variables were expressed as the means ± standard deviation (SD). The image quality scores were compared using the Wilcoxon signed-rank test. Spearman's correlation coefficient ($r$) was used as a non-parametric test to evaluate the linear association between measurements of stenosis on MRA and DSA.

The agreement of stenosis measurements between MRA and DSA and the inter-reader agreement was assessed using Bland–Altman analysis and intra-class correlation coefficient (ICC) (24), and the bias and limit of the agreement were reported. Measurement error was quantified by the coefficient of variation (CV) (CV = SD of difference/mean × 100%).

The performance of PETRA-MRA and 3D-TOF-MRA for the detection of stenosis >50% and stenosis >75% was summarized by the sensitivity, specificity, positive predictive value (PPV), and negative predictive value (NPV), using DSA as the reference standard. $P < 0.05$ indicated a significant difference and all $p$-values were two-sided.

# RESULTS

## Patient Demographics and Imaging Findings

From an initial cohort of 86 patients, 24 patients have excluded: 6 patients had Moyamoya disease, 6 patients had image degradation due to motion artifact, and 12 patients had no intracranial stenosis identified. This left 62 patients for inclusion in the final analysis. The patient selection flow chart is shown in **Figure 1**. Of these patients, 30 patients had an only pre-intervention evaluation, 23 patients had

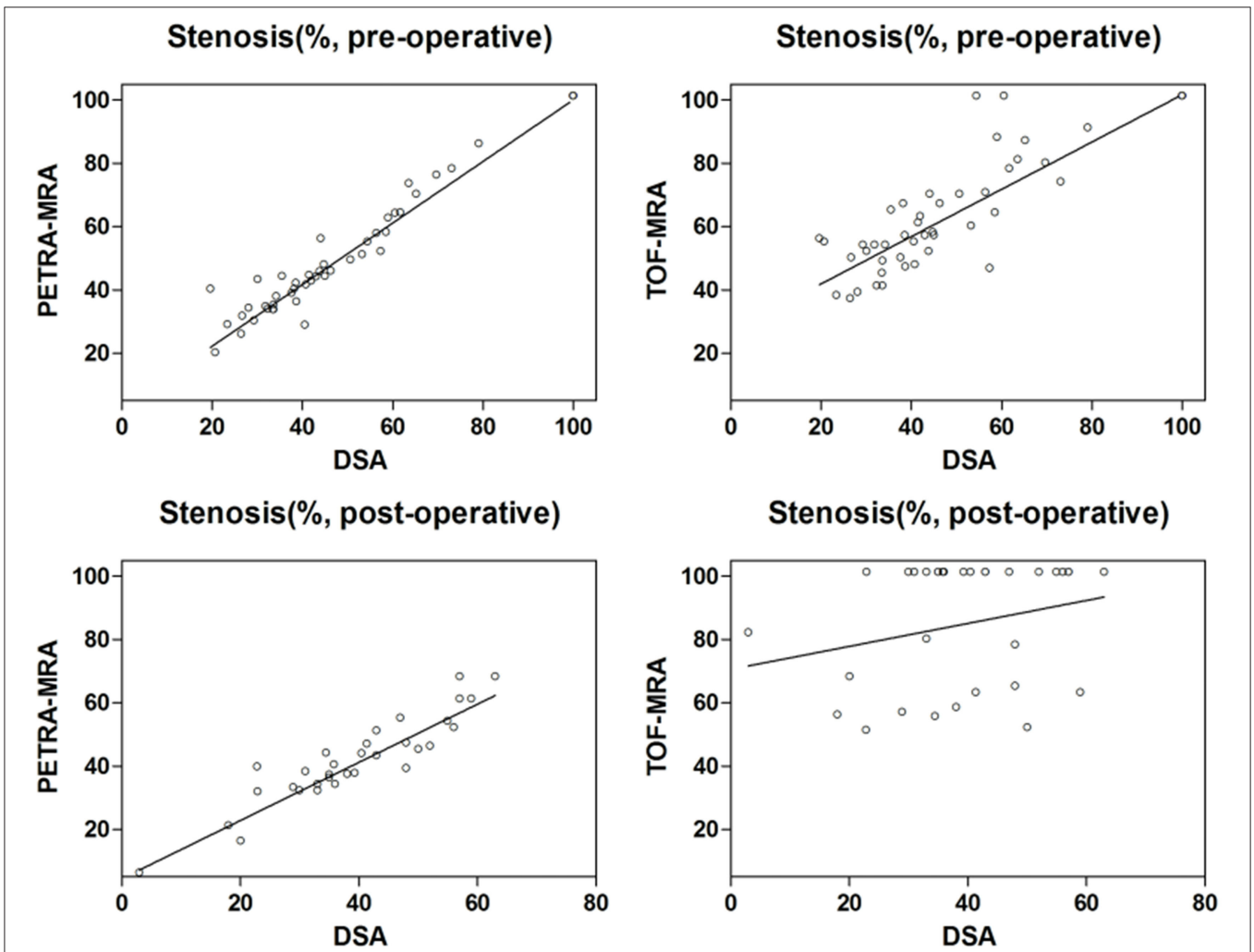


**FIGURE 3 |** Spearman correlation plots for the comparisons of stenosis measurements between PETRA-MRA/TOF-MRA and reference standard DSA. For pre-intervention evaluation, there was a better correlation in measuring stenosis between PETRA-MRA ($r = 0.96$, $CV = 4.6\%$) and DSA than between 3D-TOF-MRA ($r = 0.85$, $CV = 11.0\%$) and DSA; For post-intervention evaluation, PETRA-MRA had an excellent agreement with DSA ($r = 0.90$, $CV = 5.4\%$), while 3D-TOF-MRA had a poor agreement with DSA ($r = 0.26$, $CV = 20.9\%$).

both pre- and post-intervention evaluation, and 9 patients had only post-intervention evaluation, resulting in 53 datasets for pre-intervention comparison and 32 datasets for post-intervention comparison.

The time interval between MRI and DSA was 3.8 ± 2.4 days for pre-intervention comparison, and the interval was 3.7±1.0 days for post-intervention comparison. Thirtty-five patients had a stroke and 27 patients had a transient ischemic attack (TIA). The interval between the initial symptom onset and MRI was 41.7 ± 48.5 days, and the interval between symptom onset and DSA was 44.9 ± 48.1 days.

For pre-intervention evaluation, PETRA-MRA had better image quality than 3D-TOF-MRA (3.87 ± 0.34 vs. 3.38 ± 0.65, $P < 0.001$). For post-intervention evaluation, PETRA-MRA had better in-stent flow visualization (3.34 ± 0.60 vs. 1.50 ± 0.76, $P < 0.001$) and less susceptibility artifact (3.31 ± 0.64 vs. 1.41 ± 0.61, $P < 0.001$).

The agreement between MRAs and DSA for the degree of stenosis measurements is shown in **Table 1**, and the Bland-Altman plots and Spearman correlation plots are shown in **Figures 2**, **3**. For pre-intervention evaluation, PETRA-MRA showed better agreement with DSA in measuring the degree of stenosis compared to 3D-TOF-MRA ($r = 0.96$ vs. $r = 0.85$ and measurement error/CV 4.6 vs. 11.0%). For post-intervention evaluation, PETRA-MRA had an excellent agreement with DSA ($r = 0.90$, $CV = 5.4\%$), while 3D-TOF-MRA had a poor agreement with DSA ($r = 0.26$, $CV = 20.9\%$). For both pre- and post-intervention, 3D-TOF-MRA overestimated the degree of stenosis compared to DSA (62.0 ± 25.6 vs. 54.5 ± 25.8%, $p < 0.001$; 84.9 ± 19.7 vs. 39.3 ± 13.6%, $p < 0.001$, respectively), while PETRA-MRA had comparable stenosis measurements with DSA (53.4 ± 27.3 vs. 54.5 ± 25.8%, $p = 0.10$; 40.6 ± 13.7 vs. 39.3 ± 13.6%, $p = 0.18$, respectively).

Using DSA as the reference standard, the sensitivity, specificity, PPV, and NPV of PETRA-MRA and 3D-TOF-MRA for detecting stenosis >50% and stenosis >75% are presented in **Tables 2**, **3**. PETRA-MRA had overall better diagnostic performance than 3D-TOF-MRA when compared with DSA as the reference.

The examples from two patients having pre- and post-interventional imaging are shown in **Figures 4**, **5**.

## Inter-Reader Agreement

For the pre-intervention image quality scoring, there was good agreement among the three readers for PETRA-MRA (ICC = 0.84), but a moderate agreement for 3D-TOF-MRA (ICC = 0.66).

**TABLE 2 |** Evaluation of the diagnostic performance of PETRA-MRA and TOF-MRA for detecting stenosis >50% and stenosis >75% using DSA as reference for the pre-intervention evaluation.

| Pre-operative | Detection of >50% stenosis | | | | | | Detection of >75% stenosis | | | | | |
|---|---|---|---|---|---|---|---|---|---|---|---|---|
| | DSA (+) | DSA (-) | Sensitivity | Specificity | PPV | NPV | DSA (+) | DSA (–) | Sensitivity | Specificity | PPV | NPV |
| PETRA-MRA (+) | 23 | 0 | 95.8% (76.9–99.8)* | 100.0% (85.4–100.0) | 100.0% (82.2–100.0) | 96.7% (80.9–99.8) | 11 | 1 | 100.0% (67.9–100.0) | 97.6% (85.9–99.9) | 91.7% (59.8–99.6) | 100.0% (89.3–100.0) |
| PETRA-MRA (–) | 1 | 29 | | | | | 0 | 41 | | | | |
| TOF-MRA (+) | 23 | 6 | 95.8% (76.9–99.8) | 79.3% (59.7–91.3) | 79.3% (59.7–91.3) | 95.8% (76.9–99.8) | 11 | 4 | 100.0% (67.9–100.0) | 90.5% (76.5–96.9) | 73.7% (44.8–91.1) | 100.0% (88.6–100.0) |
| TOF-MRA (–) | 1 | 23 | | | | | 0 | 38 | | | | |

*95% confidence interval shown.
*PPV, positive predictive value; NPV, negative predictive value.*

**TABLE 3 |** Evaluation of the diagnostic performance of PETRA-MRA and TOF-MRA for detecting stenosis >50% and stenosis >75% using DSA as a reference of the post-intervention.

| Post-operative | Detection of >50% stenosis | | | | | | Detection of >75% stenosis | | | | | |
|---|---|---|---|---|---|---|---|---|---|---|---|---|
| | DSA (+) | DSA (–) | Sensitivity | Specificity | PPV | NPV | DSA (+) | DSA (–) | Sensitivity | Specificity | PPV | NPV |
| PETRA-MRA (+) | 7 | 3 | 87.5% (46.7–99.3)* | 87.5% (66.5–96.7) | 70% (35.4–91.9) | 95.5% (75.1–99.8) | 0 | 0 | 0 | 100% (86.7–100.0) | 0 | 100% (86.7–100.0) |
| PETRA-MRA (–) | 1 | 21 | | | | | 0 | 32 | | | | |
| TOF-MRA (+) | 8 | 24 | 100.0% (59.8–100.0) | 0 (0–17.2) | 25% (12.1–43.8) | 0 | 0 | 22 | 0 | 31.3% (16.7–50.1) | 0 (0–18.5) | 100.0% (65.5–100.0) |
| TOF-MRA (–) | 0 | 0 | | | | | 0 | 10 | | | | |

*95% confidence interval shown. PPV, positive predictive value; NPV, negative predictive value.*

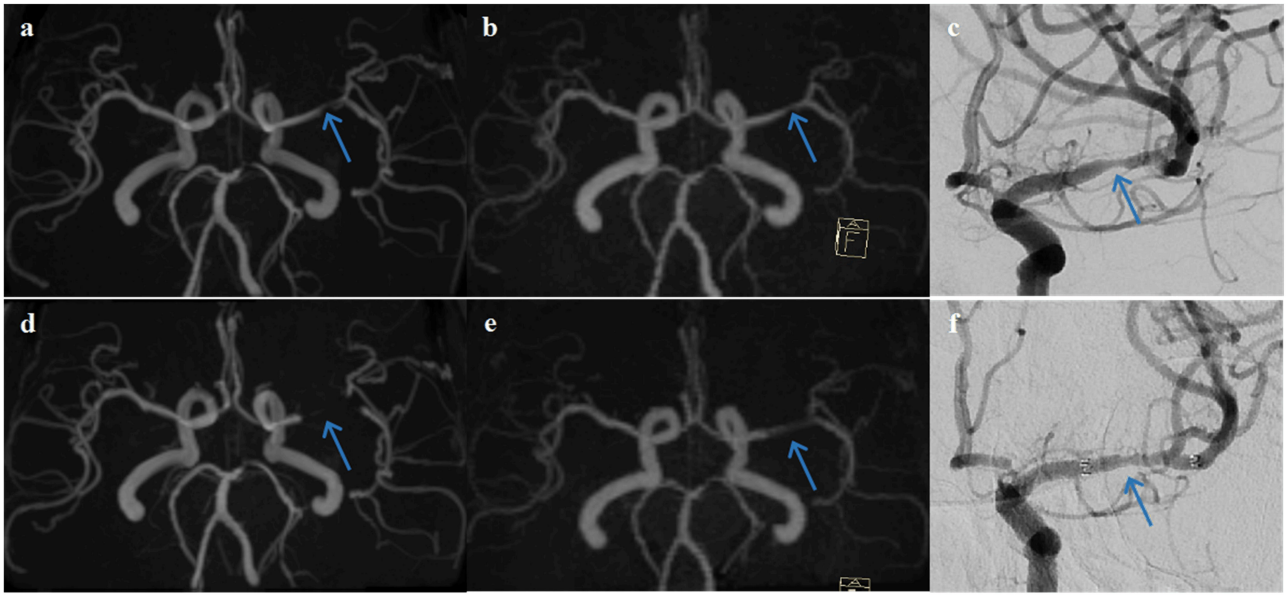


**FIGURE 4 |** A representative case of a 63-year-old female patient who underwent stent angioplasty due to atherosclerotic stenosis of the left middle cerebral artery (MCA) at the M1 segment (blue arrows). Pre-intervention images are shown on the top row **(a)** TOF-MRA, **(b)** PETRA-MRA, and **(c)** DSA. The degree of stenosis was 79.8% on TOF, 65.3% on PETRA-MRA, and 68.6% on DSA. Image quality scores of the PETRA-MRA and 3D-TOF were both 4. Post-intervention images are shown on the bottom row **(d)** 3D-TOF, **(e)** PETRA-MRA, and **(f)** DSA. Post-intervention TOF-MRA had strong signal loss near the stent, and post-intervention PETRA-MRA had mild signal loss near the stent comparing with reference DSA. PETRA-MRA had significantly higher image quality scores than those of TOF-MRA considering flow visualization within the stents (PETRA-MRA, 4; 3D-TOF, 1) and susceptibility artifact (PETRA-MRA, 3; 3D-TOF, 1).

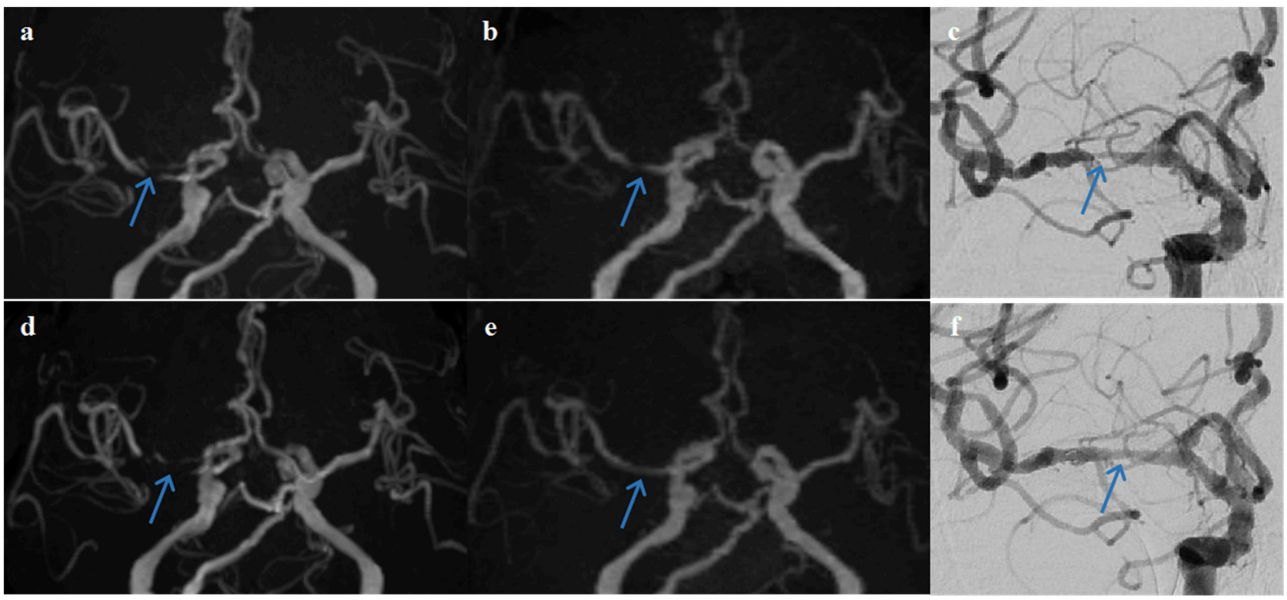


**FIGURE 5 |** A representative case of a 68-year-old female patient who underwent stent angioplasty due to atherosclerotic stenosis of the right middle cerebral artery (MCA) at the M1 segment (blue arrows). Pre-intervention images are shown on the top row **(a)** TOF-MRA, **(b)** PETRA-MRA, and **(c)** DSA. The degree of stenosis was 100% on TOF (pseudo-occlusion), 79.8% on PETRA-MRA, and 86.3% on DSA. Image quality scores of the PETRA-MRA and 3D-TOF were 4 and 3, respectively. Post-intervention images are shown on the bottom row **(d)** 3D-TOF, **(e)** PETRA-MRA, and **(f)** DSA. Post-intervention TOF-MRA had strong signal loss near the stent, and post-intervention PETRA-MRA had minimal signal loss near the stent comparing with reference DSA. PETRA-MRA had significantly higher image quality scores than those of TOF-MRA considering flow visualization within the stents (PETRA-MRA, 4; 3D-TOF, 1) and susceptibility artifact (PETRA-MRA, 4; 3D-TOF, 1).

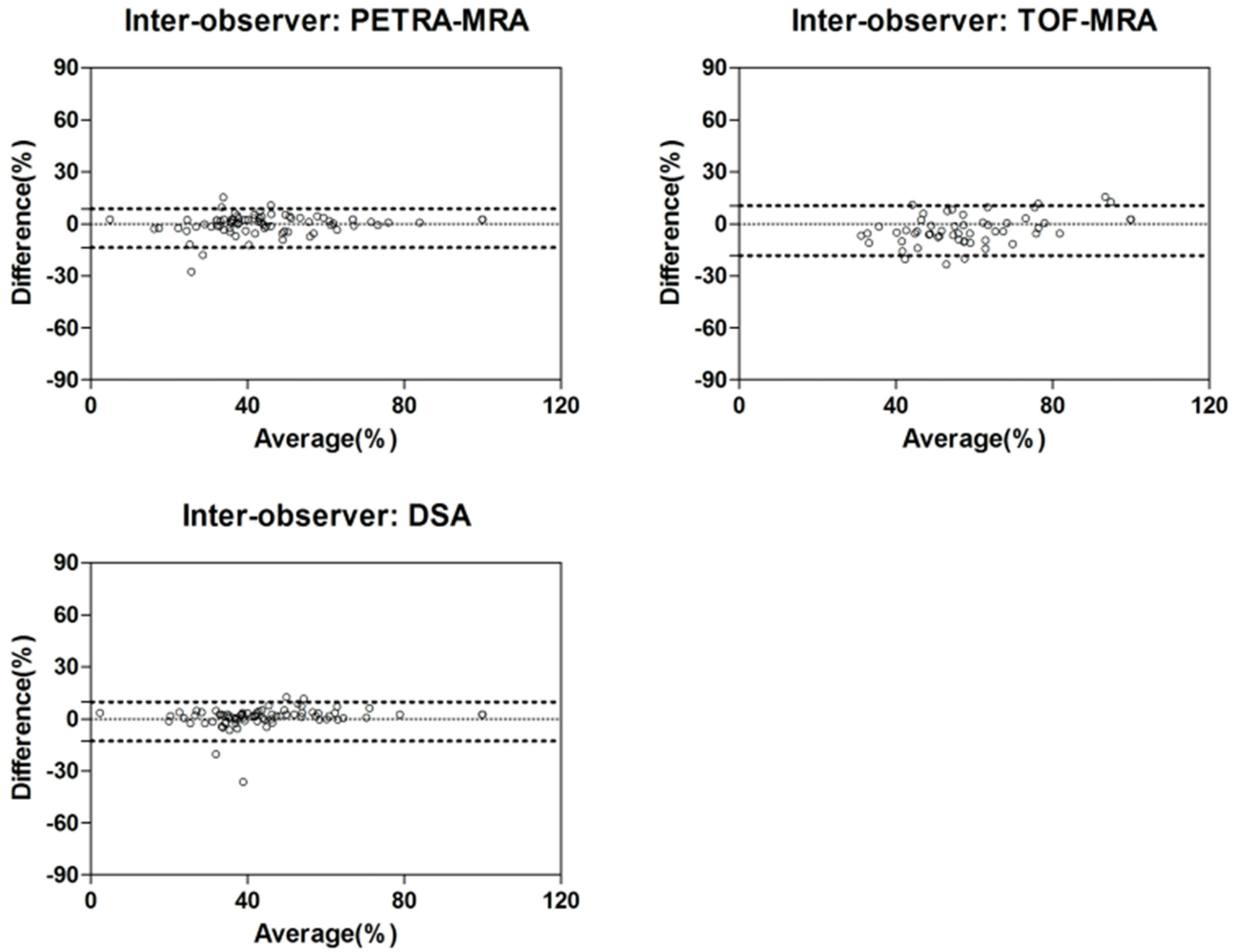


**FIGURE 6 |** Inter-observer agreement of stenosis measurements using PETRA-MRA, TOF-MRA, and DSA.

**TABLE 4 |** Summary of the inter-observer agreement for stenosis measurements.

| Stenosis (100%) | Reader 1 | Reader 2 | *CV* (%) | Bias | LOA | *ICC* |
|---|---|---|---|---|---|---|
| DSA | 48.7 ± 23.1 | 50.2 ± 21.9 | 5.7 | −1.5 | (−12.8, 9.7) | 0.96 |
| PETRA-MRA | 48.5 ± 23.8 | 51.1 ± 22.6 | 5.7 | −2.5 | (−13.7, 8.6) | 0.96 |
| TOF-MRA | 70.6 ± 26.0 | 74.5 ± 22.0 | 7.4 | −3.9 | (−18.4, 10.5) | 0.94 |

*CV, coefficient of variation; LOA, limit of the agreement; ICC, intra-class coefficient.*

For the post-intervention image quality evaluation of flow visualization, there was a good inter-reader agreement for PETRA-MRA (ICC = 0.74) and 3D-TOF-MRA (ICC = 0.91). For the susceptibility artifacts scoring, there was a good inter-reader agreement for PETRA-MRA (ICC = 0.81) and 3D-TOF-MRA (ICC = 0.87) as well.

There was an excellent inter-reader agreement for the measurement of the degree of stenosis with PETRA-MRA (ICC = 0.96), 3D-TOF-MRA (ICC = 0.94), and DSA (ICC = 0.96). The Bland-Altman plots are shown in **Figure 6** and results are shown in **Table 4**.

## DISCUSSION

This study demonstrated that PETRA-MRA had good image quality and accurate measurement of the MCA stenosis for both pre-and post-stenting comparing to gold standard DSA. The performance of PETRA-MRA was significantly better than 3D-TOF-MRA, especially after stent implementation. To our best knowledge, this was the first study using PETRA-MRA for the evaluation of intracranial stenosis post stent placement. Our study showed PETRA-MRA was a promising non-radiation non-contrast alternative to DSA for MCA stenosis

quantification, and it was especially attractive for the routine surveillance of patients after stent employment when multiple scans were required.

The accurate quantification of the degree of MCA stenosis plays an important role in the management of stroke patients to decide the treatment strategy between medical therapy and intervention (3). Because of the invasive nature of the reference standard DSA, other non-invasive techniques including CTA, CE-MRA, and 3D-TOF-MRA are often used for the initial evaluation of the stenosis (5–7). 3D-TOF-MRA doesn't require the use of contrast and is free of radiation, which is promising for clinical use, but it is vulnerable to hemodynamic fluctuations which lead to signal voids (by phase dispersion) (7, 25). A recent study by Tian et al. (7) evaluated 176 intracranial artery segments with stenosis in the Circle of Willis and found 3D-TOF-MRA overestimated stenosis compared to 3D rotational DSA ($65 \pm 19$ vs. $51 \pm 15\%$, $p < 0.001$), and our results for the pre-intervention evaluation reported similar findings. Compared with 3D-TOF-MRA with a TE value around 3–5 ms, PETRA-MRA had an ultra-short TE of <100 μs. Therefore, PETRA-MRA was less sensitive to turbulent flow artifacts around the stenotic site.

A recent study by Shang et al. included 26 patients with intracranial stenosis and compared the stenosis evaluation of PETRA-MRA with 3D-TOF-MRA using CTA as a reference (21). They found PETRA-MRA had better image quality than 3D-TOF-MRA for signal homogeneity and venous signal suppression, and PETRA-MRA had a better agreement for stenosis categorization (<30, 30–69, 70–99, 100%) with CTA than 3D-TOF-MRA had with CTA (kappa, 0.90 vs. 0.81). Our results agreed with their findings with several advantages: (1) we had a large sample size than theirs ($n = 53$ vs. $n = 26$); (2) we used DSA as the reference standard while they used CTA as a reference; (3) we performed quantitative stenosis measurements while they only did qualitative grading.

Future comparison of PETRA-MRA to other promising advanced imaging techniques for stenosis measurement and post-intervention evaluation may prove valuable to determine the ideal imaging approach. Vessel wall MRI has proven to be a valuable technique for intracranial stenosis evaluation (7, 26, 27). Tian et al. found 3D vessel wall MRI agreed better with DSA than 3D-TOF-MRA ($r = 0.91$ vs. $r = 0.70$). Compared with bright blood MRA, black blood MRI did not provide easy visualization of stenosis, but it could characterize vessel wall features related to plaque vulnerability (28–30).

Intracranial angioplasty and stenting are beneficial for selected patient cohorts and have been used widely in many experienced centers (9, 31). After stent placement, imaging surveillance is necessary to monitor for in-stent restenosis (12). Computed tomography angiography is limited for post-stenting evaluation due to metal beam hardening artifact obscuring luminal evaluation (14). Traditional MRA methods including CE-MRA and 3D-TOF-MRA are limited due to susceptibility artifacts that create signal voids around the stent, overestimating the degree of stenosis (15, 32). To the best of our knowledge, no studies have been published evaluating PETRA-MRA for post-stenting evaluation of intracranial stenosis. However, there have been a few studies evaluating PETRA-MRA for stent-assistant coiling for intracranial aneurysms (15, 20). You et al. evaluated 61 patients who underwent stent-assisted coiling of an intracranial aneurysm with zero-TE MRA (a technique comparable to PETRA-MRA), CE-MRA, 3D-TOF-MRA, and DSA (15). They found zero-TE MRA had the best visualization of in-stent flow and performed better than CE-MRA and 3D-TOF-MRA. Our study had similar findings for post-stenting of intracranial stenosis. The ultra-short TE or zero TE sequences, in principle, begin the signal acquisition nearly immediately after the excitation when the phase dispersion within the voxel is still minimal, thus there is little image distortion and signal loss (33). As PETRA-MRA is a non-invasive and non-radiation technique, it has great potential for the follow up of patients after intracranial stent placement.

Our study has several limitations. First, this is a single-center study with a small sample size for post-stenting evaluation. Future larger-scale multi-center studies are required to confirm our findings. Second, we only evaluated MCA stenosis, and the performance of PETRA-MRA in other intracranial arteries is warranted. Third, the PETRA-MRA sequence has a long scan time relative to 3D-TOF-MRA. Future evaluation of the impact the PETRA-MRA has on MRI workflows relative to the use of 3D-TOF-MRA would be helpful to better determine the feasibility of its utilization in standard imaging algorithms.

## CONCLUSIONS

PETRA-MRA is accurate and reproducible for quantifying MCA stenosis both pre- and post-stenting compared with DSA and performs better than 3D-TOF-MRA.

## DATA AVAILABILITY STATEMENT

The original contributions presented in the study are included in the article/supplementary material, further inquiries can be directed to the corresponding author/s.

## ETHICS STATEMENT

The studies involving human participants were reviewed and approved by The First Affiliated Hospital of Zhengzhou University. The patients/participants provided their written informed consent to participate in this study. Written informed consent was obtained from the individuals for the publication of any potentially identifiable images or data included in this article.

## AUTHOR CONTRIBUTIONS

FZ, YR, MZ, XG, JC, and CZ conceived and designed the experiments. FZ, YR, MZ, XL, JN, and XW performed the experiments. FZ, YR, and CZ analyzed the data. FZ, YZ, SL, JZ, and MM-B participated in the completion of the manuscript.

All authors have made significant scientific contributions to this manuscript and reviewed the manuscript.

## FUNDING

The study was supported by the medical and technology grant of Henan province (Grant Number 2018020137). CZ was supported by National Institute of Health (NIH) grant (Grant Number R00HL136883).

## ACKNOWLEDGMENTS

We are grateful to our patients and their families for their continued support for our study.

## REFERENCES

1. Krishnamurthi RV, Feigin VL, Forouzanfar MH, Mensah GA, Connor M, Bennett DA, et al. Global and regional burden of first-ever ischaemic and hemorrhagic stroke during 1990–2010: findings from the Global Burden of Disease Study (2010). *Lancet Glob Health.* (2013) 1:e259–81. doi: 10.1016/S2214-109X(13)70089-5
2. Wong KS Li H, Lam WW, Chan YL, Kay R. Progression of middle cerebral artery occlusive disease and its relationship with further vascular events after stroke. *Stroke.* (2002) 33:532–6. doi: 10.1161/hs0202.102602
3. Holmstedt CA, Turan TN, Chimowitz MI. Atherosclerotic intracranial arterial stenosis: risk factors, diagnosis, and treatment. *Lancet Neurol.* (2013) 12:1106–14. doi: 10.1016/S1474-4422(13)70195-9
4. Katzberg RW. Urography into the 21st century: new contrast media, renal handling, imaging characteristics, and nephrotoxicity. *Radiology.* (1997) 204:297–312. doi: 10.1148/radiology.204.2.9240511
5. Kuo PH, Kanal E, Abu-Alfa AK, Cowper SE. Gadolinium-based MR contrast agents and nephrogenic systemic fibrosis. *Radiology.* (2007) 242:647–9. doi: 10.1148/radiol.2423061640
6. McDonald RJ, McDonald JS, Kallmes DF, Jentoft ME, Murray DL, Thielen KR, et al. Intracranial gadolinium deposition after contrast-enhanced MR imaging. *Radiology.* (2015) 275:772–82. doi: 10.1148/radiol.15150025
7. Tian X, Tian B, Shi Z, Wu X, Peng W, Zhang X, et al. Assessment of intracranial atherosclerotic plaques using 3D black-blood MRI: comparison with 3D time-of-flight MRA and DSA. *J Magn Reson Imaging.* (2021) 53:469–78. doi: 10.1002/jmri.27341
8. Derdeyn CP, Fiorella D, Lynn MJ, Turan TN, Lane BF, Janis LS, et al. Intracranial stenting: SAMMPRIS. *Stroke.* (2013). 44(6 Suppl. 1):S41–4. doi: 10.1161/STROKEAHA.111.000370
9. Alexander MJ, Zauner A, Chaloupka JC, Baxter B, Callison RC, Gupta R, et al. WEAVE trial: final results in 152 on-label patients. *Stroke.* (2019) 50:889–94. doi: 10.1161/STROKEAHA.118.023996
10. Wang T, Wang X, Yang K, Zhang J, Luo J, Gao P, et al. Endovascular treatment for symptomatic intracranial artery stenosis: protocol for a systematic review and network meta-analysis. *BMJ Open.* (2018) 8:e022359. doi: 10.1136/bmjopen-2018-022359
11. Cai B, Peng B. Intracranial artery stenosis: current status of evaluation and treatment in China. *Chronic Dis Transl Med.* (2017) 3:197–206. doi: 10.1016/j.cdtm.2017.09.003
12. Peng G, Zhang Y, Miao Z. Incidence and risk factors of in-stent restenosis for symptomatic intracranial atherosclerotic stenosis: a systematic review and meta-analysis. *Am J Neuroradiol.* (2020) 41:1447–52. doi: 10.3174/ajnr.A6689
13. Cho WS, Kim SS, Lee SJ, Kim SH. The effectiveness of 3T time-of-flight magnetic resonance angiography for follow-up evaluations after the stent-assisted coil embolization of cerebral aneurysms. *Acta Radiol.* (2014). 55:604–13. doi: 10.1177/0284185113502335
14. Zaeske C, Hickethier T, Borggrefe J, Goertz L, Dettmeyer R, Schlamann M, et al. Postinterventional assessment after stent and flow-diverter implantation using CT: influence of spectral image reconstructions and different device types. *AJNR Amer J Neuroradiol.* (2020) 42:516–23. doi: 10.3174/ajnr.A6952
15. You SH, Kim B, Yang KS, Kim BK Ryu J. Ultrashort echo time magnetic resonance angiography in follow-up of intracranial aneurysms treated with endovascular coiling: comparison of time-of-flight, pointwise encoding time reduction with radial acquisition, and contrast-enhanced magnetic resonance angiography. *Neurosurgery.* (2021) 88:E179–89. doi: 10.1093/neuros/nyaa467
16. Grodzki DM, Jakob PM, Heismann B. Ultrashort echo time imaging using pointwise encoding time reduction with radial acquisition (PETRA). *Magn Reson Med.* (2012) 67:510–8. doi: 10.1002/mrm.23017
17. Ikushima Y, Hashido T, Watanabe Y, Doi T. Effects of imaging parameters on the quality of contrast-enhanced mr angiography of cerebral aneurysms treated using stent-assisted coiling: a phantom study. *Magn Reson Med Sci.* (2017) 16:146–51. doi: 10.2463/mrms.mp.2016-0042
18. Heo YJ, Jeong HW, Baek JW, Kim ST, Jeong YG, Lee JY, et al. Pointwise encoding time reduction with radial acquisition with subtraction-based MRA during the follow-up of stent-assisted coil embolization of anterior circulation aneurysms. *AJNR Am J Neuroradiol.* (2019) 40:815–9. doi: 10.3174/ajnr.A6035
19. Shang S, Ye J, Luo X, Qu J, Zhen Y, Wu J. Follow-up assessment of coiled intracranial aneurysms using zTE MRA as compared with TOF MRA: a preliminary image quality study. *Eur Radiol.* (2017) 27:4271–80. doi: 10.1007/s00330-017-4794-z
20. Irie R, Suzuki M, Yamamoto M, Takano N, Suga Y, Hori M, et al. Assessing blood flow in an intracranial stent: a feasibility study of MR angiography using a silent scan after stent-assisted coil embolization for anterior circulation aneurysms. *AJNR Am J Neuroradiol.* (2015) 36:967–70. doi: 10.3174/ajnr.A4199
21. Shang S, Ye J, Dou W, Luo X, Qu J, Zhu Q, et al. Validation of zero TE-MRA in the characterization of cerebrovascular diseases: a feasibility study. *AJNR Am J Neuroradiol.* (2019) 40:1484–90. doi: 10.3174/ajnr.A6173
22. Fu Q, Liu DX, Zhang XY, Deng XB, Zheng CS. Pointwise encoding time reduction with radial acquisition in subtraction-based magnetic resonance angiography to assess saccular unruptured intracranial aneurysms at 3 tesla. *Neuroradiology.* (2020) 63:189–99. doi: 10.1007/s00234-020-02512-x
23. Samuels OB, Joseph GJ, Lynn MJ, Smith HA, Chimowitz MI. A standardized method for measuring intracranial arterial stenosis. *AJNR Am J Neuroradiol.* (2000) 21:643–6.
24. Bland JM, Altman DG. Statistical methods for assessing agreement between two methods of clinical measurement. *Lancet.* (1986) 1:307–10.
25. Sarikaya B, Colip C, Hwang WD, Hippe DS, Zhu C, Sun J, et al. Comparison of time-of-flight MR angiography and intracranial vessel wall MRI for luminal measurements relative to CT angiography. *Br J Radiol.* (2021) 94:20200743. doi: 10.1259/bjr.20200743
26. Zhu C, Haraldsson H, Tian B, Meisel K, Ko N, Lawton M, et al. High resolution imaging of the intracranial vessel wall at 3 and 7 T using 3D fast spin echo MRI. *Magma (New York, NY).* (2016) 29:559–70. doi: 10.1007/s10334-016-0531-x
27. Zhu C, Wang X, Eisenmenger L, Tian B, Liu Q, Degnan AJ, et al. Surveillance of unruptured intracranial saccular aneurysms using noncontrast 3D-black-blood MRI: comparison of 3D-TOF and contrast-enhanced MRA with 3D-DSA. *AJNR Am J Neuroradiol.* (2019) 40:960–6. doi: 10.3174/ajnr.A6080
28. Shi Z, Zhu C, Degnan AJ, Tian X, Li J, Chen L, et al. Identification of high-risk plaque features in intracranial atherosclerosis: initial experience using a radiomic approach. *Eur Radiol.* (2018) 28:3912–21. doi: 10.1007/s00330-018-5395-1
29. Zhu C, Tian X, Degnan AJ, Shi Z, Zhang X, Chen L, et al. Clinical significance of intraplaque hemorrhage in low- and

high-grade basilar artery stenosis on high-resolution MRI. *AJNR Am J Neuroradiol.* (2018) 39:1286–92. doi: 10.3174/ajnr.A5676

30. Wang Y, Liu X, Wu X, Degnan AJ, Malhotra A, Zhu C. Culprit intracranial plaque without substantial stenosis in acute ischemic stroke on vessel wall MRI: A systematic review. *Atherosclerosis.* (2019) 287:112–21. doi: 10.1016/j.atherosclerosis.2019.06.907
31. Jafari M, Nguyen TN, Ortega-Gutierrez S, Hussain MS, Hassan AE, Ikram A, et al. Current advances in endovascular treatment of intracranial atherosclerotic disease and future prospective. *J Stroke Cerebrovasc Dis.* (2020) 30:105556. doi: 10.1016/j.jstrokecerebrovasdis.2020.105556
32. Agid R, Schaaf M, Farb R, CE-MRA. for follow-up of aneurysms post stent-assisted coiling. *Int Neuroradiol.* (2012) 18:275–83. doi: 10.1177/159101991201800305
33. Tyler DJ, Robson MD, Henkelman RM, Young IR, Bydder GM. Magnetic resonance imaging with ultrashort TE (UTE) PULSE sequences: technical considerations. *J Magn Reson Imaging.* (2007) 25:279–89. doi: 10.1002/jmri.20851

**Conflict of Interest:** JZ is employed by Siemens.

The remaining authors declare that the research was conducted in the absence of any commercial or financial relationships that could be construed as a potential conflict of interest.

**Publisher's Note:** All claims expressed in this article are solely those of the authors and do not necessarily represent those of their affiliated organizations, or those of the publisher, the editors and the reviewers. Any product that may be evaluated in this article, or claim that may be made by its manufacturer, is not guaranteed or endorsed by the publisher.

frontiers in Cardiovascular Medicine

SYSTEMATIC REVIEW
published: 27 October 2021
doi: 10.3389/fcvm.2021.742935

# Assessment of Therapeutic Response to Statin Therapy in Patients With Intracranial or Extracranial Carotid Atherosclerosis by Vessel Wall MRI: A Systematic Review and Updated Meta-Analysis

*Pengyu Zhou[1], Yuting Wang[1]*, Jie Sun[2], Yannan Yu[3], Mahmud Mossa-Basha[2] and Chengcheng Zhu[2]*

[1] Department of Radiology, Sichuan Provincial People's Hospital, University of Electronic Science and Technology of China, Chengdu, China, [2] Department of Radiology, University of Washington, Seattle, WA, United States, [3] Internal Medicine Department, University of Massachusetts Memorial Medical Center, Worcester, MA, United States

OPEN ACCESS

**Edited by:**
Venkatesh Mani,
Icahn School of Medicine at Mount Sinai, United States

**Reviewed by:**
Hao Li,
University of Cambridge, United Kingdom
Yisen Zhang,
Capital Medical University, China

***Correspondence:**
Yuting Wang
wangyuting_330@163.com

**Specialty section:**
This article was submitted to Cardiovascular Imaging, a section of the journal Frontiers in Cardiovascular Medicine

**Received:** 17 July 2021
**Accepted:** 28 September 2021
**Published:** 27 October 2021

**Citation:**
Zhou P, Wang Y, Sun J, Yu Y, Mossa-Basha M and Zhu C (2021) Assessment of Therapeutic Response to Statin Therapy in Patients With Intracranial or Extracranial Carotid Atherosclerosis by Vessel Wall MRI: A Systematic Review and Updated Meta-Analysis. Front. Cardiovasc. Med. 8:742935. doi: 10.3389/fcvm.2021.742935

**Background and Aims:** Statin therapy is an essential component of cardiovascular preventive care. In recent years, various vessel wall MRI (VW-MRI) techniques have been used to monitor atherosclerosis progression or regression in patients with extracranial or intracranial large-artery atherosclerosis. We aimed to perform a systematic review and meta-analysis on the effects of statin therapy on plaque evolution as assessed by VW-MRI.

**Materials and Methods:** Prospective studies investigating carotid and intracranial atherosclerotic plaques in patients on statin therapy monitored by serial VW-MRI were systematically identified in the literature. The plaque burden and lipid-rich necrotic core (LRNC) volume of carotid plaque and the imaging features of intracranial plaques were extracted and summarized. For studies investigating carotid artery wall volume and LRNC volume, combined estimates were derived by meta-analysis.

**Results:** The study identified 21 studies of carotid plaque and two studies of intracranial plaque. While 16 studies investigating carotid plaques that included 780 patients by High-resolution VW-MRI were included in the meta-analysis. There was no significant change in carotid wall volume from baseline to 12 months. A significant change in LRNC volume was observed at >12 months compared with baseline (Effect = −10.69, 95% CI = −19.11, −2.28, $P < 0.01$), while no significant change in LRNC volume at 3–6 months or 7–12 months after statin therapy initiation in 6 studies. Increases in fibrous tissue and calcium and reduction in neovascularization density of the plaque were seen in 2/3 studies (including 48/59 patients), 1/3 studies (including 17/54 patients), and 2/2 studies (including 71 patients) after statin therapy, respectively. Two studies with 257 patients in intracranial atherosclerosis showed that statins could effectively decrease wall volume and plaque enhancement volume.

**Conclusions:** Collective data indicated that statins could potentially stabilize carotid plaques by significantly reducing LRNC with 1 year of therapy as shown on serial carotid VW-MRI. There was no significant decrease in wall volume, which nonetheless indicated that plaque composition changes might be more sensitive to response monitoring than wall volume. It is likely that more sensitive, clinically relevant, and preferably quantitative indicators of therapeutic effects on intracranial vessel plaque morphology will be developed in the future.

**Keywords: vessel wall imaging, intracranial, carotid, atherosclerosis, plaque, statin**

## INTRODUCTION

Patients with extracranial or intracranial large-artery atherosclerosis are treated with aggressive risk factor control to lower their increased risk of ischemic stroke and other vascular events. This typically involves intensive low-density lipoprotein cholesterol (LDL-C) lowering with statin therapy. Meta-analyses of randomized clinical trials on statin therapies have shown that every 1 mmol/L reduction in LDL-C was associated with a 22% reduction in major vascular events (1). Despite LDL being a good marker for the effect of statins, residual stroke risk remains and other markers should be investigated for better pharmacology regime or monitoring the treatment effect (2).

A study in the Chinese population found that compared with the ipsilateral extracranial carotid artery, greater atherosclerotic plaque burden had a closer association with stroke severity (National Institutes of Health Stroke Scale) in the middle cerebral artery, suggesting that intracranial plaques deserve more attention in stroke etiology (3).

Vessel wall MRI (VW-MRI) is a non-Invasive imaging technique with high reproducibility and is used for characterizing atherosclerotic plaques in extracranial carotid or intracranial cerebral arteries (4–6), as well as plaque progression or regression (7–9). Studies of carotid atherosclerosis revealed the plaque characteristics shown on VW-MRI were highly consistent with those shown on histopathology (10, 11), providing the theoretical basis to evaluate the treatment response of atherosclerotic plaques by this imaging technique. Monitoring atherosclerosis with VW-MRI may enable the visual characterization of plaque morphologic and compositional evolution. VW-MRI studies have indicated that lowering LDL-C can remove the cholesterol from plaques, reduce the lipid content, induce plaque regression, even increase the plaque calcification, and therefore stabilize plaques (12–14). Moreover, monitoring atherosclerosis progression or regression in extracranial carotid or intracranial cerebral arteries with VW-MRI may allow for the identification of poor responders to standard-of-care medical therapy, who could be helped with novel lipid-lowering therapies or enrolling in clinical trials evaluating other endovascular treatments.

New studies have been published since the last meta-analysis of using VW-MRI to monitor changes of carotid plaques by Brinjikji et al. (15). The statins therapeutic response assessment in intracranial plaque by VW-MRI has not been systematically studied yet. Studies investigating novel techniques for vessel plaque evaluation are ongoing and show considerable promise. In this systematic review and updated meta-analysis, we aimed to evaluate the effect of statins on plaque components (such as lipid, fibrous tissue, and calcium) and plaque morphology (such as wall volume) as monitored by serial VW-MRI. The effects of statins in carotid plaques assessed by other advanced MRI techniques such as dynamic contrast-enhanced MRI (DCE-MRI), T2 mapping, and MRI targeting macrophages were also reviewed. The selection of parameters has been discussed. Finally, study results investigating intracranial plaques by VW-MRI after statin therapy were summarized.

## MATERIALS AND METHODS

This systematic review was performed with a standardized protocol with reference to the Preferred Reporting Items for Systematic reviews and Meta-Analysis (PRISMA) guidelines. Ethical committee approval and patient consent were not required because of their statistical nature.

### Search Strategy

A comprehensive search of the PubMed, Embase, Medline, and the Cochrane library databases from January 1st, 2000 through December 31st, 2020 was performed. To identify eligible studies, the following keywords were used in combination with the Boolean operators OR and AND: "intracranial atherosclerosis" or "intracranial plaque" or "intracranial artery stenosis" or "intracranial artery disease" or "cerebral artery atherosclerosis" or "carotid atherosclerosis" or "carotid plaque" or "carotid artery stenosis" or "carotid artery disease" or "lipid-rich necrotic core" and "high-resolution magnetic resonance imaging" or "vessel wall imaging" or "plaque imaging" and "statin" or "lipid-lowering treatment" or "HMG-COA (3-hydroxy-3-methyl glutaryl coenzyme A) reductase inhibitor." We also hand-searched references from key articles to find any additional studies on the use of serial carotid and intracranial plaque MRI to monitor response to statin therapy. Scoping searches were performed, and an iterative process was used to translate and refine the searches. The list of articles was supplemented with extensive cross-checking of reference lists within the included articles. The search was performed by a senior researcher and reviewed by a second researcher, and discrepancies in judgment were resolved by consensus.

## Eligibility Criteria and Study Selection

Specific inclusion criteria were: (1) English language articles; (2) all patients were on statin therapy or the results of the statin group were separately reported; (3) patients underwent serial vessel wall MRI to assess the response to statin therapy of intracranial and extracranial carotid atherosclerosis; (4) use of serial carotid or intracranial plaque MRI with dedicated surface coils; (5) minimum field strength of 1.5 T at all time points; (6) total sample size was > 10 patients; (7) follow-up duration was at least 3 months; (8) necessary data were reported to calculate the indicators of plaques. Attempts were made to contact the corresponding author for additional data details when necessary.

Studies must report at least one of the following regarding the plaques: (a) change in wall volume over time; (b) change in lipid-rich necrotic core (LRNC) volume over time; (c) change in calcium volume over time; (d) change in fibrous tissue volume over time.

If multiple studies were thought to contain overlapping patient cohorts and observed similar indicators, only the study with the largest sample size was retained. Review articles, conference abstracts, letters, comments, and case reports were excluded.

Exclusion criteria included retrospective and cross-Sectional studies, studies employing only imaging modalities other than vessel wall MRI, or studies in which the results of the statin arm could not be separated when multiple arms were involved, i.e., statin vs. non-Statin.

This selection strategy was prospectively chosen to provide sufficient and accurate data for a detailed systematic review.

## Methodological Quality Assessment

The methodological quality of included studies was independently assessed by two researchers using the "Guidelines for Assessing Quality in Prognostic Studies on the Basis of Framework of Potential Biases" (16). Discrepancies in judgment were resolved by consensus after discussion.

## Data Extraction and Analysis

Two reviewers independently extracted data from eligible studies, and disagreements were resolved by consensus. The following study characteristics were extracted: (1) sample size and demographics of study participants; (2) the regimen and dose of statins in all arms; (3) specific MRI protocols employed; (4) the changes in plaque imaging characteristics and in LDL-C levels at all monitoring time points.

We did the meta-analysis of studies investigating variable outcomes of carotid plaques at three time points: (a) 3–6 months, (b) 7–12 months, and (c) > 12 months following statin therapy initiation. The pooled results were expressed as an "Effect" with respective 95% CI. $I^2$ calculated from Q statistic was used to examine the heterogeneity among the included studies, with I values of 0–40, 30–60, 50–90, and 75–100% representing not important, moderate, substantial, and considerable inconsistency, respectively (17). A random-effects model was applicable with an $I^2$ value of over 50%, and a fixed-effects model was applicable with an $I^2$ value of < 50% (18). Meta-analysis was conducted using Stata version 12 (College Station, Texas: StataCorp LP, United States).

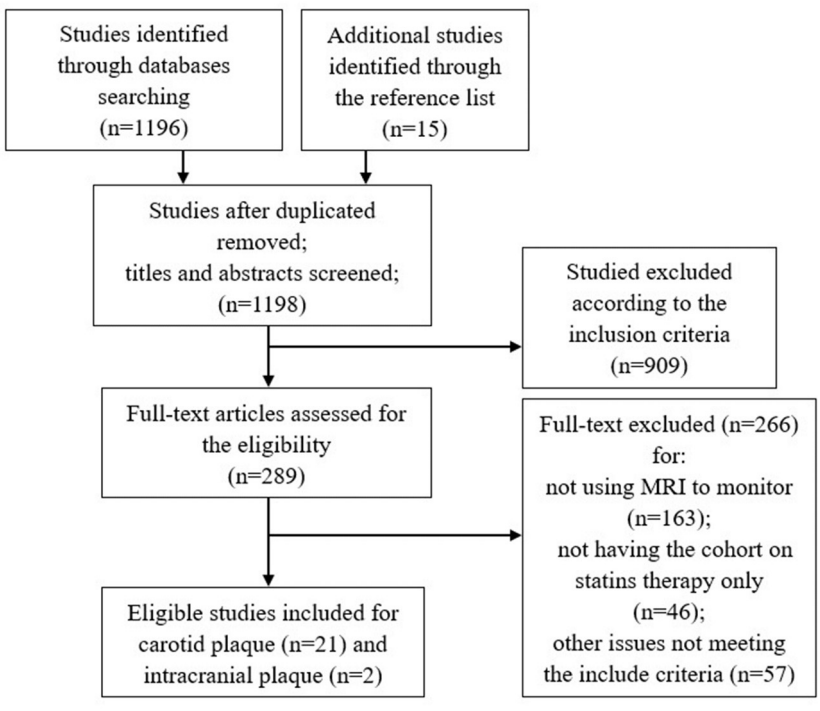


**FIGURE 1 |** Flow diagram of literature screening and selection process.

# RESULTS

## Study Selection and Characteristics

The detailed study selection flow diagram is shown in **Figure 1**. A total of 1,198 articles were identified after duplicates were removed. From these, 21 articles for carotid plaque and 2 articles for intracranial plaque were identified as eligible. Limited by the number of eligible studies on the intracranial plaque, the meta-analysis included only carotid plaque vessel wall MRI studies.

**Table 1** summarizes the 21 included prospective clinical studies that evaluated the changes of carotid plaques on longitudinal VW-MRI in patients on statin therapy published between 2000 and 2020. All studies evaluated the imaging characteristics of the plaques at baseline. There were 12 studies which had imaging follow up at 12 months, 4 studies at 18 months, and 9 studies at 24 months. Six studies did the measurements based on the T1 sequence. Two studies did the measurements based on the T2 sequence. One study did the measurements based on the PD (proton density) sequence. On the other hand, 12 studies did not make the corresponding statement. Eight studies drew the measurements manually, six studies used the automatic custom-designed image analysis tool (CASCADE, IBMarker Company, Seattle, WA, USA) (13, 29–31, 34, 35), and one used the semiautomatic software (Vessel Mass, Leiden University Medical Center, Leiden, Netherlands) (26). Six studies did not make the corresponding statement. All studies recorded the changes in the blood lipid index of the patients, including LDL-C and/or high-density lipoprotein-cholesterol (HDL-C). Nine studies employed plaque burden/volume as the only imaging observation at the experimental endpoint, one study employed LRNC as the only imaging observation, and seven studies used both plaque burden/volume and LRNC as observation indicators at the endpoint. In two studies investigating vascular dynamics, the dynamic changes in the parameters of the plaques were used as the only observation indicators at the endpoint of the experiment. Finally, one study employed plaque inflammation as the indicator (ultrasmall superparamagnetic iron oxide (USPIO) uptake by macrophages) and one employed distensibility as the only observation indicator at the endpoint.

**Table 2** summarizes the two prospective clinical studies from 2016 to 2020 evaluating treatment response to statins based on imaging findings on longitudinal intracranial VW-MRI studies. These studies monitored plaque burden/volume, intima-media thickness, and plaque number at baseline and after 6 months of statin therapy and recorded the changes of lipid panels, such as LDL-C, HDL-C, etc. The study of Chung et al. made the measurements based on the T2 sequence manually. There was no corresponding statement in another study (4, 37).

## Risk of Bias and Quality Assessment

The results of the quality assessment were generally satisfactory. There were 10 studies judged to have a low risk of bias in four assessed domains. Six studies were judged to have a moderate risk of bias in at least one domain. Common sources of moderate risk were study participation and study attrition. Study attrition bias risk came from missing data points, specifically some patients not receiving all follow-up imaging studies and/or lab values at the prescribed time points. Five studies had a high risk of bias in the domain of study participation resulting from a lack of reasonable inclusion and exclusion criteria and/or rationality in variable control. There was no study with a high risk of bias in more than one assessed domain.

## Selection of Plaque Measurements

### Morphological Parameters

The study found that 16 studies employed wall area, wall thickness, wall area index, wall volume, and lumen volume as the morphological parameters in the clinical trials of carotid atherosclerosis (**Table 1**). The wall area is defined as wall area = vessel area – lumen area. The wall thickness is the mean vessel wall thickness. The wall area index is defined as the ratio of the wall area of the stenosis site to that of the reference wall. The wall volume and lumen volume are three-dimensional indicators (volume= area × slice thickness × the number of slices) (4–6, 38). The interobserver and interscan intraclass correlation coefficient (ICC) for morphological measurement reported ranged from 0.97 to 0.99. The interobserver and interscan mean coefficient of variation (CV) of the total wall volume measurements were 4.6 and 3.8%, respectively, showing good repeatability (7–9, 20–23, 33).

### Compositional Parameters

Eight studies employed LRNC volume, fibrous tissue volume, and Calcium volume as the plaque component variables assessed on carotid VW-MRI (**Table 1**). The ICCs for component measurement reported in the included studies ranged from 0.88 to 0.96 (9, 22, 33).

### Other Novel Parameters

Two studies employed parameters of vascular permeability such as transport constant ($K^{trans}$) and fractional plasma volume ($V_p$) as the endpoints of clinical medication trials. Two studies employed USPIO-defined inflammation and stiffness as novel parameters.

In atherosclerosis, macrophage accumulation initiates lesion development and triggers clinical events by elaborating various molecules that promote inflammation, plaque disruption, and subsequent thrombus formation (39–42). To identify the plaque inflammation activity, common parameters include USPIO signal intensity in the plaque and compliance coefficient (24, 25). Amax and Amin were defined as the maximum and the minimum vessel cross-sectional areas through the cardiac cycle, respectively. The distensibility was: (Amax–Amin)/Amin* the average brachial pulse pressure. The compliance coefficient was: (Amax–Amin)/the average brachial pulse pressure (25).

## Response of Atherosclerosis on Statins

### Extracranial Carotid Atherosclerosis

#### *Lipid Rich Necrotic Core Volume*

Six studies extracted the change in LRNC volume. The mean LRNC volume was 72.3 ± 35.3 $mm^3$ at baseline and 62.3 ± 34.6 $mm^3$ at the last follow-up. There was a significant decrease in LRNC volume at > 12 months (Effect = −10.69,

**TABLE 1 |** Serial vessel wall MRI studies on effects of statin therapy on extracranial carotid atherosclerosis.

| References | Research Time | *N* | Study design | Age; Male% | Medication and dose | Monitoring time point | Monitored indicators | Change trend of monitored indicators | LDL-C levels | Manufacturer; Field strength; Sequences |
|---|---|---|---|---|---|---|---|---|---|---|
| Corti et al. (5) | 2001† | 18 | Prospective, Statins only, one arm | 63.5 ± 9; 56% | Simvastatin Dose unclear | Baseline, 6 months, 12 months | Plaque burden | VWA and maximal VWT decreased at 12 months and minimal VWT unchanged | 159 ± 32 mg/dl at baseline; decreased by 38% at 6 weeks | GE; 1.5T; T2W |
| Corti et al. (6) | 2002† | 21 | Prospective, Statins only, one arm | 63.5 ± 9; 57% | Simvastatin Dose unclear | Baseline, 6 months, 12 months, 18 months, 24 months | Plaque burden | VWA and maximal VWT decreased at 12–24 months and minimal VWT unchanged | 159 ± 32 mg/dl at baseline; decreased by 30–35% at 6 weeks | GE; 1.5T; T2W |
| Corti et al. (19) | 1999.03–2002.03 | 51 | Prospective, High vs. low dose statins, two arms | 62.6 ± 7.6 vs 62.3 ± 10.0; NA | Simvastatin 80 vs, 20 mg/d | Baseline, 6 months, 12 months, 18 months, 24 months | Plaque burden | VWA and maximal VWT decreased at 12–24 months and minimal VWT unchanged, in both arms | 173 ± 33 vs. 154 ± 31 mg/dl at baseline; 93 vs. 98 mg/dl at the first 6 weeks, then no changed, in both arms | GE; 1.5T; T2W |
| Boussel et al. (20) | 2004.02–2007.08 | 89 | Prospective, Detailed health questionnaire | 75.4 ± 9.4; 77.5% | Statins Dose unclear | Baseline, 12 months | Plaque burden/volume | VW volume increased at 12 months | Unclear | GE; 1.5T; 2D/3D TOF; T1W |
| Adams et al. (21) | 2004† | 11 | Prospective, Different statins or dose therapy, five arms. | 69; 73% | Atorvastatin 10 or 40 mg, pravastatin 20 mg, simvastatin 20 or 40 mg | Baseline, 16 months, 24 months | Plaque burden/volume | VW volume increased at 16 and 24 months | 116 ± 39 mg/dl at baseline, 92 ± 38 mg/dl at 16 months | GE; 1.5T; TOF/PDW/T1W/T2W |
| Underhill et al. (22) | 2000.01–2004.08 | 33 | Prospective, High vs. low dose statins, two arms | 64.4 ± 2.9 vs. 66.5 ± 1.8; 70 vs. 53.9% | Rosuvastatin 40 or 80 vs. 5 mg/d | Baseline, 24 months | Plaque burden/volume, LRNC | Lumen volume, VW volume, normalized wall index, or mean wall thickness unchanged; LRNC and LRNC% decreased and fibrous tissue increased at 24 months, in both arms | 145.0 ± 24.0 vs. 153.6 ± 31.0 mg/dl at baseline; decreased by 59.9 ± 3.3 vs. 38.2 ± 2.4% at 24 months | GE; 1.5T; 3D TOF; 2D PDW/T1W/T2W |
| Saam et al. (23) | 2007† | 68 | Prospective; Detailed health questionnaire | 70.3 ± 8.9; 93% | Statins Dose unclear | Baseline, 18 months | Plaque burden | Mean VWA and normalized wall index increased and mean lumen area decreased at 18 months | 80.6 ± 26.0 mg/dl at baseline; unclear at end time point | GE; 1.5T; 3D TOF; PDW/T1W/T2W |
| Tang et al. (24)* | 2006.07–2007.08 | 47 | Prospective; High vs. low dose statins, two arms | 70.8 ± 6.7 vs. 64.7 ± 7.6; 90 vs. 90% | Atorvastatin 80 vs. 10mg/d | Baseline, 6 weeks, 12 weeks | Inflammation | USPIO-defined Inflammation decreased in the high dose arm at 12 weeks | 97.06 vs. 87.78 mg/dl at baseline; decreased by 29 vs. 1% at 12 weeks | GE; 1.5T; 2D TOF/T1W/T2W |
| Sadat et al. (25)* | 2006.07–2007.08 | 47 | Prospective; High vs. low dose statins, two arms | 67 ± 2.7 vs. 72 ± 1.8; 80 vs. 75% | Atorvastatin 80 vs. 10 mg/d | Baseline, 12 weeks | Stiffness | Distensibility coefficient was higher in the high dose arm at 12 weeks | 98.61 ± 10.44 vs. 101.70 ± 5.41 mg/dl at baseline; 67.29 ± 7.73 vs. 99.38 ± 8.51 mg/dl at 12 weeks | GE; 1.5T; 2D TOF/T2W |

*(Continued)*

**TABLE 1** | Continued

| References | Research Time | *N* | Study design | Age; Male% | Medication and dose | Monitoring time point | Monitored indicators | Change trend of monitored indicators | LDL-C levels | Manufacturer; Field strength; Sequences |
|---|---|---|---|---|---|---|---|---|---|---|
| Sibley et al. (26) | 2003.09–2008.12 | 73 vs. 72 | Prospective; Statins vs. statins plus Nicotinic acid, two arms | 72; 82% | Nicotinic acid 1,500 mg/d; Statins Dose unclear | Baseline, 6 months, 12 months, 18 months | Plaque burden/volume LRNC | VW volume decreased at 18 months; lumen or LRNC volume unchanged, in both arms | 92.81 ± 30.94 mg/dl at baseline; 77.34 ± 19.33 mg/dl at 18 months | GE; 1.5T; T1W/T2W |
| Lee et al. (27) | 2008† | 24 | Prospective; Statins only, one arm | 66.0 ± 8.7; 83% | Simvastatin 10–20 or 40 mg/d; Atorvastatin 10 mg/d | Baseline, 3 months, 12 months | Plaque burden | Normalized vessel wall area decreased at 3–12 months | 112.7 ± 38.8 mg/dl at baseline; 70.8 ± 23.1 mg/dl at 3 months. 70.8 ± 23.1 mg/dl at 12 months | Siemens; 1.5T; T2W |
| Lee et al. (28) | 2009† | 29 | Prospective; Statins vs. statins plus nicotinic acid, two arms | 65 ± 9; 94% | Nicotinic acid 2 g/d; Statins Dose unclear | Baseline, 12 months | Plaque burden | Normalized vessel wall area unchanged at 12 months, in both arms | 85 ± 23 mg/dl at baseline; 64 ± 16 mg/dl at 6 months; 69 ± 21 mg/dl at 12 months | Siemens; 1.5T; T2W |
| Migrino et al. (29) | 2011† | 26 | Prospective; Statins, three arms: increase initiation, increase, maintain | 67.8 vs. 68.8 vs. 65.7; 50 vs. 85 vs. 85% | Statins Dose unclear | Baseline, 6 months | Plaque burden/volume, LRNC | Wall volume decreased in statins increasing arms (N = 13) and unchanged in statins maintain arm. LRNC and LRNC% decreased at 6 months in the total arms. | 86 ± 6 vs. 96 ± 8 vs. 77 ± 9 mg/dl at baseline; 74 ± 4 vs. 73 ± 7 vs. 62 ± 6 mg/dl at 6 months | GE; 3.0T; PDW/T1W/T2W |
| Zhao et al. (30) | 2011† | 33 | Prospective; Single therapy (included statins only), double therapy, triple therapy, seven arms | 55.0 ± 8.4; 78% | Atorvastatin 10–80 mg/d; Niacin 2 g/d; Colesevelam 3.8 g/d | Baseline, 12 months, 24 months, 36 months | Plaque burden/volume, LRNC | VW volume or VW volume percentage decreased at 12–36 months; LRNC and LRNC% decreased in first 24 months; FTV decreased and FTV% increased in first 24 months; Calcium and loose matrix unchanged. | 163 mg/dl at baseline; Unclear at endpoints | GE; 1.5T; 2D PDW/T1W/T2W |
| Du et al. (13)** | 2009.03–2012.02 | 43 | Prospective; Statins only, one arm | 60.8 ± 9.1; 78.1% | Rosuvastatin 10–80mg/d | Baseline, 3 months, 12 months, 24 months | Plaque burden/volume, LRNC | VW volume, VW percentage and lumen volume unchanged; LRNC and LRNC% decreased in first 3 months | 125.2 ± 24.4 mg/dl at baseline; 66.7 ± 17.3 mg/dl at 3 months; 65.5 ± 17.0 mg/dl at 12 months; 69.8 ± 16.6 mg/dl at 24 months | GE; 3.0T; 3D TOF; PDW/T1W/T2W |

*(Continued)*

**TABLE 1** | Continued

| References | Research Time | *N* | Study design | Age; Male% | Medication and dose | Monitoring time point | Monitored indicators | Change trend of monitored indicators | LDL-C levels | Manufacturer; Field strength; Sequences |
|---|---|---|---|---|---|---|---|---|---|---|
| Du et al. (31)** | 2009.03–2012.03 | 43 | Prospective; Statins only, one arm | 60.8 ± 9.1; 78.1% | Rosuvastatin 5–20 mg/d | Baseline, 3 months, 12 months, 24 months | Vascularity ($V_p$), vascular permeability ($K^{trans}$) | $V_p$ decreased at 3 months; $K^{trans}$ unchanged | 130 ± 24 mg/dl at baseline; 68 ± 17 mg/dl at 3months; 68 ± 18 mg/dl at 12 months; 69 ± 7 mg/dl at 24 months | GE; 3.0T; 3D TOF; PDW/T1W/T2W |
| Feng et al. (32) | 2013.09–2016.02 | 60 | Prospective; High vs. low dose statins, two arms | 61.3 vs. 61.0; 62.5 vs. 61.5% | Pivastatin 4 vs. 2 mg/d | Baseline, 48 weeks (12 months) | Plaque burden, LRNC | Lumen area increased; Normalized wall index, Plaque thickness and Wall area decreased; LRNC decreased. In both arms. | 134.57 vs. 129.93 mg/dl at baseline; unclear at endpoints | Philips; 3.0T; 3D TOF; PDW/T1W/T2W |
| Alkhalil et al. (33) | 2016.04–2016.11 | 24 | Prospective; Statins only, one arm | 64 ± 10; 71% | Atorvastatin 80 mg/d | Baseline, 3 months | LRNC | LRNC and LRNC% decreased; FTV unchanged; FTV% increased | 109 ± 30 mg/dl at baseline; unclear at endpoints | Siemens; 3.0T; TOF/T1W/T2W |
| Du et al. (34)** | 2016† | 32 | Prospective; Statins continued vs. Statins discontinued, two arms | NA; NA | Rosuvastatin; Atorvastatin; Simvastatin Dose unclear | Baseline, 24 months, 48 months | Plaque burden/volume, LRNC | VW volume percentage unchanged; LRNC and LRNC% decreased in 24–48 months; FTV, FTV% and Calcium increased in 24–48 months. | 124.02 ± 26.79 vs. 125.89 ± 22.85 mg/dl at baseline; 68.19 ± 16.29 vs. 70.79 ± 17.14 mg/dl at 24 months; 93.31 ± 35.91 vs. 130.73 ± 22.08 mg/dl at 48 months. | GE; 3.0T; 3D TOF; PDW/T1W/T2W |
| Dong et al. (35) | 2001.04–2004.05 | 28 | Prospective; Single therapy (included statins only), double therapy, triple therapy, seven arms | 55 ± 6; 82% | Atorvastatin 10–80 mg/d; Niacin 2 g/d; Colesevelam 3.8 g/d | Baseline, 12 months | Vascularity ($V_p$), vascular permeability ($K^{trans}$) | Adventitial ($K^{trans}$) decreased at 12 months, adventitial $V_p$ unchanged. | 163 mg/dl at baseline; Unclear at endpoints | GE; 1.5T; PDW/T1W/T2W |
| Hippe et al. (36) | 2018† | 86 | Prospective; Statins vs. statins plus nicotinic acid; ezetimibe was used as needed, two arms | 62; 67% | Simvastatin; nicotinic acid 1.5–2 mg/d | Baseline, 24 months | Plaque burden/volume | VW volume percentage increased in both arms. | 74 vs. 72 mg/dl at baseline; 69 vs. 67 md/dl at 24 months | GE/Philips; 3.0T; NA |

*Arranged by research time. N, number of patients; Male%, proportion of male; PDW, proton density weighted; T1W, T1 weighted; T2W, T2 weighted; $V_p$, fractional plasma volume; $K^{trans}$, transfer constant; VW, vessel wall; VWT, vessel wall thickness; VWA, vessel wall area; FTV, fibrous tissue volume; LRNC, lipid rich necrotic core; *The same patient cohort; **The same patient cohort, †published time.*

**TABLE 2** | Clinical trials of monitoring the efficacy of statins therapy in intracranial atherosclerotic plaques by vessel wall imaging.

| References | Research Time | *N* | Study Design | Age; Male% | Medication and dose | Monitoring Time Point | Monitored Indicators | Change Trend of Monitored Indicators | LDL-levels | Manufacturer; Sequences |
|---|---|---|---|---|---|---|---|---|---|---|
| Chung et al. (4) | 2011.11–2017.06 | 77 | Prospective; Statins only, one arm | 62.6 ± 13.7; 61% | Atorvastatin 40–80 mg/d; Rosuvastatin 20 mg/d | Baseline, 6 months | Plaque burden/volume, Plaque enhancement volume | Wall volume, the wall area index and stenosis degree decreased but not the remodeling index; Plaque enhancement volume decreased. | 125.81 ± 35.69 mg/dl at baseline; 60.95 ± 19.28 mg/dl at 6 months | Philips; 3.0T; 3D TOF; PDW/T1W/T2W |
| Chen et al. (37) | 2016.01–2017.02 | 180 | Prospective; Different statins, four arms | 59 vs. 61 vs. 62 vs. 60; 56 vs. 60 vs. 53 vs. 51% | Four arms: Atorvastatin 20 mg/d, Simvastatin 40 mg/d, Pravastatin 20 mg/d, Rosuvastatin 10 mg/d | Baseline, 6 months | Wall volume, plaque number and intima-media thickness | Wall volume, plaque number and intima-media thickness were decreased in all arms. | Four arms, baseline vs. 3 months, mg/dl: 152.36 ± 29.00 vs. 145.78 ± 24.75; 174.01 ± 27.46 vs. 144.62 ± 37.51; 147.33 ± 37.12 vs. 150.81 ± 25.91; 159.71 ± 25.91 vs. 148.88 ± 22.43 | Not mentioned clearly |

*N, number of patients; Male%, proportion of male; PDW, proton density weighted; T1W, T1 weighted; T2W, T2 weighted.*

95%CI = −19.11, −2.28, $P < 0$ 01). There was no significant decrease in LRNC volume at any time points < 1 year. Moderate heterogeneity was observed for the analysis of LRNC. The data is summarized in **Table 3**. Representative Forest plots and a detailed line chart are provided in **Figures 2A**, **3A**.

### *Fibrous Tissue Volume*

Only three studies had corresponding data and therefore meta-analysis was not performed. Two studies found an increase in fibrous tissue volume at the last follow-up. However, one study found a decreased volume at the 24-month time point after initiation of statin therapy and at the last follow-up. The detailed line chart is provided in **Figure 3C**.

### *Calcium Volume*

Only three studies had corresponding data and therefore meta-analysis was not performed. One study found an increase in calcium volume at the last follow-up. However, two studies found a decrease and no change in calcium volume at the last follow-up, respectively. The detailed line chart is shown in **Figure 3D**.

### *Wall Volume*

All eight studies evaluated the change in wall volume. The mean wall volume at baseline was 731.8 ± 227.1 $mm^3$ and at the last follow-up was 687.2 ± 225.6 $mm^3$. There was no significant decrease at > 12 months (Effect = −20.83, 95%CI = −46.29, 4.62, $P > 0.05$). I-squared value was 60.7% at > 12 months indicating substantial heterogeneity. There was no significant decrease at any time point except the last follow-up. The data is summarized in **Table 3**. Representative Forest plots and a detailed line chart are provided in **Figures 2B**, **3B**.

### *Neovascularization*

Two studies with 71 total patients found a decrease in $V_p$ or $K^{trans}$ of plaque at 3 and 12 months after statin therapy initiation, which indicated a reduction in plaque neovascularization density.

### *The Relationship Between LRNC Volumes and LDL Levels*

We also explored the relationship between the mean LRNC volumes and the mean LDL-C levels at various time points. Although several previous studies found that changes in the LRNC were significantly correlated with LDL-C levels (22, 32, 36), the reported LRNC volume changes varied across the reviewed studies, possibly due to the different study populations, designs, and statin regimens. The bubble chart showing the results across included studies is shown in **Figure 4**.

## Intracranial Atherosclerosis

In the evaluation of 77 patients with symptomatic acute ischemic stroke treated with high-dose statins (Atorvastatin 40–80 mg or rosuvastatin 20 mg), the study of Chung et al. found that high-dose statins could effectively decrease plaque enhancement volume, wall area index, and degree of stenosis. Longer duration (more than 1 month) of statin treatment and higher reduction of LDL-C were associated with decreased plaque enhancement volume (4, 38). Another study by Chen et al. compared the efficacy and safety of different statins in the treatment of intracranial atherosclerotic plaques involving middle cerebral

**TABLE 3 |** Results of meta-analysis.

| | Number of studies | Effect (95% CI) 3–6 months (mm3) | $I^2$ | Effect (95% CI) 7-12 months (mm3) | $I^2$ | Effect (95% CI) >12 months (mm3) | $I^2$ |
|---|---|---|---|---|---|---|---|
| LRNC volume | 6 | −5.01 (-17.65, 7.64) | 0 | −11.49 (-34.76, 11.77) | 0 | −10.69 (-19.11,−2.28) | 54.7 |
| Wall volume | 8 | - | - | −10.0 (-130.6, 110.6) | - | −20.83 (-46.29, 4.62) | 60.7 |

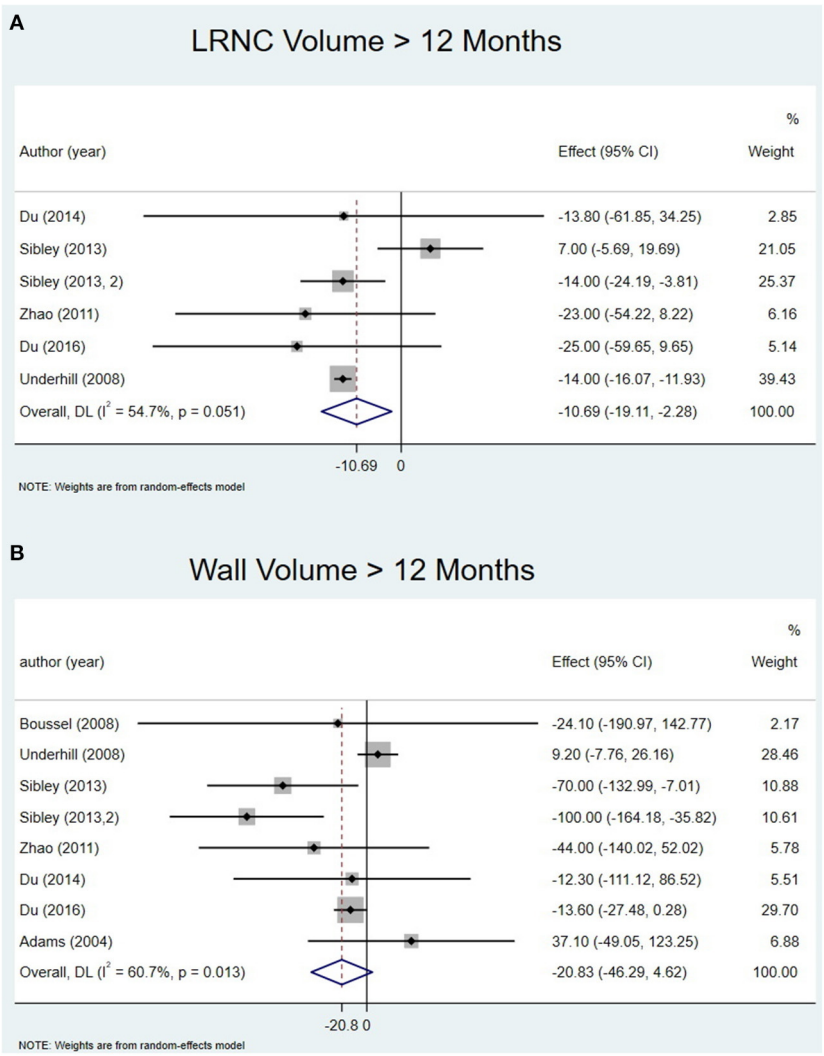


**FIGURE 2 |** Change in LRNC volume and Wall volume at > 12 months: **(A)** forest plot of change in LRNC volume at > 12 months; **(B)** forest plot of change in Wall volume at > 12 months.

arteries and found that different statins could significantly reduce blood lipid levels, intima-media thickness, plaque number, and wall volume, but rosuvastatin and atorvastatin had more effective anti-inflammatory and plaque stabilizing effects than simvastatin and pravastatin (37).

## DISCUSSION

This updated meta-analysis of patients who received serial carotid plaque imaging while on statin therapy demonstrated a significant reduction in LRNC volume only with > 1 year of therapy, whereas wall volume did not change significantly at any time points. It suggested that VW-MRI could visualize the changes of plaque components and morphology *in vivo* after statin therapies, and the former could be a more sensitive marker of therapeutic response. Increasing LRNC size was associated with the development of new ulceration, fibrous cap rupture, increasing plaque burden, as well as ischemic stroke events (43–46). Therefore, LRNC size was a good target for the evaluation of therapeutic response. A review of studies that monitored changes

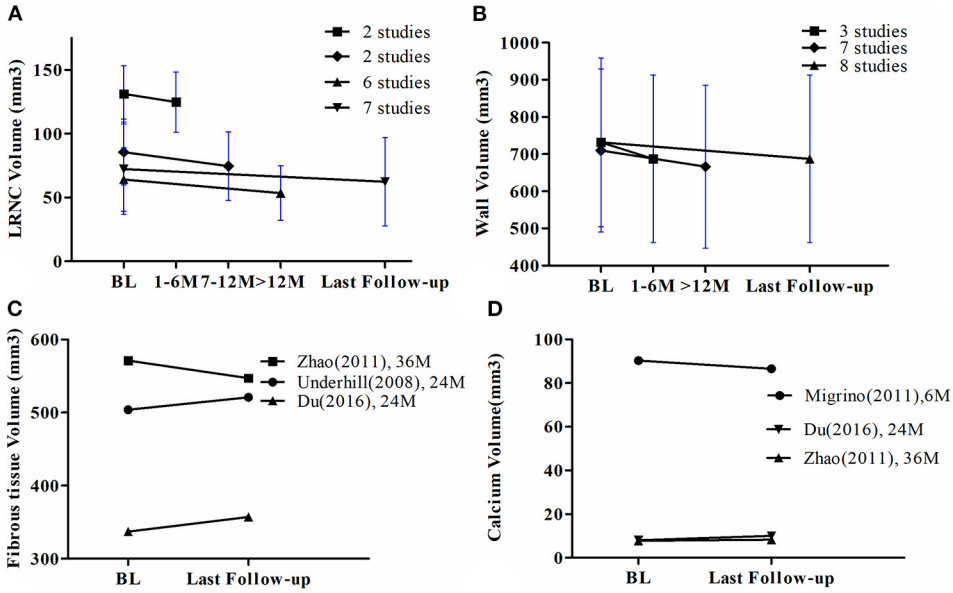


**FIGURE 3 | (A)** The line chart of LRNC volume, **(B)** The line chart of wall volume, **(C)** The line chart of fibrous tissue volume, **(D)** The line chart of calcium volume. BL = Baseline. The bars mean 95% CI.

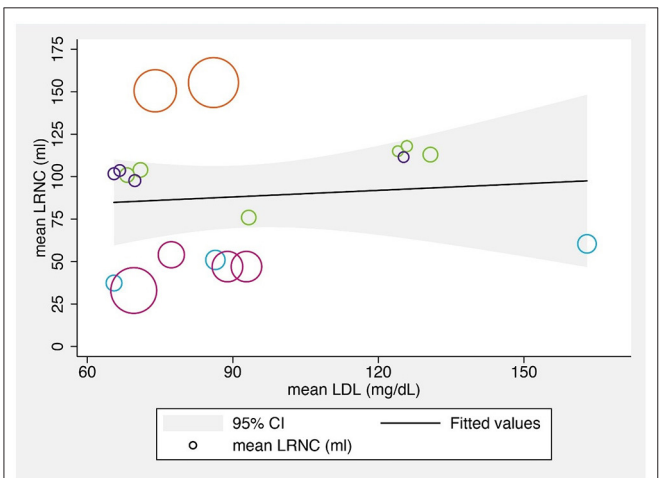


**FIGURE 4 |** The bubble chart about the relationship between mean LRNC volumes and mean LDL-C levels.

of intracranial atherosclerotic plaques by VW-MRI suggested that changes in multiple parameters such as decreased plaque number, wall volume, and plaque enhancement volume could be readily detected.

Compared with the meta-analysis by Brinjikji et al. (15) which also explored the change of plaque characteristics after statin therapies, our analysis provided additional information listed below. (1) One new prospective study with both vessel wall and LRNC data were included (34); (2) we summarized the change in plaque components such as fibrous tissue and calcium in addition to LRNC volume and wall volume; (3) the relationship between mean LRNC volumes and mean LDL-C levels were plotted; (4) given the technical developments in plaque imaging, a review of advanced MRI techniques including T2 mapping and DCE was performed and the established indicators for therapy monitoring of atherosclerotic plaques were summarized; (5) the results derived from studies of intracranial atherosclerosis were also summarized.

## Carotid Atherosclerosis

Two of three studies showed a significant increase in fibrous tissue volume of carotid plaques after 2 years of statin treatment. The timing of the change suggested that the decrease in the LRNC volume probably preceded the increase in fibrous tissue volume, which could be consistent with the proposed mechanism that the LRNC component might be replaced by fibrous tissue after statin treatment (15).

Calcium volume did not change significantly at any time points including for follow-up duration as long as 3 years (30). Sun et al. (44) reported that high plaque calcification content was not associated with poor prognosis in AIM-HIGH. Calcium might not be the crucial component to evaluate in carotid plaques when a therapeutic response of statins is being assessed by VW-MRI.

The study of Hellings et al. (47) found that carotid plaque features including IPH and intraplaque vessel formation identified in endarterectomy specimens were associated with future cardiovascular events in 818 patients who underwent carotid endarterectomy. Currently, advanced MRI techniques such as DCE MRI and USPIO enhanced MRI show unique advantages in characterizing plaque micro-vascularization and inflammation. These parameters could be further explored in

future prospective studies to monitor the effects of therapy on plaque morphology (48–51).

## Intracranial Atherosclerosis

Because of the unique structure and environment, intracranial arteries receive nutrient supply directly from cerebrospinal fluid and have fewer vasa vasorum than carotid arteries (52). Fewer vasa vasorum, however, makes intracranial arteries more vulnerable to hypoxic injury. The hypoxic environment caused by pathological wall thickening in atherosclerosis can stimulate angiogenic factors (e.g., vascular endothelial growth factor) that consequently promote neovascularization (53–55). Statins can reduce the release of vascular endothelial growth factors through anti-inflammatory effects, thereby reducing neovascularization and plaque enhancement volume on MRI seen in carotid plaque (35, 56). These observations suggest that statins might have different mechanisms to stabilize intracranial plaques than extracranial ones, and the assessment of intracranial plaque changes requires further investigation, which is indeed necessary given the crucial role that intracranial atherosclerosis plays in stroke development. Notably, a recent study on intracranial atherosclerosis indicated that 35% of patients had a poor response to statin therapy; post-Treatment VW-MRI showed no change or increased plaque enhancement volume and increased degree of stenosis. The study suggested that these patients might need to choose alternative therapeutic options such as PCSK9 inhibitors or a combination with ezetimibe to lower lipid levels (4).

Regarding the selection of measurements on imaging, several clinical studies provide a theoretical basis and report practical experience for the assessment of responses to statin therapy in extracranial atherosclerosis, however, the clinical studies investigating intracranial atherosclerotic plaques are relatively few, with a limited assessment of VW-MRI characteristics. The consensus of experts of the American Society of Neuroradiology on intracranial vessel wall imaging along with a recent meta-analysis indicates that intracranial plaque enhancement, positive remodeling, and plaque irregularity are associated with increased risk of stroke (57, 58). These features are therefore highly relevant when assessing and validating response to therapy. Furthermore, evaluation of plaque compositional characteristics in addition to morphological features on VW-MRI might be clinically relevant as suggested by the imaging features of carotid plaques. Given the unique role of neovascularization in the pathogenesis of vessel plaques, other novel techniques to assess neovascularization should be developed.

## Imaging Techniques

The standard multi-contrast black blood MRI (fast-spin-echo based) for carotid vessel wall imaging has been widely used for the evaluation of plaque morphology, and the sequences are widely available on the major commercial scanners at both 1.5 and 3T. All included studies used specific neck surface coils to improve the image signal-to-noise ratio/resolution. However, the neck surface coils are not widely available in clinical radiology departments and a separate purchase is required. Without using neck surface coils, the clinical head-neck or neurovascular coils produce noisier images which limit the image resolution and therefore limit the measurement accuracy of plaque morphology. This is a major barrier for clinical translation and multi-center trials.

In the past decade, 3D fast-spin-echo sequences with variable flip angle train (product sequence in all major vendors, termed SPACE in Siemens, CUBE in GE, and VISTA in Philips) have been widely used for carotid vessel wall imaging due to its high scan efficiency, isotropic resolution, and intrinsic blood suppression (59, 60). Such 3D techniques allow high-resolution imaging using clinical neurovascular coils (61), which significantly improve their feasibility in a clinical setting.

While the evaluation of plaque volume and LRNC volume using standard multi-contrast black blood MRI is the most popular and feasible approach, more advanced but less popular methods including T2 mapping, DCE and USPIO-MRI have their unique advantages. The T2 mapping method provides quantitative analysis of the plaque component and is more reproducible across scanners and centers. The DCE method provides unique information on the vasa vasorum, which is an important factor in plaque vulnerability. USPIO-MRI provides unique information of the vessel function and inflammation (macrophage activity). However, their disadvantages are also apparent. For the T2 mapping and DCE techniques, specific sequences are required, and specific post-Processing is required, too. Thus, only a few research centers performed such analysis. The USPIO contrast is off-label for medical imaging usage. Thus, despite that its safety profile is comparable to gadolinium, it is not widely available for imaging, and only a few centers performed USPIO MRI (62). In addition, to visualize inflammation, two imaging sessions (1–3 days apart) are required to enable macrophages to uptake the contrast agent. There is still a big gap to fill before these novel techniques can be used more widely. Better sequences and easier post-Processing pipelines will improve the availability of these techniques in the future.

# CONCLUSION

Collective data indicated that statin therapy could stabilize carotid plaques by significantly reducing LRNC of therapy as shown on serial carotid VW-MRI. Future studies and clinical practice could focus on changes in plaque characteristics (such as components) rather than morphological features. It is expected that more sensitive, clinically relevant, and preferably quantitative indicators to monitor therapeutic effects on intracranial plaques will be developed. VW-MRI may play an important role in assessing and guiding clinical statin therapies in the future.

# DATA AVAILABILITY STATEMENT

The original contributions presented in the study are included in the article/**Supplementary Material**,

further inquiries can be directed to the corresponding authors.

## AUTHOR CONTRIBUTIONS

PZ, YW, and CZ contributed to conception and design of the study. PZ organized the database, performed the statistical analysis, and wrote the first draft of the manuscript. YW, CZ, JS, MM-B, and YY wrote sections of the manuscript. All authors contributed to manuscript revision, read, and approved the submitted version.

## FUNDING

This work was supported by the Research Project of Healthcare for Cadres of Sichuan province, Grant No. 2021-229. CZ is supported by United States National Institute of Health (NIH) grant R00HL136883.

## SUPPLEMENTARY MATERIAL

The Supplementary Material for this article can be found online at: https://www.frontiersin.org/articles/10.3389/fcvm.2021.742935/full#supplementary-material

## REFERENCES

1. Cholesterol Treatment Trialists Collaboration, Baigent C, Blackwell L, Emberson J, Holland LE, Reith C, et al. Efficacy and safety of more intensive lowering of LDL cholesterol: a meta-analysis of data from 170,000 participants in 26 randomised trials. *Lancet.* (2010) 376:1670–81. doi: 10.1016/S0140-6736(10)61350-5
2. Sabatine MS, Giugliano RP, Keech AC, Honarpour N, Wiviott SD, Murphy SA, et al. Evolocumab and clinical outcomes in patients with cardiovascular disease. *N Engl J Med.* (2017) 376:1713–22. doi: 10.1056/NEJMoa1615664
3. Cao Y, Sun Y, Zhou B, Zhao HL, Zhu Y, Xu JR, et al. Atherosclerotic plaque burden of middle cerebral artery and extracranial carotid artery characterized by MRI in patients with acute ischemic stroke in China: association and clinical relevance. *Neurol Res.* (2017) 39:344–50. doi: 10.1080/01616412.2017.1281196
4. Chung JW, Cha J, Lee MJ, Yu IW, Park MS, Seo WK, et al. Intensive statin treatment in acute ischaemic stroke patients with intracranial atherosclerosis: a high-resolution magnetic resonance imaging study (STAMINA-MRI study). *J Neurol Neurosurg Psychiatry.* (2020) 91:204–11. doi: 10.1136/jnnp-2019-320893
5. Corti R, Fayad ZA, Fuster V, Worthley SG, Helft G, Chesebro J, et al. Effects of lipid-lowering by simvastatin on human atherosclerotic lesions: a longitudinal study by high-resolution, noninvasive magnetic resonance imaging. *Circulation.* (2001) 104:249–52. doi: 10.1161/01.CIR.104.3.249
6. Corti R, Fuster V, Fayad ZA, Worthley SG, Helft G, Smith D, et al. Lipid lowering by simvastatin induces regression of human atherosclerotic lesions: two years' follow-up by high-resolution noninvasive magnetic resonance imaging. *Circulation.* (2002) 106:2884–7. doi: 10.1161/01.CIR.0000041255.88750.F0
7. El Aidi H, Mani V, Weinshelbaum K, Aguiar S, Taniguchi H, Postley J, et al. Cross-sectional, prospective study of MRI reproducibility in the assessment of plaque burden of the carotid arteries and aorta. *Nat Clin Pract Cardiovasc Med.* (2009) 6:219–28. doi: 10.1038/ncpcardio1444
8. Zhang X, Zhu C, Peng W, Tian B, Chen L, Teng Z, et al. Scan-rescan reproducibility of high resolution magnetic resonance imaging of atherosclerotic plaque in the middle cerebral artery. *PLoS ONE.* (2015) 10:e0134913. doi: 10.1371/journal.pone.0134913
9. Sun J, Zhao XQ, Balu N, Hippe DS, Hatsukami TS, Isquith DA, et al. Carotid magnetic resonance imaging for monitoring atherosclerotic plaque progression: a multicenter reproducibility study. *Int J Cardiovasc Imaging.* (2015) 31:95–103. doi: 10.1007/s10554-014-0532-7
10. Cai J, Hatsukami TS, Ferguson MS, Kerwin WS, Saam T, Chu B, et al. *In vivo* quantitative measurement of intact fibrous cap and lipid-rich necrotic core size in atherosclerotic carotid plaque: comparison of high-resolution, contrast-enhanced magnetic resonance imaging and histology. *Circulation.* (2005) 112:3437–44. doi: 10.1161/CIRCULATIONAHA.104.528174
11. Takaya N, Cai J, Ferguson M, Yarnykh V, Chu B, Saam T, et al. Intra- and interreader reproducibility of magnetic resonance imaging for quantifying the lipid-rich necrotic core is improved with gadolinium contrast enhancement. *J Magn Reson Imaging.* (2006) 24:203–10. doi: 10.1002/jmri.20599
12. Alkhalil M, Chai JT, Choudhury RP. Plaque imaging to refine indications for emerging lipid-lowering drugs. *Eur Heart J Cardiovasc Pharmacother.* (2017) 3:58–67. doi: 10.1093/ehjcvp/pvw034
13. Du R, Cai J, Zhao XQ, Wang QJ, Liu DQ, Leng WX, et al. Early decrease in carotid plaque lipid content as assessed by magnetic resonance imaging during treatment of rosuvastatin. *BMC Cardiovasc Disord.* (2014) 14:83. doi: 10.1186/1471-2261-14-83
14. Mujaj B, Bos D, Selwaness M, Leening M, Kavousi M, Wentzel J, et al. Statin use is associated with carotid plaque composition: the rotterdam study. *Int J Cardiol.* (2018) 260:213–8. doi: 10.1016/j.ijcard.2018.02.111
15. Brinjikji W, Lehman VT, Kallmes DF, Rabinstein AA, Lanzino G, Murad MH, et al. The effects of statin therapy on carotid plaque composition and volume: a systematic review and meta-analysis. *J Neuroradiol.* (2017) 44:234–40. doi: 10.1016/j.neurad.2016.12.004
16. Hayden JA, Cote P, Bombardier C. Evaluation of the quality of prognosis studies in systematic reviews. *Ann Intern Med.* (2006) 144:427–37. doi: 10.7326/0003-4819-144-6-200603210-00010
17. *Cochrane Handbook for Systematic Reviews of Interventions.* Version 5.1.0. Availabli online at: https://handbook-5-1.Cochrane.Org (updated March 2011).
18. Higgins J, Thompson S, Deeks J, Altman D. Measuring inconsistency in meta-analyses. *BMJ.* (2003) 327:557–60. doi: 10.1136/bmj.327.7414.557
19. Corti R, Fuster V, Fayad ZA, Worthley SG, Helft G, Chaplin WF, et al. Effects of aggressive versus conventional lipid-lowering therapy by simvastatin on human atherosclerotic lesions: a prospective, randomized, double-blind trial with high-resolution magnetic resonance imaging. *J Am Coll Cardiol.* (2005) 46:106–12. doi: 10.1016/j.jacc.2005.03.054
20. Boussel L, Arora S, Rapp J, Rutt B, Huston J, Parker D, et al. Atherosclerotic plaque progression in carotid arteries: monitoring with high-spatial-resolution MR imaging–multicenter trial. *Radiology.* (2009) 252:789–96. doi: 10.1148/radiol.2523081798
21. Adams G, Greene J, Vick G, Harrist R, Kimball K, Karmonik C, et al. Tracking regression and progression of atherosclerosis in human carotid arteries using high-resolution magnetic resonance imaging. *Magn Reson Imaging.* (2004) 22:1249–58. doi: 10.1016/j.mri.2004.08.020
22. Underhill HR, Yuan C, Zhao XQ, Kraiss LW, Parker DL, Saam T, et al. Effect of rosuvastatin therapy on carotid plaque morphology and composition in moderately hypercholesterolemic patients: a high-resolution magnetic resonance imaging trial. *Am Heart J.* (2008) 155:584 e1–8. doi: 10.1016/j.ahj.2007.11.018
23. Saam T, Yuan C, Chu B, Takaya N, Underhill H, Cai J, et al. Predictors of carotid atherosclerotic plaque progression as measured by noninvasive magnetic resonance imaging. *Atherosclerosis.* (2007) 194:e34–42. doi: 10.1016/j.atherosclerosis.2006.08.016
24. Tang TY, Howarth SP, Miller SR, Graves MJ, Patterson AJ JM UK-I, et al. The ATHEROMA (atorvastatin therapy: effects on reduction of macrophage activity) study. evaluation using ultrasmall superparamagnetic iron oxide-enhanced magnetic resonance imaging in carotid disease. *J Am Coll Cardiol.* (2009) 53:2039–50. doi: 10.1016/j.jacc.2009.03.018
25. Sadat U, Howarth SP, Usman A, Taviani V, Tang TY, Graves MJ, et al. Effect of low-and high-dose atorvastatin on carotid artery distensibility using carotid

magnetic resonance imaging -a post-hoc sub group analysis of ATHEROMA (atorvastatin therapy: effects on reduction of macrophage activity) study. *J Atheroscler Thromb.* (2013) 20:46–56. doi: 10.5551/jat.12633
26. Sibley CT, Vavere AL, Gottlieb I, Cox C, Matheson M, Spooner A, et al. MRI-measured regression of carotid atherosclerosis induced by statins with and without niacin in a randomised controlled trial: the NIA plaque study. *Heart.* (2013) 99:1675–80. doi: 10.1136/heartjnl-2013-303926
27. Lee JM, Wiesmann F, Shirodaria C, Leeson P, Petersen SE, Francis JM, et al. Early changes in arterial structure and function following statin initiation: quantification by magnetic resonance imaging. *Atherosclerosis.* (2008) 197:951–8. doi: 10.1016/j.atherosclerosis.2007.09.001
28. Lee JM, Robson MD, Yu LM, Shirodaria CC, Cunnington C, Kylintireas I, et al. Effects of high-dose modified-release nicotinic acid on atherosclerosis and vascular function: a randomized, placebo-controlled, magnetic resonance imaging study. *J Am Coll Cardiol.* (2009) 54:1787–94
29. Migrino RQ, Bowers M, Harmann L, Prost R, LaDisa JF. Carotid plaque regression following 6-month statin therapy assessed by 3T cardiovascular magnetic resonance: comparison with ultrasound intima media thickness. *J Cardiovasc Magn Reson.* (2011) 13:37. doi: 10.1186/1532-429X-13-37
30. Zhao XQ, Dong L, Hatsukami T, Phan BA, Chu B, Moore A, et al. MR imaging of carotid plaque composition during lipid-lowering therapy a prospective assessment of effect and time course. *JACC Cardiovasc Imaging.* (2011) 4:977–86. doi: 10.1016/j.jcmg.2011.06.013
31. Du R, Cai J, Cui B, Wu H, Zhao X, Ye P. Rapid improvement in carotid adventitial angiogenesis and plaque neovascularization after rosuvastatin therapy in statin treatment-naïve subjects. *J Clin Lipidol.* (2019) 13:847–53. doi: 10.1016/j.jacl.2019.07.008
32. Feng T, Huang X, Liang Q, Liang Y, Yuan Y, Feng L, et al. Effects of pitavastatin on lipid-rich carotid plaques studied using high-resolution magnetic resonance imaging. *Clin Ther.* (2017) 39:620–9. doi: 10.1016/j.clinthera.2017.01.013
33. Alkhalil M, Biasiolli L, Akbar N, Galassi F, Chai JT, Robson MD, et al. T2 mapping MRI technique quantifies carotid plaque lipid, and its depletion after statin initiation, following acute myocardial infarction. *Atherosclerosis.* (2018) 279:100–6. doi: 10.1016/j.atherosclerosis.2018.08.033
34. Du R, Zhao XQ, Cai J, Cui B, Wu HM, Ye P. Changes in carotid plaque tissue composition in subjects who continued and discontinued statin therapy. *J Clin Lipidol.* (2016) 10:587–93. doi: 10.1016/j.jacl.2016.01.004
35. Dong L, Kerwin WS, Chen H, Chu B, Underhill HR, Neradilek MB, et al. Carotid artery atherosclerosis: effect of intensive lipid therapy on the vasa vasorum–evaluation by using dynamic contrast-enhanced MR imaging. *Radiology.* (2011) 260:224–31. doi: 10.1148/radiol.11101264
36. Hippe DS, Phan BAP, Sun J, Isquith DA, O'Brien KD, Crouse JR, et al. Lp(a) (lipoprotein(a)) levels predict progression of carotid atherosclerosis in subjects with atherosclerotic cardiovascular disease on intensive lipid therapy: an analysis of the aim-high (atherothrombosis intervention in metabolic syndrome with low hdl/high triglycerides: impact on global health outcomes) carotid magnetic resonance imaging substudy-brief report. *Arterioscler Thromb Vasc Biol.* (2018) 38:673–8. doi: 10.1161/ATVBAHA.117.310368
37. Chen X, Wang S, Lin L, Li Y, Zhang H. Drug effect of atorvastatin on middle cerebral atherosclerotic stenosis and high resolution NMR diagnosis. *Pak J Pharm Sci.* (2018) 31:1169–73.
38. Chung JW, Hwang J, Lee MJ, Cha J, Bang OY. Previous statin use and high-resolution magnetic resonance imaging characteristics of intracranial atherosclerotic plaque: the intensive statin treatment in acute ischemic stroke patients with intracranial atherosclerosis study. *Stroke.* (2016) 47:1789–96. doi: 10.1161/STROKEAHA.116.013495
39. Shah PK. Mechanisms of plaque vulnerability and rupture. *J Am Coll Cardiol.* (2003) 41(4 Suppl S):15S-22. doi: 10.1016/S0735-1097(02)02834-6
40. Aikawa M, Libby P. The vulnerable atherosclerotic plaque: pathogenesis and therapeutic approach. *Cardiovasc Pathol.* (2004) 13:125–38. doi: 10.1016/S1054-8807(04)00004-3
41. Virmani R, Burke A, Farb A, Kolodgie F. Pathology of the vulnerable plaque. *J Am Coll Cardiol.* (2006) 47:C13–8. doi: 10.1016/j.jacc.2005.10.065
42. Libby P, Aikawa M. Stabilization of atherosclerotic plaques: new mechanisms and clinical targets. *Nat Med.* (2002) 8:1257–62. doi: 10.1038/nm1102-1257
43. Porambo ME, DeMarco JK, MR imaging of vulnerable carotid plaque. *Cardiovasc Diagn Ther.* (2020) 10:1019–31. doi: 10.21037/cdt.2020.03.12
44. Sun J, Zhao XQ, Balu N, Neradilek MB, Isquith DA, Yamada K, et al. Carotid plaque lipid content and fibrous cap status predict systemic CV outcomes: the MRI substudy in AIM-HIGH. *JACC Cardiovasc Imaging.* (2017) 10:241–9. doi: 10.1016/j.jcmg.2016.06.017
45. Beddhu S, Boucher RE, Sun J, Balu N, Chonchol M, Navaneethan S, et al. Chronic kidney disease, atherosclerotic plaque characteristics on carotid magnetic resonance imaging, and cardiovascular outcomes. *BMC Nephrol.* (2021) 22:69. doi: 10.1186/s12882-021-02260-x
46. Brunner G, Virani S, Sun W, Liu L, Dodge R, Nambi V, et al. Associations between carotid artery plaque burden, plaque characteristics, and cardiovascular events: The ARIC carotid magnetic resonance imaging study. *JAMA cardiology.* (2021) 6:79–86. doi: 10.1001/jamacardio.2020.5573
47. Hellings W, Peeters W, Moll F, Piers S, van Setten J, Van der Spek P, et al. Composition of carotid atherosclerotic plaque is associated with cardiovascular outcome: a prognostic study. *Circulation.* (2010) 121:1941–50. doi: 10.1161/CIRCULATIONAHA.109.887497
48. Gkagkanasiou M, Ploussi A, Gazouli M, Efstathopoulos EP. USPIO-enhanced MRI neuroimaging: a review. *J Neuroimaging.* (2016) 26:161–8. doi: 10.1111/jon.12318
49. Kerwin WS, O'Brien KD, Ferguson MS, Polissar N, Hatsukami TS, Yuan C. Inflammation in carotid atherosclerotic plaque: a dynamic contrast-enhanced MR imaging study. *Radiology.* (2006) 241:459–68. doi: 10.1148/radiol.2412051336
50. Kerwin W, Hooker A, Spilker M, Vicini P, Ferguson M, Hatsukami T, et al. Quantitative magnetic resonance imaging analysis of neovasculature volume in carotid atherosclerotic plaque. *Circulation.* (2003) 107:851–6. doi: 10.1161/01.CIR.0000048145.52309.31
51. Ruehm S, Corot C, Vogt P, Kolb S, Debatin J. Magnetic resonance imaging of atherosclerotic plaque with ultrasmall superparamagnetic particles of iron oxide in hyperlipidemic rabbits. *Circulation.* (2001) 103:415–22. doi: 10.1161/01.CIR.103.3.415
52. Zervas N, Liszczak T, Mayberg M, Black P. Cerebrospinal fluid may nourish cerebral vessels through pathways in the adventitia that may be analogous to systemic vasa vasorum. *J Neurosurg.* (1982) 56:475–81. doi: 10.3171/jns.1982.56.4.0475
53. Moreno PR, Purushothaman KR, Sirol M, Levy AP, Fuster V. Neovascularization in human atherosclerosis. *Circulation.* (2006) 113:2245–52. doi: 10.1161/CIRCULATIONAHA.105.578955
54. Langheinrich AC, Kampschulte M, Buch T, Bohle RM. Vasa vasorum and atherosclerosis - quid novi? *Thromb Haemost.* (2007) 97:873–9. doi: 10.1160/TH06-12-0742
55. Moulton KS. Plaque angiogenesis and atherosclerosis. *Curr Atheroscler Rep.* (2001) 3:225–33. doi: 10.1007/s11883-001-0065-0
56. O'Brien K, Hippe D, Chen H, Neradilek M, Probstfield J, Peck S, et al. Longer duration of statin therapy is associated with decreased carotid plaque vascularity by magnetic resonance imaging. *Atherosclerosis.* (2016) 245:74–81. doi: 10.1016/j.atherosclerosis.2015.11.032
57. Mandell DM, Mossa-Basha M, Qiao Y, Hess CP, Hui F, Matouk C, et al. Intracranial vessel wall MRI: principles and expert consensus recommendations of the American society of neuroradiology. *AJNR Am J Neuroradiol.* (2017) 38:218–29. doi: 10.3174/ajnr.A4893
58. Lee HN, Ryu CW, Yun SJ. Vessel-wall magnetic resonance imaging of intracranial atherosclerotic plaque and ischemic stroke: a systematic review and meta-analysis. *Front Neurol.* (2018) 9:1032. doi: 10.3389/fneur.2018.01032
59. Zhu C, Sadat U, Patterson AJ, Teng Z, Gillard JH, Graves MJ. 3D high-resolution contrast enhanced MRI of carotid atheroma–a technical update. *Magn Reson Imaging.* (2014) 32:594–7. doi: 10.1016/j.mri.2014.01.019
60. Saba L, Yuan C, Hatsukami TS, Balu N, Qiao Y, DeMarco JK, et al. Carotid artery wall imaging: perspective and guidelines from the ASNR vessel wall imaging study group and expert consensus recommendations of

the American society of neuroradiology. *AJNR Am J Neuroradiol.* (2018) 39:E9–E31. doi: 10.3174/ajnr.A5488
61. Brinjikji W, DeMarco JK, Shih R, Lanzino G, Rabinstein AA, Hilditch CA, et al. Diagnostic accuracy of a clinical carotid plaque MR protocol using a neurovascular coil compared to a surface coil protocol. *J Magn Reson Imaging.* (2018) 48:1264–72. doi: 10.1002/jmri.25984
62. Hope MD, Hope TA, Zhu C, Faraji F, Haraldsson H, Ordovas KG, et al. Vascular imaging with ferumoxytol as a contrast agent. *AJR Am J Roentgenol.* (2015) 205:W366–73. doi: 10.2214/AJR.15.14534

**Conflict of Interest:** The authors declare that the research was conducted in the absence of any commercial or financial relationships that could be construed as a potential conflict of interest.

**Publisher's Note:** All claims expressed in this article are solely those of the authors and do not necessarily represent those of their affiliated organizations, or those of the publisher, the editors and the reviewers. Any product that may be evaluated in this article, or claim that may be made by its manufacturer, is not guaranteed or endorsed by the publisher.

frontiers in Cardiovascular Medicine

CASE REPORT
published: 21 January 2022
doi: 10.3389/fcvm.2021.775536

# Case Report: Dynamic Changes in Hemodynamics During the Formation and Progression of Intracranial Aneurysms

*Xiaodong Zhai*[1,2†], *Yadong Wang*[1,2,3†], *Gang Fang*[4], *Peng Hu*[1,2*], *Hongqi Zhang*[1,2*] and *Chengcheng Zhu*[5]

[1] Department of Neurosurgery, Xuanwu Hospital, Capital Medical University, Beijing, China, [2] China International Neuroscience Institute (China-INI), Beijing, China, [3] Department of Neurosurgery, Weihai Municipal Hospital, Weihai, China, [4] Department of R&D, UnionStrong (Beijing) Technology Co. Ltd., Beijing, China, [5] Department of Radiology, University of Washington School of Medicine, Seattle, WA, United States

OPEN ACCESS

**Edited by:**
Luca Biasiolli,
University of Oxford, United Kingdom

**Reviewed by:**
Natallia Maroz-Vadalazhskaya,
Belarusian State Medical University, Belarus
Ethan Winkler,
University of California, San Francisco, United States

***Correspondence:**
Peng Hu
doctor_hupeng@163.com
Hongqi Zhang
xwzhanghq@163.com

[†]These authors have contributed equally to this work

**Specialty section:**
This article was submitted to Cardiovascular Imaging, a section of the journal Frontiers in Cardiovascular Medicine

**Received:** 14 September 2021
**Accepted:** 28 December 2021
**Published:** 21 January 2022

**Citation:**
Zhai X, Wang Y, Fang G, Hu P, Zhang H and Zhu C (2022) Case Report: Dynamic Changes in Hemodynamics During the Formation and Progression of Intracranial Aneurysms. Front. Cardiovasc. Med. 8:775536. doi: 10.3389/fcvm.2021.775536

Despite the devastating consequences of aneurysmal subarachnoid hemorrhage (SAH), the mechanisms underlying the formation, progression, and rupture of intracranial aneurysms (IAs) are complex and not yet fully clear. In a real-world situation, continuously observing the process of aneurysm development in humans appears unrealistic, which also present challenges for the understanding of the underlying mechanism. We reported the relatively complete course of IA development in two real patients. On this basis, computational fluid dynamics simulation (CFD) was performed to evaluate the changes in hemodynamics and analyze the mechanism underlying the formation, progression, and rupture of IAs. Our results suggested that the formation and progression of IAs can be a dynamic process, with constantly changing hemodynamic characteristics. CFD analysis based on medical imaging provides the opportunity to study the hemodynamic conditions over time. From these two rare cases, we found that concentrated high-velocity inflow jets, flows with vortex structures, extremely high WSS, and a very steep WSSG were correlated with the formation of IAs. Complex multi-vortex flows are possibly related to IAs prior to growth, and the rupture of IAs is possibly related to low WSS, extreme instability and complexity of flow patterns. Our findings provide unique insight into the theoretical hemodynamic mechanism underlying the formation and progression of IAs. Given the small sample size the findings of this study have to be considered preliminary and exploratory.

**Keywords: intracranial aneurysms, natural history, hemodynamic analysis, dynamic changes, computational fluid dynamics**

## INTRODUCTION

Intracranial aneurysms (IAs) are a common neurovascular disease with an estimated prevalence of 3–5% in the general population (1–3). Most cases of non-traumatic subarachnoid hemorrhage (SAH), which is a devastating condition with high rates of mortality and morbidity, is caused by the rupture of IAs (4–6). The natural history of aneurysmal formation, growth, and eventual rupture are thought to be closely related to the progressive degradation of the vascular wall in response

to abnormal hemodynamics, especially, the wall shear stress (WSS) computed by computational fluid dynamics (CFD) analysis (7–10). Abnormally low or high WSS at aneurysm regions are both commonly seen on explanation of evolution of IAs (8, 11).

In a real-world situation, it is extremely rare for imaging examinations to capture the continuous progression from normal cerebral arteries to aneurysmal formation and subsequent growth and rupture in humans. It is rare to have 3D imaging of the normal artery before the development of intracranial aneurysm, and then such an aneurysm ruptured during imaging follow up. Therefore, most of the explorations can only focus on a certain stage in the development of IAs, such as the morphological or hemodynamic analysis of the rupture risk of IAs (10, 12–15). In addition, there are differences in hemodynamic analysis methods and CFD modeling used in different studies, which leads to poor comparability between the quantitative results of hemodynamics. Thus, currently, the hemodynamic mechanism of the formation, progression and rupture of IAs is not conclusively understood, and contradictory findings are frequently seen.

In this study, we reported a relatively complete progression from normal intracranial arteries to aneurysmal formation, growth, and even rupture in real patients. Furthermore, we performed hemodynamic analysis on these patients with the aim of assessing the changes in hemodynamics to provide a theoretical basis for the underlying mechanism of the formation and progression of IAs.

## CASE DESCRIPTION

Here, we report two patients. (1) The first patient was a 56-year-old female with a history of hypertension and coronary heart disease who presented with a 10-day history of limb weakness (November 18, 2014). Cranial magnetic resonance imaging (MRI) and magnetic resonance angiography (MRA) assessments did not reveal obvious abnormalities (**Figure 1A**, Baseline), and the patient's symptoms resolved spontaneously without any interventions. MRA reexamination of the patient 4 years later (October 9, 2018) showed a newly formed saccular aneurysm with a diameter of 3.2 mm in the left posterior communicating artery (**Figure 1A**, Formation). Nevertheless, due to the small size of the aneurysm, the patient opted for follow-up observation. She was diagnosed with acute SAH by cranial computed tomography (CT) performed in response to a sudden headache 4 months later (February 14, 2019). CT angiography (CTA) showed that the aneurysm had significantly increased in size, reaching a diameter of 6.9 mm (**Figure 1A**, Rupture). Microsurgical clipping of the aneurysm was immediately performed, and the patient recovered well in the ward postoperatively. (2) The second patient shared some similarities with the first in terms of the developmental process of the aneurysm. Patient 2 was a 47-year-old female who underwent MRA assessment due to dizziness on November 13, 2016; the assessment did not detect any obvious abnormalities. A newly formed basilar tip aneurysm and aneurysmal enlargement were observed in the follow-up MRA examinations performed on October 9, 2018 (**Figure 1B**, Formation), and June 7, 2020 (**Figure 1B**, Growth; from 2.1 to 3.8 mm in diameter), respectively. The patient eventually received successful endovascular treatment after aneurysmal enlargement occurred.

## IMAGE ACQUISITION AND RECONSTRUCTION

For this study, all the three-dimensional (3D) TOF- MRA were performed on the same 3.0 T Siemens scanner (Erlangen, Germany) in the same department except the Patient 1 had undergone 3D CTA at the third follow-up due to the acute rupture of aneurysm. Examinations for TOF-MRA were performed with the following parameters: TR, 20 ms; TE, 3.6 ms; slice thickness, 0.7 mm; field of view, 210 mm; flip angle, 18°; number of slices, 140; total acquisition time, 3:17 min; and voxel size, $0.3 \times 0.3 \times 0.7$ mm.

Growth of aneurysm was defined as a size increase of at least 1.0 mm in any dimension on angiographic or cross-sectional imaging (16). The tomographic data and the morphological parameters of the enrolled patients were recorded based on the Computer-Assisted Semi-Automated Measurement (CASAM) (17). CFD analysis was applied to assess these vessels and aneurysms to assess the differences in hemodynamics.

The methods used for image reconstruction and CFD simulation of hemodynamic studies were the same as described in our previous publications (18–21). CFD results are depended on the quality of image segmentation process. To maintain the consistency of the models within the same patient, we performed image registration and fusion *via* 3D Slicer (version 4.5.0), then an iterated select threshold value was applied for image segmentation to the same patient. In the subsequent thresholding step, we used the Mimics Medical software (Version 19.0, Materialize, Leuven, Belgium) to segment the models in order to preserve the length and shape of the vessel, while only the aneurysm or region of aneurysm formation was different (22). In the end, we saved the segmented surface geometry in the Standard Tessellation Language format as the input for the next step.

## CFD MODELING AND HEMODYNAMICS ANALYSIS

Each 3D aneurysm model was subdivided into aneurysm sac and parent artery regions before meshing. Then, each 3D model geometry was imported into the ICEM CFD software (ANSYS Inc., Canonsburg, Pennsylvania, USA). Different mesh sizes we set for different parts. For the inlet, outlet, and sac part, we set 0.1 mm that meets most aneurysms' size, and 0.3 mm was set for the parent artery part. The total of finite volume tetrahedral element grids are approximately 1 million with four layers of prism elements for CFD simulations.

After meshing, ANSYS CFX 18.0 (ANSYS Inc.) was then used for hemodynamic simulation. A Newtonian fluid was

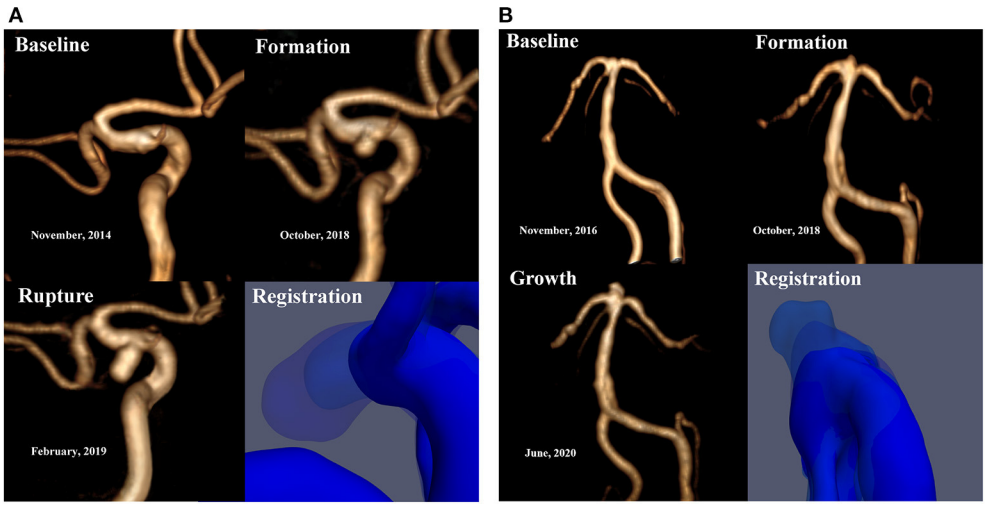


**FIGURE 1 | (A)** Patient 1 is a 56-year-old female. No significant abnormalities were observed by the baseline MRA. MRA reexamination about 4 years later showed a newly formed saccular aneurysm with a diameter of 3.2 mm in the left posterior communicating artery. CTA showed that the aneurysm had significantly increased in size, reaching a diameter of 6.9 mm. **(B)** Patient 2 is a 47-year-old female. No significant abnormalities were observed by the baseline MRA. A newly formed basilar tip aneurysm and aneurysmal enlargement were observed in the subsequent MRA examinations at follow-up (from 2.1 to 3.8 mm in diameter). Registration of 3D surfaces with different degrees of transparency showed changes on continuous follow-up angiography.

assumed, and a density of 1,060 kg/m$^3$ and a dynamic viscosity of 0.0035 N s/m$^2$ were modeled. The vessel wall was assumed to be rigid with a no-slip boundary. Because the patient-specific boundary conditions were not available, the inflow boundary condition was a representative pulsatile velocity profile obtained from the averaged normal human (23). A traction-free boundary condition was applied to all outlets (24). Initial pressure and velocity were set to zero. Three cardiac cycles were simulated to minimize transient numerical errors. Results from the third simulated cardiac cycle were collected as output for the final analyses. Validation of these methods (consistency, reliability) has been demonstrated in our previous publication (18, 19).

To analyze the hemodynamics changes that occur during the formation and progression of IAs, vital hemodynamic parameters including WSS, wall shear stress gradient (WSSG), pressure and energy loss (EL) were calculated based on the simulated pulsatile flow simulations (18, 19). Normalized wall shear stress (NWSS) and normalized pressure (NP), defined as the WSS and pressure of the aneurysm wall divided by that of the parent artery wall, respectively, were calculated (25, 26). The region of aneurysmal formation was marked by the registration technique through comparative cross-sectional imaging before and after aneurysm formation.

## RESULTS

The qualitative hemodynamic analysis revealed that, prior to aneurysm formation, the regions featured concentrated high-velocity inflow jets (**Figure 2D**) or flows with vortex structures (**Figure 2B**). A complex multi-vortex flow is associated with aneurysms prior to growth (**Figures 2B,D**), and the future aneurysm rupture is related to extreme instability and complexity of blood flow patterns (**Figure 2B**).

As shown in **Figures 2**, **3**, the results from quantitative hemodynamic analysis indicated that the WSS, WSSG, and pressure in the regions prior to aneurysm formation were significantly higher than those in the parent artery. Compared with the parent artery, the value of NWSS and NP of regions prior to aneurysm formation are larger. In the progression from normal vessels to aneurysmal formation, the WSSG and EL increased in both patients. As the aneurysm further grew, the WSS and WSSG decreased, and the pressure and EL increased (Patient 2, **Figure 3B**). As shown in **Figure 3A**, the WSS and WSSG of ruptured aneurysms were decreased, and the EL was increased (Patient 1, **Figure 3A**). The detailed numerical results from hemodynamic analysis of patients are summarized in **Table 1**.

## DISCUSSION

In this study, we reported a relatively complete progression from normal intracranial arteries to aneurysmal formation and growth in two real patients. Patient 1 experienced even rupture at the third follow-up. Furthermore, we investigated the changes in hemodynamics with the aim of providing a theoretical basis for the underlying mechanism of the formation and progression of IAs. The results of this study indicated that the formation and progression of IAs can be a dynamic process, with constantly changing hemodynamic characteristics.

Very few subjects had prophylactic cerebrovascular imaging examination prior to the formation of an aneurysm; thus, previous studies assessing the hemodynamic characteristics in the regions before aneurysmal formation usually did so after

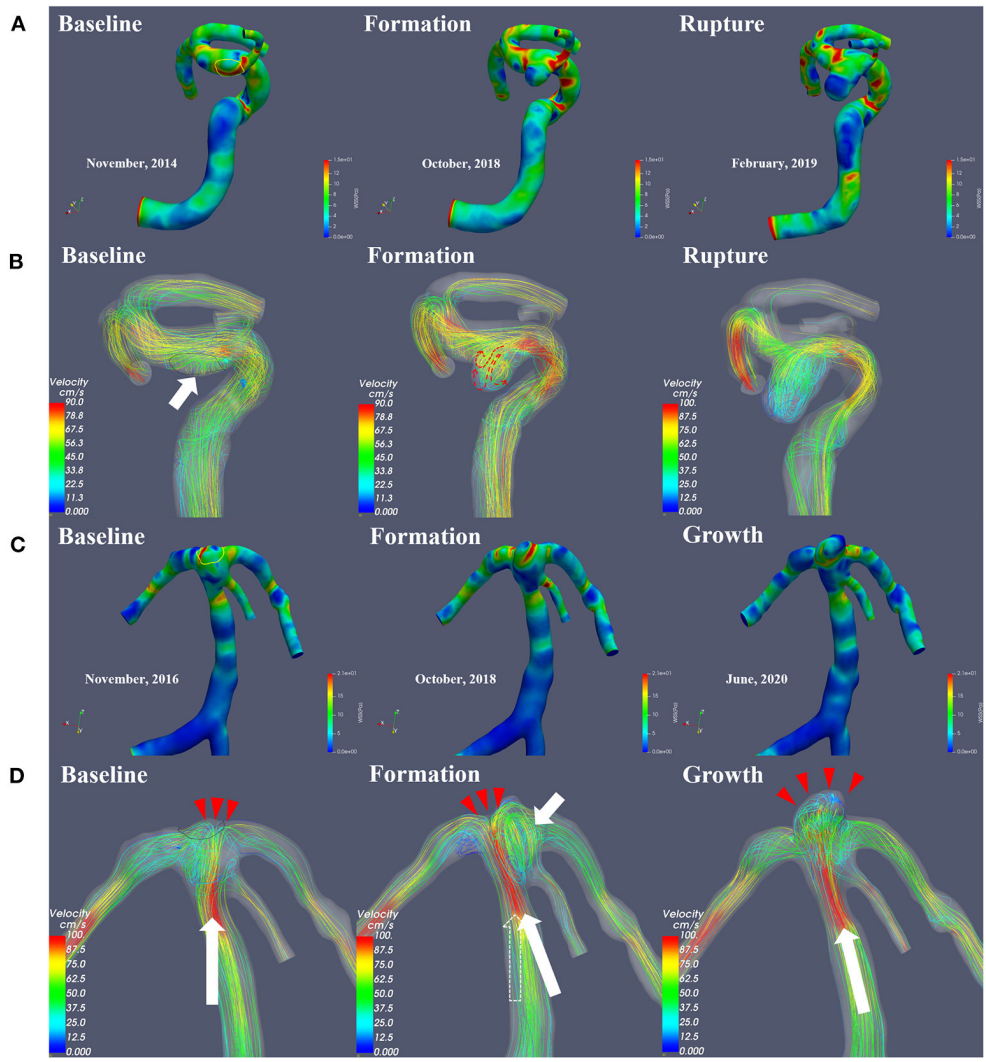


**FIGURE 2 |** This figure illustrates the change in hemodynamic parameters during the formation, progression and rupture of IAs. The WSS distribution **(A,C)** and flow velocity profile **(B,D)** were shown, respectively. The area within the yellow line is the region of aneurysmal formation marked by the registration technique. Prior to aneurysm formation, the regions feature flows with vortex structures (**B**, short white arrow). In the impact region (**D**, Baseline, red arrows) of the concentrated high-velocity inflow jet (**D**, Baseline, long white arrow indicates blood flow direction), a newly formed basilar tip aneurysm was visible on follow-up angiography **(D)**. Affected by vortex flow after the formation of the aneurysm (**D**, Formation, white short arrow), the main direction of flow shifted (**D**, Formation, from the original dotted arrow to the long white arrow), causing saccular dilatation in the new impact region (**D**, Formation, red arrows), and the size of the aneurysm increased (**D**, Growth). A complex multi-vortex flow is associated with future aneurysm growth, and rupture is related to extreme instability and complexity of blood flow patterns.

virtually removing the aneurysms and reconstructing the parent artery, thereby restoring an image of the normal artery before aneurysmal formation (27–29). However, the geometry of the parent artery can change after the aneurysm formation. In the present study, the results from real patients revealed that the regions of future aneurysm formation featured concentrated high-velocity inflow jets or flows with vortex structures. Consistent with findings from previous virtual studies (14, 30), the WSS, WSSG, and pressure at the future aneurysm sites were significantly higher than those in the parent artery. Narrowing proximal vessel leads to flow acceleration that accentuates WSS and spatial gradients at the bifurcation apex of Patient 2, large branch angles and proximal parent vessel tapering may increase the risk of IA formation (31, 32).

The contribution of hemodynamics to the progression of IAs is complex and controversial, and both high-WSS and low-WSS theories have been proposed to explain the growth and rupture of IAs (8, 33–35). The hemodynamic results of natural history data revealed that the hemodynamic parameters of IAs have constantly changed with the development of the aneurysm, and increasing or decreasing tendency presented in different stages of development. It implies that the formation and progression of IAs could be a dynamic process in which the hemodynamic characteristics are constantly changing. The

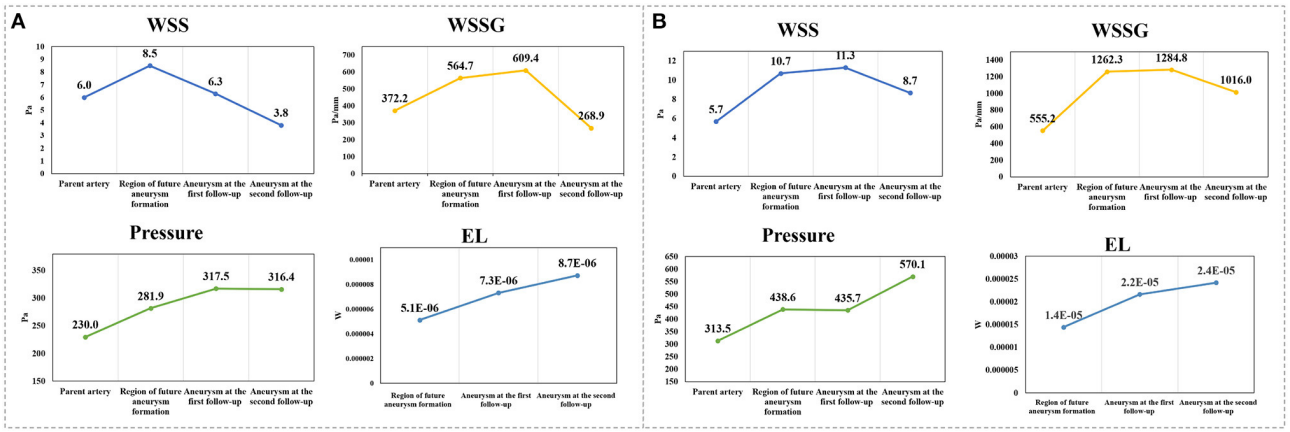


**FIGURE 3 | (A,B)** Display the trends in the main hemodynamic parameters of patient 1 and patient 2, respectively, during continuous follow-up angiography. WSS, wall shear stress; WSSG, wall shear stress gradient; EL, energy loss.

**TABLE 1 |** The hemodynamic parameters result of included patients.

| Patient no. | Subject | Mean WSS (Pa) | Mean NWSS | Mean WSSG (Pa/mm) | Mean pressure (Pa) | Mean NP | Energy loss (W) |
|---|---|---|---|---|---|---|---|
| Patient 1 | Parent artery | 6.0 | 1 | 372.2 | 230.0 | 1 | – |
| Patient 1 | Baseline | 8.5 | 1.4 | 564.7 | 281.9 | 1.2 | 5.12E-06 |
| Patient 1 | Formation | 6.3 | 0.9 | 609.4 | 317.5 | 1.2 | 7.33E-06 |
| Patient 1 | Rupture | 3.8 | 0.6 | 268.9 | 316.4 | 1.1 | 8.74E-06 |
| Patient 2 | Parent artery | 5.7 | 1 | 555.2 | 313.5 | 1 | – |
| Patient 2 | Baseline | 10.7 | 1.9 | 1,262.3 | 438.6 | 1.4 | 1.44E-05 |
| Patient 2 | Formation | 11.3 | 2.0 | 1,284.8 | 435.7 | 1.4 | 2.17E-05 |
| Patient 2 | Growth | 8.7 | 1.4 | 1,016.0 | 570.1 | 1.3 | 2.42E-05 |

*WSS, wall shear stress; WSSG, wall shear stress gradient; NWSS, normalized wall shear stress; NP, normalized pressure.*

complex interactions of hemodynamics in the progression of IAs are difficult to accommodate within high-WSS, low-WSS, or any other single existing theories. In light of previous work and our present results, we inferred that in the early stages of aneurysm formation and development, the WSS and WSSG of the aneurysm, which are higher than those of the parent artery, may continue to increase in the short term. The hemodynamic energy of the blood flowing through the aneurysm sac acts on the aneurysm wall. As the size of the aneurysm continues to grow, the energy loss of the blood flow through the aneurysm gradually increases, and the WSS and WSSG subsequently decrease. Low WSS was considered to be associated with aneurysm rupture (14, 36). As a result of degenerative remodeling, the aneurysm wall becomes too fragile to resist the stress of blood flow, and the aneurysm ultimately ruptures.

## LIMITATION

The primary limitation of this study was the small sample size, and the follow-up time varies. As the natural history data from developing IAs is very rare, the present study was only able to include two cases. Second, the image of Patient 1 after aneurysm ruptured was performed using CTA instead of MRA, which may lead to biased results. In addition, owing to the missing of patients' specific inflow conditions, the inflow boundary condition was a representative pulsatile velocity profile. But the intra-individual flow variation and the variation on subsequent hemodynamic simulations using the inlet flow as a boundary condition in serially acquired 2D phase-contrast MR data were considered relatively small for hemodynamics patterns (big for absolute values) (37). Common limitations for the hemodynamic simulations are a Newtonian fluid and have rigid walls for modeling blood vessels, which could lead to biased results. The additional limitation seems to be homeostasis, lipid status and medical treatment from the same patient over different periods, but in case of describing two cases, only the statistical impact of these clinical factors is very difficult to measure. Nevertheless, even limitations exist, this study based on rare and precious data inspires researchers for understanding the underlying hemodynamic mechanism of IAs development.

## CONCLUSION

The formation and progression of IAs can be a dynamic process, with constantly changing hemodynamic characteristics. CFD analysis based on medical imaging provides the opportunity to study the hemodynamic conditions over time and is a promising tool to study the pathology of intracranial aneurysm *in vivo*. Concentrated high-velocity inflow jets, flows with vortex structures, extremely high WSS, and a very steep WSSG were correlated with the formation of IAs in the two cases. Complex multi-vortex flows are possibly related to IAs prior to growth, and the rupture of IAs is possibly related to low WSS, extreme instability and complexity of flow patterns. Our findings provide unique insight into the theoretical hemodynamic mechanism underlying the formation and progression of IAs. Owing to the small sample size, the findings of this study have to be considered preliminary and exploratory.

## DATA AVAILABILITY STATEMENT

The original contributions presented in the study are included in the article/supplementary material, further inquiries can be directed to the corresponding authors.

## ETHICS STATEMENT

The studies involving human participants were reviewed and approved by the Ethics Board of Xuanwu Hospital, Capital Medical University. The patients/participants provided their written informed consent to participate in this study. Written informed consent was obtained from the individual(s) for the publication of any potentially identifiable images or data included in this article.

## AUTHOR CONTRIBUTIONS

XZ, YW, GF, PH, HZ, and CZ contributed to the conception, design, analysis, and interpretation of the data as well as to drafting the article and revising it critically. All authors have read and approved the final version of the manuscript.

## FUNDING

This work was supported by National Key R&D program of China with grant 2016YFC1300800, Beijing Municipal Administration of Hospitals' Ascent Plan with grant DFL20180801, and the Beijing Scientific and Technologic Project (Z201100005520021).

## REFERENCES

1. Hackenberg KAM, Hanggi D, Etminan N. Unruptured intracranial aneurysms. *Stroke.* (2018) 49:2268–75. doi: 10.1161/STROKEAHA.118.021030
2. Thompson BG, Brown RD Jr, Amin-Hanjani S, Broderick JP, Cockroft KM, Connolly ES Jr, et al. Guidelines for the management of patients with unruptured intracranial aneurysms: a guideline for healthcare professionals from the American Heart Association/American Stroke Association. *Stroke.* (2015) 46:2368–400. doi: 10.1161/STR.0000000000000070
3. Vlak MH, Algra A, Brandenburg R, Rinkel GJ. Prevalence of unruptured intracranial aneurysms, with emphasis on sex, age, comorbidity, country, and time period: a systematic review and meta-analysis. *Lancet Neurol.* (2011) 10:626–36. doi: 10.1016/S1474-4422(11)70109-0
4. Brown RD, Broderick JP. Unruptured intracranial aneurysms: epidemiology, natural history, management options, and familial screening. *Lancet Neurol.* (2014) 13:393–404. doi: 10.1016/S1474-4422(14)70015-8
5. Etminan N, Rinkel GJ. Unruptured intracranial aneurysms: development, rupture and preventive management. *Nat Rev Neurol.* (2016) 12:699–713. doi: 10.1038/nrneurol.2016.150
6. van Gijn J, Kerr RS, Rinkel GJ. Subarachnoid haemorrhage. *Lancet.* (2007) 369:306–18. doi: 10.1016/S0140-6736(07)60153-6
7. Kulcsar Z, Ugron A, Marosfoi M, Berentei Z, Paal G, Szikora I. Hemodynamics of cerebral aneurysm initiation: the role of wall shear stress and spatial wall shear stress gradient. *AJNR Am J Neuroradiol.* (2011) 32:587–94. doi: 10.3174/ajnr.A2339
8. Meng H, Tutino VM, Xiang J, Siddiqui A. High WSS or low WSS? Complex interactions of hemodynamics with intracranial aneurysm initiation, growth, and rupture: toward a unifying hypothesis. *AJNR Am J Neuroradiol.* (2014) 35:1254–62. doi: 10.3174/ajnr.A3558
9. Meng H, Wang Z, Hoi Y, Gao L, Metaxa E, Swartz DD, et al. Complex hemodynamics at the apex of an arterial bifurcation induces vascular remodeling resembling cerebral aneurysm initiation. *Stroke.* (2007) 38:1924–31. doi: 10.1161/STROKEAHA.106.481234
10. Tanaka, K., Takao, H., Suzuki, T., Fujimura, S., Uchiyama, Y., Otani, K., et al. Relationship between hemodynamic parameters and cerebral aneurysm initiation. *Annu. Int. Conf. IEEE Eng. Med. Biol. Soc.* (2018) 2018:1347–50. doi: 10.1109/EMBC.2018.8512466
11. Shojima M, Oshima M, Takagi K, Torii R, Hayakawa M, Katada K, et al. Magnitude and role of wall shear stress on cerebral aneurysm: computational fluid dynamic study of 20 middle cerebral artery aneurysms. *Stroke.* (2004) 35:2500–5. doi: 10.1161/01.STR.0000144648.89172.0f
12. Liu J, Xiang J, Zhang Y, Wang Y, Li H, Meng H, et al. Morphologic and hemodynamic analysis of paraclinoid aneurysms: ruptured versus unruptured. *J Neurointerv Surg.* (2014) 6:658–63. doi: 10.1136/neurintsurg-2013-010946
13. Sforza DM, Kono K, Tateshima S, Vinuela F, Putman C, Cebral JR. Hemodynamics in growing and stable cerebral aneurysms. *J Neurointerv Surg.* (2016) 8:407–12. doi: 10.1136/neurintsurg-2014-011339
14. Soldozy S, Norat P, Elsarrag M, Chatrath A, Costello JS, Sokolowski JD, et al. The biophysical role of hemodynamics in the pathogenesis of cerebral aneurysm formation and rupture. *Neurosurg Focus.* (2019) 47:E11. doi: 10.3171/2019.4.FOCUS19232
15. Zhai XD, Yu JX, Li CJ, Ren J, Ji Z, He C, et al. Morphological characteristics of pericallosal artery aneurysms and their high propensity for rupture. *World Neurosurg.* (2020) 133:e320–6. doi: 10.1016/j.wneu.2019.09.003
16. Hackenberg KAM, Etminan N, Wintermark M, Meyers PM, Lanzino G, Rüfenacht D, et al. Common data elements for radiological imaging of patients with subarachnoid hemorrhage: proposal of a multidisciplinary research group. *Neurocrit Care.* (2019) 30:60–78. doi: 10.1007/s12028-019-00728-1
17. Geng J, Hu P, Ji Z, Li C, Li L, Shen J, et al. Accuracy and reliability of computer-assisted semi-automated morphological analysis of intracranial aneurysms: an experimental study with digital phantoms and clinical aneurysm cases. *Int J Comput Assist Radiol Surg.* (2020) 15:1749–59. doi: 10.1007/s11548-020-02218-8
18. Hu P, Qian Y, Lee CJ, Zhang HQ, Ling F. The energy loss may predict rupture risks of anterior communicating aneurysms: a preliminary result. *Int J Clin Exp Med.* (2015) 8:4128–33.
19. Hu P, Qian Y, Zhang Y, Zhang HQ, Li Y, Chong W, et al. Blood flow reduction of covered small side branches after flow diverter treatment: a computational fluid hemodynamic quantitative analysis. *J Biomech.* (2015) 48:895–8. doi: 10.1016/j.jbiomech.2015.02.015

20. Qin H, Yang Q, Zhuang Q, Long J, Yang F, Zhang H. Morphological and hemodynamic parameters for middle cerebral artery bifurcation aneurysm rupture risk assessment. *J Korean Neurosurg Soc.* (2017) 60:504–10. doi: 10.3340/jkns.2017.0101.009
21. Zhai X, Geng J, Zhu C, Yu J, Li C, Jiang N, et al. Risk factors for pericallosal artery aneurysm rupture based on morphological computer-assisted semiautomated measurement and hemodynamic analysis. *Front Neurosci.* (2021) 15:1570. doi: 10.3389/fnins.2021.759806
22. Liu X, Haraldsson H, Wang Y, Kao E, Ballweber M, Martin AJ, et al. A volumetric metric for monitoring intracranial aneurysms: repeatability and growth criteria in a longitudinal MR imaging study. *AJNR Am J Neuroradiol.* (2021) 42, 1591–97. doi: 10.3174/ajnr.A7190
23. Ford MD, Alperin N, Lee SH, Holdsworth DW, Steinman DA. Characterization of volumetric flow rate waveforms in the normal internal carotid and vertebral arteries. *Physiol Meas.* (2005) 26:477–88. doi: 10.1088/0967-3334/26/4/013
24. Cebral JR, Castro MA, Burgess JE, Pergolizzi RS, Sheridan MJ, Putman CM. Characterization of cerebral aneurysms for assessing risk of rupture by using patient-specific computational hemodynamics models. *AJNR Am J Neuroradiol.* (2005) 26:2550–9.
25. Jou LD, Lee DH, Morsi H, Mawad ME. Wall shear stress on ruptured and unruptured intracranial aneurysms at the internal carotid artery. *AJNR Am J Neuroradiol.* (2008) 29:1761–7. doi: 10.3174/ajnr.A1180
26. Yuan J, Li Z, Jiang X, Lai N, Wang X, Zhao X, et al. Hemodynamic and morphological differences between unruptured carotid-posterior communicating artery bifurcation aneurysms and infundibular dilations of the posterior communicating artery. *Front Neurol.* (2020) 11:741. doi: 10.3389/fneur.2020.00741
27. Lauric A, Hippelheuser J, Safain MG, Malek AM. Curvature effect on hemodynamic conditions at the inner bend of the carotid siphon and its relation to aneurysm formation. *J Biomech.* (2014) 47:3018–27. doi: 10.1016/j.jbiomech.2014.06.042
28. Mantha A, Karmonik C, Benndorf G, Strother C, Metcalfe R. Hemodynamics in a cerebral artery before and after the formation of an aneurysm. *Am J Neuroradiol.* (2006) 27:1113–8.
29. Watanabe T, Isoda H, Takehara Y, Terada M, Naito T, Kosugi T, et al. Hemodynamic vascular biomarkers for initiation of paraclinoid internal carotid artery aneurysms using patient-specific computational fluid dynamic simulation based on magnetic resonance imaging. *Neuroradiology.* (2018) 60:545–55. doi: 10.1007/s00234-018-2002-8
30. Can A, Du R. Association of hemodynamic factors with intracranial aneurysm formation and rupture: systematic review and meta-analysis. *Neurosurgery.* (2016) 78:510–20. doi: 10.1227/NEU.0000000000001083
31. Lauric A, Greim-Kuczewski K, Antonov A, Dardik G, Magida JK, Hippelheuser JE, et al. Proximal parent vessel tapering is associated with aneurysm at the middle cerebral artery bifurcation. *Neurosurgery.* (2019) 84:1082–9. doi: 10.1093/neuros/nyy152
32. Sasaki T, Kakizawa Y, Yoshino M, Fujii Y, Yoroi I, Ichikawa Y, et al. Numerical analysis of bifurcation angles and branch patterns in intracranial aneurysm formation. *Neurosurgery.* (2019) 85:E31–9. doi: 10.1093/neuros/nyy387
33. Boussel L, Rayz V, McCulloch C, Martin A, Acevedo-Bolton G, Lawton M, et al. Aneurysm growth occurs at region of low wall shear stress: patient-specific correlation of hemodynamics and growth in a longitudinal study. *Stroke.* (2008) 39:2997–3002. doi: 10.1161/STROKEAHA.108.521617
34. Penn DL, Komotar RJ, Sander Connolly E. Hemodynamic mechanisms underlying cerebral aneurysm pathogenesis. *J Clin Neurosci.* (2011) 18:1435–8. doi: 10.1016/j.jocn.2011.05.001
35. Shojima M, Nemoto S, Morita A, Oshima M, Watanabe E, Saito N. Role of shear stress in the blister formation of cerebral aneurysms. *Neurosurgery.* (2010) 67:1268-74; discussion:1274–65. doi: 10.1227/NEU.0b013e3181f2f442
36. Miura Y, Ishida F, Umeda Y, Tanemura H, Suzuki H, Matsushima S, et al. Low wall shear stress is independently associated with the rupture status of middle cerebral artery aneurysms. *Stroke.* (2013) 44:519–21. doi: 10.1161/STROKEAHA.112.675306
37. Liu X, Kao E, Haraldsson H, Ballweber M, Martin A, Li Y, et al. Identification of intra-individual variation in intracranial arterial flow by MRI and the effect on computed hemodynamic descriptors. *MAGMA.* (2021) 34:659–66. doi: 10.1007/s10334-021-00917-0


**Conflict of Interest:** GF was employed by the company Union Strong (Beijing) Technology Co. Ltd.

The remaining authors declare that the research was conducted in the absence of any commercial or financial relationships that could be construed as a potential conflict of interest.

**Publisher's Note:** All claims expressed in this article are solely those of the authors and do not necessarily represent those of their affiliated organizations, or those of the publisher, the editors and the reviewers. Any product that may be evaluated in this article, or claim that may be made by its manufacturer, is not guaranteed or endorsed by the publisher.

frontiers in Cardiovascular Medicine

ORIGINAL RESEARCH
published: 27 January 2022
doi: 10.3389/fcvm.2022.818789

# Serum IL-1, Pyroptosis and Intracranial Aneurysm Wall Enhancement: Analysis Integrating Radiology, Serum Cytokines and Histology

*Qingyuan Liu[1,2†], Yisen Zhang[3,4†], Chengcheng Zhu[5], Weiqi Liu[6], Xuesheng Ma[6], Jingang Chen[6], Shaohua Mo[1,2], Linggen Dong[3], Nuochuan Wang[7], Jun Wu[1], Peng Liu[3,4*], Hongwei He[3,4*] and Shuo Wang[1,2*]*

[1] Department of Neurosurgery, Beijing Tiantan Hospital, Capital Medical University, Beijing, China, [2] China National Clinical Research Center for Neurological Diseases, Beijing, China, [3] Department of Neurointevention, Beijing Tiantan Hospital, Capital Medical University, Beijing, China, [4] Neurosurgical Institution, Beijing Tiantan Hospital, Capital Medical University, Beijing, China, [5] Department of Radiology, University of Washington, Seattle, WA, United States, [6] Medical Image Center, Tongxinyilian (Unimed), Tsinghua Tongfang Science and Technology Mansion, Beijing, China, [7] Department of Blood Transfusion, Beijing Tiantan Hospital, Capital Medical University, Beijing, China

OPEN ACCESS

**Edited by:**
*Venkatesh Mani, Integrated Research Facility (NIAID), United States*

**Reviewed by:**
*Riikka Tulamo, Helsinki University Central Hospital, Finland*
*Zhongbin Tian, Southern Medical University, China*

***Correspondence:**
*Shuo Wang*
*captain9858@126.com*
*Hongwei He*
*ttyyhhw@126.com*
*Peng Liu*
*skeletonliu1987@163.com*

*[†]These authors have contributed equally to this work*

**Specialty section:**
*This article was submitted to Cardiovascular Imaging, a section of the journal Frontiers in Cardiovascular Medicine*

**Received:** *20 November 2021*
**Accepted:** *04 January 2022*
**Published:** *27 January 2022*

**Citation:**
*Liu Q, Zhang Y, Zhu C, Liu W, Ma X, Chen J, Mo S, Dong L, Wang N, Wu J, Liu P, He H and Wang S (2022) Serum IL-1, Pyroptosis and Intracranial Aneurysm Wall Enhancement: Analysis Integrating Radiology, Serum Cytokines and Histology. Front. Cardiovasc. Med. 9:818789. doi: 10.3389/fcvm.2022.818789*

**Background and Purpose:** Aneurysm wall enhancement (AWE) is correlated with the rupture and growth risk of unruptured intracranial aneurysms (UIAs). Pyroptosis is a proinflammation mode of lytic cell death, mediated by pyroptosis-related proteins, i.e., gasdermin D and interleukin 1 β (IL-1β). Integrating serum cytokines and histology, this study aimed to investigate the correlation between AWE and pyroptosis in UIAs.

**Methods:** UIA patients receiving microsurgical clipping were prospectively enrolled from January 2017 and June 2020. UIA samples were collected, as well as the corresponding blood samples. In this study, high-resolution magnetic resonance was employed to identify the AWE. The serum 46-cytokines examination and the histological analysis were conducted to determine pyroptosis, CD68 and MMP2. The IL-1 ra/beta ratio was determined by complying with the serum IL-1β and IL-1.ra. A comparison was drawn in the differences between UIAs with and without AWE. Lastly, the correlation between inflammation in UIA samples and serums was investigated.

**Results:** This study included 34 UIA patients. The serum proinflammatory cytokines [IL-1β ($P < 0.001$) and TNF-α ($P < 0.001$)] were up-regulated, and serum anti-inflammatory cytokine (IL-1.ra, $P = 0.042$) were down-regulated in patients with AWE UIAs. The patients with AWE UIAs achieved a higher IL-1.ra/beta ratio ($P < 0.001$). The multivariate logistic analysis demonstrated IL-1β [odds ratio (OR), 1.15; 95% confidence interval (CI), 1.02–1.30; $P = 0.028$] and IL-1.ra (OR, 0.998; 95% CI, 0.997–1.000; $P = 0.017$) as the risk factors correlated with the AWE. IL-1.ra/beta ratio achieved the highest predictive accuracy [area under the curve (AUC), 0.96] for AWE, followed by IL-1.ra (AUC, 0.90), IL-1β (AUC, 0.88) and TNF-α (AUC, 0.85). As compared with the UIAs without AWE, the AWE UIAs were manifested as a severer wall remodeling, with higher relative levels of

pyroptosis-related proteins, CD68 and MMP2. The serum IL-1β, IL-1.ra and IL-1.ra/beta ratio had a positive correlation with the relative levels of pyroptosis-related proteins, CD68 and MMP2 in UIA tissues.

**Conclusion :** The serum IL-1β and IL-1.ra were correlated with the AWE. More pyroptosis-related proteins were identified in UIAs with AWE. The serum IL-1β and IL-1.ra were correlated with the pyroptosis-related proteins in aneurysm tissues.

**Keywords: unruptured intracranial aneurysm, aneurysm wall enhancement, pyroptosis, serum cytokines, IL-1**

## INTRODUCTION

Intracranial aneurysm is the major cause of non-traumatic subarachnoid hemorrhage. The rupture or growth risk of unruptured intracranial aneurysms (UIAs) is critical to clinical decision-making. Aneurysm wall enhancement (AWE) is considered a sign of rupture, growth and symptoms (1–5). Inflammation infiltration and aneurysm wall remodeling are recognized as two vital pathological characteristics of the wall of ruptured intracranial aneurysm (6). As revealed from existing studies, the inflammation is severer in the aneurysm wall of UIAs with AWE as compared with UIAs without AWE (7, 8). As revealed by the fact above, the pathological features of UIAs with AWE may be close to those of the ruptured intracranial aneurysms. Though strong AWE may indicate a high risk of aneurysm rupture or growth, the mechanism of AWE and the correlation between AWE and the characteristics of systematic inflammation have not been clarified.

Pyroptosis is a proinflammation mode of lytic cell death, which is mediated by Gasdermin D (GSDMD) and interleukin 1β (IL-1β) (9). Caspase-1 is capable of cleaving pro-IL-1β to the bioactive cytokine and cleaving the pro-GSDMD to GSDMD products. In addition, the GSDMD products can create pores to mediate IL-1β efflux and mitigate the subsequent inflammation (10). Pyroptosis is of high significance to numerous acute and chronic inflammation diseases (11, 12). Since the UIAs with AWE are generally manifested as massive inflammation infiltration, a hypothesis has been proposed that pyroptosis may be related to AWE.

This study conducted the analysis integrating serum cytokines and the histological analysis, which aimed to clarify the correlation between AWE, pyroptosis in aneurysm tissues and systematic inflammation conditions.

## METHODS

### Study Population

We prospectively enrolled UIA patients between January 2017 and June 2020. The inclusion criteria included: (1) saccular and single UIA; (2) the aneurysm size >5 mm (the size of UIA sufficiently large for resection after clipping); (3) vessel wall magnetic resonance imaging scans performed preoperatively to detect the AWE of UIAs; (4) UIAs were treated by microsurgical clipping. The exclusion criteria are presented below: (1) patients with other intracranial tumors (e.g., pituitary adenoma) and cerebrovascular malformation (e.g., arteriovenous malformation); (2) patients with dissecting, traumatic, thrombotic or infectious UIAs; (3) patients with a family history of UIAs, polycystic kidney or systematic disease (e.g., lupus); (4) patients receiving special treatment in other medical institutions before the admission to the authors' institution. Lastly, 34 patients harboring 34 UIAs were included in this study.

The demographic information (e.g., age, gender, smoking history and alcohol abuse history) comorbidities [e.g., hypertension, dyslipidemia, diabetes mellitus and transient ischemic attacks (TIA)] and medication (aspirin and antihyperlipidemic drugs) were acquired from electronic medical records.

We defined patients taking aspirin (e.g., standard and low-dose aspirin) at least three times per week as aspirin users (13). The patients treated with standard antihyperlipidemic drugs were considered the antihyperlipidemic drug users. Based on the alcohol consumption, the included patients were classified as regular alcohol abuse (drink once or more per week) and others (14). Based on the smoking condition, patients were classified into current smokers and others (15).

### Radiological Characteristics

Computed tomography angiography (CTA) was routinely performed before the surgery. The aneurysm size, height, diameter of neck and diameter of the parent artery were determined by complying with CTA by two independent investigators (YSZ and QYL, who work as vascular neurosurgeons for over 5 year, and were blind to clinical information). The mentioned characteristics were measured twice by the respective investigator, and the average of the respective investigator was then averaged for the in-depth analysis. Subsequently, the aspect ratio (AR) and the size ratio (SR) were determined following the previous study by the authors (16). AR denotes the ratio of aneurysm size and aneurysm neck diameter, and SR represents the ratio of aneurysm height and diameter of the parent artery.

The same investigators (YSZ and QYL) recorded the UIAs with and without AWE based on vessel wall magnetic resonance imaging scans. The routine sequences of vessel wall magnetic

**Abbreviations:** UIA, unruptured intracranial aneurysm; AWE, aneurysm wall enhancement; TIA, transient ischemic attack; MCA, middle cerebral artery; ICA, internal carotid artery; AcomA, anterior communicating artery; ACA, anterior cerebral artery; AR, aspect ratio; SR, size ratio; IL-1β, interleukin 1 β; IL-1. ra, interleukin 1 ra; TNF-α, tumor necrosis factor-α; GSDMD, gasderimin D; MMP2, matrix metalloproteinase-2.

resonance imaging scans consisted of pre-contrast and post-contrast T1-weighted, as well as time-of-flight (TOF). All images were acquired using the same magnetic resonance image workstation (Siemens, Germany). TOF was used to locate the UIAs with a repetition time (TR)/echo time (TE) of 3.43/21 ms, a layer thickness of 0.60 mm, a field of view of 220 × 200 mm, 52 slices, resolution of 384 × 256 under a scan time of 6 min 8 s. Vessel wall sequence was used to identify the AWE with TR/TE of 900/20 ms, a layer thickness of 0.65 mm, a field of view of 230 × 195 mm, 240 slices, resolution of 384 × 384 under a scan time of 8 min 4 s. By referencing the existing study (3), the investigators identified the UIAs with AWE when the aneurysm wall was presented to be partial (the partial aneurysm wall enhanced) and circumferential (the whole aneurysm wall enhanced) AWE by comparing the pre-contrast images with the post-contrast images. **Figure 1A** presents the representative cases.

## Serum Cytokines Detection and Histological Analysis

**Figure 1B** gives the diagram of analysis. After the vessel wall magnetic resonance imaging scans, the blood sample was acquired from the respective patient for the serum cytokines examination preoperatively. The cytokines were detected through a serum 46-cytokines examination (Wayenbio corporation, Shanghai, China) using Bio-Plex Human Cytokines Screening Panel (Bio-Rad corporation, Hercules, American). Serum samples were centrifuged for 10 min at 15,000 rpm. The supernate was collected and diluted using the standard diluent. Then, Microbeans were diluted using the Assay Buffer and incubated with samples for 30 min. Finally, each sample was mixed with Detection Antibody and then detected by Bio-Plex MAGPIX system (Bio-Rad corporation, Hercules, American). The function of each cytokine was summarized in **Supplementary Table 1**. The fold change (FC) of UIAs with AWE to those without AWE was determined. The cytokines with FC >2 and $P < 0.05$ were defined as the significantly different cytokines. The IL-1 ra/beta ratio was calculated by:

$$\text{IL}-1\ \text{ra/beta ratio} = \frac{(\text{serum IL}-1.\text{ra})}{(\text{serum IL}-1\beta)}$$

The result of serum 46-cytokines examination was further validated using the Ella workstation (Biotechne corporation, Shanghai, China). The Simple Plexes were purchased from the Biotechne corporation, which was incubated using the primary antibodies, including IL-1β, interleukin 1 ra (IL-1.ra), tumor necrosis factor-α (TNF-α) and interleukin 10 (IL-10) (R&D Systems, Biotechne corporation, Shanghai, China).

The protein-to-protein interaction (PPI) analysis was performed based on STRNG database (https://www.string-db.org/).

Subsequently, the dome of UIAs was resected after the appropriate clipping for the histological analysis. After the dehydration and the embedding, the sections were first stained with H-E (Hematoxylin-Eosin) and Masson (Solabrio, Beijing, China). In addition, the EVG (Verhoeff Van Gieson) staining was performed by Raisedragon's corporation (Beijing, China). For immunofluorescence, after antigen retrieval and permeabilization, the sections were blocked with ProteinBlock (Abcam corporation, Cambridge, UK) and then incubated with primary antibodies at 4°C overnight, including rabbit anti-CD68 (ab125212, Abcam corporation, Cambridge, UK) at 1:500, mouse anti-MMP2 antibody (ab86607, Abcam corporation, Cambridge, UK) at 1:500, rabbit anti-IL-1β antibody (ab9722, Abcam corporation, Cambridge, UK) at 1:300, Alexa Fluor® 488 Anti-IL-1.ra antibody (ab252007, Abcam corporation, Cambridge, UK) at 1:500, as well as rabbit anti-GSDMD antibody (ab219800, Abcam corporation, Cambridge, UK) at 1:500. Subsequently, the sections were incubated with secondary antibodies (Alexa Fluor® 488 Goat anti-mouse IgG, Abcam corporation, Cambridge, UK, and Alexa Fluor® 594 Goat anti-rabbit IgG, Abcam corporation, Cambridge, UK) at 1:500. Lastly, the sections were sealed with the DAPI (4',6-diamidino-2-phenylindole)-containing mounting medium (ZSGB-BIO corporation, Beijing, China). In this study, the sections with identical conditions and set integration times were scanned under the microscopy workstation (Invitrogen™ EVOS™ FL Auto 2, Thermofisher scientific corporation, Massachusetts, USA). All fluorescence channels of the whole sample were automatically recorded for further analysis. The Image J 1.8.0 (https://imagej.en.softonic.com/) was employed to measure the integrated optical density (IOD) and count the cell number by complying with the DAPI image. As for cell number count, we firstly transferred the DAPI image into 8-bit image, and then adjusted the threshold of Black and White model to select cells. After the holes filling and watershed processes, the cell number was semi-automatically analyzed using the Analyze Particles model. The ratio of IOD to cells was used for the subsequent analysis.

Based on the H-E staining and by referencing previous studies (17, 18), three random sections were classified for aneurysm wall types by two investigators (JW and PL) blinded to clinical information. To be specific, the sections were (1) type I, described as endothelialized wall with organized smooth muscle cells, (2) type II&III, defined as a thickened wall with disorganized smooth muscle cells or hypocellular wall with intimal hyperplasia or luminal thrombosis, as well as (3) type IV, i.e., an extremely thin thrombosis-lined hypocellular wall. The discrepancies were solved by consulting a senior author (SW). The severest remodeling type in three random sections was taken for further analysis. We defined the type II&III and type IV aneurysm wall as AWR wall (17). The atherosclerosis area was measured based on the Masson staining according to our previous study (17). The atherosclerotic area was stained red, and the non-atherosclerotic area was stained blue. Atherosclerosis area was defined as the ratio of red area to blue area + red area.

## Statistical Analysis

Statistical analyses were conducted by applying SPSS 22.0 (IBM corporation, American) and GraphPad Prism 8 (GraphPad Software, American). The measured data were expressed as number and percentage [*n* (%)], and the continuous data were manifested as median and inter-quartile range [m (IQR)]. The inter-observer agreement between two investigators in assessing

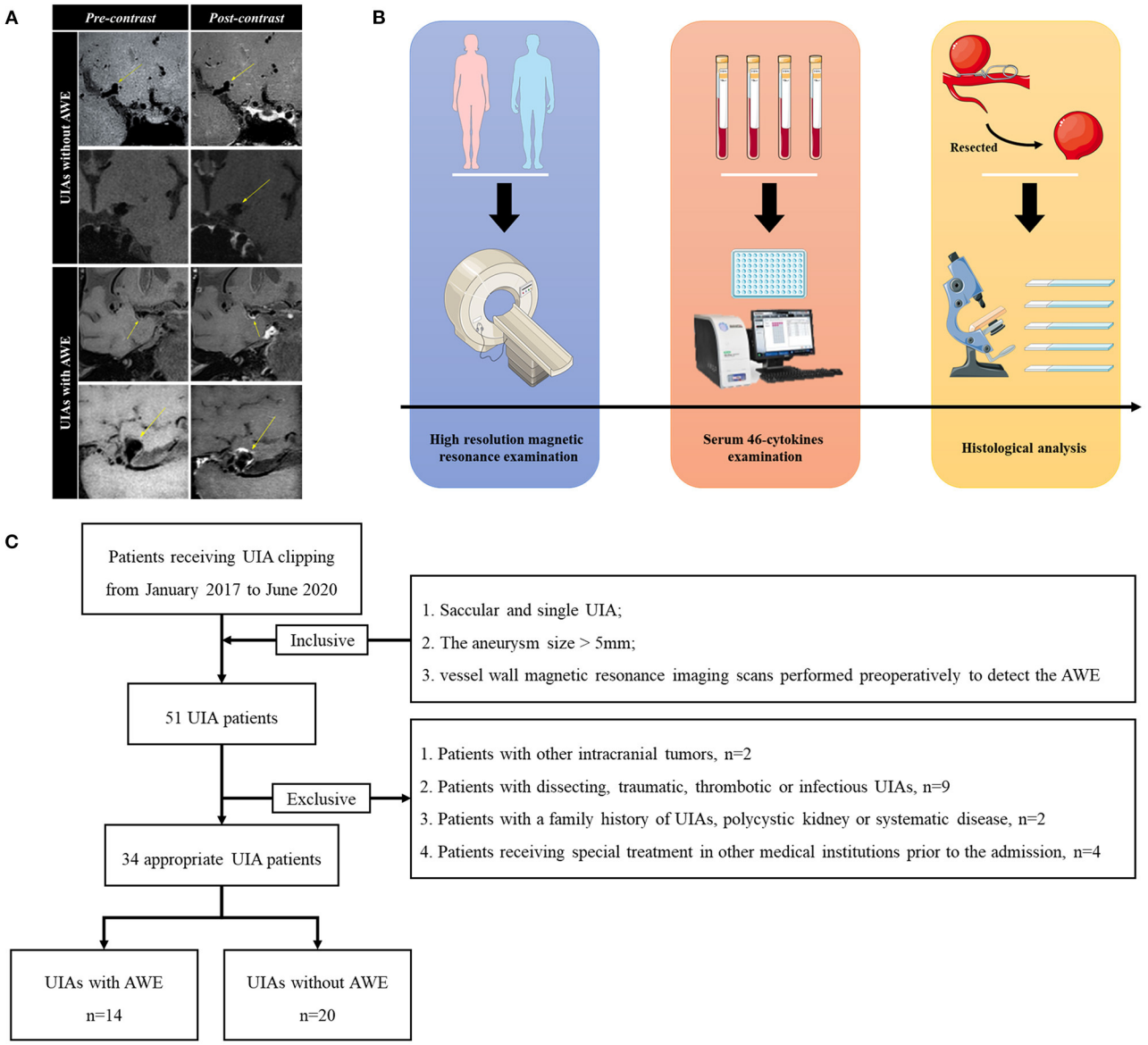


**FIGURE 1 |** The diagram of analysis. **(A)** Four representative cases of UIAs with and without AWE. To be specific, the pre-contrast and post-contrast statues of UIAs were presented. **(B)** The diagram of analysis. Preoperatively, the appropriate UIA patients would receive high-resolution magnetic resonance examinations. The blood samples of the mentioned patients would be tested with the 46-cytokines examination. After appropriate clipping, the UIAs would be resected for the histological analysis. **(C)** The flow chart of patient enrollment. This study finally recruited 34 UIA patients. UIA, unruptured intracranial aneurysm; AWE, aneurysm wall enhancement.

the morphological parameters (irregular shape, aneurysm size, AR and SR) was evaluated with Cohen's kappa and intraclass correlation coefficients; values of 0.60–0.80 and >0.80 were, respectively, considered to be of substantial and excellent inter-observer agreement. The logistic model was conducted to investigate the risk factors for the AWE. The parameters with statistical significance in univariate analysis were then input into multivariate logistic analysis. The multivariate logistic analysis was performed using a backward model. The result included odds ratio (OR) and 95% confidence interval (CI) The receiver operator characteristic curve was plotted, and the area under the curve (AUC) was generated to examine the predictive accuracy of parameters to AWE. The correlation analysis was conducted with Pearson's method. The coefficient (R) was adopted to assess the strength of correlation. The correlation with $R > 0.50$ and $P < 0.05$ was recognized as a strong correlation. A two-tailed $P$-value $< 0.05$ was assumed with statistical significance.

**TABLE 1 |** The clinical and radiological information of patients and UIAs.

| Characteristics | With AWE $n = 14$ | Without AWE $n = 20$ | *P* value |
|---|---|---|---|
| Age-m (IQR)-years | 52 (46–67) | 59 (50–63) | 0.592 |
| Male-no. (%) | 7 (50.0%) | 6 (30.0%) | 0.341 |
| **Comorbidities-no. (%)** | | | |
| Hypertension | 5 (35.7%) | 10 (50.0%) | 0.500 |
| Dyslipidemia | 1 (7.1%) | 0 (0.0%) | 0.743 |
| Diabetes mellitus | 1 (7.1%) | 1 (5.0%) | 0.931 |
| Coronary heart diseases | 4 (28.6%) | 1 (5.0%) | 0.259 |
| TIA/ischemic stroke | 2 (14.3%) | 1 (5.0%) | 0.666 |
| Current smoking-no. (%) | 4 (28.6%) | 5 (25.0%) | 0.877 |
| Regular alcohol abuse-no. (%) | 1 (7.1%) | 1 (5.0%) | 0.931 |
| **Medication using-no. (%)** | | | |
| Aspirin | 1 (7.1%) | 2 (10.0%) | 0.904 |
| Antihyperlipidemics | 2 (14.3%) | 5 (25.0%) | 0.616 |
| Site-no. (%) | | | 0.743 |
| MCA | 10 (71.4%) | 13 (65.0%) | |
| ICA | 2 (14.3%) | 3 (15.0%) | |
| AcomA/ACA/posterior | 2 (14.3%) | 4 (20.0%) | |
| Irregular shape-no. (%) | 7 (50.0%) | 6 (30.0%) | 0.341 |
| Aneurysm size-m (IQR)-mm | 6.8 (5.4–8.1) | 6.0 (5.0–7.2) | 0.416 |
| AR-m (IQR) | 1.4 (1.3–2.1) | 1.2 (0.9–1.5) | 0.053 |
| SR-m (IQR) | 2.1 (1.2–2.5) | 1.9 (1.5–2.6) | 0.796 |

*UIA, unruptured intracranial aneurysm; AWE, aneurysm wall enhancement; TIA, transient ischemic attack; MCA, middle cerebral artery; ICA, internal carotid artery; AcomA, anterior communicating artery; ACA, anterior cerebral artery; AR, aspect ratio; SR, size ratio.*

# RESULTS

## The Characteristics of Patients and UIAs

On the whole, 34 UIA patients were included here (**Figure 1C**). **Table 1** lists the characteristics of patients and UIAs. Of 34 included patients, 13 were male and 21 were female, with age ranging from 25 to 70. AWE was identified in 14 (41.2%) UIAs. 5 (35.7%) patients with AWE and 10 (50.0%) patients without AWE suffered from hypertension. 23 (67.7%) UIAs were sited in the middle cerebral artery, 5 (14.7%) were in the internal carotid artery, and 6 (17.6%) were in other arteries. The irregular rate of UIAs with AWE exceeded that of UIAs without AWE (50.0 vs. 30.0%). Inter-observer agreement between two investigators in the assessment of the morphological parameters was good (**Supplementary Table 2**). Furthermore, the difference was not identified in age, gender, dyslipidemia, diabetes mellitus, coronary heart diseases, TIA/ischemic stroke, aspirin taking, antihyperlipidemic drugs taking, smoking history, alcohol abuse, site, aneurysm size, irregular shape, AR and SR (all $P > 0.05$).

## Serum Cytokines Between UIAs With and Without AWE

Forty-six cytokines between UIAs with and without AWE were found (**Figure 2A**; **Supplementary Table 3**). The proinflammatory cytokines were up-regulated progressively, whereas anti-inflammatory cytokines were down-regulated gradually in patients with AWE UIAs (**Figure 2B**). Four cytokines, i.e., IL-1β ($P < 0.001$), IL-1.ra ($P = 0.042$), IL-4 ($P = 0.007$) and TNF-α ($P < 0.001$), were significantly different between UIAs with AWE and without AWE (**Figure 2C**). Of the mentioned cytokines, IL-1β and TNF-α were proinflammatory, and IL-1.ra was anti-inflammatory (**Figure 2D**). **Figure 2E** presents the percentage of AWE in each IL-1β and IL-1.ra level. IL-1β and IL-1.ra were integrated, and a new biomarker was promoted, termed IL-1.ra/beta ratio. The UIAs without AWE had a higher IL-1.ra/beta ratio as compared with UIAs with AWE (**Figure 2F**). The predictive accuracy of serum cytokines to AWE was tested. As indicated by the result, IL-1.ra/beta ratio had the highest accuracy (AUC, 0.96), followed by IL-1.ra (AUC, 0.90), IL-1β (AUC, 0.88) and TNF-α (AUC, 0.85); however, an appropriate predictive accuracy of IL-10 to AWE was not identified (AUC, 0.66) (**Figure 2G**; **Supplementary Table 4**). For the IL-1β, IL-1.ra and TNF-α participated in the inflammation-related process, we mainly focused on these cytokines in the subsequent analysis.

The levels of IL-1β, IL-1.ra and TNF-α were further measured using the Ella workstation. As reported previously, IL-10, an anti-inflammatory factor, was significantly down-regulated in patients with AWE UIAs (19). IL-1β, IL-1.ra and TNF-α were significantly different between UIAs with and without AWE (**Figures 2H,J**), whereas IL-10 had no statistical significance (**Figure 2K**). **Table 2** lists the result of rgw logistic analysis. As indicated by the univariate logistic analysis, IL-1β, IL-1.ra, TNF-α and IL-4 were risk factors for the AWE. The multivariate logistic analysis demonstrated IL-1β (OR, 1.15; 95% CI, 1.02–1.30; $P = 0.028$) and IL-1.ra (OR, 0.998; 95% CI, 0.997–1.000; $P = 0.017$) as the independent risk factors correlated with the AWE. The results remained consistent after being regulated. IL-1β and IL-1.ra were serum markers of pyroptosis; thus, it was assumed that AWE may be correlated with the pyroptosis in the aneurysm wall.

## Pyroptosis and Inflammation in the Aneurysm Wall Between UIAs With and Without AWE

To examine the correlation more specifically between the AWE and pyroptosis in the aneurysm wall, we performed histological analysis on UIA tissue samples. Here, as compared with UIAs without AWE, a higher aneurysm wall remodeling ratio (14/20 in UIAs without AWE, and 14/14 in UIAs with AWE), severer inflammation (CD68 and MMP2) and larger atherosclerosis area could be found in UIAs with AWE (**Figures 3A–D**). The EVG staining detected reduced elastic fibers in UIAs with and without AWE, whereas there was no significant difference. The pyroptosis-related proteins (IL-1β, IL-1.ra and GSDMD) and the inflammatory factors were further detected in UIAs. As indicated from the result, MMP2 and CD68 were both higher in UIAs with AWE. furthermore, the UIAs with AWE had a higher relative level of IL-1β and GSDMD, and a lower relative level of IL-1.ra, as compared with UIAs without AWE (**Figures 3E–K**).

## The Correlation of Inflammatory Factors in UIA Tissues and Serum Cytokines

According to **Figures 4A,B**, the relative level of serum IL-1β was positively correlated with the relative level of IL-1β in UIA tissues ($R = 0.79$, $P < 0.001$), the same as the serum IL-1.ra ($R$

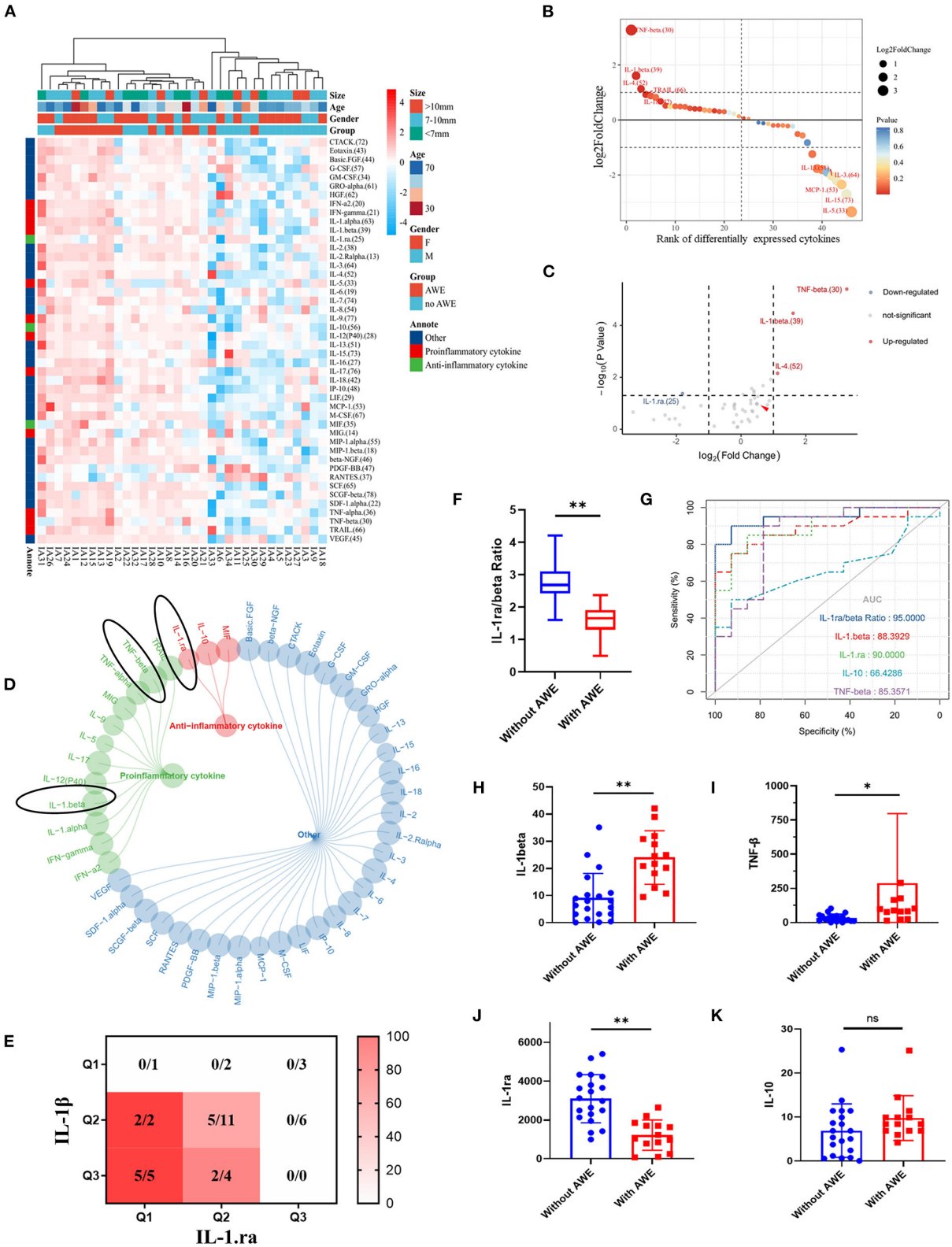


**FIGURE 2 |** The serum cytokines between UIAs with and without AWE. **(A)** The heatmap of serum cytokines between UIAs with and without AWE. Forty-six serum cytokines were identified in this study. **(B)** The proinflammatory cytokines were up-regulated in patients with AWE UIAs, whereas the anti-inflammatory cytokines were up-regulated in patients without AWE UIAs. **(C)** The volcano plot of the different cytokines in respect of UIAs with and without AWE. FC >2 and *P*-value < 0.05 were adopted to identify the significantly different cytokines. IL-1β, TNF-α and IL-4 were signnificantly up-regulated, whereas IL-1.ra was significantly down-regulated, in

*(Continued)*

**FIGURE 2 |** patients with AWE UIAs. **(D)** The summary of the function of significantly different cytokines. The black circles indicated the cytokines of interest. **(E)** The heatmap of the AWE percentage in the respective IL-1β and IL-1.ra level. The levels of IL-1β and IL-1.ra were separated using the interquartile range. **(F)** The histograms of IL-1.ra/beta ratio for UIAs with and without AWE. **(G)** The receiver operating characteristic curves of IL-1β, IL-1.ra, IL-10, TNF-α and IL-1.ra/beta ratio to AWE. **(H–K)** The histograms of IL-1β, IL-1.ra, TNF-α and IL-10 in respect of UIAs with and without AWE. $^{ns}P > 0.05$; $^{*}P < 0.05$; $^{**}P < 0.01$. UIA, unruptured intracranial aneurysm; AWE, aneurysm wall enhancement; FC, fold change; IL-1β, interleukin 1β; IL-1.ra, interleukin 1.ra, TNF-α, tumor necrosis factor-α; IL-10, interleukin 10.

**TABLE 2 |** The logistic analysis for factors related to the AWE.

| Parameters | Univariate | | Multivariate† | | Adjusted‡ | |
|---|---|---|---|---|---|---|
| | OR (95% CI) | *P*-value | OR (95% CI) | *P*-value | OR (95% CI) | *P*-value |
| IL-1.β | 1.17 (1.06–1.29) | 0.002 | 1.15 (1.02–1.30) | 0.028 | 1.16 (1.00–1.33) | 0.046 |
| IL-1.ra | 0.998 (0.997–0.999) | 0.004 | 0.998 (0.997–1.000) | 0.017 | 0.999 (0.997–1.000) | 0.038 |
| IL-4 | 2.06 (1.11–3.82) | 0.022 | Omitted | | Omitted | |
| TNF-α | 1.03 (1.01–1.06) | 0.010 | Omitted | | Omitted | |

†*the multivariate analysis was performed using forward logistic model.* ‡*the result was adjusted by age, gender, hypertension, dyslipidemia, diabetes mellitus, aspirin, antihyperlipidemics and aneurysm size. AWE, aneurysm wall enhancement; OR, odds ratio; CI, confidence interval.*

$= 0.45$, $P < 0.001$) and IL-1.ra/beta ratio. Moreover, according to **Figure 4C**, the serum IL-1β, IL-1.ra and IL-1.ra/beta ratio were correlated with the relative levels of GSDMD, CD68 and MMP2 in UIA tissues. However, the correlation of IL-4 or TNF-α and the inflammatory factors (CD68 and MMP2) in UIA tissues were not significant. The result of correlation analysis was summarized in **Supplementary Table 5**. As revealed from the protein-to-protein interaction analysis based on STRING database (**Supplementary Figure 1**), GSDMD can interact with the IL-1β, and with the IL-1.ra indirectly; the serum IL-1β can activate the IL-1 receptor, and induce pyroptosis and subsequent inflammation; IL-1.ra can inhibit the combination of IL-1β and IL-1 receptors. Thus, the biological efficacy of IL-1β and IL-1.ra is antagonistic.

## DISCUSSION

Pyroptosis is critical to numerous inflammation diseases. This study first investigated the correlation between AWE and pyroptosis. Integrating the serum cytokines and the histological analysis, this study found that the proinflammatory cytokines (IL-1β, IL-4 and TNF-α) were up-regulated, and the anti-inflammatory cytokine (IL-1.ra) was down-regulated, in patients with UIAs showing AWE. The IL-1.ra/beta ratio had the highest predictive accuracy for AWE. The subsequent analysis showed that serum IL-1β and IL-1.ra were correlated with the relative levels of pyroptosis-related proteins and the inflammatory factors in UIA tissues. The pyroptosis-related proteins, e.g., IL-1β, IL-1.ra and IL-1.ra/beta ratio, may serve as a potential biomarker to predict the aneurysm rupture or growth.

Aneurysm rupture and growth are the conflicts of vascular protective factors and damage factors (20). The strong AWE is considered the sign of severe inflammation in the aneurysm wall. Existing studies revealed the correlation of AWE and atherosclerosis, and inflammatory cell invasion (7, 8, 21, 22). In this study, our findings from histological analysis complied with existing studies. The UIAs with AWE, compared with those without AWE, showed higher levels of MMP2 and CD68. In addition, the UIAs with AWE had the manifestation of a severe wall remodeling (Type II&III, or Type IV), with the general manifestations of inflammation infiltration, luminal thrombus and extremely thin hypocellular wall. The severe inflammation and wall remodeling suggested that the pathological characteristics of UIAs with AWE were similar to the ruptured aneurysms.

IL-1β, which is secreted after the cleavage and activation of GSDMD by caspase-1, significantly affects pyroptosis. As reported by existing studies, the IL-1β increased in atherosclerotic and infectious diseases (10–12, 23–26), in which the inflammation have essential significance. As opposed to the mentioned finding, the IL-1.ra can competitively combine the IL-1β receptor (27, 28), thereby reducing the biological effect of IL-1β, and it can act as an anti-inflammatory factor. According to this study, in patients with AWE UIAs had the up-regulated serum IL-1β and the down-regulated serum IL-1.ra. As revealed by the PPI analysis, GSDMD could interact with IL-1β and IL-1.ra. Moreover, high accuracy of IL-1β and IL-1.ra predictions was achieved for AWE. Notably, the levels of serum IL-1β and IL-1.ra were correlated with the relative levels of GSDMD, MMP2 and CD68 in aneurysm tissues. Impacted by the consistent comorbidities of the included patients, serum IL-1β/IL-1.ra and IL-1β/IL-1.ra in UIA tissues were found to have probably a consistent trend and could indicate the inflammatory condition of aneurysm wall (**Figure 4D**). According to the mentioned facts, pyroptosis may be critical to the process of UIAs. However, the *in vivo* and i*n vitro* studies should be conducted to confirm the assumption above.

In this study, the serum IL-1β and IL-1.ra were further integrated, and a novel biomarker, termed as serum IL-1.ra/beta ratio, was promoted. This biomarker could reflect the conflict of damage and repairment in the aneurysm wall. This study further demonstrated the predictive accuracy of IL-1.ra/beta ratio for AWE, and IL-1.ra/beta ratio was significantly correlated with the

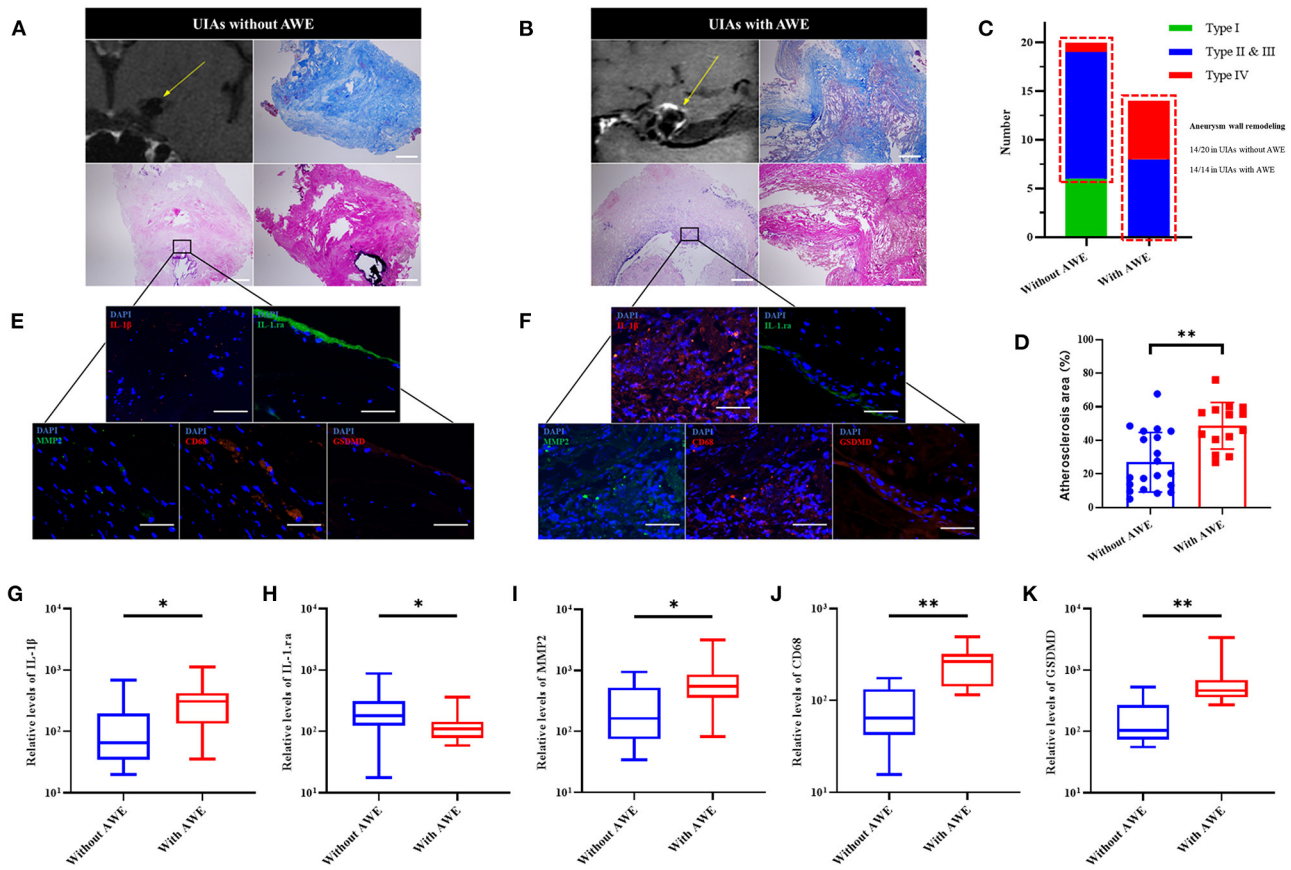


**FIGURE 3 |** The GSDMD and the inflammatory factors in UIAs with and without AWE. **(A,B)** Two representative cases of histological analysis for UIAs with and without AWE. The H-E staining indicated a severe wall remodeling and inflammation infiltration in the UIAs with AWE. The Masson staining showed that atherosclerosis was more significantly changed in the UIAs with AWE. The EVG staining reported the reduced elastic fibers in the UIAs with and without AWE. The scale bar corresponded to 100 μm. **(C)** The histograms of aneurysm wall remodeling between UIAs with and without AWE. Thus, it was known that all UIAs with AWE were manifested as significant wall remodeling (type II & III, or type IV). The red box indicated the number of aneurysm wall remodeling. **(D)** The atherosclerosis area between UIAs with and without AWE. The UIAs with AWE had a larger atherosclerosis area compared with UIAs without AWE. **(E,F)** The IL-1β, IL-1.ra, GSDMD, CD68 and MMP2 in UIA tissues were detected in this study. The scale bar corresponding to 40 μm. **(G–K)** The box plot of the relative levels of IL-1β, IL-1.ra, MMP2, CD68 and GSDMD for UIAs with and without AWE. *$P < 0.05$; **$P < 0.01$. UIA, unruptured intracranial aneurysm; AWE, aneurysm wall enhancement; GSDMD, gasdermin D; MMP2, matrix metalloproteinase-2; IL-1β, interleukin 1β; IL-1.ra, interleukin 1.ra.

relative level of GSDMD in aneurysm tissues. Accordingly, IL-1.ra/beta ratio is considered to be a potential biomarker to predict the rupture or growth risk of UIAs, which should be explored in depth.

This study had several limitations. First, the source of serum cytokines might be variable. The regulated levels of serum IL-1β and IL-1.ra might be also attributed to other comorbidities. Although we took many other comorbidities into consideration, this problem would still limit our conclusion. Second, the resectable UIAs should exhibit a certain volume. In this current study, we only included UIAs >5 mm and included only 34 UIAs. The selection bias and the limited sample size might limit the conclusion of this study. Third, not all the aneurysms were entirely resected, which demonstrated that the pathological characteristics might not reflect the entire condition of UIAs. However, regardless of the mentioned limitations, this study suggested the correlation between AWE and pyroptosis in UIA tissues, and the pyroptosis-related factors might serve as potential biomarkers to predict the rupture or growth risk of UIAs.

## CONCLUSION

This study first indicated the correlation between AWE and pyroptosis in UIA tissues. The pyroptosis-related cytokines (IL-1β and IL-1.ra) were the serum cytokines correlated with the AWE. More pyroptosis-related proteins were identified in UIAs with AWE. The serum IL-1β, IL-1.ra and IL-1.ra/beta ratio was correlated with the relative levels of pyroptosis-related proteins and the inflammatory factors in UIA tissues. The factors correlated with pyroptosis (e.g., IL-1.ra/beta ratio) may serve as biomarkers correlated with aneurysm vulnerability.

## DATA AVAILABILITY STATEMENT

The raw data supporting the conclusions of this article will be made available by the authors, without undue reservation.

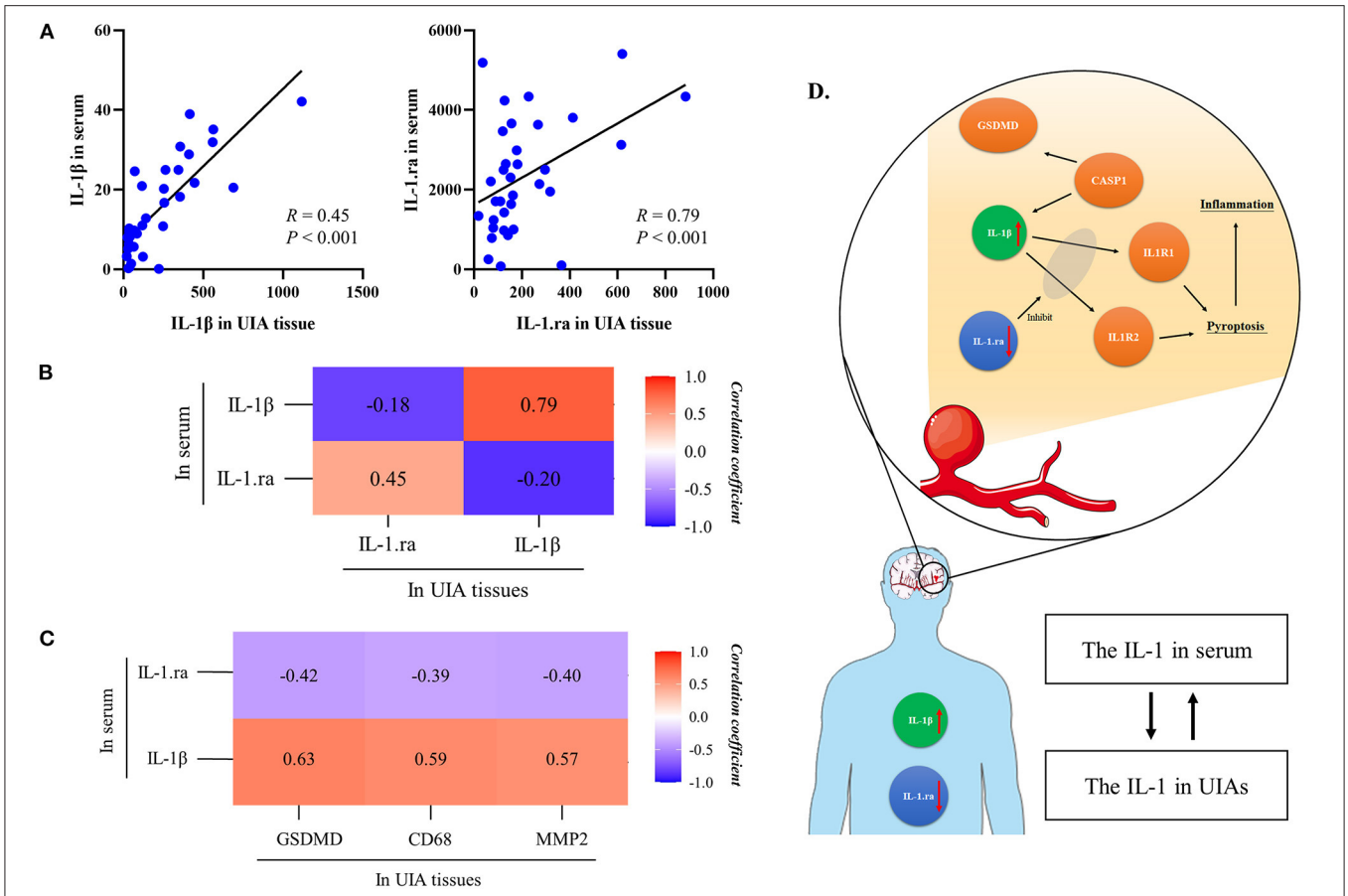


**FIGURE 4 |** The relationship between inflammatory factors in tissue samples and serum cytokines. **(A)** The relationship of IL-1β and IL-1.ra between serum and UIA tissues. **(B)** The heatmap shows the correlation of IL-1β and IL-1.ra between serum and UIA tissues. **(C)** The heatmap presents the correlation of serum IL-1β/IL-1.ra and CD68, MMP2 in UIA tissues. **(D)** There may be a correlation between systematic proinflammatory cytokines and proinflammatory factors in UIA tissues. The IL-1β can activate the IL-1 receptor, and induce pyroptosis and subsequent inflammation. IL-1.ra can block the combination of IL-1β and IL-1 receptors. This biological process may be the mechanism of AWE, which could result in a massive inflammation infiltration. Therefore, we assumed that factors correlated with pyroptosis, e.g., IL-1.ra/beta ratio, may be a potential biomarker to predict aneurysm rupture or growth. UIA, unruptured intracranial aneurysm; GSDMD, gasdermin D; IL-1β, interleukin 1β; IL-1.ra, interleukin 1.ra.

## ETHICS STATEMENT

The studies involving human participants were reviewed and approved by Institutional Ethics Committees of Beijing Tiantan Hospital. The patients/participants provided their written informed consent to participate in this study.

## AUTHOR CONTRIBUTIONS

QL and YZ: conception and design. WL, XM, JC, SM, LD, and NW: acquisition of data. QL, JW, PL, and SW: analysis and interpretation of data. QL: drafting the article. CZ and HH: critically revising the article. QL, YZ, CZ, WL, XM, JC, SM, LD, NW, JW, PL, HH, and SW: reviewing submitted version of manuscript. SW: approving the final version of the manuscript on behalf of all authors. HH and SW: study supervision. All authors contributed to the article and approved the submitted version.

## FUNDING

This study was supported by the National Natural Science Foundation of China (Nos. 81901197, 82071296, 81801158, 81671129, and 81471210), National Key Research and Development Program of the 14th Five-Year Plan (No. 2021YFC2500025), and Top Talent Support Program for young and middle-aged people of Wuxi Health Committee (No. 202014).

## ACKNOWLEDGMENTS

We thank the participants of the study and all clinical and research staff who contributed to this work.

## SUPPLEMENTARY MATERIAL

The Supplementary Material for this article can be found online at: https://www.frontiersin.org/articles/10.3389/fcvm.2022.818789/full#supplementary-material

## REFERENCES


1. Gariel F, Ben Hassen W, Boulouis G, Bourcier R, Trystram D, Legrand L, et al. Increased wall enhancement during follow-up as a predictor of subsequent aneurysmal growth. *Stroke.* (2020) 51:1868–72. doi: 10.1161/STROKEAHA.119.028431
2. Molenberg R, Aalbers MW, Appelman APA, Uyttenboogaart M, van Dijk JMC. Intracranial aneurysm wall enhancement as an indicator of instability: a systematic review and meta-analysis. *Eur J Neurol.* 28:3837–48. (2021). doi: 10.1111/ene.15046
3. Zhang Y, Fu Q, Wang Y, Cheng J, Ren C, Guan S, et al. Qualitative and quantitative wall enhancement analyses in unruptured aneurysms are associated with an increased risk of aneurysm instability. *Front Neurosci.* (2020) 14:580205. doi: 10.3389/fnins.2020.580205
4. Lv N, Karmonik C, Chen S, Wang X, Fang Y, Huang Q, et al. Relationship between aneurysm wall enhancement in vessel wall magnetic resonance imaging and rupture risk of unruptured intracranial aneurysms. *Neurosurgery.* (2019) 84:E385–91. doi: 10.1093/neuros/nyy310
5. Fu Q, Wang Y, Zhang Y, Zhang Y, Guo X, Xu H, et al. Qualitative and quantitative wall enhancement on magnetic resonance imaging is associated with symptoms of unruptured intracranial aneurysms. *Stroke.* (2021) 52:213–22. doi: 10.1161/STROKEAHA.120.029685
6. Frosen J, Tulamo R, Paetau A, Laaksamo E, Korja M, Laakso A, et al. Saccular intracranial aneurysm: pathology and mechanisms. *Acta Neuropathol.* (2012) 123:773–86. doi: 10.1007/s00401-011-0939-3
7. Quan K, Song J, Yang Z, Wang D, An Q, Huang L, et al. Validation of wall enhancement as a new imaging biomarker of unruptured cerebral aneurysm. *Stroke.* (2019) 50:1570–3. doi: 10.1161/STROKEAHA.118.024195
8. Zhong W, Su W, Li T, Tan X, Chen C, Wang Q, et al. Aneurysm wall enhancement in unruptured intracranial aneurysms: a histopathological evaluation. *J Am Heart Assoc.* (2021) 10:e018633. doi: 10.1161/JAHA.120.018633
9. Ryder CB, Kondolf HC, O'Keefe ME, Zhou B, Abbott DW. Chemical modulation of gasdermin-mediated pyroptosis and therapeutic potential. *J Mol Biol.* (2021) 2021:167183. doi: 10.1016/j.jmb.2021.167183
10. Karmakar M, Minns M, Greenberg EN, Diaz-Aponte J, Pestonjamasp K, Johnson JL, et al. N-gsdmd trafficking to neutrophil organelles facilitates il-1beta release independently of plasma membrane pores and pyroptosis. *Nat Commun.* (2020) 11:2212. doi: 10.1038/s41467-020-16043-9
11. Dinarello CA. A clinical perspective of il-1beta as the gatekeeper of inflammation. *Eur J Immunol.* (2011) 41:1203–17. doi: 10.1002/eji.201141550
12. Manthiram K, Zhou Q, Aksentijevich I, Kastner DL. The monogenic autoinflammatory diseases define new pathways in human innate immunity and inflammation. *Nat Immunol.* (2017) 18:832–42. doi: 10.1038/ni.3777
13. Weng JC, Wang J, Du X, Li H, Jiao YM, Fu WL, et al. Safety of aspirin use in patients with stroke and small unruptured aneurysms. *Neurology.* (2021) 96:e19–29. doi: 10.1212/WNL.0000000000010997
14. Cochrane J, Chen H, Conigrave KM, Hao W. Alcohol use in china. *Alcohol Alcohol.* (2003) 38:537–42. doi: 10.1093/alcalc/agg111
15. Can A, Castro VM, Ozdemir YH, Dagen S, Yu S, Dligach D, et al. Association of intracranial aneurysm rupture with smoking duration, intensity, and cessation. *Neurology.* (2017) 89:1408–15. doi: 10.1212/WNL.0000000000004419
16. Liu Q, Yang Y, Yang J, Li M, Yang S, Wang N, et al. Rebleeding of ruptured intracranial aneurysm after admission: a multidimensional nomogram model to risk assessment. (2021) 13:692615. doi: 10.3389/fnagi.2021.692615
17. Liu Q, Zhang Y, Yang J, Yang Y, Li M, Chen S, et al. The relationship of morphological-hemodynamic characteristics, inflammation, and remodeling of aneurysm wall in unruptured intracranial aneurysms. *Transl Stroke Res.* (2022) 13:88–99. doi: 10.1007/s12975-021-00917-1
18. Frosen J, Piippo A, Paetau A, Kangasniemi M, Niemela M, Hernesniemi J, et al. Remodeling of saccular cerebral artery aneurysm wall is associated with rupture: histological analysis of 24 unruptured and 42 ruptured cases. *Stroke.* (2004) 35:2287–93. doi: 10.1161/01.STR.0000140636.30204.da
19. Swiatek VM, Neyazi B, Roa JA, Zanaty M, Samaniego EA, Ishii D, et al. Aneurysm wall enhancement is associated with decreased intrasaccular il-10 and morphological features of instability. *Neurosurgery.* (2021) 89:664–71. doi: 10.1093/neuros/nyab249
20. Meng H, Tutino VM, Xiang J, Siddiqui A. High wss or low wss? Complex interactions of hemodynamics with intracranial aneurysm initiation, growth, and rupture: toward a unifying hypothesis. *AJNR Am J Neuroradiol.* (2014) 35:1254–62. doi: 10.3174/ajnr.A3558
21. Bae H, Suh SI, Yoon WK, Roh H, Kim C, Kwon TH. Correlation of aneurysmal wall enhancement of unruptured intracranial aneurysms on high-resolution vessel-wall imaging with clinical indices and surgical findings. *Neurosurgery.* (2021) 89:420–27. doi: 10.1093/neuros/nyab178
22. Ishii D, Zanaty M, Roa JA, Li L, Lu Y, Sabotin R, et al. Concentration of lp(a) (lipoprotein[a]) in aneurysm sac is associated with wall enhancement of unruptured intracranial aneurysm. *Stroke.* (2021) 52:1465–8. doi: 10.1161/STROKEAHA.120.032304
23. Semino C, Carta S, Gattorno M, Sitia R, Rubartelli A. Progressive waves of il-1beta release by primary human monocytes via sequential activation of vesicular and gasdermin d-mediated secretory pathways. *Cell Death Dis.* (2018) 9:1088. doi: 10.1038/s41419-018-1121-9
24. Xiong S, Hong Z, Huang LS, Tsukasaki Y, Nepal S, Di A, et al. Il-1beta suppression of ve-cadherin transcription underlies sepsis-induced inflammatory lung injury. *J Clin Invest.* (2020) 130:3684–98. doi: 10.1172/JCI136908
25. Sarkar A, Hall MW, Exline M, Hart J, Knatz N, Gatson NT, et al. Caspase-1 regulates escherichia coli sepsis and splenic b cell apoptosis independently of interleukin-1beta and interleukin-18. *Am J Respir Crit Care Med.* (2006) 174:1003–10. doi: 10.1164/rccm.200604-546OC
26. Mai W, Liao Y. Targeting il-1beta in the treatment of atherosclerosis. *Front Immunol.* (2020) 11:589654. doi: 10.3389/fimmu.2020.589654
27. Garlanda C, Dinarello CA, Mantovani A. The interleukin-1 family: back to the future. *Immunity.* (2013) 39:1003–18. doi: 10.1016/j.immuni.2013.11.010
28. Dinarello CA, Simon A, van der Meer JW. Treating inflammation by blocking interleukin-1 in a broad spectrum of diseases. *Nat Rev Drug Discov.* (2012) 11:633–52. doi: 10.1038/nrd3800


**Conflict of Interest:** The authors declare that the research was conducted in the absence of any commercial or financial relationships that could be construed as a potential conflict of interest.

frontiers in Cardiovascular Medicine

ORIGINAL RESEARCH
published: 31 January 2022
doi: 10.3389/fcvm.2022.749098

# Noninvasive Aortic Ultrafast Pulse Wave Velocity Associated With Framingham Risk Model: *in vivo* Feasibility Study

*Jinbum Kang*[1†], *Kanghee Han*[1], *Jihyun Hyung*[2], *Geu-Ru Hong*[2] *and Yangmo Yoo*[1,3*]

[1] Deparment of Electronic Engineering, Sogang University, Seoul, South Korea, [2] Division of Cardiology, Severance Cardiovascular Hospital, Yonsei University College of Medicine, Yonsei University Health System, Seoul, South Korea, [3] Deparment of Biomedical Engineering, Sogang University, Seoul, South Korea

OPEN ACCESS

**Edited by:**
Luca Saba,
Azienda Ospedaliero-Universitaria Cagliari, Italy

**Reviewed by:**
Guillaume Goudot,
Institut National de la Santé et de la Recherche Médicale (INSERM), France
Natallia Maroz-Vadalazhskaya,
Belarusian State Medical University, Belarus

***Correspondence:**
Yangmo Yoo
ymyoo@sogang.ac.kr

**†Present address:**
Jinbum Kang,
Department of Bioengineering, University of Washington, Seattle, WA, United States

**Specialty section:**
This article was submitted to Cardiovascular Imaging, a section of the journal Frontiers in Cardiovascular Medicine

**Received:** 29 July 2021
**Accepted:** 03 January 2022
**Published:** 31 January 2022

**Citation:**
Kang J, Han K, Hyung J, Hong G-R and Yoo Y (2022) Noninvasive Aortic Ultrafast Pulse Wave Velocity Associated With Framingham Risk Model: in vivo Feasibility Study. Front. Cardiovasc. Med. 9:749098. doi: 10.3389/fcvm.2022.749098

**Background:** Aortic pulse wave velocity (PWV) enables the direct assessment of aortic stiffness, which is an independent risk factor of cardiovascular (CV) events. The aim of this study is to evaluate the association between aortic PWV and CV risk model classified into three groups based on the Framingham risk score (FRS), i.e., low-risk (<10%), intermediate-risk (10∼20%) and high-risk (>20%).

**Methods:** To noninvasively estimate local PWV in an abdominal aorta, a high-spatiotemporal resolution PWV measurement method (>1 kHz) based on wide field-of-view ultrafast curved array imaging (ufcPWV) is proposed. In the ufcPWV measurement, a new aortic wall motion tracking algorithm based on adaptive reference frame update is performed to compensate errors from temporally accumulated out-of-plane motion. In addition, an aortic pressure waveform is simultaneously measured by applanation tonometry, and a theoretical PWV based on the Bramwell-Hill model (bhPWV) is derived. A total of 69 subjects (aged 23–86 years) according to the CV risk model were enrolled and examined with abdominal ultrasound scan.

**Results:** The ufcPWV was significantly correlated with bhPWV ($r = 0.847$, $p < 0.01$), and it showed a statistically significant difference between low- and intermediate-risk groups (5.3 ± 1.1 vs. 8.3 ± 3.1 m/s, $p < 0.01$), and low- and high-risk groups (5.3 ± 1.1 vs. 10.8 ± 2.5 m/s, $p < 0.01$) while there is no significant difference between intermediate- and high-risk groups (8.3 ± 3.1 vs. 10.8 ± 2.5 m/s, $p = 0.121$). Moreover, it showed a significant difference between two evaluation groups [low- (<10%) vs. higher-risk group (≥10%)] (5.3 ± 1.1 vs. 9.4 ± 3.1 m/s, $p < 0.01$) when the intermediate- and high-risk groups were merged into a higher-risk group.

**Conclusion:** This feasibility study based on CV risk model demonstrated that the aortic ufcPWV measurement has the potential to be a new approach to overcome the limitations of conventional systemic measurement methods in the assessment of aortic stiffness.

**Keywords: arterial stiffness, framingham risk score (FRS), abdominal aorta, pulse wave velocity (PWV), ultrafast ultrasound imaging**

## INTRODUCTION

The elasticity of proximal large arteries is determined by a high elastin to collagen ratio, and the increase in arterial stiffness is mostly caused by the progressive elastic fiber degeneration (1, 2). The physical stiffening of arteries eventually increases the risk of cardiovascular (CV) disease, such as systolic hypertension, coronary artery disease, myocardial infarction and stroke (3–5). Aortic pulse wave velocity (PWV) has been considered as one of the most reliable clinical parameters for evaluating arterial stiffness, blood pressure, therapeutic efficacy and CV risk stratification in patients (6, 7). It depends not only on structural changes associated with the elastic modulus of the wall affecting wave propagation but also on aortic pressure, which has a strong direct relationship to stiffness (3).

The PWV is defined by the speed at which a forward pressure wave is transmitted from the aorta through the vascular tree. To estimate PWV (e.g., a few meters per second), the propagating distance and the time of the arterial waveform passing between the two sites are measured, and the carotid-femoral PWV is currently being regarded as the gold standard method (8–10). However, these systemic or regional PWV measurements cannot accurately assess biomechanical properties of vessel segments so that the invasive methods using a pressure catheter are still required for the assessment of local aortic compliance (11, 12). Therefore, several local based PWV measurement techniques have been introduced to noninvasively evaluate aortic segments along the arterial tree.

Cardiovascular magnetic resonance (CMR) based PWV assessment substantially reduces errors by using accurate aortic length and transit times between flow waves (13, 14). Doppler ultrasound or pulse wave imaging with electrocardiogram (ECG) synchronization allows the estimation of PWV values using the time delay between two close positions during a cardiac cycle along the vessels (15–17). However, these approaches suffer from a relatively low frame rate compared to PWV. To improve accuracy diminished by limited temporal resolution, a plane wave transmission based ultrafast PWV measurement method was recently proposed and it showed a real-time direct measurement of local PWV with high spatiotemporal resolution (18–21). With the advantages of simplicity and accessibility, it has been extensively studied for various clinical usages, such as carotid stiffness assessment (22–27).

From the previous studies, a local PWV measurement technique based on high spatiotemporal resolution is strongly required, and the ultrafast PWV measurement for aortic segments in human abdomen are still rarely studied due to low accessibility and technical limitations, such as a deep and wide field-of-view (FOV). Here, we propose a high spatiotemporal resolution aortic PWV measurement method based on wide FOV ultrafast curved array imaging (28) using diverging wave transmission (ufcPWV). In addition, a new aortic wall motion tracking algorithm based on adaptive reference frame update was also conducted to compensate errors from temporally accumulated out-of-plane motion. Using the proposed method, a feasibility study to investigate the correlation between PWV for abdominal aorta and a CV risk model was performed. The aortic central pressure waveform was simultaneously measured by the applanation tonometer, and a theoretical PWV based on Bramwell-Hill model (bhPWV) (29) was derived. The CV risk model was classified into three groups based on the Framingham risk score (FRS), which is one of the scoring systems used to estimate the 10-year CV risk (30), i.e., low-risk (<10%), intermediate-risk (10∼20%) and high-risk (>20%). We hypothesized that aortic ufcPWV is associated with the Framingham risk model.

**Abbreviations:** PWV, pulse wave velocity; CV, cardiovascular; FRS, Framingham risk score; ECG, electrocardiogram; FOV, field-of-view; CMR, Cardiovascular magnetic resonance; ufcPWV, ultrafast curved array imaging; bhPWV, theoretical PWV based on the Bramwell-Hill model.

## MATERIALS AND METHODS

### Study Protocol

The CV risk model was classified into three groups based on the Framingham risk score (FRS), i.e., low-risk (<10%), intermediate-risk (10∼20%) and high-risk (>20%). The study was approved by the Institutional Review Board of the Clinical Trials Center of Yonsei University Health System, and the written informed consent was obtained from all patients. 31 patients for each risk group (total 93 patients) were recruited, but a few patients in the intermediate- and high-risk groups were excluded due to the poor image quality or incomplete scanning of the abdominal aorta. The study population's characteristics of the remaining 69 patients were presented in **Table 1**. The population contained a wide range of age, i.e., 23–86 years, and the heart rate and blood pressure were within normal range. FRS showed a significant difference between each risk groups. Abdominal ultrasound scans in longitudinal and transverse views were performed by the commercialized ultrasound research platform (E-Cube 12R, Alpinion Medical Systems Co., Ltd., Anyang-si, Gyeonggi-do, Korea) using a convex array transducer (C1-6, Alpinion Medical Systems Co., Ltd., Anyang-si, Gyeonggi-do, Korea). The radiofrequency (RF) data of three cardiac cycles were captured based on a real-time ultrafast curved array imaging (28) at a frame rate of 1 kHz. The acoustical energy was measured and set under FDA safety limit (mechanical index (MI) <1.9 and spatial peak time average intensity (Ispta) <720 mW/cm$^2$).

### A Real-Time Ultrafast Curved Array Imaging

To assess pulse wave velocities (PWVs) in aortas, the recently proposed ultrafast curved array imaging technique (28), which provides high spatiotemporal resolution with a wide field-of-view (FOV) for abdominal applications, was employed as illustrated in **Figure 1A**. For a diverging wave transmission, the virtual source was located in a circular line with the radius of the curved array transducer to obtain a wide FOV and 3-tilted diverging waves in linear increments ranging from −12 to +12 were utilized (the frame rate >1 kHz). The ultrafast curved array imaging based on diverging wave transmissions was implemented in the ultrasound research scanner for a real-time scanning and a full scanline RF data acquisition.

**TABLE 1 |** Baseline characteristics and measurements of the study population ($n = 69$) classified by Framingham risk model.

| | All ($n = 69$) | Low-risk ($n = 31$) | Intermediate-risk ($n = 22$) | High-risk ($n = 16$) | *p* |
|---|---|---|---|---|---|
| Sex, male/female | 48/21 | 18/13 | 14/8 | 16/0 | |
| Age, years | 54.0 ± 18.1 | 40.5 ± 16.2 | 61.9 ± 10.9[a] | 69.1 ± 8.9[b] | <0.001 |
| Body mass index, kg/m$^2$ | 24.0 ± 2.8 | 23.2 ± 3.0 | 24.8 ± 2.8 | 24.6 ± 2.0 | 0.105 |
| Heart rate, beats/min | 75.0 ± 11.7 | 74.1 ± 12.3 | 75.5 ± 10.1 | 73.9 ± 13.1 | 0.891 |
| Systolic blood pressure, mmHg | 126.6 ± 15.4 | 124.7 ± 17.2 | 128.8 ± 10.7 | 127.0 ± 17.6 | 0.635 |
| Diastolic blood pressure, mmHg | 76.3 ± 11.1 | 74.9 ± 11.7 | 78.5 ± 10.5 | 76.1 ± 11.0 | 0.519 |
| Total cholesterol, mg/dL | 169.0 ± 38.9 | 169.7 ± 31.1 | 167.9 ± 49.3 | 168.8 ± 39.1 | 0.986 |
| HDL cholesterol, mg/dL | 53.5 ± 13.0 | 54.5 ± 12.5 | 55.0 ± 13.2 | 49.7 ± 13.6 | 0.407 |
| Hypertension, *n* (%) | 39 (57%) | 7 (23%) | 20 (91%) [a] | 12 (75%) [b] | <0.001 |
| Current smoker, *n* (%) | 10 (14%) | 4 (13%) | 3 (14%) | 3 (19%) | 0.862 |
| Diabetes mellitus, *n* (%) | 16 (23%) | 0 (0%) | 4 (18%) | 12 (75%) [b,c] | <0.001 |
| FRS | 14.4 ± 13.9 | 3.6 ± 2.5 | 13.9 ± 2.6[a] | 36.1 ± 10.5[b,c] | <0.001 |

*FRS, Framingham risk score.*

*The subjects were classified into three risk groups according to FRSs: low risk (<10%), intermediate risk (10–20%), and high risk (>20%).*

*Values are means ± SD.*

[a]*Statistically significant difference ($p < 0.05$) between Low risk and Intermediate risk after Bonferroni correction.*

[b]*Statistically significant difference ($p < 0.05$) between Low risk and High risk after Bonferroni correction.*

[c]*Statistically significant difference ($p < 0.05$) between Intermediate risk and High risk after Bonferroni correction.*

## Adaptive Reference Frame Update Based Speckle Correlation

For PWV measurements, vessel wall motion tracking (speckle correlation) is usually conducted, and the selection of a reference frame is crucial to accurately estimate arterial wall motion. In addition, the out-of-phase motion or unexpected noise may disrupt highly accurate motion estimation, and the unwanted errors (e.g., drift errors) are typically accumulated with a common fixed reference or interframe-based motion estimation methods (31–33). As illustrated in **Figure 1B**, to improve the performance of vessel wall motion tracking, an adaptive reference frame update (ARFD)-based speckle correlation is proposed, and the flow chart of the proposed ARFD is described in **Figure 1C**. In the ARFD, the reference frame is dynamically updated in accordance with the correlation coefficient determined by a threshold value (e.g., 0.9 in **Figure 1B**). By applying the proposed ARFD method to the vessel wall motion estimation, the intrinsic error or bias from out-of-plane motion or scanning can be properly compensated, and it enables more robust Lagrangian speckle correlation (34) with a minimal accumulation of errors, as shown in **Figure 1B**. For vessel wall motion tracking, the axial displacement in the anterior or posterior wall was measured by using the time domain phase shift estimation based on the 1-D cross-correlation. The window size of 8λ was used for the motion tracking within the search range of 9 times the window size, and the window overlap was 90%.

## Pulse Wave Velocity Imaging and Measurement

Based on the ultrafast curved array imaging and ARFD-based speckle correlation algorithm, the aortic ultrafast PWV (ufcPWV) imaging and measurement was conducted. To do this, a high-spatiotemporal resolution pulse wave-induced wall displacement was estimated. Anterior or posterior vessel wall segmentation was first performed, and the distance of the vessel wall was calculated. Then, the wall velocity waveform was derived from the estimated displacement using a 9-point Savitzky-Golay digital differentiator for the temporal derivative (35). Therefore, the 2-D spatiotemporal wall velocity variation map (i.e., PWV imaging), which depicts the pulse wave propagation, was produced for a PWV measurement, as illustrated in **Figure 1D**. To measure a PWV along the vessels, the time-distance plot was first generated using the 50% upstroke points of the forward wave (e.g., the black circles on A, B and C velocity waveforms in **Figure 1D**) (systolic foot) as the tracking feature in the wall velocity waveform. Then, a linear regression fitting on the detected upstroke points was conducted for PWV calculation (PWV $= \Delta$distance/$\Delta$time) as described in **Figure 1D**. The PWVs of three cardiac cycles (i.e., data acquisition time of 3.0 sec) were measured and averaged for each case.

## Local Pulse Wave Velocity Measurement by Bramwell-Hill Equation

To investigate the association and agreement between the direct PWV measurement (ufcPWV) and theoretical PWVs derived from arterial distensibility, a local aortic PWV was obtained with the Bramwell-Hill equation (bhPWV) (36). The Bramwell-Hill model describes the relation between vascular wall stiffness expressed in arterial distensibility and the PWV. Aortic distensibility can be defined as the relative change in vessel

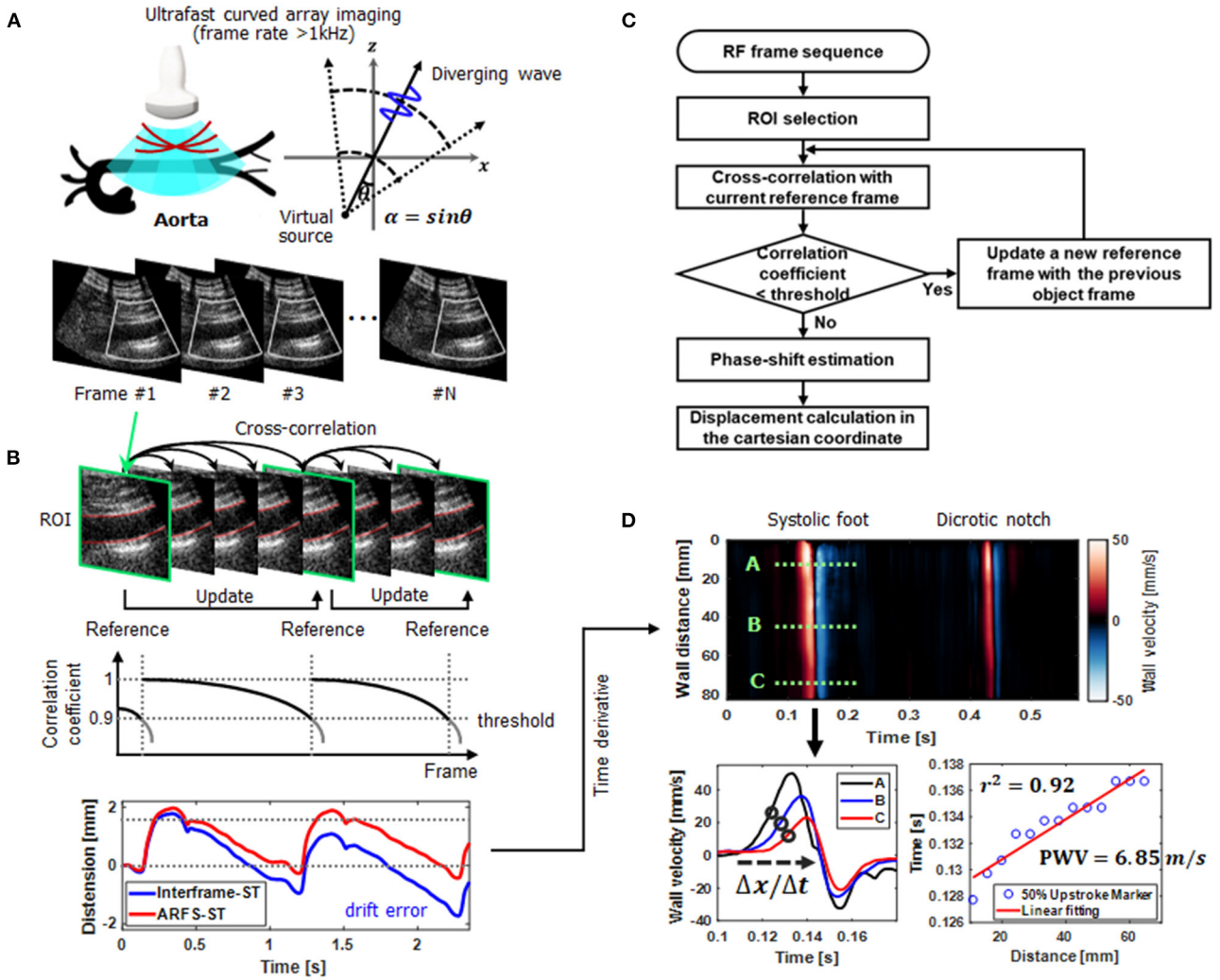


**FIGURE 1 |** An overall schematic representation of aortic ultrafast pulse wave velocity (PWV) assessment procedure. **(A)** Real-time scanning and a full scanline RF data acquisition using ultrafast curved array imaging based on diverging wave transmissions. For a diverging wave transmission, the virtual source was located in a circular line with the radius of the curved array transducer and the steering angle ($\theta$). **(B)** Aortic wall motion tracking (speckle correlation) based on a new adaptive reference frame update (ARFD) method. By dynamically updating the reference frame in accordance with the correlation coefficient, the intrinsic error or bias (e.g., drift error) from out-of-plane motion or scanning is compensated. **(C)** The flow chart of the ARFD implementation. **(D)** Aortic ultrafast PWV (ufcPWV) imaging and calculation (PWV = Δdistance/Δtime) based on the time-distance plot for the 50% upstroke marker of the forward wave.

diameter over local pulse pressure (29):

$$\mathrm{bhPWV} = \sqrt{\frac{\mathrm{A_d} \cdot \mathrm{PP}}{\rho \cdot \Delta \mathrm{A}}} \quad (1)$$

where $A_d$ is the cross-sectional area in diastole, and $A$ is the difference of the cross-sectional area between systole and diastole in the cardiac cycle. To measure the cross-sectional area of aortic vessel, the envelope image in the transversal view was utilized and the diameter was calculated assuming a circular shape. $\rho$ is the blood density (1060 kg/m$^3$), and $PP$ is the local pulse pressure. To noninvasively measure the local $PP$ in aorta, the arterial applanation tonometry (SphygmoCor, AtCor Medical, Sydney, NSW, Australia) was performed and the central blood pressure waveform was obtained.

## Data Analysis

Data from a total of 69 patients were processed, and a statistical analysis was performed to examine differences between each risk groups. The initial three evaluation groups were further classified into two evaluation groups by merging the intermediate- and the high-risk groups into a higher-risk group [i.e., low-risk (<10%, $n$ = 31) and higher-risk (≥10%, $n$ = 38)]. The signal and image processing were externally conducted with MATLAB R2019b (The MathWorks, Natick, Massachusetts, USA). The coefficient of determination ($r^2$) in linear regression was evaluated to indicate the reliability of PWV calculation (**Figure 1D**) (37).

The statistical data assessment was also conducted with the statistics analysis software (SPSS, IBM, Armonk, NY, USA). For the three evaluation groups, the Kruskal-Wallis one-way analysis of variance (ANOVA) test was performed in accordance with normality and homogeneity of variance, and a significance probability was corrected by the Bonferroni *post-hoc* analysis. To demonstrate a difference between two evaluation groups, the Welch's *t*-test was conducted in the similar way with the three evaluation groups. The association and agreement between ufcPWV and bhPWV were also analyzed and the relationships were determined by calculating the Pearson's correlation coefficient ($r$).

# RESULTS

## Correlation Between ufcPWV and bhPWV Measurement

The association between the ufcPWV and the bhPWV was evaluated for all subjects ($n = 69$). As illustrated in **Figure 2A**, the ufcPWV was significantly correlated with bhPWV measured via Bramwell-Hill model ($r = 0.85$, $p < 0.01$). **Figure 2B** represents the Bland-Altman plot to assess the agreement between the ufcPWV and the bhPWV, and they showed a nonsignificant difference between the two measurements (the limits of agreements: −2.7–3.8 m/s).

## Comparison Between CV Risk Groups

In the analysis of the three evaluation groups (low- ($n = 31$), intermediate- ($n = 22$) and high-risk ($n = 16$); **Table 1**) according to Framingham risk score, the bhPWV showed a statistically significant difference, i.e., low- and intermediate-risk ($5.1 \pm 0.9$ vs. $7.7 \pm 2.0$ m/s, $p < 0.01$), low- and high-risk groups ($5.1 \pm 0.9$ vs. $9.8 \pm 2.5$ m/s, $p < 0.01$) and intermediate- and high-risk group ($7.7 \pm 2.0$ vs. $9.8 \pm 2.5$ m/s, $p < 0.01$), respectively, as illustrated in **Figure 2C**. For the ufcPWV measurement, as illustrated in **Figure 2D**, it showed a statistically significant difference between low- and intermediate-risk ($5.3 \pm 1.1$ vs. $8.3 \pm 3.1$ m/s, $p < 0.01$), and low- and high-risk groups ($5.3 \pm 1.1$ vs. $10.8 \pm 2.5$ m/s, $p < 0.01$) while there is no significant difference between intermediate- and high-risk group ($8.3 \pm 3.1$ vs. $10.8 \pm 2.5$ m/s, $p = 0.121$).

To further analyze the differences between the CV risk models, two modified evaluation groups consisting of the low-risk group (<10%, $n = 31$) and the higher-risk group (≥10%, $n = 38$; the intermediate and the high-risk), were analyzed in the same manner. **Figures 2E,F** show the comparison results using the ufcPWV based on the ultrafast curved array imaging and the bhPWV measured via the Bramwell-Hill equation, respectively. As illustrated in **Figures 2E,F**, there was a statistically significant difference between low- and higher-risk group in both the bhPWV ($5.1 \pm 0.9$ vs. $8.6 \pm 2.4$ m/s, $p < 0.01$) and the ufcPWV measurements ($5.3 \pm 1.1$ vs. $9.4 \pm 3.1$ m/s, $p < 0.01$).

## Association of ufcPWV With Framingham Risk Score

A significant correlation was found between the ufcPWV and FRS ($r = 0.41$, $p < 0.05$; **Figure 3A**) in the low-risk case while there were no correlation in the intermediate- and high-risk groups, as shown in **Figures 3B,C**. The linear fitting between the ufcPWV and FRS in the low-risk case showed an increase of 0.19 m/s in ufcPWV per 1-FRS. Moreover, the ufcPWV in the case of the higher-risk group combined with the intermediate and the high-risk subjects was also significantly correlated with the FRS ($r = 0.44$, $p < 0.01$) as described in **Figure 3D**, and the linear fitting indicated an increase of 1.0 m/s per 10-FRS.

## Association of ufcPWV With Systolic Blood Pressure

The relation of ufcPWV to systolic blood pressure (**Table 1**), which is a classic measure of arterial stiffness, was additionally assessed, as illustrated in **Figure 4**. **Figure 4A** represents the relation between ufcPWV and systolic blood pressure for all subjects ($n = 69$), and it showed a significant correlation ($r = 0.26$, $p < 0.05$) between the two clinical parameters. To further analyze the association according to the CV risk model, systolic blood pressures for the three evaluation groups were respectively evaluated. As shown in **Figures 4B–D**, the ufcPWV was significantly correlated with the systolic blood pressure in the intermediate and high-risk groups, respectively, ($r = 0.47$ and $r = 0.45$, all $p < 0.05$) while the low-risk group showed no significant association ($r = 0.10$, $p = 0.60$).

# DISCUSSION

Pulse waves are propagated through arteries, and PWV is affected by the mechanical properties in the pathological process of arterial wall changes along the arterial system. Therefore, PWV is not constant and varies from one location to another since the geometrical and mechanical properties vary along the arterial tree, and there are differences between central elastic arteries and more peripheral, muscular arteries. For these reasons, the importance of measuring local PWV is increasing in contrast to measuring systemic PWV, which can only be estimated an averaged PWV. For example, aortic PWV, which is one of the most reliable clinical parameters for evaluating arterial stiffness, has been generally measured in two different sites (e.g., carotid and femoral arteries). The carotid-femoral PWV measurement is currently accepted as the gold-standard technique for arterial stiffness assessments. For carotid-femoral PWV measurements, several tonometry techniques based on pressure sensors with ECG gating (e.g., PulsePen, Complior and SphygmoCor) have been widely used in research and clinical settings (11). However, distance measurements of the pulse wave pathway are approximately estimated with the sensor location on the body surface, thus causing a crucial systemic error in the PWV measurements. To overcome this limitation, local PWV measurement methods through direct visualization of local vessels have been introduced based on ultrasound or MRI imaging techniques. The ultrasound technique allows the determination of the PWV by estimating the time delay between the diameter waveforms at two close positions in a local site, e.g., Doppler-derived PWV, flow-area method and pulse wave imaging (15–17, 38). The MRI-based PWV estimation uses

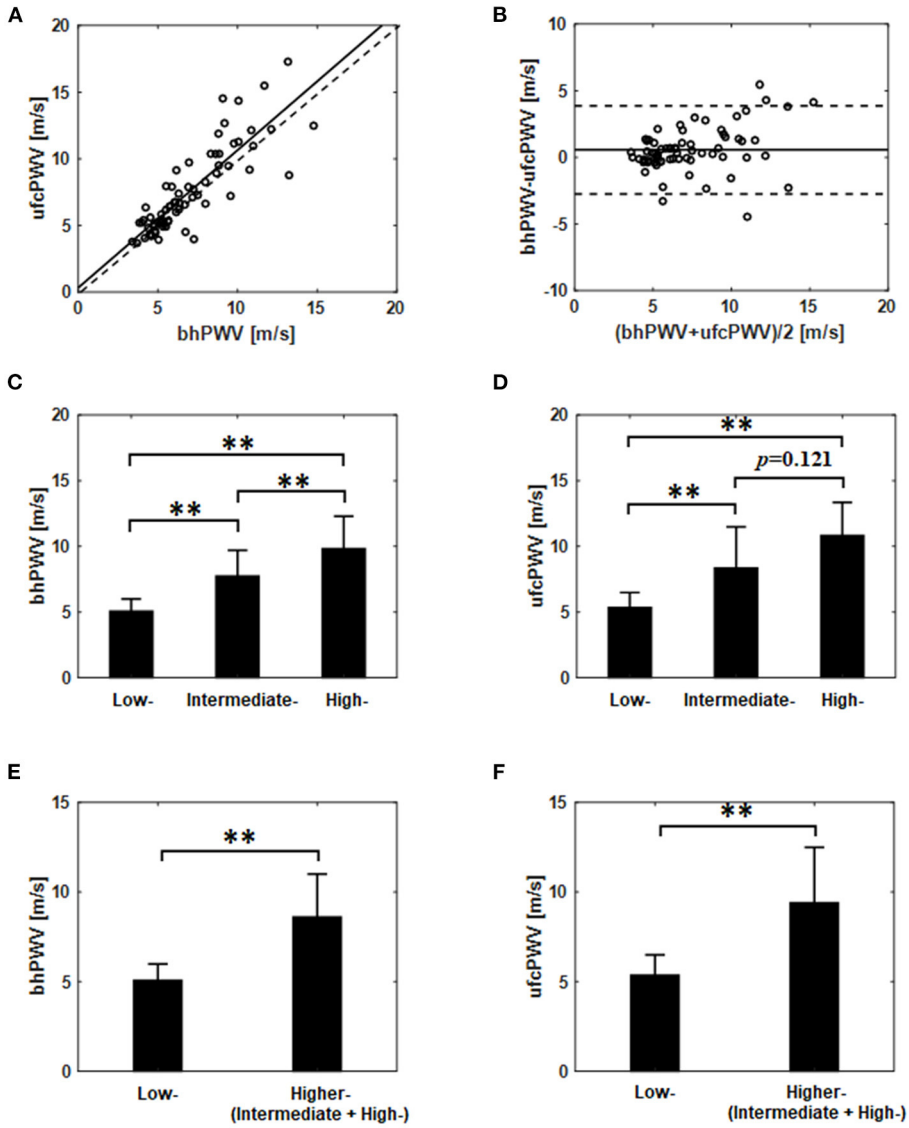


**FIGURE 2 | (A)** Correlation and **(B)** agreement assessment between the ufcPWV based on the ultrafast curved array imaging and the bhPWV measured via Bramwell-Hill equation (solid line indicates the mean difference between the two measurements and dashed lines represent mean ± 1.96SD). Comparisons between the three evaluation groups [i.e., low- (<10%), intermediate- (10∼20%) and high-risk (>20%)] based on Framingham risk score from **(C)** the bhPWV and **(D)** the ufcPWV measurement. Comparisons between the two evaluation groups [i.e., low- (<10%) vs. higher-risk (≥10%)] from **(E)** the bhPWV and **(F)** the ufcPWV measurement. ** indicates $p < 0.01$.

the accurate and direct measurement of the path length of pulse waves between two imaging levels and provides aortic vascular parameters (aortic distensibility, aortic compliance, aortic elastic modulus and aortic stiffness index) (39, 40). These imaging-guided PWV measurements take advantage of the direct measurement for the pulse wave pathway and can avoid the systemic error induced by the coarse estimation of distance.

A major advantage of the local measurement of PWV is that a direct measurement of local vessels is strongly related to wall stiffness. In the early stage of arterial stiffness, the elastic properties are affected by locally scattered fibrous spots on the arterial wall, and the heterogeneous structure of arterial walls at different sites produces different functional properties between vessel segments. Regarding strongly localized wall heterogeneity, arterial wall mechanical properties can be dramatically altered within a small region (from a few millimeters to a few centimeters), e.g., abdominal aortic aneurysms or arterial plaques. However, the most current PWV measurements (e.g., carotid-femoral PWV) cannot assess biomechanical properties in local vessels, and they cannot directly evaluate the arterial stiffness of vessel segments due to the accessibility and the limited temporal resolution of the techniques. The temporal

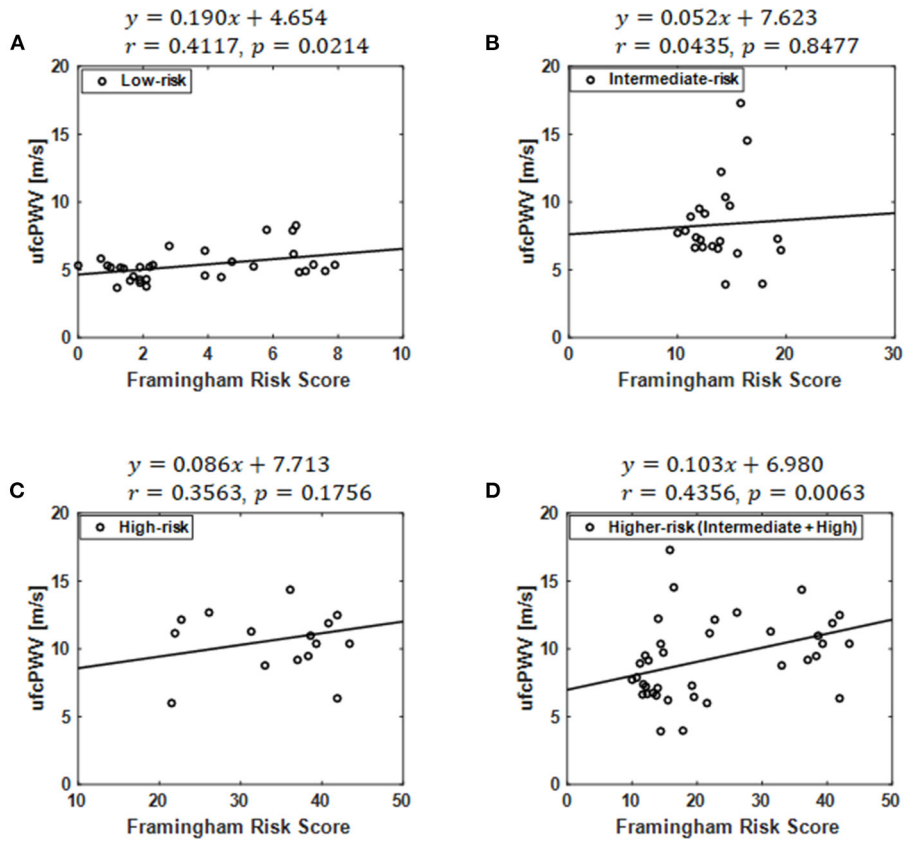


**FIGURE 3 |** Correlation between the ufcPWV based on ultrafast curved array imaging and Framingham risk score in the case of **(A)** the low-risk model, **(B)** the intermediate-risk model, **(C)** the high-risk model and **(D)** the higher-risk model combined with the intermediate and the high-risk groups.

resolution (i.e., frame-rate) is the most significant technical factor in the PWV measurements. To properly snapshot the accelerated pulse wave (5∼10 m/s), data acquisition rates must be increased relative to the PWV. However, the accuracy and reliability of the PWV measurement approaches usually suffer from an inherent technical tradeoff between spatial resolution (image quality) and temporal resolution (frame rate). Inaccurate measurements imposed by frame-rate limitations can increase errors as the PWV increases by arterial stiffening. Therefore, a high-frame-rate-based accurate PWV measurement technique is still required.

The FRS, which estimates the 10-year CV risk of an individual, is calculated based on a variety of risk factors such as age, smoking history, diabetes mellitus, systolic blood pressure, HDL-C concentration. The FRS is considered as a useful tool for quantitative assessment of the risk for CV disease in the general populations (30, 41–43) and it can be closely related to PWV since both FRS and PWV are widely used as surrogate markers to predict future CV disease by quantifying total CV risk. However, the correlation between FRS and PWV is rarely reported although it has potentials to develop into a more powerful biomarker for CV risk prediction (6, 44–46).

In this article, we investigated the association between the Framingham risk model classified with FRS and aortic PWV. To measure local PWV in a specific aortic segment (i.e., abdominal aorta) with high spatiotemporal resolution (>1 kHz), wide field-of-view ultrafast curved array imaging based PWV measurement method (ufcPWV) was proposed (**Figure 1**). In the result for the three risk groups (**Figure 2**), the ufcPWV showed a statistically significant difference between low- and intermediate-risk, and low- and high-risk groups, but there is no significant difference between intermediate- and high-risk groups. To compensate this factor, two evaluation groups consisting of the low- (FRS<10%) and the higher-risk group (FRS $\geq$ 10%) were additionally assessed, and it showed a highly significant difference in both bhPWV and ufcPWV (**Figure 2**). The additional analysis to investigate the direct correlation between FRS and ufcPWV was performed, and only the low- and the higher-risk groups showed a significant correlation with different increments of PWV (**Figure 3**). The direct association between FRS and aortic PWV should be more investigated with large populations.

The association between aortic PWV and systolic blood pressure among the clinical parameters (**Table 1**) was additionally evaluated since the systolic blood pressure is

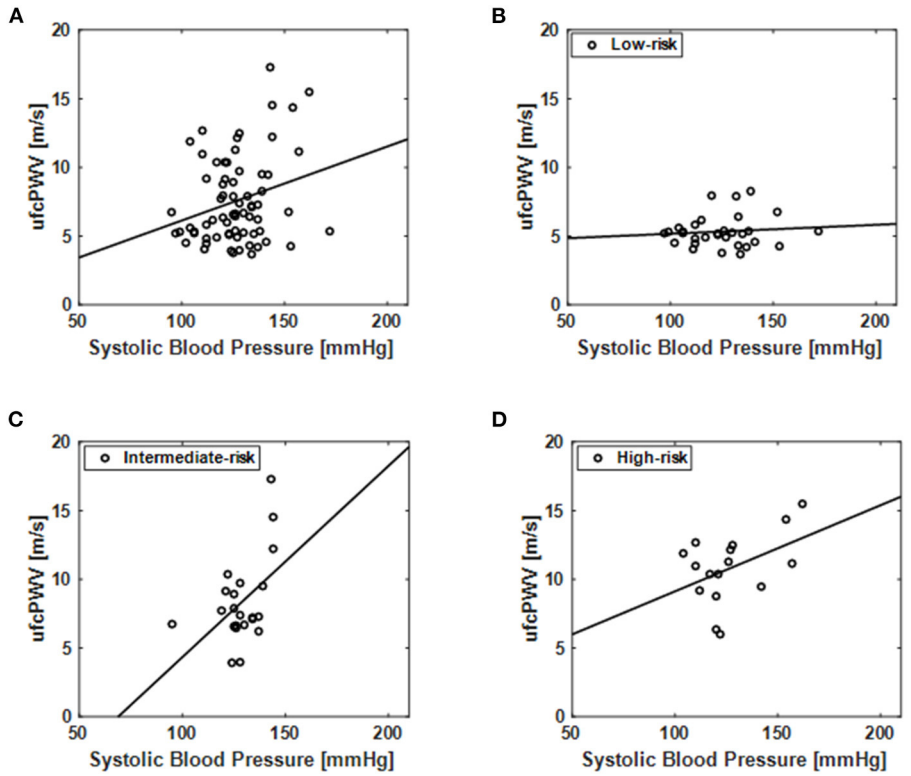


**FIGURE 4 |** Correlation of the ufcPWV based on ultrafast curved array imaging with systolic blood pressure (**Table 1**) for **(A)** all subjects ($n = 69$) and individual CV risk groups [**(B)** low-, **(C)** intermediate- and **(D)** high-risk].

one of the mostly contributing factors to PWV (47). In the assessment for all subjects, the ufcPWV and systolic blood pressure showed a significant relationship, as illustrated in **Figure 4A**. However, in the analysis according to the CV risk model, only the intermediate and high-risk groups showed a significant association between the two parameters although the groups of the systolic blood pressure showed no significant differences (**Table 1**). It means that aortic PWV in higher risk group may be correlated with CV risk independently of the systolic blood pressure, but it should be investigated with more obvious control groups as well as large populations.

One of the limitations of this study is the lack of comparison with carotid-femoral PWV based on tonometry, which is the most validated technique to estimate arterial stiffness and correlated with CV risk (48). A validation study between carotid-femoral PWV and local ufcPWV may further improve an aortic PWV as a useful biomarker for predicting CV risk. The other limitation is that any tags for the same scanning site (i.e., abdominal aorta) were not utilized during examinations although patients in the supine position were basically scanned by experienced sonographers. In addition, there was no assessment of intra- and inter-observer variability in PWV measurements. A number of data sets in the intermediate- ($n = 9$) and the high-risk ($n = 15$) groups (**Table 1**) were excluded due to poor image quality or a history of CV disease. The main cause for the deterioration of image quality may be due to the degradation in receive beamforming since a thick layer of fat in obese patients incurs severe phase aberration. Furthermore, linear regression with $r^2$ <0.5 was considered unreliable and the corresponding PWV estimate would be rejected.

For the future PWV measurements, relatively inexpensive techniques with fewer approximations, leading to an accurate evaluation, will be needed for the more efficient diagnostic tool in detecting CV diseases in early stages. In addition, highly accurate PWV measurements and direct arterial stiffness assessments may also improve the management of the process of CV risks or the monitoring of therapy in patients with conditions such as isolated systolic hypertension. In future work, aortic PWVs in different segmental regions (e.g., ascending aorta, arch of aorta and descending aorta) will be measured and evaluated in various clinical settings (e.g., atherosclerosis).

## CONCLUSION

In this paper, a high-spatiotemporal resolution aortic PWV measurement method based on ultrafast curved array imaging (ufcPWV) was proposed and it showed the association with Framingham risk model. This feasibility study demonstrated that the ufcPWV measurement has the potential to be a

new approach to overcome the limitations of conventional systemic measurement methods in the assessment of aortic stiffness.

## DATA AVAILABILITY STATEMENT

The original contributions presented in the study are included in the article/supplementary material, further inquiries can be directed to the corresponding author.

## ETHICS STATEMENT

The studies involving human participants were reviewed and approved by Institutional Review Board of the Clinical Trials Center of Yonsei University Health System (IRB number: 1-2019-0065). The patients/participants provided their written informed consent to participate in this study.

## AUTHOR CONTRIBUTIONS

JK and KH performed the theoretical and experimental analyses and implementation of *the in vivo* study. JH and G-RH designed the clinical study protocol and obtained data from patients. G-RH and YY supervised the study. JK, G-RH, and YY wrote the manuscript. All authors contributed to the article and approved the submitted version.

## FUNDING

This work was supported by the National Research Foundation of Korea (NRF) grant funded by the Korean government (MSIT) (NRF-2021R1A2C3006264) and the Korea Medical Device Development Fund grant funded by the Korea government (the Ministry of Science and ICT, the Ministry of Trade, Industry and Energy, the Ministry of Health & Welfare, and the Ministry of Food and Drug Safety) (Project Number: 202011A01).

## REFERENCES

1. Zieman SJ, Melenovsky V, Kass DA. Mechanisms, pathophysiology, and therapy of arterial stiffness. *Arterioscler Thromb Vasc Biol.* (2005) 25:932–43. doi: 10.1161/01.ATV.0000160548.78317.29
2. Shirwany NA, Zou MH. Arterial stiffness: a brief review. *Acta Pharmacol Sin.* (2010) 31:1267–76. doi: 10.1038/aps.2010.123
3. Cohn JN. Arterial stiffness, vascular disease, and risk of cardiovascular events. *Circulation.* (2006) 113:601–3. doi: 10.1161/CIRCULATIONAHA.105.600866
4. Sun Z. Aging, arterial stiffness, and hypertension. *Hypertension.* (2015) 65:252–6. doi: 10.1161/HYPERTENSIONAHA.114.03617
5. Mattace-Raso FUS, van der Cammen TJM, Hofman A, van Popele NM, Bos ML, Schalekamp MADH, et al. Arterial stiffness and risk of coronary heart disease and stroke: the Rotterdam Study. *Circulation.* (2006) 113:657–63. doi: 10.1161/CIRCULATIONAHA.105.555235
6. Blacher J, Asmar R, Djane S, London GM, Safar ME. Aortic pulse wave velocity as a marker of cardiovascular risk in hypertensive patients. *Hypertension.* (1999) 33:1111–7. doi: 10.1161/01.HYP.33.5.1111
7. Sutton-Tyrrell K, Najjar SS, Boudreau RM, Venkitachalam L, Kupelian V, Simonsick EM, et al. Elevated aortic pulse wave velocity, a marker of arterial stiffness, predicts cardiovascular events in well-functioning older adults. *Circulation.* (2005) 111:3384–90. doi: 10.1161/CIRCULATIONAHA.104.483628
8. Salvi P, Scalise F, Rovina M, Moretti F, Salvi L, Grillo A, et al. Noninvasive estimation of aortic stiffness through different approaches. *Hypertension*. (2019) 74:117–29. doi: 10.1161/HYPERTENSIONAHA.119.12853
9. Rajzer MW, Wojciechowska W, Klocek M, Palka I, Brzozowska-Kiszka M, Kawecka-Jaszcz K. Comparison of aortic pulse wave velocity measured by three techniques: Complior, SphygmoCor and Arteriograph. *J Hypertens.* (2008) 26:2001–7. doi: 10.1097/HJH.0b013e32830a4a25
10. Bortel LMV, Laurent S, Boutouyrie P, Chowienczyk P, Cruickshank JK, Backer TD, et al. Expert consensus document on the measurement of aortic stiffness in daily practice using carotid-femoral pulse wave velocity. *J Hypertens.* (2012) 30:445–8. doi: 10.1097/HJH.0b013e32834fa8b0
11. Pereira T, Correia C, Cardoso J. Novel methods for pulse wave velocity measurement. *J Med Biol Eng.* (2015) 35:555–65. doi: 10.1007/s40846-015-0086-8
12. Styczynski G, Rdzanek A, Pietrasik A, Kochman J, Huczek Z, Sobieraj P, et al. Echocardiographic assessment of aortic pulse-wave velocity: validation against invasive pressure measurements. *J Am Soc Echocardiogr.* (2016) 29:1109–16. doi: 10.1016/j.echo.2016.07.013
13. Wentland AL, Grist TM, Wieben O. Review of MRI-based measurements of pulse wave velocity: a biomarker of arterial stiffness. *Cardiovasc Diagn Ther.* (2014) 4:193–206. doi: 10.3978/j.issn.2223-3652.2014.03.04
14. Ohyama Y, Ambale-Venkatesh B, Noda C, Kim JY, Tanami Y, Teixido-Tura G, et al. Aortic arch pulse wave velocity assessed by magnetic resonance imaging as a predictor of incident cardiovascular events: The MESA (Multi-Ethnic Study of Atherosclerosis). *Hypertension.* (2017) 70:524–30. doi: 10.1161/HYPERTENSIONAHA.116.08749
15. Calabia J, Torguet P, Garcia M, Garcia I, Martin N, Guasch B, et al. Doppler ultrasound in the measurement of pulse wave velocity: agreement with the Complior method. *Cardiovasc Ultrasound.* (2011) 9:13. doi: 10.1186/1476-7120-9-13
16. Nandlall SD, Konofagou EE. Assessing the stability of aortic aneurysms with pulse wave imaging. *Radiology.* (2016) 281:772–81. doi: 10.1148/radiol.2016151407
17. Li RX, Apostolakis IZ, Kemper P, McGarry MDJ, Ip A, Connolly ES, et al. Pulse wave imaging in carotid artery stenosis human patients in vivo. *Ultrasound Med Biol.* (2019) 45:353–66. doi: 10.1016/j.ultrasmedbio.2018.07.013
18. Couade M, Pernot M, Messas E, Emmerich J, Hagègec A, Fink M, et al. Ultrafast imaging of the arterial pulse wave. *IRBM.* (2011) 32:106–8. doi: 10.1016/j.irbm.2011.01.012
19. Apostolaski IZ, McGarry MDJ, Bunting EA, Konofagou EE. Pulse wave imaging using coherent compounding in a phantom and in vivo. *Phys Med Biol.* (2017) 62:1700–30. doi: 10.1088/1361-6560/aa553a
20. Couade M, The advent of ultrafast ultrasound in vascular imaging: a review. *J. Vasc. Diag. Interv*. (2016) 4:9–22. doi: 10.2147/JVD.S68045
21. Goudot G, Papadacci C, Dizier B, Baudrie V, Ferreira I, Boisson-Vidal C, et al. Arterial stiffening with ultrafast ultrasound imaging gives new insight into arterial phenotype of vascular Ehlers-Danlos mouse models. *Ultraschall Med.* (2019) 40:734–42. doi: 10.1055/a-0599-0841
22. Li X, Jiang J, Zhang H, Wang H, Han D, Zhou Q, et al. Measurement of carotid pulse wave velocity using ultrafast ultrasound imaging in hypertensive patients. *J Med Ultrason.* (2001) 44:183–90. doi: 10.1007/s10396-016-0755-4
23. Mirault T, Pernot M, Frank M, Couade M, Niarra R, Azizi M, et al. Carotid stiffness change over the cardiac cycle by ultrafast ultrasound imaging in healthy volunteers and vascular Ehlers-Danlos syndrome. *J Hypertens.* (2015) 33:1890–6. doi: 10.1097/HJH.0000000000000617
24. Zhu ZQ, Chen LS, Wang H, Liu FM, Luan Y, Wu LL, et al. Carotid stiffness and atherosclerotic risk: non-invasive quantification with ultrafast ultrasound pulse wave velocity. *Eur Radiol.* (2019) 29:1507–17. doi: 10.1007/s00330-018-5705-7
25. Yin LX, Ma CY, Wang S, Wang YH, Meng PP, Pan XF, et al. Reference values of carotid ultrafast pulse-wave velocity: a prospective,

multicenter, population-based study. *J Am Soc Echocardiogr.* (2021) 34:629–41. doi: 10.1016/j.echo.2021.01.003
26. GoudotG, Mirault T, Khider L, Pedreira O, Cheng C, Porée J, et al. Carotid Stiffness Assessment With Ultrafast Ultrasound Imaging in Case of Bicuspid Aortic Valve. *Front. Physiol.* (2019) 23:1330. doi: 10.3389/fphys.2019.01330
27. Yang W, Wang Y, Yu Y, Mu L, Kong F, Yang J, et al. Establishing normal reference value of carotid ultrafast pulse wave velocity and evaluating changes on coronary slow flow. *Int J Cardiovasc Imaging.* (2020) 36:1931–9. doi: 10.1007/s10554-020-01908-3
28. Kang J, Go D, Song I, Yoo Y. Wide field-of-view ultrafast curved array imaging using diverging waves. *IEEE Trans Biomed Eng.* (2020) 67:1638–49. doi: 10.1109/TBME.2019.2942164
29. Westenberg JJM, van Poelgeest EP, Steendijk P, Grotenhuis HB, Jukema JW, de Roos A. Bramwell-Hill modeling for local aortic pulse wave velocity estimation: a validation study with velocity-encoded cardiovascular magnetic resonance and invasive pressure assessment. *J Cardiovasc Magn Reson.* (2012) 14:2. doi: 10.1186/1532-429X-14-2
30. D'Agostino Sr RB, Vasan RS, Pencina MJ, Wolf PA, Cobain M, Massaro JM, et al. General cardiovascular risk profile for use in primary care: the framingham heart study. *Circulation.* (2008) 117:743–53. doi: 10.1161/CIRCULATIONAHA.107.699579
31. Taki H, Yamakawa M, Shiina T, Sato T. Compensation technique for the intrinsic error in ultrasound motion estimation using a speckle tracking method. *Japanese J Appl Phy.* (2015) 54:07HF03. doi: 10.7567/JJAP.54.07HF03
32. Voigt JU, Pedrizzetti G, Lysyansky P, Marwick TH, Houle H, Baumann R, et al. Definitions for a common standard for 2D speckle tracking echocardiography: consensus document of the EACVI/ASE/Industry Task Force to standardize deformation imaging. *J Am Soc Echocardiogr.* (2015) 28:183–93. doi: 10.1016/j.echo.2014.11.003
33. Ye X, Liu Z, Ma Y, Song Y, Hu L, Luo J, et al. A novel normalized cross-correlation speckle-tracking ultrasound algorithm for the evaluation of diaphragm deformation. *Front Med.* (2021) 8:612933. doi: 10.3389/fmed.2021.612933
34. Maurice RL, Bertrand M. Lagrangian speckle model and tissue-motion estimation—theory. *IEEE Trans Med Imag.* (1999) 18:593–603. doi: 10.1109/42.790459
35. Luo J, Ying K, He P, Bai J. Properties of Savitzky-Golay digital differentiators. *Dig Sig Proc.* (2005) 15:122–36. doi: 10.1016/j.dsp.2004.09.008
36. Bramwell JC, Hill AV. The velocity of the pulse wave in man. *Proc R Soc Lond B.* (1922) 93:298–306. doi: 10.1098/rspb.1922.0022
37. Huang C, Guo D, Lan F, Zhang H, Luo J. Noninvasive measurement of regional pulse wave velocity in human ascending aorta with ultrasound imaging: an in-vivo feasibility study. *J Hypertens.* (2016) 34:2026–37. doi: 10.1097/HJH.0000000000001060
38. Rabben SI, Stergiopulos N, Hellevik LR, Smiseth OA, Slørdahl S, Urheim S, et al. An ultrasound-based method for determining pulse wave velocity in superficial arteries. *J Biomech.* (2004) 37:1615–22. doi: 10.1016/j.jbiomech.2003.12.031
39. van der Meer RW, Diamant M, Westenberg JJM, Doornbos J, Bax JJ, de Roos A, et al. Magnetic resonance assessment of aortic pulse wave velocity, aortic distensibility, and cardiac function in uncomplicated type 2 diabetes mellitus. *J Cardiovasc Magn Reson.* (2007) 9:645–51. doi: 10.1080/10976640601093703
40. Joly L, Perret-Guillaume C, Kearney-Schwartz A, Salvi P, Mandry D, Marie PY, et al. Pulse wave velocity assessment by external noninvasive devices and phase-contrast magnetic resonance imaging in the obese. *Hypertension.* (2009) 54:421–6. doi: 10.1161/HYPERTENSIONAHA.109.133645
41. Wannamethee SG, Shaper AG, Lennon L, Morris RW. Metabolic syndrome vs framingham risk score for prediction of coronary heart disease, stroke, and type 2 diabetes mellitus. *Arch Intern Med.* (2005) 165:2644–50. doi: 10.1001/archinte.165.22.2644
42. Fowkes FGR, Murray GD, Butcher I, Heald CL, Lee RJ, Chambless LE, et al. Ankle brachial index combined with framingham risk score to predict cardiovascular events and mortality: a meta-analysis. *JAMA.* (2008) 300:197–208. doi: 10.1001/jama.300.2.197
43. de Ruijter W, Westendorp RGJ, Assendelft WJJ, den Elzen WPJ, de Craen AJM, le Cessie S, et al. Use of Framingham risk score and new biomarkers to predict cardiovascular mortality in older people: population based observational cohort study. *BMJ.* (2009) 338:a3083. doi: 10.1136/bmj.a3083
44. Yamashina A, Tomiyama H, Arai T, Hirose K, Koji Y, Hirayama Y, et al. Brachial-ankle pulse wave velocity as a marker of atherosclerotic vascular damage and cardiovascular risk. *Hypertens Res.* (2003) 26:615–22. doi: 10.1291/hypres.26.615
45. Kim YK, Kim D. The relation of pulse wave velocity with framingham risk score and SCORE risk score. *Korean Circ J.* (2005) 35:22–9. doi: 10.4070/kcj.2005.35.1.22
46. Park KH, Kim MK, Kim HS, Park WJ, Cho GY, Choi YJ. Clinical significance of framingham risk score, flow-mediated dilation and pulse wave velocity in patients with stable angina. *Circ J.* (2011) 75:1177–83. doi: 10.1253/circj.CJ-10-0811
47. Kim EJ, Park CG, Park JS, Suh SY, Choi CU, Kim JW, et al. Relationship between blood pressure parameters and pulse wave velocity in normotensive and hypertensive subjects: invasive study. *J Hum Hypertens.* (2007) 21:141–8. doi: 10.1038/sj.jhh.1002120
48. Ben-Shlomo Y, Spears M, Boustred C, May M, Anderson SG, Benjamin EJ, et al. Aortic pulse wave velocity improves cardiovascular event prediction: an individual participant meta-analysis of prospective observational data from 17,635 subjects. *J Am Coll Cardiol.* (2014) 63:636–46. doi: 10.1016/j.jacc.2013.09.063

**Conflict of Interest:** The authors declare that the research was conducted in the absence of any commercial or financial relationships that could be construed as a potential conflict of interest.

frontiers in Cardiovascular Medicine

CASE REPORT
published: 04 March 2022
doi: 10.3389/fcvm.2022.792531

# Case Report: Dual-Energy Computed Tomography of Cardiac Changes in IgG4-Related Disease

*Ying Wang*[1,2], *Hui Zhou*[1,2*], *Ping Hu*[1,2], *Jie Zhao*[1,2], *Yitao Mao*[1,2], *Zhixiao Li*[1,2] *and Xi Zhao*[3]

[1] *Department of Radiology, Xiangya Hospital, Central South University, Changsha, China,* [2] *National Clinical Research Center for Geriatric Disorders, Xiangya Hospital, Central South University, Changsha, China,* [3] *Siemens Healthineers China, Shanghai, China*

OPEN ACCESS

**Edited by:**
*Luca Saba,*
*Azienda Ospedaliero-Universitaria Cagliari, Italy*

**Reviewed by:**
*David C. Rotzinger,*
*Centre Hospitalier Universitaire Vaudois (CHUV), Switzerland*
*Kenichiro Otsuka,*
*Massachusetts General Hospital and Harvard Medical School, United States*
*Konstantin V. Zavadovsky,*
*Cardiology Research Institute, Tomsk National Research Medical Center (RAS), Russia*
*Filippo Cademartiri,*
*Gabriele Monasterio Tuscany Foundation (CNR), Italy*

***Correspondence:**
*Hui Zhou*
*huistanzhou@csu.edu.cn*

**Specialty section:**
*This article was submitted to Cardiovascular Imaging, a section of the journal Frontiers in Cardiovascular Medicine*

**Received:** *10 October 2021*
**Accepted:** *31 January 2022*
**Published:** *04 March 2022*

**Citation:**
*Wang Y, Zhou H, Hu P, Zhao J, Mao Y, Li Z and Zhao X (2022) Case Report: Dual-Energy Computed Tomography of Cardiac Changes in IgG4-Related Disease. Front. Cardiovasc. Med. 9:792531. doi: 10.3389/fcvm.2022.792531*

**Background:** Dual-energy computed tomography (DECT) is used in coronary plaque characterization, myocardial perfusion imaging, and pulmonary embolism diagnosis; however, there is no relevant research on DECT in IgG4-related diseases (IgG4-RD) involving the coronary artery. We are the first to report DECT findings of cardiac morphology and function in IgG4-RD.

**Patient Findings:** Multimodality cardiovascular imaging from a 63-year-old male patient, who presented with IgG4-related pancreatitis, was analyzed. An iodine map and spectral curves were obtained from the DECT, which can help to distinguish between non-calcified plaques and IgG4 lesions of the coronary artery, noninvasive $FFR_{CT}$ (fractional flow reserve derived from coronary computed tomography angiography) and ECV (extracellular volume fraction) demonstrated myocardial ischemia and myocardial fibrosis, respectively.

**Conclusion:** The DECT can detect coronary artery tumor-like lesions caused by IgG4-RD and simultaneously assess the morphological, functional, and histological characteristics of the myocardium. This may help to guide individualized and timely treatment and avoid potentially life-threatening complications.

**Keywords: dual energy computed tomography (DECT), coronary computed tomography angiography (CCTA), myocardial ischemia (MI), myocardial fibrosis (MF), IgG4-related disease (IgG4-RD), coronary heart disease**

## BACKGROUND

It is now generally believed that IgG4-related diseases (IgG4-RD) are systemic diseases that can affect multiple organs. Numerous studies have shown that coronary artery involvement is related to poor prognosis due to life-threatening complications such as myocardial infarction and aneurysmal rupture (1). Since it is difficult to obtain a coronary artery tissue biopsy, imaging plays an important role in the assessment of IgG4-related coronary disease. However, no imaging method can simultaneously distinguish IgG4 lesions from non-calcified plaques and analyze myocardial function. Considering the current applications of dual-energy computed tomography (DECT) in heart diagnostics, we present the first report of DECT findings in IgG4-related coronary disease.

## CASE PRESENTATION

A 63-year-old male presented with abdominal pain was admitted to our hospital. Laboratory examination showed that IgG4 (19.3 g/L) was elevated at nearly 8 times the upper limit of normal. Abdominal CT demonstrated a pancreatic mass and soft tissue lesions around the abdominal aorta and biliary tree. After completing a series of examinations and multidisciplinary discussions, the patient had a cumulative score of 38 points according to the inclusion criteria of the 2019 ACR/EULAR Classification Criteria for IgG4-RD (2) and was diagnosed with IgG4-RD. His past medical history included hypertension, type II diabetes, coronary artery disease with stable angina, and a splenectomy due to trauma. Coronary computed tomography angiography (CCTA) was conducted *via* DECT (SOMATOM Drive, Siemens Healthineers, Forchheim, Germany) and Syngo. *Via* workstation, "CT coronary artery," "CT dual-energy," and "CT cardiac function," tools were used for measuring under the guidance of professional engineers. The circular regions of interest (ROI) were manually drawn to ensure that the ROIs were in the center of the lesions based on multiplanar three-dimensional reconstruction. The intra-observer and inter-observer intraclass correlation efficient (ICC) were 0.90 and 0.96, respectively. The measurements of deep learning-based fractional flow reserve derived from coronary computed tomography angiography ($FFR_{CT}$) were performed by an independent core laboratory at Keya Medical (3).

The CCTA showed multiple coronary arteries with moderate to severe stenosis lesions (**Figures 1B–D**); the left anterior-descending branch (LAD) was the most severely affected, which had 75–99% stenosis, the diagonal branch had 90% stenosis, the left circumflex branch (LCX) had 75–90% stenosis, and the right coronary artery (RCA) had 50–90% stenosis, which was confirmed *via* invasive coronary angiography (ICA) (**Figures 1F–H**). Interestingly, this patient had both non-calcified plaques and a lot of tumor-like lesions around the triple vessels (**Figure 1A**). The latter lesions might be caused by IgG4-RD, which were neglected during ICA. As we have known, IgG4-RD causes periarteritis that is predominantly affecting the adventitia, while the intima and media are less involved (1). However, non-calcified plaques are primarily located inside the lumen because it initially occurs in the intima of the coronary artery. The plaque inside the proximal LAD was easier to distinguish from the IgG4-related infiltration surrounding the coronary artery; therefore, we chose this area to measure the two lesions (**Figure 1I**). The mean CT attenuation value of the tumor-like lesion in proximal LAD was 38 HU in non-contrast images (Tube Voltage 100 keV), which was like the fibrous fatty plaque (45HU) located on the same slice of CT axial images. During the delayed contrast phase, the mean CT attenuation of the non-calcified plaque was 64 HU, while the tumor-like lesion was 100 HU. Combining with their enhanced features, we can further determine the non-calcified plaques and the IgG4-related infiltrates.

Firstly, we compared the iodine density of different lesions in LAD. In the arterial phase, tumor-like lesions took up more iodine than the non-calcified plaques, and the gap was widened with time (**Figures 1I,N**). The absolute and normalized iodine concentrations of the non-calcified plaques were 0.9 mg/ml and 5.2%; the IgG4-related components were 2.2 mg/ml and 12.8%, respectively. Normalized iodine concentration = plaque iodine concentration/aortic iodine concentration. Secondly, we compared the iodine density in different myocardial segments based on AHA segmentation (**Figure 1L**). The concentration of myocardial iodine, supplied by each coronary artery, can be seen on a Bull's eye plot (**Figure 1K**). The mid-anterior wall supplied by LAD had the least iodine deposits, indicating critical myocardial ischemia. The results of $FFR_{CT}$ arrived at the same conclusion (**Figure 1E**). The most severely affected myocardium is supplied by LAD, followed by RCA and LCX. Referencing the $FFR_{CT}$ threshold of myocardial ischemia (0.8), the $FFR_{CT}$ value of the LAD was 0.58, which was much lower than LCX (0.75) and RCA (0.74). Subsequently, we calculated the myocardial ECV values. The iodine density-derived ECV was calculated as follows: ECV (%) = (1 − hematocrit) × (iodine density in myocardium)/(iodine density in the blood) ×100%. The IgG4-related component had higher ECV values compared to the non-calcified plaques (**Figure 1O**); the values of the mid-cavity myocardium are shown in **Figure 1P**. Meanwhile, the cardiac function analysis in CT showed that left ventricle ejection fraction (LVEF) was 72%, left ventricle end-diastolic volume index (LVEDVI) was 72 ml/$m^2$, LV mass index was 82 g/$m^2$, right ventricle ejection fraction (RVEF) was 44%, and the right ventricle end-diastolic volume index (RVEDVI) was 104 ml/$m^2$, which suggested the normal biventricular volume and function. In addition, we made energy spectrum curves and calculated the slope values (**Figures 1J,M**). The CT values and the energy spectrum curves of the non-calcified plaques, the IgG4-related lesions, and the descending aorta were measured at the same level in the arterial and delayed stage. The CT values corresponding to 70 and 40 keV single energy points were selected as the reference points within the energy spectrum curve. The slope of the energy spectrum curve was calculated by the formula "(40–70 Kev)/(70–40)," 40, and 70 Kev, which were the CT values of the 40 and 70 keV energy points, respectively. The curves of the non-calcified plaques and the IgG4-related components were well-separated. In the arterial phase, the slopes of the non-calcified plaques and the IgG4 substance were 4 and 5.3, respectively, while, in the delayed contrast phase, the corresponding values were 1.3 and 2, respectively.

Through the comprehensive analysis of the patient's cardiac examination, he had indications of coronary stent implantation; however, considering the patient's older age, multiple complications, and high anesthesia risk, after multidisciplinary discussion and full communication with the patient and his family members, stent implantation was postponed, and the corticosteroid therapy (prednisone) was chosen as the first treatment. Other main treatments and corresponding medications included anticoagulation and antithrombosis (aspirin and clopidogrel), lowering lipid (atorvastatin), controlling blood sugar (metformin), controlling blood pressure, and protecting myocardium (irbesartan, metoprolol, and isosorbide mononitrate), etc. Meanwhile, the patient has been treated with particular caution and strict follow-up. The IgG4 level decreased from 19.3 to 3 g/L under

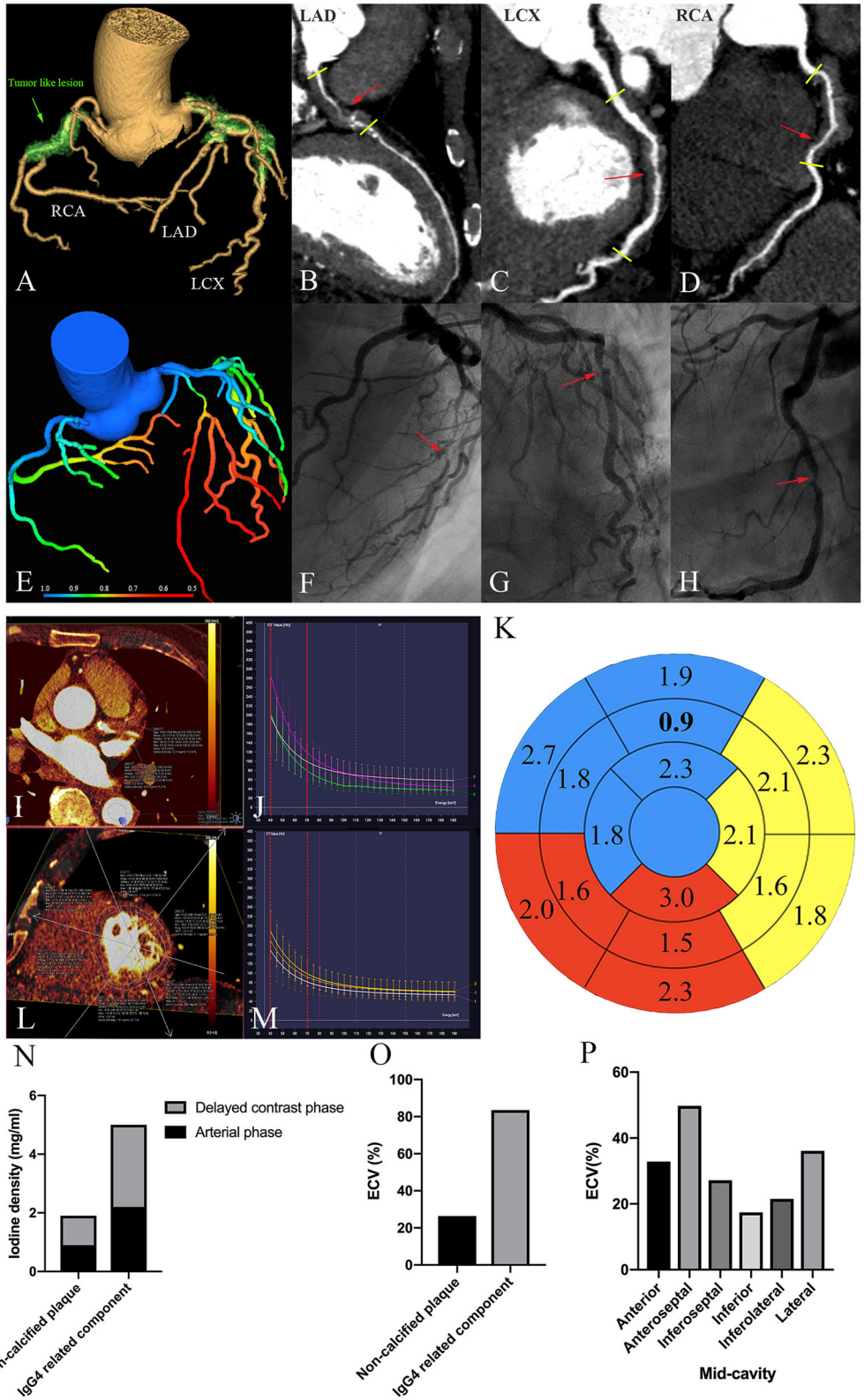


**FIGURE 1 |** Multimodality imaging of IgG4-RD involving the coronary artery. **(A)** 3D volume-rendered-reconstructed CCTA demonstrates tumor-like lesions involving the RCA, LAD, and LCX (a green arrow). **(B–D)** Curved planar reformation of the CCTA. The red arrow indicates the most severe stenosis. The short yellow line shows

*(Continued)*

**FIGURE 1 |** the obvious arterial wall thickening within three vessels. **(E)** Myocardial ischemia shown by Fractional Flow Reserve (FFR) derived from CCTA. About 0.8 is the threshold for myocardial ischemia. **(F–H)** Invasive coronary angiogram. The red arrow shows the most severity stenosis corresponding to **(B–D)**. **(I)** Iodine density of non-calcified plaques and the IgG4 substance located in the proximal LAD in the arterial phase. **(N)** is the corresponding histogram. **(J)** The energy spectral curve in the arterial phase. Green: a non-calcified plaque; purple: An IgG4 substance; peach: septal myocardium. The reference points (40 and 70 Kev) are marked as a red-dotted line. **(K)** Bully's eye indicating iodine density in different myocardial segments. The blue, yellow, and red areas represent the myocardium dominated by LAD, LCX, and RCA, respectively. Bold number represents mid-anterior myocardium, which has the least iodine deposits. **(L)** Iodine density within mid-cavity myocardium. **(P)** is the corresponding histogram. **(M)** An energy spectral curve in the delayed contrast phase. White: a non-calcified plaques; yellow: an IgG4 substance; orange: septal myocardium. The reference points (40 Kev and 70 Kev) are marked as a red-dotted line. **(N)** Iodine density of the non-calcified plaques and the IgG4 substance in the arterial and delayed contrast phases. **(O)** $ECV_{CT}$ of the non-calcified plaques and the IgG4 substance. **(P)** $ECV_{CT}$ of the mid-cavity myocardium.

systemic therapy within 7 months. The mass in the pancreas and soft tissue lesions around the biliary tree were reduced in size.

## DISCUSSION

Given that IgG4-related coronary artery disease has fatal consequences, differential diagnosis has significant clinical importance. Because pathological findings of the coronary artery are hard to obtain, imaging plays a vital role in diagnosis due to its non-invasiveness and repetitiveness. Intravascular ultrasound, CCTA, and $^{18}$FDG-PET/CT are used to evaluate the lesions according to morphology. There are three types of coronary artery involvement: stenotic, aneurysmal, and diffuse wall thickening. As our case shows, the typical "mistletoe sign" in CCTA is a characteristic radiologic finding in IgG4-RD involving the coronary artery (4). However, the assessment of the disease's morphology and myocardial function cannot be performed concurrently using a single modality image. In our case, DECT solves this problem well. Iodine density mapping and spectral curve analysis can be used to analyze the components of IgG4-related coronary artery disease; $FFR_{CT}$ and ECV can evaluate the degree of myocardial ischemia and myocardial fibrosis and may better guide clinical diagnosis and treatment.

The coronary plaque characteristics can be evaluated by measuring the CT attachment values; however, it is difficult to distinguish the tumor-like lesions from the non-calcified plaques on plain CT scans due to their similar CT attenuation values. The CCTA can detect periarteritis as a non-smooth soft tissue thickening around the arteries. One previous study shows that increasing iodine density after enhancement is related to perivascular inflammation (5). Coronary arteritis and periarteritis in IgG4-RD are primarily associated with adventitia, consisting of IgG4-positive plasma cell infiltration and fibrosis. The primary reason for the increase of iodine density within the tumor-like lesions after enhancement may be explained by coronary perivasculitis caused by IgG4-RD, which provides more information to help make a distinction. In recent years, intraluminal abnormalities and coronary artery aneurysms of IgG4-RD have been concerned (6, 7). We speculate that IgG4-RD induced coronary arteritis and vascular endothelial cell injury can lead to thrombosis and secondary lumen stenosis.

At the time of coronary angiography, FFR is the gold standard in evaluating hemodynamic significance of moderate coronary stenosis; however, $FFR_{CT}$ offers a non-invasive and economical assessment. $FFR_{CT}$ values less than or equal to 0.8 are considered as the threshold of myocardial ischemia (8). Myocardial fibrosis is an important indicator of myocardial damage and cardiac dysfunction. The ECV has been proved to correlate significantly with diffuse fibrosis within the myocardium (9). Emerging studies have found that, for detecting myocardial ECV changes, DECT is as useful as MRI (10). In our case, myocardial ischemia already existed in the rest situation, myocardial fibrosis has also occurred, and LAD contained the most severe lesions regardless of the non-calcified plaques or the IgG4-RD. It is interesting to note that the most obvious decrease of $FFR_{CT}$ value was in the mid and distal LAD, but the most obvious decrease of iodine deposition was in the mid-anterior segment. We estimate that the collateral circulation formation in different segments is not alike, and the mid-segment may have the worst collateral circulation.

Since the previous study demonstrated that steroid therapy might lead to mild regression of the coronary stenosis on CCTA (11), it may also be possible to evaluate the efficacy of coronary periarteritis by comparing the changes of iodine deposition within the tumor-like lesions before and after steroid treatments, thus, providing clinical insight into the characterizations of plaques with an emphasis on the importance of early therapeutic intervention in IgG4-RD involving coronary arteries, such as corticosteroid therapy, surgery, immunomodulators, and immunosuppressants.

There are still some shortcomings in this study. Stress perfusion cannot be performed due to the lack of vasodilators and more cases, and prospective studies are needed to further validate our findings.

## CONCLUSION

The DECT provides a valuable basis for comprehensive assessments of IgG4-related infiltration, plaque composition, coronary stenosis, hemodynamic abnormality, cardiac function, and myocardial perfusion by one-step cardiac CT examination, especially for patients with MRI contraindications. Moreover, this wide range of information is beyond the reach of ICA. It is promising to be translated into clinical practice to improve the diagnosis and treatment of coronary artery disease of patients with IgG4-RD.

## DATA AVAILABILITY STATEMENT

The original contributions presented in the study are included in the article/supplementary material, further inquiries can be directed to the corresponding author.

## ETHICS STATEMENT

The studies involving human participant was reviewed and approved by Ethics Committee of the Xiangya Hospital of Central South University. The patient/participant provided his written informed consent to participate in this study.

## AUTHOR CONTRIBUTIONS

All authors listed have made a substantial, direct, and intellectual contribution to the work and approved it for publication.

## FUNDING

This work was supported by Natural Science Foundation of Hunan Province (2021JJ31131), China.

## ACKNOWLEDGMENTS

The authors would like to acknowledge all who contributed to this case diagnosis, therapy, and decision-making.

## REFERENCES

1. Akiyama M, Kaneko Y, Takeuchi T. Characteristics and prognosis of IgG4-related periaortitis/periarteritis: a systematic literature review. *Autoimmun Rev.* (2019) 18:102354. doi: 10.1016/j.autrev.2019.102354
2. Wallace ZS, Naden RP, Chari S, Choi H, Della-Torre E, Dicaire JF, et al. The 2019 American College of Rheumatology/European league against rheumatism classification criteria for IgG4-related disease. *Arthritis Rheumatol.* (2020) 72:7–19. doi: 10.1002/art.41120
3. Liu X, Mo X, Zhang H, Yang G, Shi C, Hau WK, et al. 2-year investigation of the impact of the computed tomography-derived fractional flow reserve calculated using a deep learning algorithm on routine decision-making for coronary artery disease management. *Eur Radiol.* (2021) 31:7039–46. doi: 10.1007/s00330-021-07771-7
4. Maurovich-Horvat P, Suhai FI, Czimbalmos C, Toth A, Becker D, Kiss E, et al. Coronary artery manifestation of Ormond disease: the "Mistletoe Sign". *Radiology.* (2017) 282:356–60. doi: 10.1148/radiol.2016160644
5. Yamazaki M, Takano H, Miyauchi H, Daimon M, Funabashi N, Nagai T, et al. Detection of Takayasu arteritis in early stage by computed tomography. *Int J Cardiol.* (2002) 85:305–7. doi: 10.1016/s0167-5273(02)00252-8
6. Koseki K, Yahagi K, Okuno T, Kikushima H, Saito A, Ninomiya K, et al. Immunoglobulin G4-related coronary periarteritis with multiple intracoronary images. *JACC Cardiovasc Interv.* (2019) 12:e59–61. doi: 10.1016/j.jcin.2018.11.018
7. Ansari-Gilani K, Gilkeson RC. Multimodality imaging of IgG4 related coronary artery aneurysm. *Echocardiography.* (2020) 37:979–81. doi: 10.1111/echo.14746
8. Raja J, Seitz MP, Yedlapati N, Khouzam RN. Can computed fractional flow reserve coronary CT angiography (FFRCT) offer an accurate noninvasive comparison to invasive coronary angiography (ICA)? "The Noninvasive CATH": a comprehensive review. *Curr Probl Cardiol.* (2021) 46:100642. doi: 10.1016/j.cpcardiol.2020.100642
9. Abadia AF, van Assen M, Martin SS, Vingiani V, Griffith LP, Giovagnoli DA, et al. Myocardial extracellular volume fraction to differentiate healthy from cardiomyopathic myocardium using dual-source dual-energy CT. *J Cardiovasc Comput Tomogr.* (2020) 14:162–7. doi: 10.1016/j.jcct.2019.09.008
10. Ohta Y, Kishimoto J, Kitao S, Yunaga H, Mukai-Yatagai N, Fujii S, et al. Investigation of myocardial extracellular volume fraction in heart failure patients using iodine map with rapid-kV switching dual-energy CT: segmental comparison with MRI T1 mapping. *J Cardiovasc Comput Tomogr.* (2020) 14:349–55. doi: 10.1016/j.jcct.2019.12.032
11. Xu X, Bai W, Ma H, Dong P, Xie H, Shi Y, et al. Remission of "mistletoe sign" after treatment. *J Cardiovasc ComputTomogr.* (2020) 14:e118–e9. doi: 10.1016/j.jcct.2019.08.002

**Conflict of Interest:** XZ is employed by Siemens Healthineers China.

The remaining authors declare that the research was conducted in the absence of any commercial or financial relationships that could be construed as a potential conflict of interest.

**Publisher's Note:** All claims expressed in this article are solely those of the authors and do not necessarily represent those of their affiliated organizations, or those of the publisher, the editors and the reviewers. Any product that may be evaluated in this article, or claim that may be made by its manufacturer, is not guaranteed or endorsed by the publisher.

frontiers in Cardiovascular Medicine

REVIEW
published: 15 March 2022
doi: 10.3389/fcvm.2022.852173

# Carotid Artery Stiffness: Imaging Techniques and Impact on Cerebrovascular Disease

*Hediyeh Baradaran*[1]* *and Ajay Gupta*[2,3]

[1] Department of Radiology, University of Utah, Salt Lake City, UT, United States, [2] Department of Radiology, Weill Cornell Medicine, New York, NY, United States, [3] Feil Family Brain and Mind Research Institute, Weill Cornell Medicine, New York, NY, United States

Arterial stiffness is an important measure of vascular aging and atherosclerosis. Though it is measured in many well-known epidemiologic cohort studies, arterial stiffness is often overlooked in routine clinical practice for a number of reasons including difficulties in measurement, variations in definition, and uncertainties surrounding treatment. Central arterial stiffness, a surrogate for aortic stiffness, is the most commonly measured marker of arterial stiffness. In addition to central stiffness, there are also a number of ultrasound based techniques to measure local vascular stiffness, including carotid stiffness. There is evidence that both local carotid stiffness and central arterial stiffness measures are associated with multiple cerebrovascular processes, including stroke and cognitive dysfunction. Mechanistic explanations supporting this association include increased flow load experienced by the cerebral microvasculature leading to cerebral parenchymal damage. In this article, we review definitions of carotid artery stiffness measures and pathophysiologic mechanisms underpinning its association with plaque development and downstream cerebral pathology. We will review the evidence surrounding the association of carotid stiffness measures with downstream manifestations including stroke, cerebral small vessel disease detected on brain MR such as white matter hyperintensities and covert brain infarctions, brain atrophy, and cognitive dysfunction. With consistent definitions, measurement methods, and further scientific support, carotid stiffness may have potential as an imaging-based risk factor for stroke and cognitive decline.

**Keywords: carotid artery disease, cerebrovascular disorders, cognitive dysfunction, magnetic resonance imaging, stroke**

OPEN ACCESS

***Edited by:***
*Luca Saba,*
*Azienda Ospedaliero-Universitaria Cagliari, Italy*

***Reviewed by:***
*Kenichiro Otsuka,*
*Massachusetts General Hospital and Harvard Medical School, United States*
*Annagrazia Cecere,*
*University of Padua, Italy*

***Correspondence:**
*Hediyeh Baradaran*
*hediyeh.baradaran@hsc.utah.edu*

***Specialty section:***
*This article was submitted to Cardiovascular Imaging, a section of the journal Frontiers in Cardiovascular Medicine*

***Received:*** *10 January 2022*
***Accepted:*** *16 February 2022*
***Published:*** *15 March 2022*

***Citation:***
*Baradaran H and Gupta A (2022) Carotid Artery Stiffness: Imaging Techniques and Impact on Cerebrovascular Disease. Front. Cardiovasc. Med. 9:852173. doi: 10.3389/fcvm.2022.852173*

## INTRODUCTION

Diseases of the carotid artery are a major cause of worldwide morbidity and mortality, with carotid atherosclerosis accounting for nearly 1 in 5 acute ischemic strokes (1). Though stroke risk from carotid disease is most directly caused by wall thickening and plaque formation, the stiffening of the arterial wall likely plays an important role in the deleterious effects of carotid vascular disease (2). Though not routinely measured in clinical practice, arterial stiffness may play a role

in downstream cerebrovascular ischemia, including contributing to stroke, cognitive impairment, and overall mortality (3–5). The exact role of arterial stiffness in contributing to these diseases is unclear as arterial stiffness increases with age and is associated with many conditions which are also associated with increased cardiovascular risk, such as hypertension, diabetes mellitus, and hypercholesterolemia. In addition to its association with downstream cognitive deficits, arterial stiffening may also potentiate the development of plaque (6), and may therefore play an under recognized role in increasing stroke risk.

Though arterial stiffness is not commonly measured in routine clinical practice, it has been well-studied in part because of its inclusion in multiple large epidemiologic cohort studies (7–9). Most commonly, arterial stiffness is a general term used to describe central arterial stiffness calculated via non-invasive techniques, usually pulse wave velocity (10). There are a number of methods used to measure arterial stiffness and the rigidity of a vessel wall both locally and systemically. The use of multiple techniques in various vascular beds accounts for some of the confusion regarding measuring stiffness measures (11). One of the barriers to widespread clinical adoption of arterial stiffness measurement is the lack of specific and uniform definitions and methods of measurement.

In this article, we will review common methods for measuring arterial stiffness including definitions of the most common measures of stiffness. We will also review mechanisms by which arterial stiffness may contribute to cerebrovascular ischemia, cognitive function, and carotid plaque formation.

## ARTERIAL STIFFNESS DEFINITIONS AND MEASUREMENTS

Arterial stiffness is a general term to describe rigidity of the arterial walls. It is frequently assessed by measuring the velocity of a given pulse-wave in a specific vessel segment (12), though "stiffness" is also used more generally for direct measures of wall rigidity. There is further confusion surrounding the terminology because some stiffness measurements can be used in both local and systemic vascular beds and at times stiffness terms are used interchangeably. There is no single, unanimously agreed upon measurement to describe stiffness. Instead, there are several specific vascular wall properties or other pressure-related measurements which act as surrogates for stiffness. Further clouding the picture, the definition of arterial stiffness depends on whether local or central stiffness is being measured. We have searched the literature using PubMed for all articles referencing arterial and carotid stiffness published after 1990 in the English language. We considered studies including randomized controlled trials and retrospective and prospective cohort studies. We will briefly discuss the definitions of some of the most commonly acquired measures of arterial wall properties and their means of measurement (**Table 1**; **Figure 1**).

### Pulse Wave Velocity

Pulse wave velocity (PWV) is perhaps the most commonly used and most well-known technique to evaluate arterial stiffness. PWV is a measure that evaluates the propagation of a wave through the vasculature by taking simultaneous recordings at two separate sites. The PWV increases as arterial stiffness increases. Carotid-femoral PWV (cfPWV) is often considered the gold standard of measuring central artery stiffness and is recommended by the American Heart Association with the highest level of supporting evidence as a method for evaluating arterial stiffness (13). This usually non-invasive method requires simultaneous measurement of pressure waves at two points across the body, in the case of cfPWV, the carotid and femoral arteries. The basic principal of PWV measurement involves recording pressure waves at two sites and then calculating transit time between those sites to determine PWV. This measurement can be accomplished with the help of a number of devices including applanation tonometers, echotracking devices, mechanotransducers, or Doppler probes (10).

One major limitation of cfPWV is that it is based on models for wave propagation through the arterial tree, which may not accurately reflect true stiffness, especially in aging arteries (10). cfPWV is a measure of central arterial stiffness and though the carotid artery is one of the main arteries measured, it is a surrogate measure for aortic stiffness, rather than a direct measure of carotid stiffness. Besides not being a direct measure of carotid stiffness, other limitations with using cfPWV include the difficulty in precisely measuring distances between arterial sites of measurement, especially in obese patients (10). Despite these limitations, cfPWV is the most commonly performed measure of arterial stiffness and has been routinely performed in many epidemiologic cohort studies. In fact, it serves as the primary method for measurement of many of the frequently cited studies describing arterial stiffness.

### Cardio-Ankle Vascular Index

Cardio-Ankle Vascular Index (CAVI) is another type of systemic measure of arterial stiffness which differs from PWV in that it is not dependent on blood pressure measurement (14). CAVI is a non-invasive method for measuring stiffness in the aorta, femoral, and tibial arteries and is strongly associated with the stiffness parameter ß (15). Further, there is evidence that CAVI is strongly associated with stroke and other cardiovascular events (16, 17). While not routinely used in clinical practice, CAVI is another non-invasive measure of arterial stiffness which may provide valuable information regarding cardiovascular risk.

### Local Stiffness Measures

Though PWV is the most commonly performed measure of central arterial stiffness, there are several measures for direct, local measurement of stiffness. Most of these measures of local arterial stiffness are determined via ultrasound techniques. Ultrasound is frequently performed throughout the cardiac cycle to determine changes in vessel diameter in diastole and systole. In addition to measuring luminal diameter to determine changes in volume throughout the cardiac cycle, ultrasound can also be used to measure wall thickness which can be used to determine the elastic properties of the arterial wall. Since most local stiffness measurement calculations require pressure measurements, local blood pressure measurements obtained

**TABLE 1 |** Overview of arterial stiffness measurement techniques.

| Measure | Definition | Equation | Type of measure | Notes |
|---|---|---|---|---|
| **Compliance** | For a given pressure change, the absolute change in arterial lumen area in systole | ΔD/ΔP | Local measure of stiffness | Higher compliance indicates more arterial stiffness |
| **Distensibility** | For a given pressure change, the relative change in arterial lumen area in systole | ΔD/ΔPxD | Local measure of stiffness | Accounts for arterial size |
| **Young's Elastic modulus** | The pressure change necessary for theoretical 100% stretch per unit area | ΔPxD/(ΔDxh) | Local measure of stiffness | Can account for wall thickness, such as intima-media thickness in the carotid artery |
| **Pulse wave velocity** | Velocity of travel of a pulse along a specific artery length | Distance/Δt | Central measure of stiffness | Most common measurement of arterial stiffness; surrogate for aortic stiffness |

*P, pressure; D, diameter; h, wall thickness; t, time.*

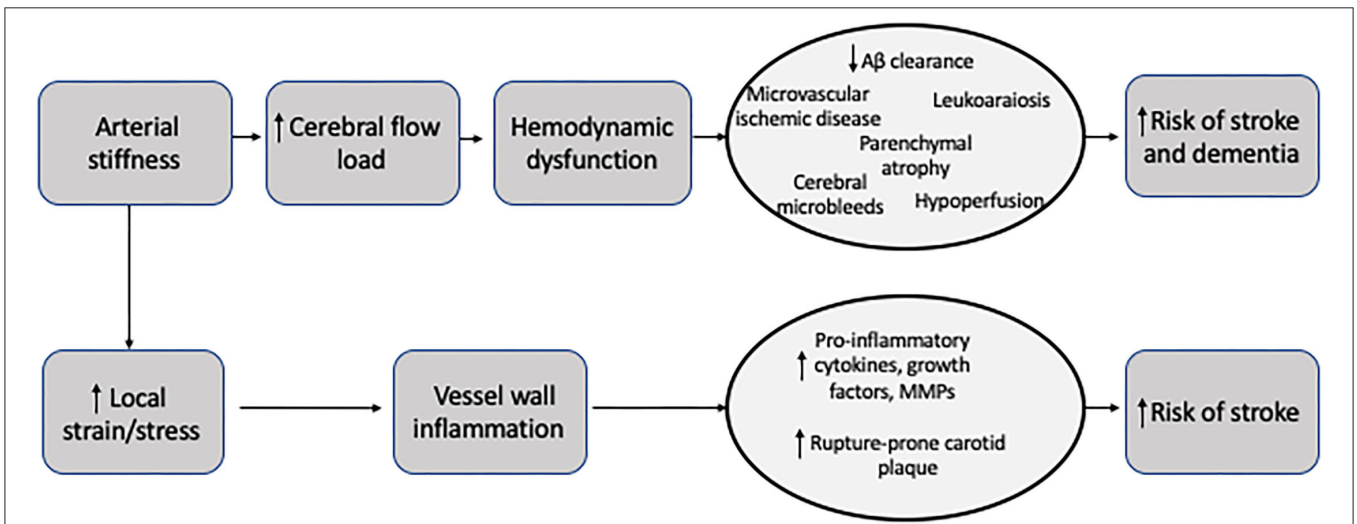


**FIGURE 1 |** Schematic representation of changes to an artery wall in diastole compared to systole. The change in the diameter of the lumen is used in all local stiffness measurements.

via applanation tonometers are often calibrated to brachial pressures measured with standard sphygmomanometer. Given the lack of precise measurements on ultrasound, some studies utilize specific echotracking techniques to measure the lumen diameters which can provide more detailed measurements than ultrasound techniques (10). Local measurements of arterial stiffness can more directly measure arterial stiffness, rather than PWV which relies on assumptions from circulatory models and does not provide site-specific stiffness information. We will review several of the most common measures of local stiffness.

## Compliance

Compliance is a local measure of stiffness and can be used to directly measure carotid arterial wall stiffness. Compliance is defined as the ratio of any volume change (i.e., arterial lumen area) for a given pressure change. (ΔD/ ΔP cm/mm Hg). Compliance is an inverse measure of stiffness, meaning the greater the compliance, the lower the arterial stiffness. Larger arteries with higher cross-sectional volumes can general accommodate more volume for a given pressure change compared to smaller arteries.

## Distensibility

Distensibility is another local measure of stiffness. It is similar to compliance but can be more useful when comparing arteries of different sizes across the arterial tree. It is defined as the relative change in arterial lumen diameter or area for given pressure change [ΔD/ (ΔP x ΔD)].

## Elastic Modulus

Elastic modulus is another measure of stiffness that is defined as the pressure change necessary for theoretical 100% stretch ($\Delta P \times \Delta D$)/ ($\Delta D$). Young's elastic modulus is more commonly used and is defined as elastic modulus per unit area. Young's elastic modulus is used to measure elastic properties of a given vessel and can take the arterial wall thickness into account, including intima-media thickness in the carotid artery. Accounting for wall thickness is important, especially in the setting of atherosclerosis and plaque.

One of the reasons that arterial stiffness measures are not commonly performed in clinical practice is the difficulty in identifying the ideal measure for stiffness. While PWV is currently the simplest non-invasive method for measuring arterial stiffness, it has several limitations as discussed above, including inability to provide local stiffness measurement. In order for measures of arterial stiffness to become more mainstream, more uniformity in measurement techniques, definitions, and clinical application are necessary.

## MECHANISMS BY WHICH ARTERIAL STIFFENING IMPACTS THE BRAIN

Arterial stiffness is a prominent feature of aging, but also a result of many systemic processes including atherosclerosis, diabetes, and even chronic renal disease. Stiffening is the product of complex interactions on the vessel wall, including hemodynamic forces, extrinsic effects such as hormonal changes and salt intake, and structural changes to the wall itself (18). Variations in the amount of collagen and elastin proteins within the arterial wall that occurs with aging can lead to structural alterations in the integrity of all layers of the vessel wall. In addition, smooth muscle tone changes, mediated by multiple factors including angiotensin II and nitric oxide, also result in changes to vascular compliance through changes in the media (18). Endothelial dysfunction may also play a role in the development of arterial stiffness via local reactive oxygen species. These complex diverse processes occur as a result of natural aging and are likely hastened by cardiovascular risk factors.

The exact role that carotid stiffness plays in the development of cerebrovascular ischemia and atherosclerosis is still under investigation. Given the shared risk factors for arterial stiffness and stroke, it is difficult to disentangle the complex relationship between stiffness, cardiovascular risk factors, and stroke. Still, one widely proposed link between arterial stiffness and cerebrovascular ischemia may be that arterial stiffness causes large arteries to become less responsive to normal pulsatile flow. This inability to respond to fluctuations of blood pressure throughout the cardiac cycle may result in more continuous perfusion, rather than pulsatile perfusion. Ultimately, more continuous perfusion results in increased flow load experienced by end-organs, especially the cerebral parenchyma (19, 20). The brain parenchyma is particularly susceptible to the increased flow load due to its overall low impedance leading to deep penetration of the flow load into the cerebral microvasculature (21). These alterations in the cerebral microvasculature appear to lead to parenchymal damage including ischemia and hemorrhage and other markers of small vessel disease. Eventually, this end-organ damage may manifest in a number of ways including stroke, cognitive dysfunction, or cerebral small vessel disease evident on brain imaging (**Figure 2**) (22).

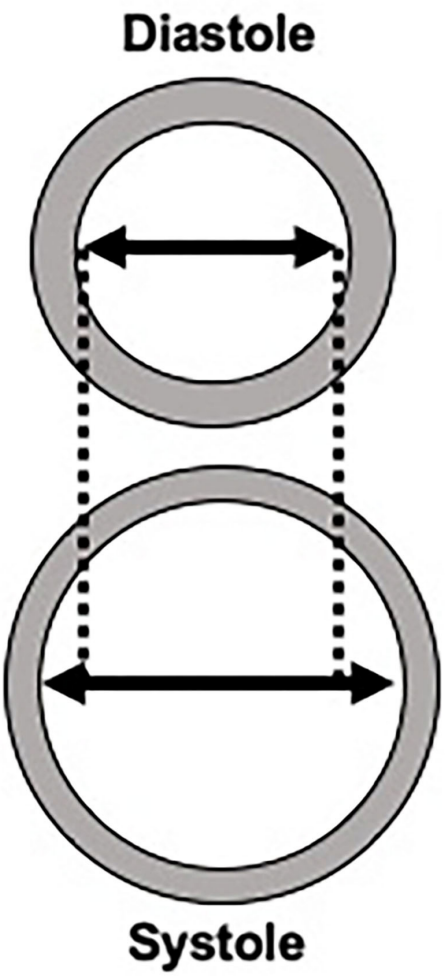


**FIGURE 2 |** Potential mechanisms for the role of arterial stiffness in the development of stroke and dementia.

Another potential mechanism by which arterial stiffness leads to stroke is through the development of plaque formation, specifically the formation of vulnerable plaque features (6). Emerging evidence suggests that arteries with increased stiffness may lead to increased shear strain in the adventitial layer. This increased strain may precipitate a local inflammatory reaction that facilitates plaque formation. Specifically, certain local stress signals and inflammatory responses, such as radical oxidants, growth factors and other pro-inflammatory cytokines can contribute to local endothelial dysfunction leading to increased angiogenesis and atherosclerotic plaque formation (18). Other studies have shown that increased arterial stiffness as measured by PWV is associated with increased calcified plaque

(23). Further, there is a complex association between central arterial stiffness and aortic plaques with evidence that aortic plaques are also associated with downstream effects, including decreased brain volume and brain infarctions (24, 25). The exact relationship between arterial stiffness and the development of atherosclerotic plaque is a topic of considerable interest given that a more complete understanding of plaque formation may open new avenues for treating carotid atherosclerosis. This complex association may be more fully elucidated with the help of newer imaging technologies, such as optical coherence tomography, which allows for in vivo characterization of plaque as well as collagen and smooth muscle cells (26–29). This technology and others may help in furthering our mechanistic understanding of arterial stiffness.

Similarly, arterial stiffness may contribute to cerebral small vessel disease. Given the increased flow load experienced by the cerebral microvasculature in the setting of increased arterial stiffness, there is evidence of cerebral microvascular dysfunction and damage which can be detected on brain magnetic resonance (MR) imaging. The sequelae of cerebral microvascular damage can be seen as white matter hyperintensities, covert brain infarctions and cerebral microbleeds on MR. In addition, the increased flow load from altered cerebral microvascular flow leading to microstructural damage is thought to contribute to brain parenchymal atrophy, which is considered another marker of cerebral small vessel disease (30).

In addition to overt ischemia such as stroke, there is also evidence of downstream cognitive dysfunction in those with increased arterial stiffness. The microvascular damage from constant high flow loads leading to cerebral small vessel disease may in turn lead to cognitive impairment and dementia, given the very strong association between markers of cerebral small vessel disease and cognitive dysfunction (31–34). In addition to worsening cerebral small vessel disease, arterial stiffness may contribute to cognitive dysfunction by impaired blood flow leading to cerebral hypoperfusion, which may promote amyloid ß deposition (35). Another possibility is that arterial stiffness may impair amyloid clearance via decreased perivascular drainage of amyloid ß, leading to increased amyloid deposition which is seen in Alzheimer's disease (36–38).

# EVIDENCE SUPPORTING A SHARED LINK BETWEEN ARTERIAL STIFFNESS AND BRAIN DISEASE

## Stiffness and Stroke

Arterial stiffness may lead to stroke both because of increased flow load on the cerebral vasculature and due to accelerated development of rupture-prone atherosclerotic plaque in the carotid artery. Meta-analyses and individual-participant level data from epidemiologic cohorts demonstrate strong evidence of an association between central arterial stiffness and incident stroke (5, 39), including a study showing an association between central arterial stiffness and stroke independent of aortic plaque (24). There have also been several studies evaluating the association between local measures of carotid stiffness and incident stroke. A systematic review and meta-analysis of 22,472 participants found that greater carotid stiffness is associated with incident stroke (HR = 1.18; 95% CI 1.05–1.33), even when adjusting for cardiovascular risk factors (40, 41). When evaluating individual patient data and adjusting for cfPWV, a measure of central arterial stiffness, carotid stiffness was still statistically significantly associated with stroke.

Another study using a large epidemiologic cohort found that the addition of carotid distensibility measures improved ischemic stroke risk prediction (42). Accounting for baseline measures of carotid stiffness improved risk prediction beyond standard clinical markers for stroke risk and Framingham stroke risk score factors (40, 42). These findings suggest that carotid stiffness may be used as a tool for stroke risk stratification and prediction. Further confirmatory studies of this association are important, as is exploration of preventative and treatment methods of mitigating carotid stiffness.

Arterial stiffness also has a complex association with atrial fibrillation, which is the most common chronic arrhythmia and a strong predictor of stroke and mortality (43, 44). Several studies have shown that having high arterial stiffness and high pulsatile load increase the likelihood of developing atrial fibrillation (45–47). Conversely, having atrial fibrillation may itself lead to hemodynamic alterations including altered flow load leading to downstream effects (48). The relationship between atrial fibrillation and arterial stiffness warrants further evaluation to characterize this complex association, especially because atrial fibrillation is a treatable cause of ischemic stroke.

## Stiffness and Brain volume

Generalized cerebral parenchymal volume loss and hippocampal volume loss are commonly encountered findings on routine brain imaging. In addition to being closely associated with advancing age, low cerebral parenchymal volume is also associated with Alzheimer's disease, stroke, and generalized cognitive dysfunction (49). Multiple studies have shown a strong association between low carotid distensibility (or high carotid stiffness) with baseline lower total brain and cortical gray matter volume (22, 50). In addition to being associated with baseline lower cerebral volumes, there is evidence that carotid stiffness is associated with future lower parahippocampal and hippocampal volumes. Though the cause for this association is unclear, it is possible that arterial stiffness leads to generalized cerebral hypoperfusion which then, in turn, leads to atrophy. Another potential explanation is that high pressure pulsatility from arterial stiffness is transmitted to the cerebral microvasculature leading to microvascular dysfunction and damage in the brain, micro- and macrostructural neuronal damage, and ultimately leading to lower brain volumes (22, 51).

There are also a number of studies correlating aortic and central arterial stiffness with decreased parenchymal brain volume (52–54) though it is unclear if these studies can be generalized to carotid artery stiffness. In one of these studies, greater central arterial stiffness (cfPWV) was associated with lower volumes in signature Alzheimer's disease regions (53). There are several studies in large epidemiologic cohorts which have demonstrated the association between measures of arterial

stiffness, as measured by cfPWV, to low total brain and hippocampal volumes, indicating a potential association with cognitive dysfunction.

## Stiffness and Markers of Cerebral Small Vessel Disease

Several markers of cerebral small vessel disease evident on routine brain imaging, including white matter hyperintensities (WMH), covert brain infarctions (CBI), and cerebral microbleeds (CMBs) are associated with mortality, stroke, cognitive dysfunction, and dementia (31, 32, 34, 55, 56). There is mixed evidence of an association between carotid artery stiffness and increased burden of cerebral small vessel disease. In a large epidemiologic cohort, baseline carotid artery stiffness was found to be associated with WMH 20 years later (8). Another small study found that local carotid stiffness measures were associated with MRI markers of cerebral small vessel disease (57). Other studies have also shown that increased arterial stiffness is associated with CMBs (58). All of these studies point to a potential association of carotid artery stiffness to downstream markers of cerebral small vessel disease, however, other cohorts found no association between carotid stiffness measures and markers of cerebral small vessel disease (59).

Despite the uncertainty surrounding the contribution of local carotid stiffness to markers of small vessel disease, there is stronger evidence of central arterial stiffness being associated with markers of cerebral small vessel disease, including white matter hyperintensities (53, 54). There are several systematic reviews and meta-analyses confirming the association between arterial stiffness, measured using multiple methods but most commonly with cfPWV, with white matter hyperintensities, cerebral microbleeds, and cerebral infarctions (4, 9, 60). Another study found that central arterial stiffness (cfPWV) was associated with overall burden of cerebral small vessel disease including lacunar infarctions and enlarged perivascular spaces in the basal ganglia (61).

## Stiffness and Cognitive Dysfunction

Several studies show that markers of central arterial stiffness are independent predictors of cognitive dysfunction. A recent cohort study found that higher central arterial stiffness (cfPWV) was associated with cognitive dysfunction and that association was in part mediated by markers of cerebral small vessel disease on brain MR (59). Data from the Framingham Heart Study suggest that central arterial stiffness, as measured by cfPWV, is an independent predictor of incident mild cognitive impairment within the entire cohort and incident dementia in the non-diabetic participants (62). Another longitudinal study found that increased central arterial stiffness (cfPWV) was associated with more pronounced cognitive decline in a cohort of institutionalized patients (63). Other longitudinal studies evaluating aortic stiffness have also confirmed an association with cognitive decline (64, 65). Other smaller studies have shown a cross-sectional association of central arterial stiffness with cognitive dysfunction (66–69).

The data supporting a link between carotid stiffness is less clear than for central arterial stiffness. For example, several studies have shown that carotid stiffness via distensibility or compliance measures is associated with cognitive dysfunction (70–75). Other studies have found no association between measures of carotid stiffness and cognitive dysfunction (7, 76). For example, one of the largest and most recent studies found no association between carotid distensibility and cognitive dysfunction after adjusting for potential confounders (59). The question of the association between direct measures of carotid stiffness and cognitive dysfunction is not definitively answered and future longitudinal studies would be helpful in elucidating this association.

One of the possible explanations for the association between central arterial stiffness and cognitive dysfunction, specifically Alzheimer's dementia is the thought that there is decreased clearance of amyloid protein, leading to disproportionate accumulation and the development of Alzheimer's dementia (36). Those individuals with higher central arterial stiffness (cfPWV) have been found to have worse performance of cognitive testing (53). Arterial stiffness as measured centrally with hcPWV (heart-carotid) was shown to be associated with lower brain volumes and higher white matter hyperintensity burden, but also greater amyloid-β deposition with an OR of 1.31 (95% CI 1.01–1.71) (54). One study following a large epidemiologic cohort, the Rotterdam study, found an association with PWV and poorer performance on the Stroop test but not on other cognitive tests (7). The study found no association between either central arterial stiffness (cfPWV) and carotid distensibility and cognitive dysfunction and dementia (7). Another study has shown that carotid stiffness specifically, rather than aortic stiffness, was independently associated with amyloid-β burden in patients with amnestic mild cognitive impairment after adjusting for confounders (77).

# CONCLUSION

Arterial stiffness, a specific measure of wall rigidity, can be measured both centrally in the aorta and locally in certain vascular beds such as the carotid artery. Having increased carotid stiffness is associated with multiple downstream effects including cardiovascular disease, stroke, and cognitive dysfunction. One of the leading pathophysiologic mechanisms underpinning these associations is the loss of vascular regulation from stiffness leading to increased flow load experienced by the cerebral parenchymal microvasculature. Both local measurements of carotid stiffness and measures of central arterial stiffness are variably associated with stroke, cognitive dysfunction, markers of cerebral small vessel disease, and low cerebral parenchymal volume. Currently, the lack of validated measurements precludes the routine use of measures of arterial stiffness in clinical practice. Future studies including those using optical With more standardized methods of measurements and continued validation, carotid stiffness measures may achieve greater clinical

adoption as imaging-based risk factors for the development of stroke and dementia.

## AUTHOR CONTRIBUTIONS

HB and AG designed the overall manuscript with the collection and assembly of data by HB. HB drafted manuscript with critical revision and feedback from AG. Both AG and HB gave final approval of the manuscript. All authors contributed to the article and approved the submitted version.

## FUNDING

HB was supported by a grant from the Association of University Radiologists- GE Radiology Research Academic Fellowship Award. AG was in part supported by National Institutes of Health grants R01HL144541 and R21HL145427. Research by HB was in part supported by the National Center for Advancing Translational Sciences of the National Institutes of Health under Award Number UL1TR002538.

## REFERENCES

1. Kolominsky-Rabas PL, Weber M, Gefeller O, Neundoerfer B, Heuschmann PU. Epidemiology of ischemic stroke subtypes according to TOAST criteria: incidence, recurrence, and long-term survival in ischemic stroke subtypes: a population-based study. *Stroke.* (2001) 32:2735–40. doi: 10.1161/hs1201.100209
2. O'Rourke MF, Safar ME, Dzau V. The Cardiovascular Continuum extended: aging effects on the aorta and microvasculature. *Vasc Med.* (2010) 15:461–8. doi: 10.1177/1358863X10382946
3. Mattace-Raso FU, van der Cammen TJ, Hofman A, van Popele NM, Bos ML, Schalekamp M, et al. Arterial stiffness and risk of coronary heart disease and stroke. *Circulation.* (2006) 113:657–63. doi: 10.1161/CIRCULATIONAHA.105.555235
4. Pase MP, Herbert A, Grima N, Pipingas A, O'Rourke MF. Arterial stiffness as a cause of cognitive decline and dementia: a systematic review and meta-analysis. *Intern Med J.* (2012) 42:808–15. doi: 10.1111/j.1445-5994.2011.02645.x
5. Vlachopoulos C, Aznaouridis K, Stefanadis C. Prediction of cardiovascular events and all-cause mortality with arterial stiffness: a systematic review and meta-analysis. *J Am Coll Cardiol.* (2010) 55:1318–27. doi: 10.1016/j.jacc.2009.10.061
6. Selwaness M. Bouwhuijsen Qvd, Mattace-Raso FUS, Verwoert GC, Hofman A, Franco OH, et al. Arterial stiffness is associated with carotid intraplaque hemorrhage in the general population. *Arterioscler Thromb Vasc Biol.* (2014) 34:927–32. doi: 10.1161/ATVBAHA.113.302603
7. Poels MM, van Oijen M, Mattace-Raso FU, Hofman A, Koudstaal PJ, Witteman JC, et al. Arterial stiffness, cognitive decline, and risk of dementia: the Rotterdam study. *Stroke.* (2007) 38:888–92. doi: 10.1161/01.STR.0000257998.33768.87
8. de Havenon A, Wong K-H, Elkhetali A, McNally J, Majersik J, Rost N. Carotid artery stiffness accurately predicts white matter hyperintensity volume 20 years later: a secondary analysis of the atherosclerosis risk in the community study. *Am J Neuroradiol.* (2019) 40:1369–73. doi: 10.3174/ajnr.A6115
9. van Sloten TT, Protogerou AD, Henry RM, Schram MT, Launer LJ, Stehouwer CD. Association between arterial stiffness, cerebral small vessel disease and cognitive impairment: a systematic review and meta-analysis. *Neurosci Biobehav Rev.* (2015) 53:121–30. doi: 10.1016/j.neubiorev.2015.03.011
10. Laurent S, Cockcroft J, Van Bortel L, Boutouyrie P, Giannattasio C, Hayoz D, et al. Expert consensus document on arterial stiffness: methodological issues and clinical applications. *Eur Heart J.* (2006) 27:2588–605. doi: 10.1093/eurheartj/ehl254
11. Mackenzie IS, Wilkinson IB, Cockcroft JR. Assessment of arterial stiffness in clinical practice. *QJM: Intern J Med.* (2002) 95:67–74. doi: 10.1093/qjmed/95.2.67
12. O'Rourke MF, Staessen JA, Vlachopoulos C, Duprez D. Clinical applications of arterial stiffness; definitions and reference values. *Am J Hypertens.* (2002) 15:426–44. doi: 10.1016/S0895-7061(01)02319-6
13. Townsend RR, Wilkinson IB, Schiffrin EL, Avolio AP, Chirinos JA, Cockcroft JR, et al. Recommendations for improving and standardizing vascular research on arterial stiffness: a scientific statement from the American heart association. *Hypertension.* (2015) 66:698–722. doi: 10.1161/HYP.0000000000000033
14. Shirai K, Utino J, Otsuka K, Takata M, A. novel blood pressure-independent arterial wall stiffness parameter; cardio-ankle vascular index (CAVI). *J Atheroscler Thromb.* (2006) 13:101–7. doi: 10.5551/jat.13.101
15. Saiki A, Sato Y, Watanabe R, Watanabe Y, Imamura H, Yamaguchi T, et al. The role of a novel arterial stiffness parameter, cardio-ankle vascular index (CAVI), as a surrogate marker for cardiovascular diseases. *J Atheroscler Throm.* (2015) 23:32797. doi: 10.5551/jat.32797
16. Sato Y, Yoshihisa A, Ichijo Y, Watanabe K, Hotsuki Y, Kimishima Y, et al. Cardio-ankle vascular index predicts post-discharge stroke in patients with heart failure. *J Atheroscler Throm.* (2020) 25:58727. doi: 10.5551/jat.58727
17. Otsuka K, Fukuda S, Shimada K, Suzuki K, Nakanishi K, Yoshiyama M, et al. Serial assessment of arterial stiffness by cardio-ankle vascular index for prediction of future cardiovascular events in patients with coronary artery disease. *Hypertension Research.* (2014) 37:1014–20. doi: 10.1038/hr.2014.116
18. Zieman SJ, Melenovsky V, Kass DA. Mechanisms, pathophysiology, and therapy of arterial stiffness. *Arterioscler Thromb Vasc Biol.* (2005) 25:932–43. doi: 10.1161/01.ATV.0000160548.78317.29
19. Mitchell GF. Effects of central arterial aging on the structure and function of the peripheral vasculature: implications for end-organ damage. *J Appl Physiol.* (2008) 105:1652–60. doi: 10.1152/japplphysiol.90549.2008
20. van Sloten TT, Schram MT, van den Hurk K, Dekker JM, Nijpels G, Henry RM, et al. Local stiffness of the carotid and femoral artery is associated with incident cardiovascular events and all-cause mortality: the Hoorn study. *J Am Coll Cardiol.* (2014) 63:1739–47. doi: 10.1016/j.jacc.2013.12.041
21. Climie RE, van Sloten TT, Bruno R-M, Taddei S, Empana J-P, Stehouwer CD, et al. Macrovasculature and microvasculature at the crossroads between type 2 diabetes mellitus and hypertension. *Hypertension.* (2019) 73:1138–49. doi: 10.1161/HYPERTENSIONAHA.118.11769
22. Mitchell GF, van Buchem MA, Sigurdsson S, Gotal JD, Jonsdottir MK, Kjartansson Ó, et al. Arterial stiffness, pressure and flow pulsatility and brain structure and function: the age, gene/environment susceptibility–Reykjavik study. *Brain.* (2011) 134:3398–407. doi: 10.1093/brain/awr253
23. Cecelja M, Jiang B, Bevan L, Frost ML, Spector TD, Chowienczyk PJ. Arterial stiffening relates to arterial calcification but not to non-calcified atheroma in women. *J Am Coll Cardiol.* (2011) 57:1480–6. doi: 10.1016/j.jacc.2010.09.079
24. Sugioka K, Hozumi T, Sciacca RR, Miyake Y, Titova I, Gaspard G, et al. Impact of aortic stiffness on ischemic stroke in elderly patients. *Stroke.* (2002) 33:2077–81. doi: 10.1161/01.STR.0000021410.83049.32
25. Aparicio HJ, Petrea RE, Massaro JM, Manning WJ, Oyama-Manabe N, Beiser AS, et al. Association of descending thoracic aortic plaque with brain atrophy and white matter hyperintensities: the Framingham heart study. *Atherosclerosis.* (2017) 265:305–11. doi: 10.1016/j.atherosclerosis.2017.06.919
26. Ughi GJ, Marosfoi MG, King RM, Caroff J, Peterson LM, Duncan BH, et al. A neurovascular high-frequency optical coherence tomography system enables *in situ* cerebrovascular volumetric microscopy. *Nat Commun.* (2020) 11:1–10. doi: 10.1038/s41467-020-17702-7
27. Chen C-J, Kumar JS, Chen SH, Ding D, Buell TJ, Sur S, et al. Optical coherence tomography: future applications in cerebrovascular imaging. *Stroke.* (2018) 49:1044–50. doi: 10.1161/STROKEAHA.117.019818
28. Otsuka K, Villiger M, Nadkarni SK, Bouma BE. Intravascular polarimetry: clinical translation and future applications of catheter-based polarization sensitive optical frequency domain imaging. *Front Cardiovas Med.* (2020) 7:146. doi: 10.3389/fcvm.2020.00146

29. Otsuka K, Villiger M, Karanasos A, van Zandvoort LJ, Doradla P, Ren J, et al. Intravascular polarimetry in patients with coronary artery disease. *Cardiovascular Imaging.* (2020) 13:790–801. doi: 10.1016/j.jcmg.2019.06.015
30. Wardlaw JM, Smith EE, Biessels GJ, Cordonnier C, Fazekas F, Frayne R, et al. Neuroimaging standards for research into small vessel disease and its contribution to ageing and neurodegeneration. *Lancet Neurol.* (2013) 12:822–38. doi: 10.1016/S1474-4422(13)70124-8
31. Vermeer SE, Prins ND, den Heijer T, Hofman A, Koudstaal PJ, Breteler MM. Silent brain infarcts and the risk of dementia and cognitive decline. *N Eng J Med.* (2003) 348:1215–22. doi: 10.1056/NEJMoa022066
32. Debette S, Seshadri S, Beiser A, Au R, Himali JJ, Palumbo C, et al. Midlife vascular risk factor exposure accelerates structural brain aging and cognitive decline. *Neurology.* (2011) 77:461–8. doi: 10.1212/WNL.0b013e318227b227
33. Debette S, Markus HS. The clinical importance of white matter hyperintensities on brain magnetic resonance imaging: systematic review and meta-analysis. *BMJ.* (2010) 341:666. doi: 10.1136/bmj.c3666
34. Debette S, Beiser A, DeCarli C, Au R, Himali JJ, Kelly-Hayes M, et al. Association of MRI markers of vascular brain injury with incident stroke, mild cognitive impairment, dementia, and mortality. *Stroke.* (2010) 41:600–6. doi: 10.1161/STROKEAHA.109.570044
35. Ruitenberg A, den Heijer T, Bakker SL, van Swieten JC, Koudstaal PJ, Hofman A, et al. Cerebral hypoperfusion and clinical onset of dementia: the Rotterdam study. *Ann Neurol.* (2005) 57:789–94. doi: 10.1002/ana.20493
36. Mawuenyega KG, Sigurdson W, Ovod V, Munsell L, Kasten T, Morris JC, et al. Decreased clearance of CNS β-amyloid in Alzheimer's disease. *Science.* (2010) 330:1774. doi: 10.1126/science.1197623
37. de la Torre JC. Is Alzheimer's disease a neurodegenerative or a vascular disorder? Data, dogma, and dialectics. *Lancet Neurol.* (2004) 3:184–90. doi: 10.1016/S1474-4422(04)00683-0
38. Gupta A, Iadecola C. Impaired Aβ clearance: a potential link between atherosclerosis and Alzheimer's disease. *Front Aging Neurosci.* (2015) 7:115. doi: 10.3389/fnagi.2015.00115
39. Ben-Shlomo Y, Spears M, Boustred C, May M, Anderson SG, Benjamin EJ, et al. Aortic pulse wave velocity improves cardiovascular event prediction: an individual participant meta-analysis of prospective observational data from 17,635 subjects. *J Am Coll Cardiol.* (2014) 63:636–46. doi: 10.1016/j.jacc.2013.09.063
40. Sloten TTv, Sedaghat S, Laurent S, London GM, Pannier B, Ikram MA, et al. Carotid stiffness is associated with incident stroke. *J Am College Cardiol.* (2015) 66:2116–25. doi: 10.1016/j.jacc.2015.08.888
41. Dijk JM. Graaf Yvd, Grobbee DE, Bots ML. Carotid stiffness indicates risk of ischemic stroke and TIA in patients with internal carotid artery stenosis. *Stroke.* (2004) 35:2258–62. doi: 10.1161/01.STR.0000141702.26898.e9
42. Baradaran H, Delic A, Wong KH, Sheibani N, Alexander M, McNally JS, et al. Using ultrasound and inflammation to improve prediction of ischemic stroke: a secondary analysis of the multi-ethnic study of atherosclerosis. *Cerebrovasc Dis Extra.* (2021) 11:37–43. doi: 10.1159/000514373
43. Wolf PA, Abbott RD, Kannel WB. Atrial fibrillation as an independent risk factor for stroke: the Framingham study. *stroke.* (1991) 22:983–8. doi: 10.1161/01.STR.22.8.983
44. Benjamin EJ, Wolf PA, D'Agostino RB, Silbershatz H, Kannel WB, Levy D. Impact of atrial fibrillation on the risk of death: the Framingham Heart Study. *Circulation.* (1998) 98:946–52. doi: 10.1161/01.CIR.98.10.946
45. Cremer A, Lainé M, Papaioannou G, Yeim S, Gosse P. Increased arterial stiffness is an independent predictor of atrial fibrillation in hypertensive patients. *J Hypertens.* (2015) 33:2150–5. doi: 10.1097/HJH.0000000000000652
46. Chen LY, Foo DC, Wong RC, Seow S-C, Gong L, Benditt DG, et al. Increased carotid intima-media thickness and arterial stiffness are associated with lone atrial fibrillation. *Int J Cardiol.* (2013) 168:3132–4. doi: 10.1016/j.ijcard.2013.04.034
47. Shaikh AY, Wang N, Yin X, Larson MG, Vasan RS, Hamburg NM, et al. Relations of arterial stiffness and brachial flow 2013; mediated dilation with new-onset atrial fibrillation. *Hypertension.* (2016) 68:590–6. doi: 10.1161/HYPERTENSIONAHA.116.07650
48. Saji N, Toba K, Sakurai T. Cerebral small vessel disease and arterial stiffness: tsunami effect in the brain. *Pulse.* (2015) 3:182–9. doi: 10.1159/000443614
49. Chao L, Mueller S, Buckley S, Peek K, Raptentsetseng S, Elman J, et al. Evidence of neurodegeneration in brains of older adults who do not yet fulfill MCI criteria. *Neurobiol Aging.* (2010) 31:368–77. doi: 10.1016/j.neurobiolaging.2008.05.004
50. Jochemsen HM, Muller M, Bots ML, Scheltens P, Vincken KL, Mali WP, et al. Arterial stiffness and progression of structural brain changes: the SMART-MR study. *Neurology.* (2015) 84:448–55. doi: 10.1212/WNL.0000000000001201
51. Mitchell GF, Vita JA, Larson MG, Parise H, Keyes MJ, Warner E, et al. Cross-sectional relations of peripheral microvascular function, cardiovascular disease risk factors, and aortic stiffness: the Framingham heart study. *Circulation.* (2005) 112:3722–8. doi: 10.1161/CIRCULATIONAHA.105.551168
52. Maillard P, Mitchell GF, Himali JJ, Beiser A, Tsao CW, Pase MP, et al. Effects of arterial stiffness on brain integrity in young adults from the framingham heart study. *Stroke.* (2016) 47:1030–6. doi: 10.1161/STROKEAHA.116.012949
53. Palta P, Sharrett AR, Wei J, Meyer ML, Kucharska-Newton A, Power MC, et al. Central arterial stiffness is associated with structural brain damage and poorer cognitive performance: the ARIC study. *J Am Heart Assoc.* (2019) 8:e011045. doi: 10.1161/JAHA.118.011045
54. Hughes TM, Wagenknecht LE, Craft S, Mintz A, Heiss G, Palta P, et al. Arterial stiffness and dementia pathology: atherosclerosis risk in communities (ARIC)-PET study. *Neurology.* (2018) 90:e1248–e56. doi: 10.1212/WNL.0000000000005259
55. Vermeer SE, Koudstaal PJ, Oudkerk M, Hofman A, Breteler MM. Prevalence and risk factors of silent brain infarcts in the population-based Rotterdam scan study. *Stroke.* (2002) 33:21–5. doi: 10.1161/hs0102.101629
56. Bernick C, Kuller L, Dulberg C, Longstreth Jr W, Manolio T, Beauchamp N, et al. Silent MRI infarcts and the risk of future stroke The cardiovascular health study. *Neurology.* (2001) 57:1222–9. doi: 10.1212/WNL.57.7.1222
57. Huang X, Kang X, Xue J, Kang C, Lv H, Li Z. Evaluation of carotid artery elasticity changes in patients with cerebral small vessel disease. *Int J Clin Exp Med.* (2015) 8:18825–30.
58. Ding J, Mitchell GF, Bots ML, Sigurdsson S, Harris TB, Garcia M, et al. Carotid arterial stiffness and risk of incident cerebral microbleeds in older people: the age, gene/environment susceptibility (AGES)-Reykjavik study. *Arterioscler Thromb Vasc Biol.* (2015) 35:1889–95. doi: 10.1161/ATVBAHA.115.305451
59. Rensma SP, Stehouwer CD, Van Boxtel MP, Houben AJ, Berendschot TT, Jansen JF, et al. Associations of arterial stiffness with cognitive performance, and the role of microvascular dysfunction: the maastricht study. *Hypertension.* (2020) 75:1607–14. doi: 10.1161/HYPERTENSIONAHA.119.14307
60. Singer J, Trollor JN, Baune BT, Sachdev PS, Smith E. Arterial stiffness, the brain, and cognition: a systematic review. *Ageing Res Rev.* (2014) 15:16–27. doi: 10.1016/j.arr.2014.02.002
61. Riba-Llena I, Jiménez-Balado J, Castañé X, Girona A, López-Rueda A, Mundet X, et al. Arterial stiffness is associated with basal ganglia enlarged perivascular spaces and cerebral small vessel disease load. *Stroke.* (2018) 49:1279–81. doi: 10.1161/STROKEAHA.118.020163
62. Pase MP, Beiser A, Himali JJ, Tsao C, Satizabal CL, Vasan RS, et al. Aortic stiffness and the risk of incident mild cognitive impairment and dementia. *Stroke.* (2016) 47:2256–61. doi: 10.1161/STROKEAHA.116.013508
63. Benetos A, Watfa G, Hanon O, Salvi P, Fantin F, Toulza O, et al. Pulse wave velocity is associated with 1-year cognitive decline in the elderly older than 80 years: the PARTAGE study. *J Am Med Dir Assoc.* (2012) 13:239–43. doi: 10.1016/j.jamda.2010.08.014
64. Watson NL, Sutton-Tyrrell K, Rosano C, Boudreau RM, Hardy SE, Simonsick EM, et al. Arterial stiffness and cognitive decline in well-functioning older adults. *J Gerontol Series A: Biomed Sci Med Sci.* (2011) 66:1336–42. doi: 10.1093/gerona/glr119
65. Elias MF, Robbins MA, Budge MM, Abhayaratna WP, Dore GA, Elias PK. Arterial pulse wave velocity and cognition with advancing age. *Hypertension.* (2009) 53:668–73. doi: 10.1161/HYPERTENSIONAHA.108.126342
66. Muela HC, Costa-Hong VA, Yassuda MS, Moraes NC, Memória CM, Machado MF, et al. Higher arterial stiffness is associated with lower cognitive performance in patients with hypertension. *J Clin Hyperten.* (2018) 20:22–30. doi: 10.1111/jch.13129
67. Mehrabian S, Raycheva M, Gateva A, Todorova G, Angelova P, Traykova M, et al. Cognitive dysfunction profile and arterial stiffness in type 2 diabetes. *J Neurol Sci.* (2012) 322:152–6. doi: 10.1016/j.jns.2012.07.046

68. Scuteri A, Brancati AM, Gianni W, Assisi A, Volpe M. Arterial stiffness is an independent risk factor for cognitive impairment in the elderly: a pilot study. *J Hypertens.* (2005) 23:1211–6. doi: 10.1097/01.hjh.0000170384.38708.b7
69. Triantafyllidi H, Arvaniti C, Lekakis J, Ikonomidis I, Siafakas N, Tzortzis S, et al. Cognitive impairment is related to increased arterial stiffness and microvascular damage in patients with never-treated essential hypertension. *Am J Hypertens.* (2009) 22:525–30. doi: 10.1038/ajh.2009.35
70. Huck DM, Hanna DB, Rubin LH, Maki P, Valcour V, Springer G, et al. Carotid artery stiffness and cognitive decline among women with or at risk for HIV infection. *J Acq Immune Def Syn* 1999. (2018) 78:338. doi: 10.1097/QAI.0000000000001685
71. Geijselaers SL, Sep SJ, Schram MT, van Boxtel MP, van Sloten TT, Henry RM, et al. Carotid stiffness is associated with impairment of cognitive performance in individuals with and without type 2 diabetes. *The Maastricht Study Atherosclerosis.* (2016) 253:186–93. doi: 10.1016/j.atherosclerosis.2016.07.912
72. DuBose LE, Voss MW, Weng TB, Kent JD, Dubishar KM, Lane-Cordova A, et al. Carotid β-stiffness index is associated with slower processing speed but not working memory or white matter integrity in healthy middle-aged/older adults. *J Appl Physiol.* (2017) 122:868–76. doi: 10.1152/japplphysiol.00769.2016
73. Lim SL, Gao Q, Nyunt MSZ, Gong L, Lunaria JB, Lim ML, et al. Vascular health indices and cognitive domain function: singapore longitudinal ageing studies. *J Alzheimers Dis.* (2016) 50:27–40. doi: 10.3233/JAD-150516
74. Tarumi T, Gonzales MM, Fallow B, Nualnim N, Pyron M, Tanaka H, et al. Central artery stiffness, neuropsychological function, and cerebral perfusion in sedentary and endurance-trained middle-aged adults. *J Hypertens.* (2013) 31:2400–9. doi: 10.1097/HJH.0b013e328364decc
75. Hoth KF, Moreau KL, Weinberger HD, Holm KE, Meschede K, Crapo JD, et al. Carotid artery stiffness is associated with cognitive performance in former smokers with and without chronic obstructive pulmonary disease. *J Am Heart Assoc.* (2020) 9:e014862. doi: 10.1161/JAHA.119.014862
76. Chiesa ST, Masi S, Shipley MJ, Ellins EA, Fraser AG, Hughes AD, et al. Carotid artery wave intensity in mid-to late-life predicts cognitive decline: the Whitehall II study. *Eur Heart J.* (2019) 40:2300–9. doi: 10.1093/eurheartj/ehz189
77. Pasha EP, Rutjes E, Tomoto T, Tarumi T, Stowe A, Claassen JA, et al. Carotid stiffness is associated with brain amyloid-β burden in amnestic mild cognitive impairment. *J Alzheimers Dis.* (2020) 74:1–11. doi: 10.3233/JAD-191073


**Conflict of Interest:** The authors declare that the research was conducted in the absence of any commercial or financial relationships that could be construed as a potential conflict of interest.

**Publisher's Note:** All claims expressed in this article are solely those of the authors and do not necessarily represent those of their affiliated organizations, or those of the publisher, the editors and the reviewers. Any product that may be evaluated in this article, or claim that may be made by its manufacturer, is not guaranteed or endorsed by the publisher.

frontiers in Cardiovascular Medicine

ORIGINAL RESEARCH
published: 22 March 2022
doi: 10.3389/fcvm.2022.823436

# A Deep Learning System for Fully Automated Retinal Vessel Measurement in High Throughput Image Analysis

*Danli Shi*[1], *Zhihong Lin*[2], *Wei Wang*[1], *Zachary Tan*[3], *Xianwen Shang*[4], *Xueli Zhang*[4], *Wei Meng*[5], *Zongyuan Ge*[6] *and Mingguang He*[1,3,4]*

[1] State Key Laboratory of Ophthalmology, Zhongshan Ophthalmic Center, Sun Yat-sen University, Guangzhou, China, [2] Faculty of Engineering, Monash University, Melbourne, VIC, Australia, [3] Centre for Eye Research Australia, East Melbourne, VIC, Australia, [4] Department of Ophthalmology, Guangdong Provincial People's Hospital, Guangdong Eye Institute, Guangdong Academy of Medical Sciences, Guangzhou, China, [5] Guangzhou Vision Tech Medical Technology Co., Ltd., Guangzhou, China, [6] Research Center and Faculty of Engineering, Monash University, Melbourne, VIC, Australia

OPEN ACCESS

**Edited by:**
*Luca Biasiolli,*
*University of Oxford, United Kingdom*

**Reviewed by:**
*Rolando Jose Estrada,*
*Georgia State University, United States*
*Alicja Rudnicka,*
*University of London, United Kingdom*

***Correspondence:**
*Mingguang He*
*mingguang.he@unimelb.edu.au*

**Specialty section:**
*This article was submitted to Cardiovascular Imaging, a section of the journal Frontiers in Cardiovascular Medicine*

**Received:** *27 November 2021*
**Accepted:** *22 February 2022*
**Published:** *22 March 2022*

**Citation:**
*Shi D, Lin Z, Wang W, Tan Z, Shang X, Zhang X, Meng W, Ge Z and He M (2022) A Deep Learning System for Fully Automated Retinal Vessel Measurement in High Throughput Image Analysis. Front. Cardiovasc. Med. 9:823436. doi: 10.3389/fcvm.2022.823436*

**Motivation:** Retinal microvasculature is a unique window for predicting and monitoring major cardiovascular diseases, but high throughput tools based on deep learning for in-detail retinal vessel analysis are lacking. As such, we aim to develop and validate an artificial intelligence system (Retina-based Microvascular Health Assessment System, RMHAS) for fully automated vessel segmentation and quantification of the retinal microvasculature.

**Results:** RMHAS achieved good segmentation accuracy across datasets with diverse eye conditions and image resolutions, having AUCs of 0.91, 0.88, 0.95, 0.93, 0.97, 0.95, 0.94 for artery segmentation and 0.92, 0.90, 0.96, 0.95, 0.97, 0.95, 0.96 for vein segmentation on the AV-WIDE, AVRDB, HRF, IOSTAR, LES-AV, RITE, and our internal datasets. Agreement and repeatability analysis supported the robustness of the algorithm. For vessel analysis in quantity, less than 2 s were needed to complete all required analysis.

**Keywords: artificial intelligence, automated analysis, hierarchical vessel morphology, cardiovascular disease, epidemiology**

## INTRODUCTION

The morphology of the retinal vessels is closely correlated with the microvascular state of the body. The retinal vasculature is organized within a delicate, optimized structure that minimizes shear stresses due to blood flow and energy used for perfusion, achieving sufficient energy supply with minimal cost (1). Changes in retinal vascular morphology have previously been reported to be associated with a wide range of ocular and systemic diseases (2–5), including life-threatening cardiovascular disease. Deviation from the geometric ideal and measurement of vessel changes may provide a quantitative assessment of vessel deformity and pathology. Quantification of these changes may enhance our understanding of the relationship between ocular and systemic

changes and promote the use of the retinal vessels as novel biomarkers in the management of chronic diseases.

Computer-assisted technology has enabled the quantification of retinal morphology. A series of machine learning methods and software tools have been developed for the quantified assessment of the retinal vasculature. Widespread use of these tools however has been limited due to their need for manual input [IVAN (6), SIVA (7), VAMPIRE (8)], time-consuming nature [IVAN (6), SIVA (7)], applicability to only specific retinal regions [IVAN (6), SIVA (7)], or a limited number of measurement parameters [IVAN (6), VAMPIRE (8), QUARTZ (9, 10)].

Deep learning (DL) has been established in recent years as the dominant paradigm for retinal image processing. It has outperformed other machine learning (ML) methods in achieving retinal vessel segmentation with minimal time and state-of-the-art accuracy (11). Widespread adoption in real-world settings however depends on its ability to address variations in image quality and artifacts, resolutions and modality of various fundus cameras, and the interference of pathologic lesions on vessel segmentation. A further common challenge for vessel segmentation is broken vessels at branching or crossing points, which often result in misclassification of arteries and veins, or discontinued vessels. In addition to vessel segmentation, SIVA-DLS (12) is a recently developed deep learning system that directly predicts vessel caliber based on cropped retinal fundus without performing segmentation. However, this tool is restricted to a limited region of the retina and evaluates only a small number of vessel parameters.

Training deep learning algorithms with larger datasets and sufficient variation may help address these challenges. However, given the labor intensiveness in labeling vessels manually, there are much fewer training data available for vessel segmentation than disease classification. Most databases with annotated vessels used in algorithm development are homogeneous, small, and free of eye diseases, compromising the adoption of algorithms trained on these data in real-world clinical settings.

As such, we developed and validated a deep learning system (Retina-based Microvascular Health Assessment System, RMHAS) using multi-source data to provide fast, reliable, and detailed retinal vessel quantification. We intend to provide RMHAS as a public tool to enable automated high-throughput retinal vessel analysis on large collections of fundus images.

**Abbreviations:** RMHAS, retina-based microvascular health assessment system; AMD, age-related macular degeneration; PM, pathologic myopia; DR, diabetic retinopathy; HR, hypertensive retinopathy; LECS, lingtou eye cohort study; GTES, guangzhou twin eye study; CLAHE, contrast limited adaptive histogram equalization; CNN, convolutional neural network; FOV, field of view; CRAE, central retinal artery equivalent; CRVE, central retinal vein equivalent; AVRe, artery to vein ratio from equivalents; LDR, length diameter ratio; BA, branching angle; BA_edge, branching angle from edges; BC, branching coefficient; AA, angular asymmetry; AR, asymmetry ratio; JED, Junctional exponent deviation; SD, standard deviation; CI, confidence interval; ICC, intraclass correlation coefficient; ROC, receiver operator characteristic; AUC, area under the receiver operator characteristic curve; ROI, region of interest.

# METHODS

## Study Design and Overview

RMHAS consisted of several functional parts. Firstly, the image quality assessment module assessed overall image quality before segmentation. Secondly, the segmentation module generated artery, vein, and optic disc segmentation maps. Thirdly, based on segmentation, the measurement module computed region-specific measurements within the Standard zone (a zone 0.5–1.0 disc diameter away from the optic disk margin), (13) and global physical or geometric measures for the whole fundus image. Lastly, a second quality assessment was carried out to filter out abnormal measurements and exclude incompetent detections based on specific criteria. Final results were subsequently generated. **Figure 1A** outlines a flowchart of the software development process.

## Fundus Datasets

### In-house Dataset

To train the segmentation algorithm for RMHAS, we built a large manually labeled retinal artery/vein segmentation database. This database included diverse eye diseases, age groups, and imaging devices. Two hundred and twenty images with significant variations were initially included, of which 20 came from the UK Biobank (14), 120 from the LabelMe platform (15). 50 from the Lingtou Eye Cohort Study (LECS) (16). and 30 from the Guangzhou Twin Eye Study (GTES) (17). These images were composed of 60 images with diabetic retinopathy ranging from mild to severe non-proliferative, 20 images with age-related macular degeneration (AMD), 20 with glaucoma, 20 with pathologic myopia (PM), and 20 with hypertension. 20 images for each age group of $<$18, 18 to 50, and $\geq$ 50 years were included. To represent healthy images, another 200 images were randomly selected from the UK Biobank population-based study (**Table 1**).

Vessel annotation was performed according to the following procedure. Firstly, we generated artery/vein (A/V) segmentation maps by supplying the fundus images to the W-Net model (18). After this, image graders using custom software can modify or fine-tune vessel segmentation as per A/V segmentation maps. Secondly, to make low-contrast small vessels more identifiable, we carried out image enhancements using contrast limited adaptive histogram equalization (CLAHE). Pre-segmentations generated by the W-Net model could be overlaid on the original fundus or the augmented image. Image graders could switch between different modalities to verify their segmentation and erase or add vessels. The custom software interface developed for this image annotation process is illustrated in **Supplementary Figure 1**.

All images were randomly assigned to one of four image graders who were trained by an ophthalmologist. These image graders were requested to independently modify and segment the retinal arteries, veins, and optic disc. To assess inter-observer variability, ∼10 percent of images were repeatedly labeled between different graders. To assess intra-observer consistency, around 10 percent of the images were repeatedly labeled by the same grader. Cohen's

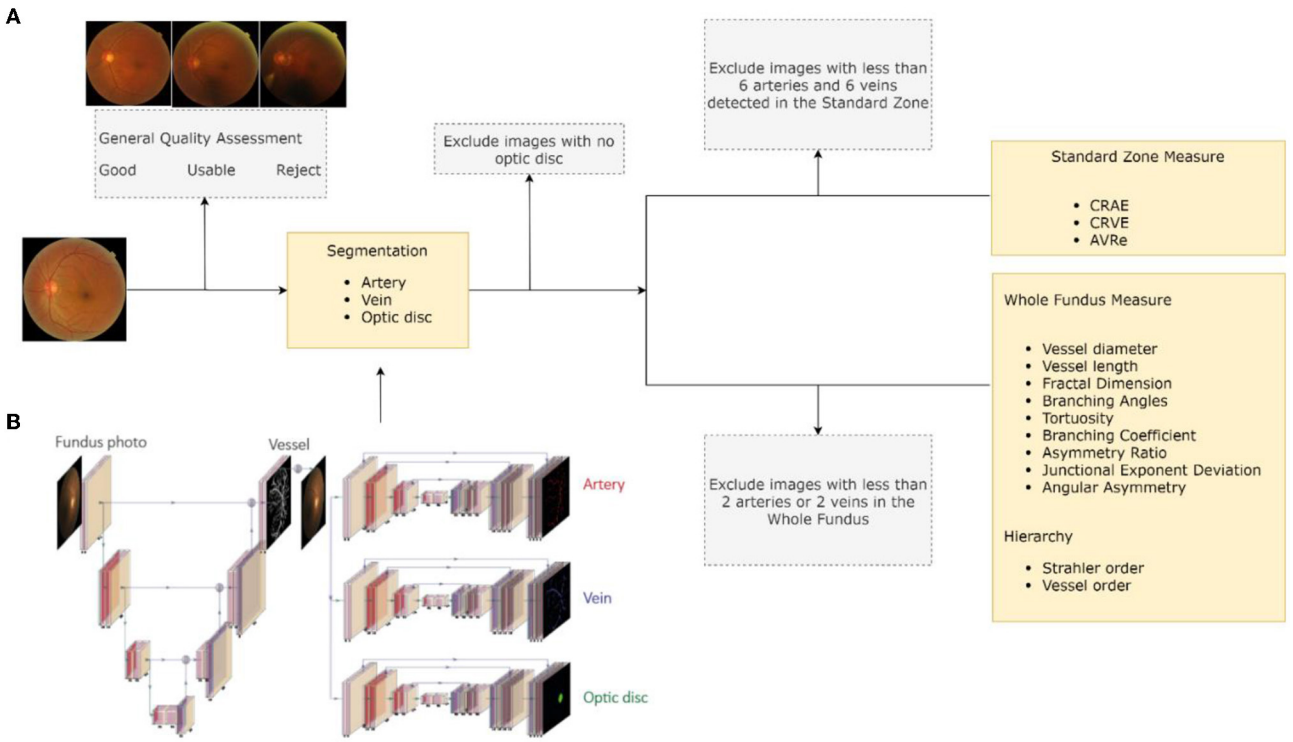


**FIGURE 1 |** Software development flowchart. **(A)** Retina-based Microvascular Health Assessment System (RMHAS) workflow. **(B)** The multi-branch U-Net used in RMHAS for segmentation. The trunk generates an intermediate retinal vessel feature map, which is concatenated with the input image and divided into three separate branches for retinal artery, vein, and optic disc segmentation.

kappa score was computed to assess inter-observer and intra-observer reliability.

### Public Datasets

To improve model generalizability and robustness, data from 20 public datasets were also used in the development of the segmentation algorithm. The STARE (19), VEVIO (20, 21). CHASEDB (22), DR HAGIS (23), UoA-DR (24), and PRIME-FP20 (25) datasets were used for vessel segmentation. The RITE (26), HRF (27), AV-WIDE (28, 29), IOSTAR (30, 31), LES-AV (32), and AVRDB (33) datasets were used for artery and vein classification. For optic disc segmentation, the ONHSD (34), DRIONS-DB (35), Drishti-GS (36), RIGA (37), REFUGE (38), G1020 (39), PALM (40), and ADAM (41) datasets were used. Although those datasets have previously been used to develop segmentation algorithms, their label quality varies.

In summary, a diverse collection of datasets composed of fundus images of varying image qualities, resolutions, pathologies, and modalities were included in developing this algorithm. As the size of datasets varied significantly, training and validation set splits were carried out as follows: 20 official training and test set images were split from the CHASEDB dataset; if the dataset had fewer than 100 total images, training and test images followed an 80/20 split; and if the dataset had more than 100 images, only 20 images were split into the test set. **Table 2** describes the characteristics of the 21 datasets used to develop the segmentation algorithm. Diagrams in **Supplementary Figure 2** outlines the train/test division.

The study was conducted in accordance with the Declaration of Helsinki, using deidentified retinal photographs from previously published studies. Ethics Committee ruled that approval was not required for this study.

## Image Quality Assessment

As noted earlier, the first functional part of RMHAS is a classification of overall image quality before before vessel segmentation. This was carried out using a convolutional neural network (CNN) model built from the EyeQ dataset (42), and enabled classification of overall image quality into three grades: "good," "usable," and "reject." Images with clear and identifiable main structures and lesions, but with some low-quality factors (blur, insufficient illumination, shadows) were classified as "usable". Images with serious quality issues that could not be reliably diagnosed by an ophthalmologist were classified as "reject".

A second quality assessment was performed after segmentation. Images with the following conditions were excluded: no detectable optic disc; <6 arteries six veins detectable in the Standard zone; or <2 arteries and two veins detected in the whole fundus. Excluded images, the reason for their exclusion, and their available measurements were saved separately from the main measurements.

**TABLE 1 |** The composition of the newly-built dataset for retinal artery, vein, and optic disc segmentation. LECS, Lingtou Eye Cohort Study; GTES, Guangzhou Twin Eye Study.

| Category | Number of images | | Source |
|---|---|---|---|
| DR | | 60 | LabelMe |
| r1 | 20 | | |
| r2 | 20 | | |
| r3 | 20 | | |
| Glaucoma | | 20 | LabelMe |
| AMD | | 20 | LabelMe |
| PM | | 20 | LabelMe |
| HBP | | 20 | LECS |
| Age | | 60 | |
| <18 | 20 | | GTES |
| 18–50 | 20 | | GTES, LECS |
| 50+ | 20 | | LECS |
| UK Biobank | | 20 | UK Biobank |
| UK Biobank | | 200 | UK Biobank |
| **Total** | | **420** | |

## Optic Disc and Vessel Segmentation

We extended the U-Net component from W-Net (18) into multiple branches to enable simultaneous and efficient retinal artery, vein, and optic disc segmentation. **Figure 1B** outlines the details of the RMHAS segmentation architecture. The input for RMHAS was a fundus image, cropped to the field of view (FOV) and resized to 512×512 pixels. The first intermediate layer generated a segmentation map based on the whole retinal vessel map and concatenated it to the original fundus image. This first segmentation map could then be used by the downstream network as an attention map, to focus more on targeted areas of the image. The following segmentations were carried out in three separate branches for the retinal arteries, veins, and optic disc, using these features as guidance.

We trained the RMHAS step-by-step by first training the root branch to generate an intact vessel map. The root branch was then frozen, with the artery, vein, and optic branches unfrozen and trained iteratively. We trained RMHAS with a preset of 200 epochs, a batch size of 8, and a cosine-shaped learning rate from 0.1 to 0.00001. To tackle class imbalance issues – i.e., far more background pixels than foreground (vessel) pixels, we used a weighted combination of Cross-entropy loss and Dice loss (1:3) as the objective function (detailed in the **Supplementary Methods**). The Adam optimizer (43) was used in backpropagation to minimize the objective function by optimizing the model parameters. To reduce overfitting, we did data augmentation by random horizontal and vertical flipping, rotating between 0 and 45°, and by transforming contrast and illumination (**Supplementary Methods**). We also used early stopping if validation loss did not improve for 10 epochs. To alleviate issues of broken vessels at branch-ing/crossing points, we performed further data augmentation by specifically cropping out a random number of branching/crossing regions with random sizes for training (to create more pieces of crossing vessel segments and increase variations). This model was trained on the PyTorch platform.

## Retinal Vessel Measurement

We measured retinal vessel morphology by using custom region-specific summarization and global physical/geometric parameters. For region-specific summarization, the vessel calibers were summarized as central retinal artery equivalent (CRAE) and central retinal vein equivalent (CRVE) from the 6 largest arteries and veins detected in the Standard zone, based on the revised Knudtson-Parr-Hubbard formula (44). Artery to vein ratio from equivalents (AVRe) was generated by dividing CRAE by CRVE. For global physical/geometric parameters, vessels were converted into segments separated by interruptions at the branching or crossing points. Short vessels <10 pixels in length were excluded from the analysis. Using methods similar to SIVA (13), the diameters (mean, standard deviation [SD]), arc length, chord length, length diameter ratio (LDR), tortuosity, branching angle (BA), branching angle from edges (BA_edge), branching coefficient (BC), angular asymmetry (AA), asymmetry ratio (AR), junctional exponent deviation (JED) were measured and computed. The vessel orders and Strahler orders of each segment were built using graphical representation, resulting in a series of hierarchical nodes and edges. In summary, 16 basic parameters were included. Detailed formulas and methods are presented in the **Supplementary Methods**. Graphs were built using the Python package NetworkX.

## Accuracy of Segmentation

We assessed the accuracy of segmentation at the pixel level.

Quantitative evaluation criteria including the area under the receiver operator characteristic curve (AUC), accuracy, sensitivity, specificity, between manually labeled and predicted segmentations were computed.

Qualitative evaluation was performed by overlaying predicted segmentations with manually labeled segmentation, using different colors for visual analysis.

For external validation, we performed retinal vessel segmentation and width measure using the pubic REVIEW (45) dataset as reference.

## Reliability of Vessel Measurements

For reliability, intraclass correlation coefficient (ICC) and Bland–Altman plots were used to assess agreement in Standard zone measurements between manually labeled and predicted segmentation.

For repeatability, the ICCs were computed between all measurements on photographs taken repeatedly under similar illumination and locations for the same eye with the same camera.

ICC values of <0.5, 0.5–0.75, 0.75–0.9, and ≥ 0.90 are indicative of poor, moderate, good, and excellent reliability, respectively (46).

Statistical analysis was completed with R version 4.0.1 and Python 3.6.

**TABLE 2 |** Characteristics of the 21 datasets used to develop the segmentation algorithm. Only images with available labels were included. AMD, age-related macular degeneration; HR, hypertensive retinopathy; PM, pathologic myopia; DR, diabetic retinopathy.

| Dataset | Label | Year | No. | Centered | Field | Size | Eye disease | Camera |
|---|---|---|---|---|---|---|---|---|
| STARE | vessel | 2000 | 20 | macula | 30°-45° | 605 × 700 | various | TRV-50 fundus camera (Topcon) |
| VEVIO | vessel | 2011 | 16 | macula | | 640 × 480<br>600 × 500 | | Video indirect ophthalmoscopy |
| CHASEDB | vessel | 2012 | 28 | optic-disc | 25° | 960 × 999 | – | NM-200D (Nidek, Japan) |
| DR HAGIS | vessel | 2017 | 40 | macula | 45° | 2816 × 1,880<br>4,752 × 3,168 | DR, HBP, AMD, glaucoma | TRC-NW6s (Topcon), TRC-NW8 (Topcon), or CR-DGi (Canon) |
| UoA-DR | vessel, optic disc | 2017 | 200 | macula-disc | 45° | – | DR | – |
| PRIME-FP20 | vessel | 2020 | 15 | macula | 200° | 4,000 × 4,000 | DR | Optos 200Tx (Optos plc, Dunfermline, Scotland, UK) |
| RITE | artery/vein | 2013 | 40 | macula | 45° | 565 × 584 | DR | CR5 non-mydriatic 3CCD camera (Canon) |
| HRF | artery/vein, optic disc | 2013 | 45 | macula | 45° | 3,504 × 2,336 | DR, glaucoma | |
| AV-WIDE | artery/vein | 2015 | 30 | macula | 200° | 1,300 × 800<br>2,816 × 1,880<br>1,500 × 900 | DR | Optos 200Tx (Optos plc, Dunfermline, Scotland, UK) |
| IOSTAR | artery/vein, optic disc | 2015 | 30 | macula | 45° | 1,024 × 1,024 | | SLO (i-Optics Inc., the Netherlands) |
| LES-AV | artery/vein | 2018 | 22 | optic-disc | 30°−45° | 1,620 × 1,444<br>1,958 × 2,196 | glaucoma | |
| AVRDB | artery/vein | 2020 | 100 | macula-disc | 30° | 1,504 × 1,000 | HR, DR | |
| ONHSD | optic disc | 2004 | 99 | macula | 45° | 640 × 480 | DR | CR6 45MNf fundus camera (Canon) |
| DRIONS-DB | optic disc | 2008 | 110 | optic-disc | 30° | 600 × 400 | glaucoma, ocular hypertension | |
| Drishti-GS | optic disc | 2014 | 50 | macula | 25° | 2,045 × 1,752 | glaucoma | – |
| RIGA dataset | optic disc | 2018 | 750 | macula-disc | – | 2,240 × 1,488<br>2,743 × 1,936<br>2,376×1,584 | DR, glaucoma | – |
| REFUGE2 | optic disc | 2020 | 1200 | macula | | 2,124 × 2,056<br>1,634 × 1,634 | glaucoma | Zeiss Visucam 500/Canon CR-2 |
| G1020 | optic disc | 2020 | 1020 | macula-disc | 45° | – | various | – |
| PALM | optic disc | 2019 | 400 | macula-disc | – | – | PM | – |
| ADAM | optic disc | 2020 | 400 | macula | – | – | AMD | – |
| Ours | artery/vein, optic disc | 2021 | 420 | macula-disc | various | various | DR, glaucoma, AMD, PM | Various |

## Data Availability Statement

The UK Biobank is an open-access resource to researchers through registration of proposed research. The remaining in-house dataset is available from the corresponding author upon reasonable request.

## Code Availability Statement

The code of this study is available from the corresponding author upon request. All models were built using publicly available software and packages.

# RESULTS

The four observers achieved moderate consistency in intra- and inter-observer agreement analysis. Detailed kappa scores are presented in **Supplementary Table 1**. For segmentation accuracy, the algorithm achieved AUC (95% CI) of 0.914 (0.914–0.915), 0.913 (0.913–0.914), 0.948 (0.948–0.948), 0.919 (0.918–0.920), 0.959 (0.959–0.960), 0.953 (0.952–0.953), 0.922 (0.922–0.922) for artery segmentation and 0.930 (0.929–0.931), 0.940 (0.939–0.940), 0.956 (0.956–0.956), 0.935 (0.934–0.936), 0.961 (0.961–0.962), 0.959 (0.959–0.960), 0.948 (0.948–0.949) for vein segmentation on the AV-WIDE, AVRDB, HRF, IOSTAR, LES-AV, RITE and our dataset, respectively. **Figure 2** plots the model's ROC curves in different datasets. Detailed evaluation results are presented in **Table 3**. **Figure 3** shows representative examples of overlaid segmentations for images with different features, including a normal fundus, fundus image from young participants with prominent retinal nerve fiber layer reflections, blurred image from older participants, fundus with AMD, PM,

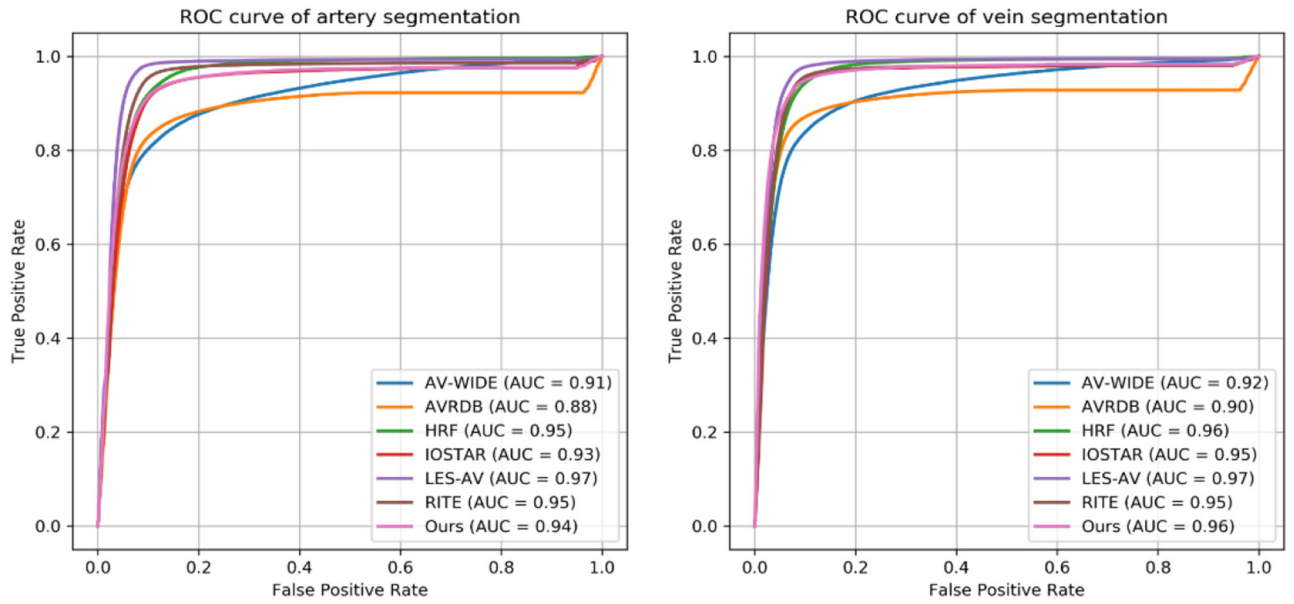


**FIGURE 2 |** Receiver operating characteristic (ROC) curves of Retina-based Microvascular Health Assessment System (RMHAS) for segmentation of artery and vein within different datasets.

**TABLE 3 |** Segmentation performance of Retina-based Microvascular Health Assessment System (RMHAS) on the test set in different datasets.

| | Accuracy | | Sensitivity | | Specificity | | F1 score | |
|---|---|---|---|---|---|---|---|---|
| | Artery | Vein | Artery | Vein | Artery | Vein | Artery | Vein |
| AV-WIDE | 0.95 | 0.95 | 0.68 | 0.73 | 0.96 | 0.96 | 0.45 | 0.47 |
| AVRDB | 0.94 | 0.95 | 0.72 | 0.78 | 0.95 | 0.96 | 0.47 | 0.62 |
| HRF | 0.93 | 0.94 | 0.83 | 0.87 | 0.93 | 0.94 | 0.46 | 0.50 |
| IOSTAR | 0.94 | 0.95 | 0.72 | 0.77 | 0.95 | 0.96 | 0.51 | 0.59 |
| LES-AV | 0.95 | 0.95 | 0.86 | 0.85 | 0.96 | 0.96 | 0.58 | 0.61 |
| RITE | 0.94 | 0.94 | 0.86 | 0.87 | 0.94 | 0.95 | 0.57 | 0.63 |
| Ours | 0.95 | 0.96 | 0.72 | 0.80 | 0.96 | 0.97 | 0.48 | 0.57 |

and severe DR. Blue pixels represent false negatives (pixels that were manually labeled but missed by the model). Red pixels represent false positives (pixels identified by the model but missed by manual labeling). Green pixels represent pixels with consistent segmentation between model and manual labeling.

For external validation, the vessel segmentation performance and width measure results in the REVIEW database are shown in the **Supplementary Table 2** and **Supplementary Figure 3**.

Agreement between retinal vessel caliber in the Standard zone, measured on RMHAS predicted segmentation and human segmentations were estimated using ICC. Agreements of vessel equivalent measurements on our dataset were excellent, good, or excellent on LES-AV (a dataset composed purely of disc-centered fundus images) but moderate or below on AVRDB, HRF, RITE (composed of macula-centered photos), suggesting to achieve ideal Standard zone measures, images should be optic-disc centered (similar to SIVA). Detailed ICC results are presented in **Table 4**. Bland-Altman plots of the agreement of (a) retinal arteriolar caliber and (b) retinal venular caliber, (c) AVRe between manual and predicted vessel maps, (d) differences between AVRe measures on manual and predicted vessel maps; vs. the distance of the optic disc center to the edge of FOV are displayed in **Supplementary Figure 3**.

The reproducibility and robustness of the measurements were measured by comparing measurements generated from photographs taken repeatedly under similar conditions. For measurements in the Standard zone, 198 of 1290 (15.3%) images failed quality control in Standard zone measures. Of these, 9, 22, and 120 images were classified as good, usable, and reject in the first quality assessment module. The model achieved excellent agreement for measurements generated under similar conditions (**Table 5A**). For measurements within the whole fundus, 8 (0.6%) of images failed quality control in whole fundus measures and generated 114,809 vessel segments for analysis. The model achieved moderate to good agreement for measurements based on all vessels (**Table 5B**).

**Figure 4** shows an example of the RMHAS model output. Measures are demonstrated and plotted visually. Users can easily evaluate the performance of each functional part throughout the analysis.

# DISCUSSION

## Algorithm Development

Retinal vessel segmentation is challenging and often compromised by interference from the central light reflex, image quality variation and artifact, poor image contrast of

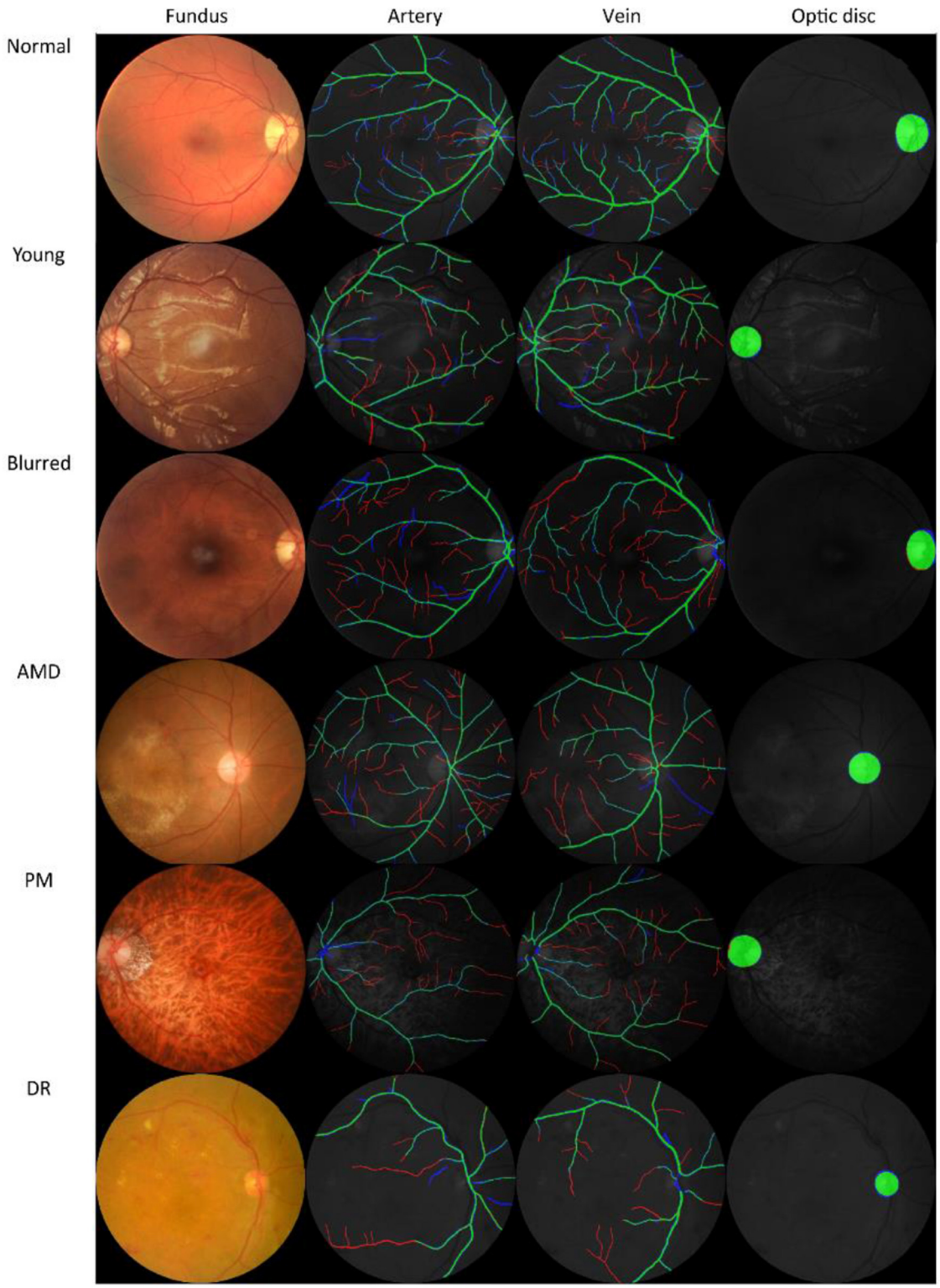


**FIGURE 3 |** Examples of model prediction by Retina-based Microvascular Health Assessment System (RMHAS) versus manual segmentation. Blue pixels: false negatives (pixels that were manually labeled but missed by the model). Red pixels: false positives (pixels identified by the model but missed by manual labeling). Green pixels: pixels with consistent segmentation between model and manual labeling. AMD, age-related macular degeneration; PM, pathologic myopia; DR, diabetic retinopathy.

**TABLE 4 |** Agreement estimates of retinal-vessel caliber in the Standard zone for measurements on RMHAS segmentation and manual segmentation.

| | ICC (95%CI) | |
|---|---|---|
| **Dataset** | **CRAE** | **CRVE** |
| AVRDB ($n = 54$) | 0.55 (0.37–0.69)* | 0.30 (0.08–0.49) |
| HRF ($n = 38$) | 0.59 (0.38–0.74)* | 0.42 (0.18–0.62) |
| LES-AV ($n = 20$) | 0.89 (0.78–0.95)** | 0.90 (0.80–0.95)*** |
| Ours ($n = 238$) | 0.93 (0.91–0.94)*** | 0.97 (0.96–0.97)*** |
| RITE ($n = 34$) | 0.43 (0.17–0.64) | 0.55 (0.31–0.72)* |

**Moderate: between 0.5 and 0.75, **Good: between 0.75 and 0.9, ***Excellent: >0.90. ICC, intraclass correlation; CI, confidence interval; CRAE, central retinal artery equivalent; CRVE, central retinal vein equivalent; n, the number of images.*

**TABLE 5A |** Agreement estimates of measurements in the Standard zone on photographs taken repeatedly under similar conditions.

| **Location** | **Quality** | **ICC (95%CI)** | |
|---|---|---|---|
| | | **CRAE** | **CRVE** |
| Disc centered | Good ($n = 67$) | 0.89 (0.84–0.93)** | 0.92 (0.88–0.95)*** |
| | Reject ($n = 129$) | 0.78 (0.71–0.83)** | 0.83 (0.78–0.87)** |
| | Usable ($n = 14$) | 0.98 (0.94–0.99)*** | 0.94 (0.86–0.98)*** |
| Macula centered | Good ($n = 264$) | 0.94 (0.93–0.95)*** | 0.95 (0.94–0.96)*** |
| | Reject ($n = 43$) | 0.78(0.65–0.86)** | 0.81(0.70–0.88)** |
| | Usable ($n = 29$) | 0.93 (0.88–0.96)*** | 0.91 (0.84–0.95)*** |

**Moderate: between 0.5 and 0.75, **Good: between 0.75 and 0.9, ***Excellent: >0.90. ICC, intraclass correlation; CI, confidence interval; CRAE, central retinal artery equivalent; CRVE, central retinal vein equivalent.*

**TABLE 5B |** Agreement estimates of measurements based on the whole fundus on photographs taken repeatedly under similar conditions.

| | **Good** | **Usable** | **Reject** |
|---|---|---|---|
| **Artery** | ***n* = 330** | ***n* = 35** | ***n* = 161** |
| Arc | 0.75 (0.70–0.79)* | 0.55 (0.32–0.72)* | 0.56 (0.46–0.64)* |
| Chord | 0.76 (0.71–0.79)** | 0.54 (0.31–0.71)* | 0.56 (0.46–0.64)* |
| Length diameter ratio | 0.80 (0.76–0.83)** | 0.64 (0.44–0.78)* | 0.59 (0.50–0.67)* |
| Mean diameter | 0.78 (0.74–0.81)** | 0.74 (0.58–0.85)* | 0.65 (0.57–0.72)* |
| Weighted diameter | 0.81 (0.78–0.84)** | 0.80 (0.68-0.88)** | 0.74 (0.68–0.80)* |
| **Vein** | ***n* = 330** | ***n* = 34** | ***n* = 137** |
| Arc | 0.75 (0.71–0.79)** | 0.68 (0.49–0.80)* | 0.58 (0.48–0.66)* |
| Chord | 0.76 (0.72–0.79)** | 0.66 (0.46–0.79)* | 0.59 (0.49–0.67)* |
| Length diameter ratio | 0.78 (0.74–0.81)** | 0.76 (0.60–0.86)** | 0.63 (0.53–0.70)* |
| Mean diameter | 0.80 (0.76–0.83)** | 0.61 (0.40–0.76)* | 0.73(0.66–0.79)* |
| Weighted diameter | 0.82 (0.78–0.85)** | 0.69 (0.51–0.82)* | 0.74 (0.66–0.79)* |

**Moderate: between 0.5 and 0.75, **Good: between 0.75 and 0.9, ***Excellent: >0.90. ICC, intraclass correlation; CI, confidence interval; CRAE, central retinal artery equivalent; CRVE, central retinal vein equivalent; Weighted diameter: mean diameter weighted by segment length.*

small vessels, broken vessels at branching/crossing points, and pathological retinal lesions.

To tackle these challenges, we first built the largest manually labeled retinal artery and vein segmentation dataset known to date, to train the segmentation algorithm. Secondly, we specifically designed a deep learning architecture that harnessed a two-stage sequential segmentation, where the intermediate vessel segmentation was used to guide subsequent multi-branch segmentations. The separate branches that segmented arteries, veins, and the optic disc reduced the difficulty in distinguishing artery and vein pixels from a single branch. Thirdly, we carried out data augmentation specifically for artery and vein crossing areas.

## Functionality

RMHAS addresses the limitations of existing algorithms and software, including IVAN (6), SIVA (7), and VAMPIRE (8). which are semi-automatic and have limited regions of interest (ROI). IVAN (6) and SIVA (7) require more than 20 min to process each image, and QUARTZ (9) takes on average 53.6 s per analysis. The QUARTZ (9) platform can analyze whole fundus images but has few output parameters (artery/vein width and tortuosity). SIVA-DLS (12) is the only published deep learning system to use fundus images and predict vessel caliber end-to-end without vessel segmentation. It was built based on measured CRAE, CRVE values from SIVA. This method is straightforward but might lack interpretability. Further, SIVA-DLS is restricted to examining the Extended zone (from 0.5 to 2.0-disc diameter) (13) and has limited output parameters (CRAE, CRVE, AVR only).

In comparison, the RMHAS algorithm provides a far larger number of physical and geometric parameters without sacrificing efficiency. In addition to standard vessel caliber measurements, RMHAS provides measurements on tortuosity, LDR, JED, AR with additional topological information. These measurements are unitless and are less sensitive to diametric measurement noise. The Strahler order corresponds to branching complexity (47). Vessel order describes the conventional order of division of each branch of a vessel. These measurements facilitate flexibility in subsequent analysis. For example, they could be stratified when summarizing the thickness or length of a vessel; or calculated as a global representation of the overall or specified retinal vascular network.

## Accuracy of Segmentation

AUC scores were high across different datasets, achieving high pixel-level segmentation accuracy. Interestingly, the visualization of overlaid manual-predicted segmentation suggested that model predictions outperformed manual labeling, especially for small vessels that human graders often missed. For challenging cases, including images from young participants with highly reflective retinal nerve fiber layers, elderly participants with blurred retinal images, or retinal images with existing eye diseases, the algorithm provided segmentations more accurate than human graders.

## Validity and Repeatability of Vessel Measurement

Internal validation demonstrated reproducibility and robustness in vessel measurements. In general, vessel calibers measured

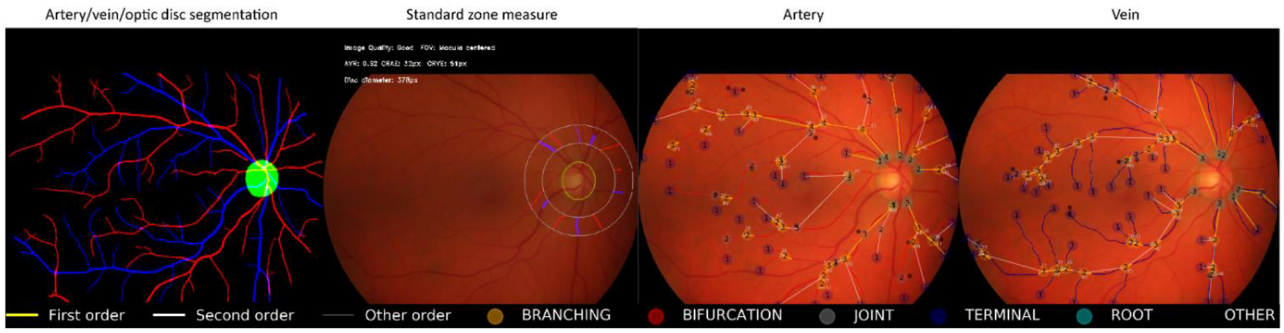


**FIGURE 4 |** Illustration of Retina-based Microvascular Health Assessment System (RMHAS) output. From left to right: artery, vein, and optic disc segmentation; parameters measured in the standard zone; parameters measured in the whole fundus for artery and vein, respectively. Measures are demonstrated and plotted visually. Users can examine the performance of each functional part throughout the analysis.

**TABLE 6 |** Comparison of different algorithms and software for retinal vessel analysis.

| | IVAN | SIVA | VAMPIRE | QUARTZ | SIVA-DLS | RMHAS (ours) |
|---|---|---|---|---|---|---|
| Processing time | 20 min | 25 min | - | 53.57s | A few seconds | <2 s |
| Kind | Semi-automatic | Semi-automatic | Semi-automatic | Automatic | Automatic | Automatic |
| ROI | Standard | Standard + Extended | Whole fundus | Whole fundus | Standard + Extended | Standard + Whole fundus |
| Algorism | ML | ML | ML | ML | DL | DL |
| AVR | √ | √ | √ | √ | √ | √ |
| Mean vessel diameter | √ | √ | √ | √ | √ | √ |
| Length-diameter ratio | × | √ | × | √ | × | √ |
| Vessel tortuosity | × | √ | √ | √ | × | √ |
| Branching coefficients | × | √ | √ | × | × | √ |
| Branching angle | × | √ | √ | √ | × | √ |
| Angular asymmetry | × | √ | × | × | × | √ |
| Asymmetry ratio | × | √ | × | × | × | √ |
| Junctional exponent deviation | × | √ | × | × | × | √ |
| Fractal dimension | × | √ | √ | × | × | √ |
| Hierarchical vessel tree | × | × | × | × | × | √ |
| Year | 2004 | 2010 | 2011 | 2015 | 2020 | 2021 |

*ROI, region of interest; AVR, artery to vein ratio.*

within the Standard zone in disc-centered images were most robust. All measurements achieved good or better agreement.

For external validation, we should note that measurements are often not directly comparable between different algorithms or software, particularly for measurements with units. For example, CRAE and CRVE measurements between SIVA and other software tools have been previously reported as not equivalent, despite these caliber measurements being associated with the same systemic health risk factors (48). Discrepancy in caliber measurement is often due to variation in magnification during image acquisition. A meaningful comparison would require Littmann's method (49) to adjust the magnification factor by considering refractive error, corneal curvature, and axial length and adapting them for Gullstrand's schematic eye. More importantly, this adjustment method would require fundus cameras to be constructed based on a telecentric ray path. However, most fundus cameras currently on the market do not strictly follow this principl (50). Further, even when magnification is appropriately adjusted, caliber should ideally be measured when the structure of interest is in the same position within the photo, although this is virtually impossible. All of these factors may result in variations in the caliber measurement (50). Given these challenges and the need to enable measures on images with unknown fundus camera and magnification settings, we chose to present caliber measurements in pixel units rather than micron values. Notably in the Bland-Altmann plots (**Supplementary Figure 3**), the variance in differences increases as retinal vessel caliber increases for both venules and arterioles in our dataset, which we assume was resulted from the diversity of the dataset, which is constituted of images from different cameras. However, their ratios were more stable. This suggests when analyzing images across different cameras,

relevant measurements should be adjusted, for example, CRAE be adjusted by CRAE, or use the ratio values instead.

### Efficiency and Potential for Future Adoption

**Table 6** summarizes and compares existing retinal vessel measurement algorithms and software. RMHAS achieved sufficient reliability and efficiency in critical retinal vessel measurements. With 558,420 parameters, the algorithm required $<2$ s to complete all the segmentation and analysis when running images in batches on a server with one GeForce GTX TITAN GPU (Nvidia Inc., CA, USA) and an Intel Core i7-4790K CPU. The mean time cost for each task within the algorithm, as tested by analyzing 100 images, were as follows: image quality: 0.02 s; artery, vein, optic disc segmentation: 0.05 s; Standard zone measure: 0.17 s; vessel graph building: 0.51 s; graph plotting: 1 s.

RMHAS has several strengths. It is fast, fully automatic, interpretable, easily accessible, and provides a wide range of measurement parameters with orders. It can handle challenging images, including retinal images with DR, AMD, glaucoma, or images collected from the very young or elderly. Finally, the algorithm is compatible with images obtained from various fundus cameras with different image resolutions. RMHAS limitations include its measurement of retinal caliber value based on pixel units rather than micron measures due to unknown image magnification factors.

## CONCLUSION

RMHAS achieved good segmentation accuracy across datasets with diverse eye conditions and image resolutions. Compared with manual segmentation, RMHAS performed better at outlining small vessels than human graders, especially in challenging cases. The agreement and repeatability analysis supported the robustness of the algorithm. RMHAS was feasible for application in automated high throughput retinal vessel analysis and required minimal time. We intend to provide RMHAS as a public tool for the research community. The algorithm demo is publicly available (https://www.retinavessel.com/) for testing and analysis. For batch analysis in large quantities, please contact us.

## DATA AVAILABILITY STATEMENT

The raw data supporting the conclusions of this article will be made available by the authors, without undue reservation.

## AUTHOR CONTRIBUTIONS

MH conceptualized and designed the study and had full access to all data. DS and ZL did the deep learning modeling. DS did the literature search and wrote the first draft of the manuscript. DS, WW, and XS did the statistical analysis. ZT, WW, XZ, ZG, and MH reviewed and modified the manuscript. All authors commented on the manuscript.

## FUNDING

This work was supported by Fundamental Research Funds of the State Key Laboratory of Ophthalmology, National Natural Science Foundation of China (82171075), Science and Technology Program of Guangzhou, China (202002020049), and Project of Special Research on Cardiovascular Diseases (2020XXG007). MH receives support from the University of Melbourne Research Accelerator Program and the CERA Foundation. The Center for Eye Research Australia receives Operational Infrastructure Support from the Victorian State Government. The sponsor or funding organization had no role in the design or conduct of this research. The sponsor or funding organization had no role in the design, conduct, analysis, or reporting of this study. The funding sources did not participate in the design and conduct of the study, collection, management, analysis interpretation of the data, preparation, review, or approval of the manuscript, and decision to submit the manuscript for publication.

## SUPPLEMENTARY MATERIAL

The Supplementary Material for this article can be found online at: https://www.frontiersin.org/articles/10.3389/fcvm.2022.823436/full#supplementary-material

## REFERENCES

1. Murray CD. The Physiological Principle of Minimum Work. *Proc Natl Acad Sci U S A*. (1926) 12:207–14. doi: 10.1073/pnas.12.3.207
2. Ikram MK, Ong YT, Cheung CY, Wong TY. Retinal Vascular Caliber Measurements: Clinical Significance, Current Knowledge and Future Perspectives. *Ophthalmologica*. (2013) 229:125–36. doi: 10.1159/000342158
3. Newman A, Andrew N, Casson R. Review of the association between retinal microvascular characteristics and eye disease. *Clin Experiment Ophthalmol*. (2018) 46:531–52. doi: 10.1111/ceo.13119
4. Farrah TE, Dhillon B, Keane PA, Webb DJ, Dhaun N. The eye, the kidney, and cardiovascular disease: old concepts, better tools, and new horizons. *Kidney Int*. (2020) 98:323–42. doi: 10.1016/j.kint.2020.01.039
5. Kashani AH, Asanad S, Chan JW, Singer MB, Zhang J, Sharifi M, et al. Past, present and future role of retinal imaging in neurodegenerative disease. *Prog Retin Eye Res*. (2021) 83:100938. doi: 10.1016/j.preteyeres.2020.100938
6. Wong T. Computer-assisted measurement of retinal vessel diameters in the Beaver Dam Eye Study*1methodology, correlation between eyes, and effect of refractive errors. *Ophthalmology*. (2004) 111:1183–90. doi: 10.1016/j.ophtha.2003.09.039
7. Yim-lui Cheung C, Hsu W, Lee ML, Wang JJ, Mitchell P, Peter Lau Q, et al. A New Method to Measure Peripheral Retinal Vascular Caliber over an Extended Area. *Microcirculation*. (2010) 17:495–503. doi: 10.1111/j.1549-8719.2010.00048.x
8. Perez-Rovira A, MacGillivray T, Trucco E, Chin KS, Zutis K, Lupascu C, et al. VAMPIRE: Vessel assessment and measurement platform for images of the REtina. In: *2011 Annual International Conference of the IEEE Engineering in Medicine and Biology Society*. Boston, MA: IEEE (2011). p. 3391–4.

9. Fraz MM, Welikala RA, Rudnicka AR, Owen CG, Strachan DP, Barman SA, et al. Quantitative Analysis of Retinal Vessel Topology and size – An automated system for quantification of retinal vessels morphology. *Expert Syst Appl.* (2015) 42:7221–34. doi: 10.1016/j.eswa.2015.05.022
10. AlBadawi S, Fraz MM. Arterioles and venules classification in retinal images using fully convolutional deep neural network. In: Campilho A, Karray F, ter Haar Romeny B, editors. *Image Analysis and Recognition*. Cham: Springer International Publishing (2018). p. 659–68.
11. Mookiah MRK, Hogg S, MacGillivray TJ, Prathiba V, Pradeepa R, Mohan V, et al. A review of machine learning methods for retinal blood vessel segmentation and artery/vein classification. *Med Image Anal.* (2021) 68:101905. doi: 10.1016/j.media.2020.101905
12. Cheung CY, Xu D, Cheng CY, Sabanayagam C, Tham YC, Yu M, et al. A deep-learning system for the assessment of cardiovascular disease risk via the measurement of retinal-vessel calibre. *Nat Biomed Eng.* (2020) 5:498–508. doi: 10.1038/s41551-020-00626-4
13. Ng EYK, Acharya UR, Suri JS, Campilho A. *Image Analysis and Modeling in Ophthalmology*. CRC press (2014) p. 402.
14. Chua SYL, Thomas D, Allen N, Lotery A, Desai P, Patel P, et al. Cohort profile: design and methods in the eye and vision consortium of UK Biobank. *BMJ Open.* (2019) 9:e025077. doi: 10.1136/bmjopen-2018-025077
15. Li Z, Keel S, Liu C, He Y, Meng W, Scheetz J, et al. An Automated Grading System for Detection of Vision-Threatening Referable Diabetic Retinopathy on the Basis of Color Fundus Photographs. *Dia Care.* (2018) 41:2509–16. doi: 10.2337/dc18-0147
16. Hu Y, Niu Y, Wang D, Wang Y, Holden BA, He M. The association of longitudinal trend of fasting plasma glucose with retinal microvasculature in people without established diabetes. *Invest Ophthalmol Vis Sci.* (2015) 56:842–8. doi: 10.1167/iovs.14-15943
17. Ding X, Wang W, Scheetz J, He M. The Guangzhou Twin Eye Study: 2019 Update. *Twin Res Hum Genet.* (2019) 22:492–8. doi: 10.1017/thg.2019.118
18. Galdran A, Anjos A, Dolz J, Chakor H, Lombaert H, Ayed IB. The Little W-Net That Could: State-of-the-Art Retinal Vessel Segmentation with Minimalistic Models. *ArXiv*. 200901907 [Cs, Eess] (2020).
19. The STARE Project n.d. Available online at: http://cecas.clemson.edu/ahoover/stare/ (accessed December 1, 2020).
20. Estrada R, Tomasi C, Cabrera MT, Wallace DK, Freedman SF, Farsiu S. Exploratory Dijkstra forest based automatic vessel segmentation: applications in video indirect ophthalmoscopy (VIO). *Biomed Opt Express, BOE.* (2012) 3:327–39. doi: 10.1364/BOE.3.000327
21. Estrada R, Tomasi C, Cabrera MT, Wallace DK, Freedman SF, Farsiu S. Enhanced video indirect ophthalmoscopy (VIO) via robust mosaicing. *Biomed Opt Express, BOE.* (2011) 2:2871–87. doi: 10.1364/BOE.2.002871
22. Fraz MM, Remagnino P, Hoppe A, Uyyanonvara B, Rudnicka AR, Owen CG, et al. An Ensemble Classification-Based Approach Applied to Retinal Blood Vessel Segmentation. *IEEE Trans Biomed Eng.* (2012) 59:2538–48. doi: 10.1109/TBME.2012.2205687
23. Holm S, Russell G, Nourrit V, McLoughlin N, DR. HAGIS—a fundus image database for the automatic extraction of retinal surface vessels from diabetic patients. *J Med Imag.* (2017) 4:014503. doi: 10.1117/1.JMI.4.1.014503
24. Chalakkal RJ, Abdulla WH, Sinumol S. Comparative Analysis of University of Auckland Diabetic Retinopathy Database. In: *Proceedings of the 9th International Conference on Signal Processing Systems*. New York, NY, USA: Association for Computing Machinery (2017). p. 235–239.
25. Ding L, Kuriyan AE, Ramchandran RS, Wykoff CC, Sharma G. Weakly-Supervised Vessel Detection in Ultra-Widefield Fundus Photography Via Iterative Multi-Modal Registration and Learning. *IEEE Trans Med Imaging.* (2020) 40:2748–58. doi: 10.36227/techrxiv.12283736.v1
26. Hu Q, Abràmoff MD, Garvin MK. Automated separation of binary overlapping trees in low-contrast color retinal images. *Med Image Comput Comput Assist Interv.* (2013) 16:436–43. doi: 10.1007/978-3-642-40763-5_54
27. Budai A, Bock R, Maier A, Hornegger J, Michelson G. Robust Vessel Segmentation in Fundus Images. *Int J Biomed Imaging.* (2013) 2013:154860. doi: 10.1155/2013/154860
28. Estrada R, Tomasi C, Schmidler SC, Farsiu S. Tree Topology Estimation. *IEEE Trans Pattern Anal Mach Intell.* (2015) 37:1688–701. doi: 10.1109/TPAMI.2014.2382116
29. Estrada R, Allingham MJ, Mettu PS, Cousins SW, Tomasi C, Farsiu S. Retinal artery-vein classification via topology estimation. *IEEE Trans Med Imaging.* (2015) 34:2518–34. doi: 10.1109/TMI.2015.2443117
30. Abbasi-Sureshjani S, Smit-Ockeloen I, Zhang J, Ter Haar Romeny B. Biologically-Inspired Supervised Vasculature Segmentation in SLO Retinal Fundus Images. In: Kamel M, Campilho A, editors. *Image Analysis and Recognition*. Cham: Springer International Publishing (2015). p. 325–334. doi: 10.1007/978-3-319-20801-5_35
31. Zhang J, Dashtbozorg B, Bekkers E, Pluim JPW, Duits R, Romeny BM. Robust Retinal Vessel Segmentation via Locally Adaptive Derivative Frames in Orientation Scores. *IEEE Trans Med Imaging.* (2016) 35:2631–44. doi: 10.1109/TMI.2016.2587062
32. Orlando JI, Breda JB, Keer K, Blaschko MB, Blanco PJ, Bulant CA. *Towards a Glaucoma Risk Index Based on Simulated Hemodynamics from Fundus Images.* Medical Image Computing and Computer Assisted Intervention – MICCAI 2018. Cham: Springer (2018). p. 65–73.
33. Akram MU, Akbar S, Hassan T, Khawaja SG, Yasin U, Basit I. Data on fundus images for vessels segmentation, detection of hypertensive retinopathy, diabetic retinopathy and papilledema. *Data Brief.* (2020) 29:105282. doi: 10.1016/j.dib.2020.105282
34. Lowell J, Hunter A, Steel D, Basu A, Ryder R, Fletcher E, et al. Optic Nerve Head Segmentation. *IEEE Trans Med Imaging.* (2004) 23:256–64. doi: 10.1109/TMI.2003.823261
35. Carmona EJ, Rincón M, García-Feijoó J. Martínez-de-la-Casa JM. Identification of the optic nerve head with genetic algorithms. *Artif Intell Med.* (2008) 43:243–59. doi: 10.1016/j.artmed.2008.04.005
36. Sivaswamy J, Krishnadas SR, Joshi GD, Jain M, Tabish AUS. Drishti-GS: Retinal image dataset for optic nerve head (ONH) segmentation. In: *2014 IEEE 11th International Symposium on Biomedical Imaging (ISBI)*. IEEE (2014). p. 53–56.
37. Almazroa A, Alodhayb S, Osman E, Ramadan E, Hummadi M, Dlaim M, et al. Retinal fundus images for glaucoma analysis: the RIGA dataset. Medical Imaging 2018: Imaging Informatics for Healthcare, Research, and Applications. *Int Soc Opt Photon*. (2018) 10579:105790B. doi: 10.1117/12.2293584
38. Orlando JI, Fu H, Barbossa Breda J, van Keer K, Bathula DR, Diaz-Pinto A, et al. REFUGE Challenge: A unified framework for evaluating automated methods for glaucoma assessment from fundus photographs. *Med Image Anal.* (2020) 59:101570. doi: 10.1016/j.media.2019.101570
39. Bajwa MN, Singh GAP, Neumeier W, Malik MI, Dengel A, Ahmed S. G1020: A Benchmark Retinal Fundus Image Dataset for Computer-Aided Glaucoma Detection. *ArXiv*. 200609158 [Cs, Eess] (2020). doi: 10.1109/IJCNN48605.2020.9207664
40. Fu H, Li F, Orlando JI, Bogunovic H, Sun X, Liao J, et al. PALM: Pathologic myopia challenge. *IEEE Dataport*. (2019).
41. Fu H. *ADAM: Automatic Detection Challenge on Age-related Macular Degeneration* (2020).
42. Fu H, Wang B, Shen J, Cui S, Xu Y, Liu J, et al. Evaluation of Retinal Image Quality Assessment Networks in Different Color-spaces. *ArXiv*. 190705345 [Cs] (2019) 11764:48–56. doi: 10.1007/978-3-030-32239-7_6
43. Kingma DP, Ba J. Adam: A Method for Stochastic Optimization. *ArXiv*. 14126980 [Cs] (2017).
44. Knudtson MD, Lee KE, Hubbard LD, Wong TY, Klein R, Klein BEK. Revised formulas for summarizing retinal vessel diameters. *Curr Eye Res.* (2003) 27:143–9. doi: 10.1076/ceyr.27.3.143.16049
45. Al-Diri B, Hunter A, Steel D, Habib M, Hudaib T, Berry S. REVIEW - A reference data set for retinal vessel profiles. In: *2008 30th Annual International Conference of the IEEE Engineering in Medicine and Biology Society*. Vancouver, BC: IEEE (2008). p. 2262–2265. doi: 10.1109/IEMBS.2008.4649647
46. Koo TK, Li MY. A Guideline of Selecting and Reporting Intraclass Correlation Coefficients for Reliability Research. *J Chiropr Med.* (2016) 15:155–63. doi: 10.1016/j.jcm.2016.02.012
47. Reeb C, Kaandorp J, Jansson F, Puillandre N, Dubuisson JY, Cornette R, et al. Quantification of complex modular architecture in plants. *New Phytol.* (2018) 218:859–72. doi: 10.1111/nph.15045
48. Yip W, Tham YC, Hsu W, Lee ML, Klein R, Klein B, et al. Comparison of Common Retinal Vessel Caliber Measurement Software and a Conversion Algorithm. *Trans Vis Sci Tech.* (2016) 5:11. doi: 10.1167/tvst.5.5.11

49. Bennett AG, Rudnicka AR, Edgar DF. Improvements on Littmann's method of determining the size of retinal features by fundus photography. *Graefe's Arch Clin Exp Ophthalmol.* (1994) 232:361–7. doi: 10.1007/BF00175988
50. Iwase A, Sekine A, Suehiro J, Tanaka K, Kawasaki Y, Kawasaki R, et al. A New Method of Magnification Correction for Accurately Measuring Retinal Vessel Calibers From Fundus Photographs. *Invest Ophthalmol Vis Sci.* (2017) 58:1858–64. doi: 10.1167/iovs.16-21202

**Conflict of Interest:** WM was employed by Guangzhou Vision Tech Medical Technology Co., Ltd.

The remaining authors declare that the research was conducted in the absence of any commercial or financial relationships that could be construed as a potential conflict of interest.

**Publisher's Note:** All claims expressed in this article are solely those of the authors and do not necessarily represent those of their affiliated organizations, or those of the publisher, the editors and the reviewers. Any product that may be evaluated in this article, or claim that may be made by its manufacturer, is not guaranteed or endorsed by the publisher.

frontiers | Frontiers in Cardiovascular Medicine

MINI REVIEW
published: 16 May 2022
doi: 10.3389/fcvm.2022.885483

# Carotid Plaque Composition and the Importance of Non-Invasive in Imaging Stroke Prevention

*Martin Andreas Geiger[1]*, Ronald Luiz Gomes Flumignan[2], Marcone Lima Sobreira[3], Wagner Mauad Avelar[4], Carla Fingerhut[5], Sokrates Stein[1] and Ana Terezinha Guillaumon[1]*

[1] Division of Vascular Surgery, Department of Surgery, Universidade Estadual de Campinas—UNICAMP, São Paulo, Brazil, [2] Division of Vascular and Endovascular Surgery, Department of Surgery, Universidade Federal de São Paulo, São Paulo, Brazil, [3] Division of Vascular and Endovascular Surgery, Department of Surgery and Orthopedics, Botucatu Medical School, Universidade Estadual Paulista (UNESP), São Paulo, Brazil, [4] Department of Neurology, Universidade Estadual de Campinas—UNICAMP, São Paulo, Brazil, [5] Division of Radiology, Department of Anesthesiology and Radiology, Universidade Estadual de Campinas—UNICAMP, São Paulo, Brazil

Luminal stenosis has been the standard feature for the current management strategies in patients with atherosclerotic carotid disease. Histological and imaging studies show considerable differences between plaques with identical degrees of stenosis. They indicate that specific plaque characteristics like Intraplaque hemorrhage, Lipid Rich Necrotic Core, Plaque Inflammation, Thickness and Ulceration are responsible for the increased risk of ischemic events. Intraplaque hemorrhage is defined by the accumulation of blood components within the plaque, Lipid Rich Necrotic Core is composed of macrophages loaded with lipid, Plaque Inflammation is defined as the process of atherosclerosis itself and Plaque thickness and Ulceration are defined as morphological features. Advances in imaging methods like Magnetic Resonance Imaging, Ultrasound, Computed Tomography and Positron Emission Tomography have enabled a more detailed characterization of the plaque, and its vulnerability is linked to these characteristics, changing the management of these patients based only on the degree of plaque stenosis. Studies like Rotterdam, ARIC, PARISK, CAPIAS and BIOVASC were essential to evaluate and prove the relevance of these characteristics with cerebrovascular symptoms. A better approach for the prevention of stroke is needed. This review summarizes the more frequent carotid plaque features and the available validation from recent studies with the latest evidence.

**Keywords: ICA stenosis, ischemic stroke, vulnerable plaque biomarker, MRI, Atherosclerosis**

OPEN ACCESS

***Edited by:***
*Steven Rogers,*
*The University of Manchester,*
*United Kingdom*

***Reviewed by:***
*Karlheinz Peter,*
*Baker Heart and Diabetes*
*Institute, Australia*

****Correspondence:***
*Martin Andreas Geiger*
*m.geiger@hc.unicamp.br*

***Specialty section:***
*This article was submitted to*
*Cardiovascular Imaging,*
*a section of the journal*
*Frontiers in Cardiovascular Medicine*

***Received:*** *28 February 2022*
***Accepted:*** *27 April 2022*
***Published:*** *16 May 2022*

***Citation:***
*Geiger MA, Flumignan RLG, Sobreira ML, Avelar WM, Fingerhut C, Stein S and Guillaumon AT (2022) Carotid Plaque Composition and the Importance of Non-Invasive in Imaging Stroke Prevention. Front. Cardiovasc. Med. 9:885483. doi: 10.3389/fcvm.2022.885483*

## INTRODUCTION

Stroke is the second leading cause of death worldwide. More than 12 million people have a stroke annually, of which more than 6 million die as a result of the event (1–3). The atherosclerotic carotid disease accounts for 10–15% of stroke and transient ischemic attack (TIA) cases. It usually occurs at the carotid bifurcation and internal carotid artery (ICA) (1). Vessel stenosis is the main parameter for classifying and stratifying the disease and is adopted by the main guidelines to determine surgical intervention. However, recent evidence suggests that specific plaque features may be more directly associated with stroke than just stenosis. The study of the vessel and

plaque is the current target of several researchers. This change of focus reveals its importance for primary and secondary stroke prevention (4).

These observations were previously made in the coronary territory where non-contrast cardiac computed tomography is routinely performed for risk stratification in primary prevention, to quantify coronary artery calcification as an imaging test of subclinical atherosclerosis. The assessment of coronary inflammation represents, as in carotid disease, a new aspect in the assessment of coronary artery disease resulting in an improvement in the prediction, discrimination and reclassification of all causes and cardiac mortality. Analysis of plaque extent, plaque composition, and inflammation has the potential to establish a more accurate risk prediction compared to coronary calcium score assessed by non-contrast cardiac CT (5).

In the first part of this review, we recall the current features of carotid plaques vulnerability, the best imaging methods, and its characteristics for the assessment. In the second part, we discuss the predictive value of plaque imaging in primary and secondary prevention, linking plaque characteristics and their role in clinical decision-making.

# PLAQUE CHARACTERISTICS

## Intraplaque Hemorrhage

Intraplaque hemorrhage (IPH) is considered a major predictor of patient symptoms from carotid plaque (**Figures 1A,B**) (6). The atheroma neovascularization is immature (7). There is a difference observed between the neovessels in the external part of the media and the neovessels which reach the plaque (8). The development and maturation of normal neovascularisation seems to be impaired by a proteolytic environment within the plaque (9). IPH is the fundamental process for plaque growth in more advanced atherosclerotic plaque stages (10).

In a recent systematic review, the hazard ratio (HR) of 7.14 was the highest in the presence of IPH in recurrent Stroke/Transient Ischemic Attack (TIA) compared to other plaque characteristics such as lipid-rich necrotic core and fibrous cap rupture (11). In another systematic review focusing on stenosis <50% in patients with embolic stroke of undetermined cause, the prevalence of IPH in the ipsilateral carotid was 24.4% (95% CI 17.9 to 31.5) compared to 0.6% (95% CI 0.0 to 3.7) in the contralateral carotid (12).

Schindler *et al.* showed in a recent published meta-analysis that IPH increased the risk of future ipsilateral stroke in patients with symptomatic and asymptomatic carotid stenosis, with HRs of 10.2 and 7.9, respectively (13).

Magnetic resonance imaging (MRI) is the best imaging technique to atherosclerotic plaque characterization, specially IPH (**Figure 1B**) (14–16). Computed tomography (CT) can overestimate the disease in heavily calcified lesions, besides being difficult to differentiate between fibrous, lipid, and intraplaque hemorrhage (17).

## Fibrous Cap and Lipid-Rich Necrotic Core

The fibrous cap (FC) separates the Lipid Rich Necrotic Core (LRNC) from the vessel lumen (**Figures 1C,D**). It is composed of muscle cells, macrophages, foam cells, lymphocytes, collagen, and elastin (18). FC rupture exposes the necrotic core to blood resulting in cerebral microembolization (19).

In vulnerable plaques, it is observed that a thin FC enfolds a large LRNC containing mainly inflammatory cells and macrophages (20).

## Plaque Inflammation/ Neovascularisation

Inflammation is a pathogenic event characterized by several structural changes in the vessel wall. In this process, fundamental steps are observed like endothelial dysfunction, macrophage activation and migration, oxidative stress, lipid deposition, proliferation and migration of smooth muscle cells and formation of neovessels within the plaque. (7) Neovascularization increases the local flow of nutrients and O2 promoting plaque growth. The incomplete maturation of these neovessels associated with fragility promotes IPH leaving the plaque vulnerable and prone to rupture (21).

Contrast-enhanced ultrasound (CEUS) allows an objective analysis of atherosclerotic plaque inflammation (Additional File) (22). In the early phase, after contrast administration, the neovessels of the atherosclerotic plaque are filled with blood, and the intact microspheres amplify their echo. In the late phase of contrast injection, juxtaluminal black areas (JBA) can be observed and distinguished, which are very hypoechoic areas without a fibrous cap with fragments of lipid core in ruptured plaques with echogenicity lower than 25 gray-scale median (GSM) units (Additional File) (23).

Previous studies using either CEUS or dynamic contrast-enhanced magnetic resonance imaging have demonstrated associations between imaging measurements of neovessels and recent symptoms. Both methods are validated non-invasive techniques for *in vivo* imaging of neo-vessels (24, 25). Van den Oord *et al.* estimated the Cardiovascular risk of recruited patients by calculating the Prospective Cardiovascular Münster Heart Study (PROCAM) risk. Carotid CEUS was performed in these patients. Interestingly, CEUS changed the risk category in practically all asymptomatic patients previously classified by the traditional risk stratification model (26).

MRI has demonstrated its importance in the detailed characterization of the carotid plaque. Other imaging methods are being used to search for more careful definition. $^{18}$F-fluorodeoxyglucose (FDG) positron emission tomography (PET) may be an alternative technique to identify a plaque with inflammation (27). Tawakol *et al.* firstly found histological association of plaque inflammation with the degree of $^{18}$F-FDG uptake (28). The abundance of inflammatory cells is observed in the highly inflamed vulnerable plaque. FDG is a glucose analog taken up by inflammatory cells. A more significant accumulation of FDG is observed with higher metabolic activity (27). More recently, another commonly employed radiotracer, NaF, is being used due to its affinity to hydroxyapatite. More extensive calcium deposits can be easily observed with CT; however, micro-calcifications are not. NaF accumulates in areas of active micro-calcification within the atheroma. An interesting feature is that $^{18}$F-NaF uptake does not overlap with macrocalcifications as seen on CT (29).

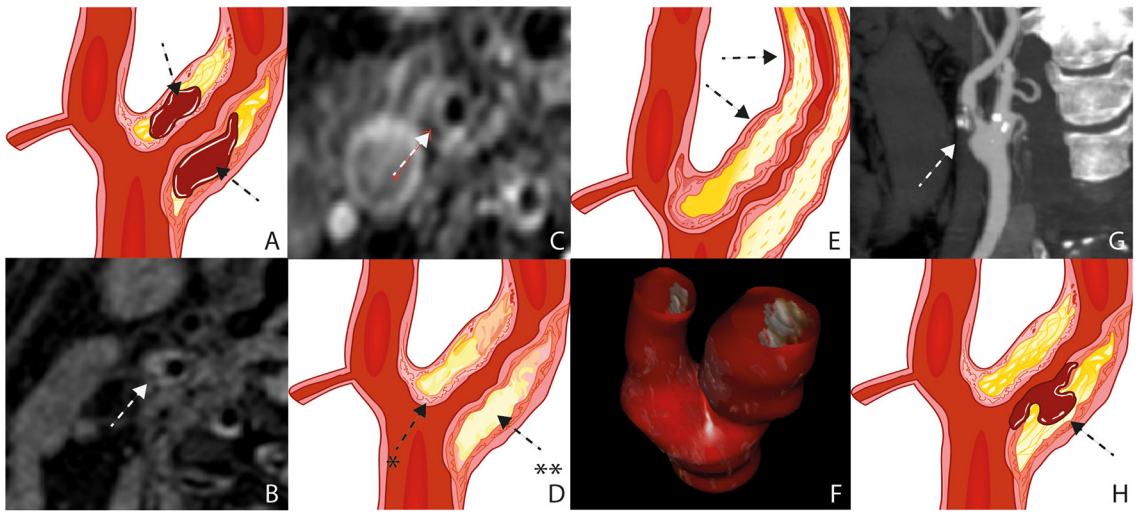


**FIGURE 1 |** Plaque Characteristics. Schematic figure illustrating intraplaque hemorrhage **(A)**, MRI on a 3 Tesla scanner **(B)**; white arrow), The axial T1 turbo spin-echo with fat saturation image post gadolinium shows a pronounced LRNC covered by an intact fibrous cap **(C)**; white arrow), Schematic figure illustrating a pronounced LRNC (**) covered by an intact fibrous cap (*) **(D)**, Schematic figure illustrating a pronounced bulky plaque **(E)**; black arrows), 3D ultrasound volume analysis **(F)**, surface morphology, image obtained by CT **(G)**, Schematic figure illustrating plaque rupture with an ulceration **(H)**; black arrow). LRNC, lipid-rich necrotic core; MRI, Magnetic Resonance Imaging; CT,Computed Tomography.

Skagen *et al.* demonstrated that $^{18}$F-FDG uptake on PET/CT was higher in patients with symptomatic compared with asymptomatic carotid artery plaques (30).

Fujimoto *et al.* in a recent publication demonstrated that 18F Sodium Fluoride ($^{18}$F-NaF) uptake was associated with the severity of ischemic vascular brain disease on MRI, suggesting its possible use in the risk classification of cerebrovascular disease (31).

## Carotid Plaque Thickness

The plaque thickness is a feature of plaque vulnerability being associated with the size and volume of the plaque (**Figure 1E**) (32). It is well quantifiable with ultrasound, CT, and MRI. Zhao X *et al.* observed that wall thickness was found to be a stronger feature when compared to stenosis for high risk carotid plaques, already observed and published by the same author in 2011 analyzing stenosis, percentage of wall volume (PWV) and mean wall thickness (33). The possible explanation is positive remodeling of the plaque. The outward expansion of the outer wall boundary would preserve the vessel lumen. In other words, wall thickness may be an important feature for screening of high-risk plaques composition (34).

Recently, Ball S. *et al.* published a study using a technology called tomographic ultrasound (tUS) (**Figure 1F**) (35). It consist of a three-dimensional (3D) ultrasound system with a spacial tracker (Piur, Wien, Austria) Multiplanar reconstructions are computed to produce 3D ultrasound volumes. It showed to be an accurate method with all the advantages of ultrasound.

## Carotid Plaque Surface (Ulceration)

High-risk carotid plaques are not only characterized by its compositional features but also by the irregularity of the plaque surface (36). Ulceration is defined as a discontinuous fibrous cap with an excavated necrotic core. (**Figures 1G,H**) (8) Jin Li et al. found a direct association between irregular plaque surface and carotid plaque features, such as LRNC, IPH, stenosis, and maximum wall thickness (37).

Homburg et al. demonstrated an association between plaque composition and volume with plaque ulceration and ischemic stroke patients independently of the degree of the carotid plaque stenosis (38).

IPH, apparently, increase inflammation resulting in irregular plaque surface. Hamada et al. validated plaque ulceration assessed by CEUS with histology analysis in patients undergoing carotid endarterectomy confirming CEUS's high sensitivity for identifying plaque ulceration and fibrous cap disruption (39).

# DISCUSSION

## Prediction of Primary Stroke

The occurrence of a carotid plaque rupture is independent of the degree of stenosis and the plaque features described above are related to (40).

In a recent meta-analysis of 64 studies enrolling 20,751 asymptomatic participants, the authors observed that the incidence of ipsilateral ischemic events was higher in patients with high-risk features than in those without high-risk features with a corresponding OR of 3.0. (12). In another meta-analysis of 8 studies, the presence of IPH at baseline was associated with a 6-fold higher risk of cerebrovascular events, with an annualized event rate of 17.7% compared with 2.43% in patients with no IPH (41). Schindler *et al.,* comparing the risk of stroke between patients with and without the presence of IPH on MRI, observed 5.4% event rates among patients with asymptomatic carotid

stenosis in those with IPH vs. 0.8% in those without IPH (13). These facts suggest that carotid IPH might be a fundamental biomarker of clinical ischemic events.

IPH is detected as a high signal intensity on T1-weighted imaging. In a study with 1,190 patients, carotid T1-high-intense plaque was at higher risk of a subsequent cerebrovascular ischemic event suggesting that carotid IPH might contribute to the risk stratification of a future ischemic event (42). Adding to that affirmative, Bos D et al., in a large population-based sample of asymptomatic individuals, associate IPH with new-onset stroke and cardiovascular disease (CVD), independent of other plaque characteristics (43). Patients with IPH are prone to develop two times more stroke or coronary heart disease (CHD) within 5 years. Their findings showed that even in asymptomatic individuals with low-grade stenosis, IPH is crucial for developing a first-ever stroke.

## Prediciton of Secondary Stroke

The majority of recurrences occur within 1 year and in the same anatomic region as the first stroke (44). Especially in patients with high-grade (70–99%) timely intervention can prevent recurrent ischemic stroke (45).

Two major trials, the European Carotid Surgery Trial (ECST) and the North American Symptomatic Carotid Endarterectomy Trial (NASCET), provided the vascular community in the early '90s with information regarding symptomatic patients. They showed that benefit from surgery was more significant in men than in women and in the elderly, and benefit decreased with time since the last symptoms. These observations were consistent across the 50% to 69%, and 70% to 99% stenosis groups and the two trials. These subgroup observations were sufficiently robust to guide the use of carotid endarterectomy (CEA) in routine clinical practice (46, 47).

Schindler A *et al.* showed an HRs of 10.2 for future ipsilateral stroke patients with symptomatic stenosis and 7.9 in patients with asymptomatic stenosis when IPH was characterized. In symptomatic patients, IPH demonstrated an increased risk of stroke at any degree of stenosis, even among patients with plaques $<$50% of stenosis (13).

With improved imaging methods, identifying patients with a higher risk of stroke may benefit the selection for CEA, allowing surgery to be indicated in patients with the highest benefit. Based on observed HRs on multivariable Cox regression in recently symptomatic patients with carotid stenosis, Kelly PJ *et al.* derived the SCAIL (symptomatic carotid atheroma inflammation lumen-stenosis) score by assigning points based on $^{18}$F-fluorodeoxyglucose ($^{18}$F-FDG) uptake and stenosis severity, further discussed (48).

## Latest Studies Result on Vulnerable Carotid Plaques

Current studies and research groups aim to establish a relation between plaque vulnerability biomarkers, showing that identifying vulnerable carotid plaques with MRI helps predict ischemic stroke (**Table 1**).

MRI currently provides the most proper imaging technique to specify lumen stenosis and features of plaque vulnerability, accurately assessing LRNC, FC, IPH, calcification, and plaque surface. This imaging technique has been used in almost every trial (49).

In the Rotterdam study, Van den Bouwhuijsen *et al.* showed a correlation between hypertension, current smoking, and presence of IPH and between hypercholesterolemia and LRNC in asymptomatic patients (50). They also showed a correlation of IPH and cortical infarcts. The size of IPH and not the presence of a lipid core was associated with symptomatic plaques in patients with recent ischemic event (51).

The ARIC Study also observed that carotid artery plaque burden and plaque eccentricity measures were directly associated with atherogenic cholesterol content. Their results suggested that measures of plaque burden could be use to control disease progression during the usage of therapies that lower atherogenic lipids. In contrast, LRNC could be an interesting imaging feature to follow (52).

Wasserman *et al.* previously already observed in the first study of associations between plaque lipid core and cardiovascular risk factors, the MESA study, a strong association with plasma cholesterol but not with hypertension, smoking, diabetes, or inflammatory factors, deducing that non-High-density lipoprotein cholesterol (non-HDL-C), which includes low-density lipoprotein (LDL) and Lipoproteins (Lp), may be of prime importance for the development of the clinically significant lipid-rich atherosclerotic plaque (53).

The MAGNETIC Study found no association between vulnerable plaque features and a history of hypertension, diabetes mellitus, hypercholesterolemia, and smoking. The authors speculate that optimizing medical therapy and a healthier lifestyle might have altered the association between plaque vulnerability and risk factors. A critical limit in this study concerns the absence of information on how long patients have been receiving treatment on atherosclerosis at the enrollment. This information could be used for a better understanding of medical therapy impact and lifestyle on plaque vulnerability (54).

The same rationale of a progression from vulnerable plaques to more stable plaques, both in carotid arteries, has been recently observed in the HeCES Study, published by Nuotio *et al.* In 10 years follow up, plaques related to ischemic event reveal more fibrous and non-inflammatory characteristics when compared to the initial features, due to lifestyle changes and effects of statins (55).

In the PARISK study, in patients with recent TIA or minor ischemic stroke, novel associations between (Lp)(a), concentrations and plaque features were identified. In women, elevated plasma Lp(a) levels were associated with higher prevalence of IPH and in men, elevated Lp(a) levels were associated with a higher degree of stenosis. The association between Lp(a) concentration and these vulnerable plaque characteristics supports the hypothesis that Lp(a) has a role in the process of atherosclerosis (56).

The CAPIAS prospective Study was a multicenter study with plaque imaging obtained within 10 days after symptom onset. The most frequent feature of ipsilateral carotid plaque was IPH. Ipsilateral LRNCs, a feature that is not part of the American Heart

**TABLE 1 |** Imaging studies analyzing carotid plaque components and morphology on cerebrovascular risk in symptomatic and asymptomatic patients.

| Study | Imaging method | Variable analyzed | Central conclusion |
|---|---|---|---|
| Rotterdam Study | MRI | IPH, LRNC | The size of IPH and not the presence of a lipid core was associated with symptomatic plaques in patients with recent ischemic event |
| ARIC Study | MRI | PT, LRNC | The presence of a lipid core was independently associated with incident CVD events when adjusted for traditional CVD risk factors and maximum CA wall thickness |
| Magnetic Study | MRI | IPH, FC, LRNC | Plaque composition in patients on treatment for asymptomatic carotid atherosclerosis shows no correlation between plaque vulnerability and the most well-controlled modifiable RF. Optimized therapy might have altered the association. |
| PARISK Study | MRI | IPH | The association between Lp(a) concentration and IPH supports the hypothesis that Lp(a) has a role in the process of atherosclerosis |
| CAPIAS Study | MRI | IPH, FC, LRNC | IPH, a ruptured FC, or the presence of a mural thrombus, was more frequent ipsilateral to ischemic stroke compared with that of the contralateral side |
| BIOVASC | PET/CT | $^{18}$F-FDG uptake | Plaque $^{18}$F-FDG uptake was associated with early recurrent stroke in patients with recently symptomatic carotid stenosis. |

*MRI, Magnetic Resonance Imaging; US, Ultrasound; IPH, intraplaque haemorrhage; LRNC, lipid-rich necrotic core; PT, plaque thickness; FC, fibrous cap; RF, risk factor; Lp, Lipoprotein; $^{18}$F-FDG, $^{18}$F-fluorodeoxyglucose.*

Association–lesion type definition, were larger in cryptogenic stroke compared with the reference group (57).

In a recently published cohort study by Kelly PJ *et al.*, the Biomarkers/Imaging Vulnerable Atherosclerosis in Symptomatic Carotid disease Study (BIOVASC), patients with carotid stenosis and recent stroke/(TIA) were followed up, being the primary outcome any non-procedural ipsilateral recurrent stroke within 90 days of the index stroke/TIA. One hundred and nine patients were recruited into BIOVASC and had positron emission tomography (PET)/CT completed. In patients with recently symptomatic carotid stenosis. Plaque $^{18}$F-FDG uptake was associated with early recurrent stroke in patients with recently symptomatic carotid stenosis. They showed for the first time that plaque FDG uptake independently predicts early stroke after PET. This finding suggests that higher plaque FDG uptake is a marker of vulnerable carotid plaque leading to stroke recurrence and not a secondary consequence of recurrent brain infarction (58). These results led to a novel score called SCAIL Score.

## Symptomatic Carotid Atheroma Inflammation Lumen Stenosis Score (SCAIL)

This recently published model for estimating the risk of recurrent ischemic stroke included $^{18}$F-FDG standardized uptake values on PET-CT as a parameter for plaque inflammation. (48) Uptake of radiolabeled $^{18}$F-FDG on PET is a validated marker for plaque metabolism caused by inflammation and is associated with markers of plaque instability and late clinical events (59).

This model categorized $^{18}$F-FDG uptake and stenosis. On multivariable analysis, the SCAIL score independently predicted recurrent stroke after PET imaging, in addition to its association with all recurrent stroke events before or after PET. This suggests that early $^{18}$F-FDG-PET after hospital presentation may have prognostic utility to identify high-risk patients with carotid stenosis. It was shown for the first time that incorporating information relating to plaque inflammation-related metabolism and lumen stenosis in a single measure identifies patients at the highest risk of early recurrent stroke.

# PERSPECTIVES

The big challenge remains in defining, among the many plaque features, those that are pivotal for the optimized treatment. Big imaging data acquisition associated with artificial intelligence analysis is leading this field of research to a higher level.

The development of a score system based on imaging features of plaque vulnerability may provide clinicians with a better tool to approach the disease.

# AUTHOR CONTRIBUTIONS

MG and RF contributed to the conception and design of the review. MG, RF, MS, and CF wrote the first draft of the manuscript. MG, RF, MS, WA, CF, SS, and AG wrote sections of the manuscript. All authors contributed to manuscript revision, read, and approved the submitted version.

# SUPPLEMENTARY MATERIAL

The Supplementary Material for this article can be found online at: https://www.frontiersin.org/articles/10.3389/fcvm.2022.885483/full#supplementary-material

# REFERENCES

1. Aboyans V, Ricco JB, Bartelink MLEL, Björck M, Brodmann M, Cohnert T, et al. 2017 ESC guidelines on the diagnosis and treatment of peripheral arterial diseases, in collaboration with the European Society for Vascular Surgery (ESVS). *Eur Heart J*. (2018) 39:763–816. doi: 10.1093/eurheartj/ehx095
2. Eliasziw M, Rankin RN, Fox AJ, Haynes RB, Barnett HJM. Accuracy and prognostic consequences of ultrasonography in identifying severe

carotid artery stenosis. *Stroke.* (1995) 26:1747–52. doi: 10.1161/01.STR.26.10.1747
3. Flumignan CDQ, Flumignan RLG, Navarro TP. Extracranial carotid stenosis: evidence based review. *Rev Col Bras Cir.* (2017) 44:293–301. doi: 10.1590/0100-69912017003012
4. Saba L, Saam T, Jäger HR, Yuan C, Hatsukami TS, Saloner D, et al. Imaging biomarkers of vulnerable carotid plaques for stroke risk prediction and their potential clinical implications. *Lancet Neurol.* (2019) 18:559–72. doi: 10.1016/S1474-4422(19)30035-3
5. Mahabadi AA, Rassaf T. Imaging of coronary inflammation for cardiovascular risk prediction. *Lancet.* (2018) 392:894–6. doi: 10.1016/S0140-6736(18)31716-1
6. Kerwin WS, Miller Z, Yuan C. Imaging of the high-risk carotid plaque: magnetic resonance imaging. *Semin Vasc Surg.* (2017) 30:54–61. doi: 10.1053/j.semvascsurg.2017.04.009
7. Michel JB, Martin-Ventura JL, Nicoletti A, Ho-Tin-Noé B. Pathology of human plaque vulnerability: Mechanisms and consequences of intraplaque haemorrhages. *Atherosclerosis.* (2014) 234:311–9. doi: 10.1016/j.atherosclerosis.2014.03.020
8. Kolodgie FD, Yahagi K, Mori H, Romero ME, Trout HH, Finn AV, et al. High-risk carotid plaque: lessons learned from histopathology. *Semin Vasc Surg.* (2017) 30:31–43. doi: 10.1053/j.semvascsurg.2017.04.008
9. Le Dall J, Ho-Tin-Noe B, Louedec L, Meilhac O, Roncal C, Carmeliet P, et al. Immaturity of microvessels in haemorrhagic plaques is associated with proteolytic degradation of angiogenic factors. *Cardiovasc Res.* (2010) 85:184–93. doi: 10.1093/cvr/cvp253
10. Dilba K, van Dijk AC, Crombag GAJC, van der Steen AFW, Daemen MJ, Koudstaal PJ, et al. Association between intraplaque hemorrhage and vascular remodeling in carotid arteries: the Plaque at RISK (PARISK) study. *Cerebrovasc Dis.* (2021) 50:94–9. doi: 10.1159/000511935
11. Deng F, Mu C, Yang L, Li H, Xiang X, Li K, et al. Carotid plaque magnetic resonance imaging and recurrent stroke risk: a systematic review and meta-analysis. *Medicine (Baltimore).* (2020) 99:e19377. doi: 10.1097/MD.0000000000019377
12. Kamtchum-Tatuene J, Wilman A, Saqqur M, Shuaib A, Jickling GC. Carotid plaque with high-risk features in embolic stroke of undetermined source: systematic review and meta-analysis. *Stroke.* (2020) 51:311–4. doi: 10.1161/STROKEAHA.119.027272
13. Schindler A, Schinner R, Altaf N, Hosseini AA, Simpson RJ, Esposito-Bauer L, et al. Prediction of stroke risk by detection of hemorrhage in carotid plaques. *JACC Cardiovasc Imaging.* (2020) 13:395–406. doi: 10.1016/j.jcmg.2019.03.028
14. McNally JS, Kim SE, Mendes J, Hadley JR, Sakata A, De Havenon AH, et al. Magnetic resonance imaging detection of intraplaque hemorrhage. *Magn Reson Insights.* (2017) 10:1178623X1769415. doi: 10.1177/1178623X17694150
15. Altaf N, Daniels L, Morgan PS, Auer D, MacSweeney ST, Moody AR, et al. Detection of intraplaque hemorrhage by magnetic resonance imaging in symptomatic patients with mild to moderate carotid stenosis predicts recurrent neurological events. *J Vasc Surg.* (2008) 47:337–42. doi: 10.1016/j.jvs.2007.09.064
16. Qiao Y, Etesami M, Malhotra S, Astor BC, Virmani R, Kolodgie FD, et al. Identification of intraplaque hemorrhage on MR angiography images: a comparison of contrast-enhanced mask and time-of-flight techniques. *Am J Neuroradiol.* (2011) 32:454–9. doi: 10.3174/ajnr.A2320
17. Boodt N, Compagne KCJ, Dutra BG, Samuels N, Tolhuisen ML, Alves HCBR, et al. Stroke etiology and thrombus computed tomography characteristics in patients with acute ischemic stroke: a MR CLEAN registry substudy. *Stroke.* (2020) 51:1727–35. doi: 10.1161/STROKEAHA.119.027749
18. Daghem M, Bing R, Fayad ZA, Dweck MR. Noninvasive imaging to assess atherosclerotic plaque composition and disease activity. *JACC Cardiovasc Imaging.* (2020) 13:1055–68. doi: 10.1016/j.jcmg.2019.03.033
19. Shi X, Han Y, Li M, Yin Q, Liu R, Wang F, et al. Superficial calcification with rotund shape is associated with carotid plaque rupture: an optical coherence tomography study. *Front Neurol.* (2020) 11:563334. doi: 10.3389/fneur.2020.563334
20. Kolodgie FD, Burke AP, Farb A, Gold HK, Yuan J, Narula J. et al. The thin-cap fibroatheroma: a type of vulnerable plaque: the major precursor lesion to acute coronary syndromes. *Curr Opin Cardiol.* (2001) 16:285–92. doi: 10.1097/00001573-200109000-00006
21. Hjelmgren O, Johansson L, Prahl U, Schmidt C, Fredén-Lindqvist J, Bergström GML, et al. study of plaque vascularization and inflammation using quantitative contrast-enhanced US and PET/CT. *Eur J Radiol.* (2014) 83:1184–9. doi: 10.1016/j.ejrad.2014.03.021
22. Fedak A, Chrzan R, Chukwu O, Urbanik A. Ultrasound methods of imaging atherosclerotic plaque in carotid arteries: examinations using contrast agents. *J Ultrason.* (2020) 20:191–200. doi: 10.15557/JoU.2020.0032
23. Fedak A, Ciuk K, Urbanik A. Ultrasonography of vulnerable atherosclerotic plaque in the carotid arteries: B-mode imaging. *J Ultrason.* (2020) 20:e135–45. doi: 10.15557/JoU.2020.0022
24. Moguillansky D, Leng X, Carson A, Lavery L, Schwartz A, Chen X, et al. Quantification of plaque neovascularization using contrast ultrasound: a histologic validation. *Eur Heart J.* (2011) 32:646–53. doi: 10.1093/eurheartj/ehq197
25. Kerwin W, Hooker A, Spilker M, Vicini P, Ferguson M, Hatsukami T, et al. Quantitative magnetic resonance imaging analysis of neovasculature volume in carotid atherosclerotic plaque. *Circulation.* (2003) 107:851–6. doi: 10.1161/01.CIR.0000048145.52309.31
26. van den Oord SCH. ten Kate GL, Sijbrands EJG, van der Steen AFW, Schinkel AFL. Effect of carotid plaque screening using contrast-enhanced ultrasound on cardiovascular risk stratification. *Am J Cardiol.* (2013) 111:754–9. doi: 10.1016/j.amjcard.2012.11.033
27. Saito H, Kuroda S, Hirata K, Magota K, Shiga T, Tamaki N, et al. Validity of dual MRI and $^{18}$ F-FDG PET imaging in predicting vulnerable and inflamed carotid plaque. *Cerebrovasc Dis.* (2013) 35:370–7. doi: 10.1159/000348846
28. Tawakol A, Migrino RQ, Bashian GG, Bedri S, Vermylen D, Cury RC, et al. *In Vivo* 18F-fluorodeoxyglucose positron emission tomography imaging provides a noninvasive measure of carotid plaque inflammation in patients. *J Am Coll Cardiol.* (2006) 48:1818–24. doi: 10.1016/j.jacc.2006.05.076
29. Derlin T, Richter U, Bannas P, Begemann P, Buchert R, Mester J, et al. Feasibility of $^{18}$ F-Sodium Fluoride PET/CT for imaging of atherosclerotic plaque. *J Nucl Med.* (2010) 51:862–5. doi: 10.2967/jnumed.110.076471
30. Skagen K, Johnsrud K, Evensen K, Scott H, Krohg-Sørensen K, Reier-Nilsen F, et al. Carotid plaque inflammation assessed with $^{18}$ F-FDG PET/CT is higher in symptomatic compared with asymptomatic patients. *Int J Stroke.* (2015) 10:730–6. doi: 10.1111/ijs.12430
31. Fujimoto K, Norikane T, Yamamoto Y, Takami Y, Mitamura K, Okada M, et al. Association between carotid 18F-NaF and 18F-FDG uptake on PET/CT with ischemic vascular brain disease on MRI in patients with carotid artery disease. *Ann Nucl Med.* (2019) 33:907–15. doi: 10.1007/s12149-019-01403-3
32. Tardif JC, Lesage F, Harel F, Romeo P, Pressacco J. Imaging biomarkers in atherosclerosis trials. *Circ Cardiovasc Imaging.* (2011) 4:319–33. doi: 10.1161/CIRCIMAGING.110.962001
33. Zhao X, Underhill HR, Zhao Q, Cai J, Li F, Oikawa M. et al. Discriminating carotid atherosclerotic lesion severity by luminal stenosis and plaque burden: a comparison utilizing high-resolution magnetic resonance imaging at 30 tesla. *Stroke.* (2011) 42:347–53. doi: 10.1161/STROKEAHA.110.597328
34. Glagov S, Weisenberg E, Zarins CK, Stankunavicius R, Kolettis GJ. Compensatory enlargement of human atherosclerotic coronary arteries. *N Engl J Med.* (1987) 316:1371–5. doi: 10.1056/NEJM198705283162204
35. Ball S, Rogers S, Kanesalingam K, Taylor R, Katsogridakis E, McCollum C. Carotid plaque volume in patients undergoing carotid endarterectomy. *Br J Surg.* (2018) 105:262–9. doi: 10.1002/bjs.10670
36. Rafailidis V, Chryssogonidis I, Tegos T, Kouskouras K, Charitanti-Kouridou A. Imaging of the ulcerated carotid atherosclerotic plaque: a review of the literature. *Insights Imaging.* (2017) 8:213–25. doi: 10.1007/s13244-017-0543-8
37. Li J, Li D, Yang D, Hang H, Wu Y, Yao R, et al. Irregularity of carotid plaque surface predicts subsequent vascular event: a MRI study. *J Magn Reson Imaging.* (2020) 52:185–94. doi: 10.1002/jmri.27038
38. Homburg PJ, Rozie S, van Gils MJ, van den Bouwhuijsen QJA, Niessen WJ, Dippel DWJ, et al. Association between carotid artery plaque ulceration and plaque composition evaluated with multidetector CT angiography. *Stroke.* (2011) 42:367–72. doi: 10.1161/STROKEAHA.110.597369
39. Hamada O, Sakata N, Ogata T, Shimada H, Inoue T. Contrast-enhanced ultrasonography for detecting histological carotid plaque rupture: quantitative analysis of ulcer. *Int J Stroke.* (2016) 11:791–8. doi: 10.1177/1747493016641964

40. Bos D, van Dam-Nolen DHK, Gupta A, Saba L, Saloner D, Wasserman BA, et al. Advances in multimodality carotid plaque imaging: *AJR* expert panel narrative review. *Am J Roentgenol.* (2021) 217:16–26. doi: 10.2214/AJR.20.24869
41. Saam T, Hetterich H, Hoffmann V, Yuan C, Dichgans M, Poppert H, et al. Meta-Analysis and systematic review of the predictive value of carotid plaque hemorrhage on cerebrovascular events by magnetic resonance imaging. *J Am Coll Cardiol.* (2013) 62:1081–91. doi: 10.1016/j.jacc.2013.06.015
42. Kurosaki Y, Yoshida K, Fukuda H, Handa A, Chin M, Yamagata S. Asymptomatic carotid T1-high-intense plaque as a risk factor for a subsequent cerebrovascular ischemic event. *Cerebrovasc Dis.* (2017) 43:250–6. doi: 10.1159/000455973
43. Bos D, Arshi B, van den Bouwhuijsen QJA, Ikram MK, Selwaness M, Vernooij MW, et al. Atherosclerotic carotid plaque composition and incident stroke and coronary events. *J Am Coll Cardiol.* (2021) 77:1426–35. doi: 10.1016/j.jacc.2021.01.038
44. Sacco RL, Wolf PA, Kannel WB, McNamara PM. Survival and recurrence following stroke. the framingham study. *Stroke.* (1982) 13:290–5. doi: 10.1161/01.STR.13.3.290
45. Orrapin S, Rerkasem K. Carotid endarterectomy for symptomatic carotid stenosis. *Cochrane Database Syst Rev*. (2017) 2017:CD001081. doi: 10.1002/14651858.CD001081.pub3
46. Randomised trial of endarterectomy for recently symptomatic carotid stenosis: final results of the MRC European Carotid Surgery Trial (ECST). *Lancet Lond Engl.* (1998) 351:1379–87. doi: 10.1016/S0140-6736(97)09292-1
47. Paciaroni M, Eliasziw M, Kappelle LJ, Finan JW, Ferguson GG, Barnett HJ. Medical complications associated with carotid endarterectomy. North American Symptomatic Carotid Endarterectomy Trial (NASCET). *Stroke.* (1999) 30:1759–63. doi: 10.1161/01.STR.30.9.1759
48. Kelly PJ, Camps-Renom P, Giannotti N, Martí-Fàbregas J, McNulty JP, Baron JC, et al. A risk score including carotid plaque inflammation and stenosis severity improves identification of recurrent. *Stroke.* (2020) 51:838–45. doi: 10.1161/STROKEAHA.119.027268
49. Porambo ME, DeMarco JK, MR. imaging of vulnerable carotid plaque. *Cardiovasc Diagn Ther.* (2020) 10:1019–31. doi: 10.21037/cdt.2020.03.12
50. van den Bouwhuijsen QJA, Vernooij MW, Verhaaren BFJ, Vrooman HA, Niessen WJ, Krestin GP, et al. Carotid plaque morphology and ischemic vascular brain disease on MRI. *Am J Neuroradiol.* (2017) 38:1776–82. doi: 10.3174/ajnr.A5288
51. Ikram MA, van der Lugt A, Niessen WJ, Koudstaal PJ, Krestin GP, Hofman A, et al. The Rotterdam Scan Study: design update 2016 and main findings. *Eur J Epidemiol.* (2015) 30:1299–315. doi: 10.1007/s10654-015-0105-7
52. Virani SS, Catellier DJ, Pompeii LA, Nambi V, Hoogeveen RC, Wasserman BA, et al. Relation of cholesterol and lipoprotein parameters with carotid artery plaque characteristics: the Atherosclerosis Risk in Communities (ARIC) carotid MRI study. *Atherosclerosis.* (2011) 219:596–602. doi: 10.1016/j.atherosclerosis.2011.08.001
53. Wasserman BA, Sharrett AR, Lai S, Gomes AS, Cushman M, Folsom AR, et al. Risk factor associations with the presence of a lipid core in carotid plaque of asymptomatic individuals using high-resolution MRI: the Multi-Ethnic Study of Atherosclerosis (MESA). *Stroke.* (2008) 39:329–35. doi: 10.1161/STROKEAHA.107.498634
54. Catalano O, Bendotti G, Mori A, De Salvo M, Falconi M, Aloi TL, et al. Evolving determinants of carotid atherosclerosis vulnerability in asymptomatic patients from the MAGNETIC observational study. *Sci Rep.* (2021) 11:2327. doi: 10.1038/s41598-021-81247-y
55. Nuotio K, Ijäs P, Heikkilä HM, Koskinen SM, Saksi J, Vikatmaa P, et al. Morphology and histology of silent and symptom-causing atherosclerotic carotid plaques – rationale and design of the Helsinki Carotid Endarterectomy Study 2 (the HeCES2). *Ann Med.* (2018) 50:501–10. doi: 10.1080/07853890.2018.1494851
56. van Dam-Nolen DHK, van Dijk AC, Crombag GAJC, Lucci C, Kooi ME, Hendrikse J, et al. Lipoprotein(a) levels and atherosclerotic plaque characteristics in the carotid artery: the Plaque at RISK (PARISK) study. *Atherosclerosis.* (2021) 329:22–9. doi: 10.1016/j.atherosclerosis.2021.06.004
57. Kopczak A, Schindler A, Bayer-Karpinska A, Koch ML, Sepp D, Zeller J, et al. Complicated carotid artery plaques as a cause of cryptogenic stroke. *J Am Coll Cardiol.* (2020) 76:2212–22. doi: 10.1016/j.jacc.2020.09.532
58. Kelly PJ, Camps-Renom P, Giannotti N, Martí-Fàbregas J, Murphy S, McNulty J, et al. Carotid plaque inflammation imaged by $^{18}$ F-Fluorodeoxyglucose positron emission tomography and risk of early recurrent stroke. *Stroke.* (2019) 50:1766–73. doi: 10.1161/STROKEAHA.119.025422
59. Masteling MG, Zeebregts CJ, Tio RA, Breek JC, Tietge UJF, de Boer JF, et al. High-resolution imaging of human atherosclerotic carotid plaques with micro18F-FDG PET scanning exploring plaque vulnerability. *J Nucl Cardiol.* (2011) 18:1066–75. doi: 10.1007/s12350-011-9460-2


**Conflict of Interest:** The authors declare that the research was conducted in the absence of any commercial or financial relationships that could be construed as a potential conflict of interest.

**Publisher's Note:** All claims expressed in this article are solely those of the authors and do not necessarily represent those of their affiliated organizations, or those of the publisher, the editors and the reviewers. Any product that may be evaluated in this article, or claim that may be made by its manufacturer, is not guaranteed or endorsed by the publisher.

frontiers | Frontiers in Cardiovascular Medicine

TYPE Original Research
PUBLISHED 12 September 2022
DOI 10.3389/fcvm.2022.913707



OPEN ACCESS

EDITED BY
Luca Saba,
Azienda Ospedaliero-Universitaria Cagliari, Italy

REVIEWED BY
Su-Zhen Dong,
Shanghai Jiao Tong University, China
Gabriele Bonanno,
Siemens Healthineers and University of Bern, Switzerland

*CORRESPONDENCE
Yining Wang
wangyining@pumch.cn

†These authors have contributed equally to this work and share first authorship

SPECIALTY SECTION
This article was submitted to Cardiovascular Imaging, a section of the journal Frontiers in Cardiovascular Medicine

RECEIVED 06 April 2022
ACCEPTED 19 August 2022
PUBLISHED 12 September 2022

CITATION
Lin L, Liu P, Sun G, Wang J, Liang D, Zheng H, Jin Z and Wang Y (2022) Bi-ventricular assessment with cardiovascular magnetic resonance at 5 Tesla: A pilot study.
*Front. Cardiovasc. Med.* 9:913707.
doi: 10.3389/fcvm.2022.913707



# Bi-ventricular assessment with cardiovascular magnetic resonance at 5 Tesla: A pilot study

Lu Lin[1†], Peijun Liu[1†], Gan Sun[2], Jian Wang[1], Dong Liang[3], Hairong Zheng[3], Zhengyu Jin[1] and Yining Wang[1*]

[1]State Key Laboratory of Complex Severe and Rare Diseases, Department of Radiology, Peking Union Medical College Hospital, Chinese Academy of Medical Sciences and Peking Union Medical College, Beijing, China, [2]State Key Laboratory of Complex Severe and Rare Diseases, Department of Medical Science Research Center, Peking Union Medical College Hospital, Chinese Academy of Medical Sciences and Peking Union Medical College, Beijing, China, [3]Lauterbur Research Center for Biomedical Imaging, Shenzhen Institute of Advanced Technology, China Academy of Sciences, Shenzhen, China

**Background:** Cardiovascular magnetic resonance (CMR) imaging at ultra-high fields (UHF) such as 7T has encountered many challenges such as faster $T_2^*$ relaxation, stronger $B_0$ and $B_{1+}$ field inhomogeneities and additional safety concerns due to increased specific absorption rate (SAR) and peripheral nervous stimulation (PNS). Recently, a new line of 5T whole body MRI system has become available, and this study aims at evaluating the performance and benefits of this new UHF system for CMR imaging.

**Methods:** Gradient echo (GRE) CINE imaging was performed on healthy volunteers at both 5 and 3T, and was compared to balanced steady-state-free-procession (bSSFP) CINE imaging at 3T as reference. Higher spatial resolution GRE CINE scans were additionally performed at 5T. All scans at both fields were performed with ECG-gating and breath-holding. Image quality was blindly evaluated by two radiologists, and the cardiac functional parameters (e.g., EDV/ESV/mass/EF) of the left and right ventricles were measured for statistical analyses using the Wilcoxon signed-rank test and Bland-Altman analysis.

**Results:** Compared to 3T GRE CINE imaging, 5T GRE CINE imaging achieved comparable or improved image quality with significantly superior SNR and CNR, and it has also demonstrated excellent capability for high resolution ($1.0 \times 1.0 \times 6.0\ mm^3$) imaging. Functional assessments from 5T GRE CINE images were highly similar with the 3T bSSFP CINE reference.

**Conclusions:** This pilot study has presented the initial evaluation of CMR CINE imaging at 5T UHF, which yielded superior image quality and accurate functional quantification when compared to 3T counterparts. Along with reliable ECG gating, the new 5T UHF system has the potential to achieve well-balanced performance for CMR applications.

KEYWORDS

**5T, UHF, cardiac MR, cine, ventricular function**

# Introduction

As one of the frequently employed techniques in cardiac magnetic resonance imaging (CMR), cardiac CINE imaging enables accurate measurements of heart motion in a full cardiac cycle (1–4). Because CMR CINE imaging enables visualization and measurement of the periodic beating of the cardiac chambers and ventricular walls, it is routinely used for cardiac functional analysis (5, 6), such as chamber volume, myocardium muscle mass and blood ejection fraction (EF). Typically, clinical CINE images are collected either using 2D balanced steady-state-free-precession (bSSFP) or 2D spoiled gradient echo (GRE) sequences (7, 8).

To date, the majority of clinical CMR scans are performed at 1.5 and 3.0T. The studies to perform CMR at ultra-high fields (UHF), such as 7T, have been relatively limited (9–13). Generally speaking, UHF offers advantages of higher signal-to-noise ratio (SNR) and gradient performance for improved imaging workflow and quality (14). While such benefits also apply to CMR, CMR at UHF encounters many challenges that combinedly outweigh those benefits (15). The practical challenges include the shorter $T_2/T_2^*$ relaxation times, stronger $B_0$ and $B_{1+}$ inhomogeneities, higher specific absorption rate (SAR) of the radio frequency (RF) energy and stronger interference to the electrocardiogram for reliable cardiac gating, as well as the more stringent safety screening criteria (16, 17). Currently, CMR at UHF (≥7T) is at best considered as feasible or comparable to the 3T CMR (9, 13, 18).

Recently, a new 5T UHF MRI system was introduced for whole body imaging (19). At the midway between 3 and 7T, the field strength of 5T may have the potential to achieve a better balance between CMR performance/quality and those aforementioned challenges associated with UHF. In this work, we aimed to evaluate, for the first time, the feasibility and performance of CMR at the 5T whole body system. Specifically, we analyzed and compared CMR CINE results from 5T to those from 3T, both qualitatively and quantitatively.

Abbreviations: ARVD, arrhythmogenic right ventricular dysplasia; bSSFP, balanced steady state free precession; CMR, cardiac magnetic resonance; CINE, cinematic imaging; CNR/SNR, contrast/signal-to-noise ration; ECG, electrocardiogram; EDV, end diastolic volume; EF, ejection fraction; ESV, end-systolic volume; FOV, field-of-view; GRE, gradient echo; LV/RV, left/right ventricle; MHD, magneto-hydrodynamic; RF, radiofrequency; ROI, region of interest; SAR, specific absorption rate; SAX, stack of short axis; STD, standard deviation; UHF, ultra-high fields.

# Materials and methods

## Subjects

Seventeen healthy adult volunteers (12 males and 5 females, age range 23–54) were recruited to participate in this pilot study with approval from the local ethics committee at Peking Union Medical College Hospital. All subjects passed the MRI safety screening with CMR-specific exclusion criteria, which strictly excluded candidates with prior or current cardiovascular diseases, severe arrhythmias, claustrophobia, metallic implants and tattoos, etc. All subjects provided written consents before undergoing CMR scans at both 3 (uMR790, United Imaging Healthcare, Shanghai, China) and 5T (uMR Jupiter, United Imaging Healthcare, Shanghai, China). Each volunteer underwent all MRI scans within the same day. The scanning order between 5T and 3T was randomized for each subject, with 7 subjects being scanned at 5T first.

## Experimental setups

The whole body 5T scanner was equipped with a bore size of 60 cm and a gradient system with 120 mT/m maximum amplitude and 200 T/m/s slew rate. For the RF system, an 8-channel loop array volumetric coil (19, 20) was used for transmission, and a 24-channel flexible body coil plus the upper portion of a 48-channel spine coil were used for reception during CMR scans. For $B_{1+}$ inhomogeneity control within the field-of-view (FOV) of body scans, the complex $B_{1+}$ map of each transmit channel was first obtained with a calibration scan and was then used to adjust the amplitude and phase of the respective transmit channel *via* parallel transmission techniques (21). Moreover, five 2nd order and one 3rd order shim coils were equipped for active $B_0$ field shimming.

The 3T scanner has gradient system specifications of 100 mT/m maximum amplitude and 200 mT/m/ms slew rate, and the RF system was comprised of a dual-channel volumetric coil transmission coil and a 24-channel CMR-dedicated coil plus a portion of the spinal coil for signal reception. For $B_0$ shimming, the volumetric shimming mode for cardiac scans was used.

For all CINE scans at both fields, cardiac gating was performed using routine ECG with the 4-electrode placement scheme, the typical signals of which are shown in Figure 1.

## Imaging parameters

For 5T CMR scans, 2D GRE CINE images with a spatial resolution of 1.6 × 1.6 × 8.0 $mm^3$ were acquired with the following parameters: TE/TR = 2.84/5.55 ms, flip angle (FA) = 10°, field of view (FOV) = 360 × 280∼320 $mm^2$, matrix

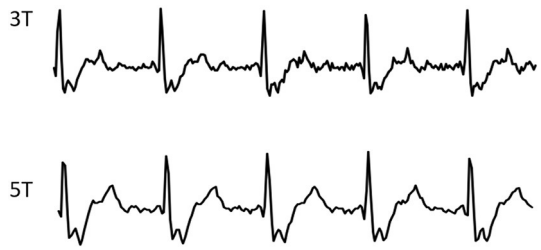


FIGURE 1
Typical ECG wave forms from one volunteer, recorded during CMR CINE scans at 3 and 5T respectively.

size = 224 × 174∼199, readout bandwidth = 300 Hz/px, 25 phases per cardiac cycle, and two-fold parallel imaging for acceleration, leading to a breath-hold duration of ∼11 s per slice. Additionally, high resolution images (HR, 1.0 × 1.0 × 6.0 $mm^3$) were also obtained using the same 2D GRE CINE sequence with increased matrix size of 352 × 274∼313 and an additional 5∼7 s (totaling 16∼18 s) for breath-hold.

For 3T CMR scans, both 2D GRE CINE and 2D bSSFP CINE sequences were scanned with the same spatial resolution of 1.6 × 1.6 × 8.0 $mm^3$. The GRE CINE protocol was: TE/TR = 2.65∼2.69/5.42∼5.45 ms, FA = 15°, readout bandwidth = 300 Hz/px, 25 phases per cardiac cycle, and two-fold parallel imaging for acceleration, leading to a breath-hold duration of ∼11 s per slice. The bSSFP CINE protocol was: TE/TR = 1.37/2.98 ms, FA = 60°, readout bandwidth = 1,000 Hz/px, 25 phases per cardiac cycle, and two-fold parallel imaging for acceleration, leading to a breath-hold duration of ∼6 s per slice. Other parameters were set the same as the 5T regular resolution protocol unless stated otherwise.

For all CMR scans, images of two-chamber (2 ch) and four-chamber (4 ch) views, as well as of a stack of short axis (SAX) view covering both left and right ventricles were obtained. Table 1 shows the summary of the scanning parameters. To achieve sufficient coverage for SAX scans, 10 slices with 20% gaps were acquired for regular scans, and 12 slices with 20% gaps for HR scans. Particularly, the TE of GRE scans were set to as close as possible to the nearest water-fat out-of-phase echo times (3T: 2.65 ms vs. the theoretical 2.20 ms; 5T: 2.84 or 3.04 ms vs. the theoretical 2.72 ms), to create a natural boundary between myocardium and fats for better tissue delineation in subsequent image analysis.

## Image analysis

All image analyses described below were performed by two experienced radiologists with 10 and 5 years of experience in CMR. The readers were blinded to the acquisition parameters, field strengths and subject demography, and they received all the CMR CINE images in a randomized order.

## Quality evaluation

Overall image quality (jointly on boundary sharpness, anatomic feature visibility and noise level) and the presence of artifacts (including those related to motion and reconstruction) were evaluated with qualitative scores from 0 to 3. The scoring criteria on image quality were defined as: 0, poor, non-diagnostic; 1, impaired image quality for potential misdiagnosis; 2, good quality meeting routine standards; and 3, excellent, exceeding routine quality. And the scoring criteria on artifacts were: 0, no artifact present; 1, mild artifacts not impairing diagnostic quality; 2, moderate artifacts partially impairing diagnostic quality; and 3, severe artifacts with non-diagnostic quality. Scores were independently given by the two radiologists on SAX and long-axis images of each subject. The Wilcoxon matched pairs test was used to compare the results.

## SNR-CNR analysis

For SNR and CNR assessment, regions of interest (ROI) signals were manually extracted from end-diastole SAX slices on the midventricular level (10). One ROI was positioned in the center of the left ventricle (LV) cavity, and 6 ROIs were drawn in the myocardium according to a six-segment model (22) and the mean result were reported. The noise level was estimated by drawing three background ROIs free from any visible artifacts and taking the average of the signal standard deviation (SD). The SNR was calculated by dividing the mean signal intensity of the LV cavity by the noise:

$$\mathrm{SNR} = \frac{S_{cavity}}{mean(SD(air))}$$

The CNR was estimated as the ratio of the mean signal difference between LV cavity and LV myocardium to the noise SD:

$$\mathrm{CNR} = \frac{S_{cavity} - mean(S_{myocardium})}{mean(SD(air))}$$

The Wilcoxon matched pairs test was used to compare the results.

## Functional analysis

Quantitative functional measurements on end-diastolic volume (EDV), end-systolic volume (ESV), EF for both LV and right ventricle (RV) were assessed by the same radiologists using CVI42 (Circle Cardiovascular Imaging, Calgary, AB, Canada).

TABLE 1 CMR scanning parameters in this study.

| | | 3T bSSFP | 3T GRE | 5T GRE | 5T GRE HR |
|---|---|---|---|---|---|
| Short axis | Field of view (mm) | 360 × 280∼320 | *360 × 280∼320 | 360 × 280∼320 | 360 × 280∼320 |
| | Spatial resolution (mm) | 1.6 × 1.6 | 1.6 × 1.6 | 1.6 × 1.6 | 1.0 × 1.0 |
| | Matrix | 224 × 174∼199 | 224 × 174∼199 | 224 × 174∼199 | 352 × 274∼313 |
| | Number of slices | 10 | 10 | 10 | 12 |
| | Slice thickness (mm) | 8 | 8 | 8 | 6 |
| | Slice gap (mm) | 1.6 | 1.6 | 1.6 | 1.2 |
| | TE/TR (ms) | 1.37/2.98 | 2.65∼2.69/5.42∼5.45 | 2.84/5.55 | 3.06/5.95 |
| | Flip angle (°) | 60° | 15° | 10° | 10° |
| | Bandwidth (Hz/pixel) | 1,000 | 300 | 300 | 300 |
| 2 Chamber | Field of view (mm) | 360 × 280∼320 | 360 × 280∼320 | 360 × 280∼320 | 360 × 280∼320 |
| | Spatial resolution (mm) | 1.6 × 1.6 | 1.6 × 1.6 | 1.6 × 1.6 | 1.0 × 1.0 |
| | Matrix | 224 × 174∼199 | 224 × 174∼199 | 224 × 174∼199 | 352 × 274∼313 |
| | Number of slices | 1 | 1 | 1 | 1 |
| | Slice thickness (mm) | 8 | 8 | 8 | 6 |
| | TE/TR (ms) | 1.37/2.98 | 2.65∼2.69/5.42∼5.45 | 2.42/4.48 | 3.06/5.95 |
| | Flip angle (°) | 60° | 15° | 10° | 10° |
| | Bandwidth (Hz/pixel) | 1,000 | 300 | 500 | 300 |
| 4 Chamber | Field of view (mm) | 360 × 260∼320 | 360 × 260∼320 | 360 × 260∼300 | 360 × 260∼300 |
| | Spatial resolution (mm) | 1.6 × 1.6 | 1.6 × 1.6 | 1.6 × 1.6 | 1.0 × 1.0 |
| | Matrix | 224 × 162∼187 | 224 × 162∼187 | 224 × 162∼187 | 352 × 254∼293 |
| | Number of slices | 1 | 1 | 1 | 1 |
| | Slice thickness (mm) | 8 | 8 | 8 | 6 |
| | TE/TR (ms) | 1.37/2.98 | 2.65/5.42 | 2.42/4.48 | 3.06/5.95 |
| | Flip angle (°) | 60° | 15° | 10° | 10° |
| | Bandwidth (Hz/pixel) | 1,000 | 300 | 500 | 300 |

The myocardium boundaries on SAX images were initialized using the software and manually adjusted when necessary. The myocardium mass of LV was also assessed, with papillary muscles and trabeculae excluded from the myocardium mass but included in the blood pool volume calculation.

Statistical analyses on the functional measurements were performed using Student's *t*-test after normality test. *P*-values of multiple comparisons were adjusted using Holm-Bonferroni method. A difference was considered significant with $p < 0.05$. Correlations among measurements were evaluated using Bland-Altman analysis.

# Results

Figure 1 shows the typical ECG signals recorded from both 5 and 3T during the CINE scans, both showing highly similar and reliable wave forms.

Figure 2 shows representative CINE images at both 5 and 3T, all displaying image quality that meets the routine clinical needs. Note that the fine structures of papillary muscles are clearly visible in the 5T GRE HR images.

Figure 3 compares the 5T GRE and 5T GRE HR SAX images. While both scans yielded excellent image quality, image contrasts and SNR, the HR images enabled better delineation of finer structures such as myocardium-blood boundaries, papillary muscles and trabecular structures.

## Quality evaluation

The evaluation scores on image quality and artifact presence are summarized in Table 2. All GRE results, i.e., 3T GRE, 5T GRE, and 5T GRE HR, showed statistically similar scores in SAX images. For long axis images, 5T GRE, and 5T GRE HR images mostly received significantly better scores in both image quality and artifact control than 3T GRE, except the artifact control of 5T GRE being similar to 3T GRE ($p = 0.07$). 3T bSSFP showed significantly better scores than 3T GRE in all categories, as expected.

Table 3 shows the SNR of myocardium signals and CNR between myocardium and blood pool. In accordance to literatures (10), SNR of 3T bSSFP (130.9 ± 23.2) was significantly higher than 3T GRE (91.8 ± 10.0). On the

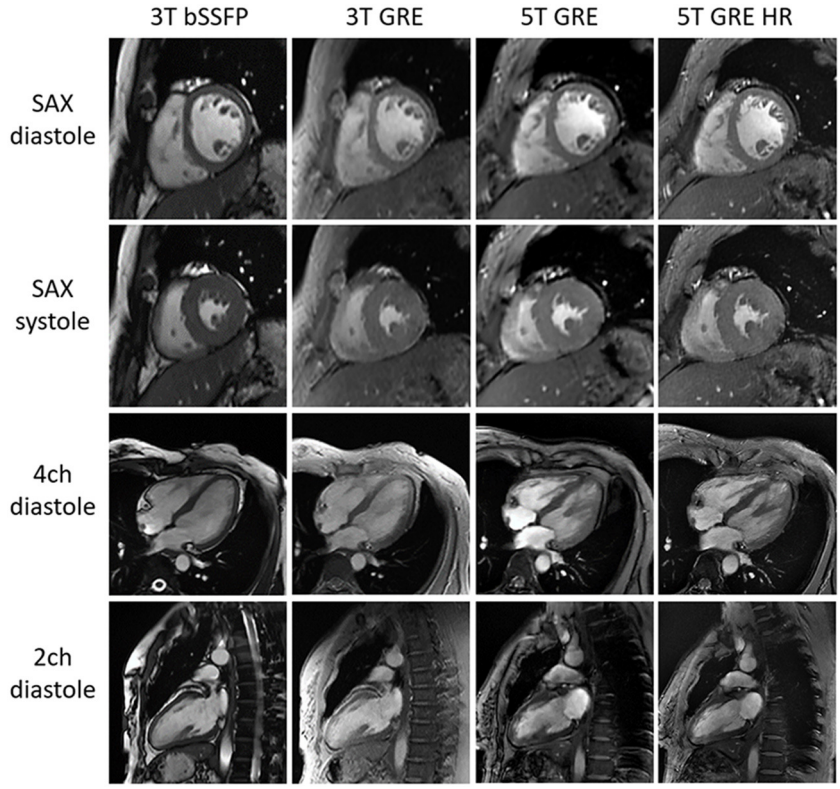


FIGURE 2
Typical CMR cine images of one subject. All images are free of major artifacts and show good image quality.

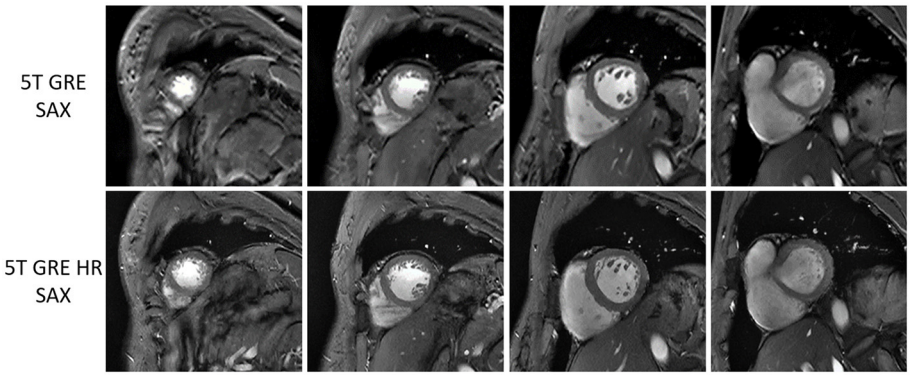


FIGURE 3
Multi-slice short-axis GRE images at 5T of one volunteer, comparing between routine resolution (top row) and high resolution (bottom row).

other hand, the 5T GRE results, under the same routine resolution of 1.6 × 1.6 × 8 $mm^3$, also achieved significantly higher myocardium SNR (1,438.0 ± 26.3) and CNR (92.5 ± 22.7) than 3T GRE images. With ∼70% smaller voxel volume, the GRE HR images at 5T achieved lower SNR (62.5 ± 9.9) and CNR (37.4 ± 10.2) when compared to 3T GRE.

## Functional statistics

Table 4 compares all the functional parameters (i.e., LV EDV/ESV/Mass/EF and RV EDV/ESV/EF) among the 4 CINE image sets (i.e., 3T bSSFP/GRE and 5T GRE/GRE HR), using the 3T bSSFP results as reference. The consistency of all functional parameters are in good agreement with literatures (10, 12). Most

TABLE 2 Rating of overall image quality and presence of artifacts, using 3T GRE as reference.

| Slice orientation | Sequence | Voxel size ($mm^3$) | Image quality (mean ± STD) | Artifacts rating (mean ± STD) |
|---|---|---|---|---|
| SAX | 3T GRE | 1.6 × 1.6 × 8 | 2.0 ± 0.5 | 1.2 ± 0.4 |
| | 3T bSSFP | 1.6 × 1.6 × 8 | 2.5 ± 0.6 ($p = 0.014$)* | 0.6 ± 0.6 ($p = 0.002$)* |
| | 5T GRE | 1.6 × 1.6 × 8 | 2.2 ± 0.5 ($p = 0.250$) | 1.2 ± 0.4 ($p = 1.000$) |
| | 5T GRE HR | 1.0 × 1.0 × 6 | 2.1 ± 0.8 ($p = 0.424$) | 1.4 ± 0.5 ($p = 0.219$) |
| Long axis | 3T GRE | 1.6 × 1.6 × 8 | 1.5 ± 0.5 | 1.4 ± 0.6 |
| | 3T bSSFP | 1.6 × 1.6 × 8 | 2.6 ± 0.5 ($p < 0.001$)* | 0.4 ± 0.5 ($p < 0.001$)* |
| | 5T GRE | 1.6 × 1.6 × 8 | 1.9 ± 0.5 ($p = 0.039$)* | 1.1 ± 0.5 ($p = 0.070$) |
| | 5T GRE HR | 1.0 × 1.0 × 6 | 2.3 ± 0.7 ($p < 0.001$)* | 1.1 ± 0.4 ($p = 0.039$)* |

Both rating scores ranged from 0 to 3, and a higher rating denotes better image quality, but worse artifact control.
Asteroids indicate significant differences, i.e., $p < 0.05$, when compared to 3T GRE.

TABLE 3 Comparison on SNR and CNR of SAX images, using 3T GRE as reference.

| Sequence | Voxel size ($mm^3$) | SNR (mean ± SD) | Relative SNR | CNR (mean ± SD) | Relative CNR |
|---|---|---|---|---|---|
| 3T GRE | 1.6 × 1.6 × 8 | 91.8 ± 10.0 | 1.00 | 52.1 ± 13.7 | 1.00 |
| 3T bSSFP | 1.6 × 1.6 × 8 | 130.9 ± 23.2 ($p = 0.016$)* | 1.43 | 94.0 ± 21.5 ($p = 0.007$)* | 1.80 |
| 5T GRE | 1.6 × 1.6 × 8 | 143.8 ± 26.3 ($p = 0.013$)* | 1.57 | 92.5 ± 22.7 ($p = 0.034$)* | 1.78 |
| 5T GRE HR | 1.0 × 1.0 × 6 | 62.5 ± 9.9 ($p = 0.012$)* | 0.68 | 37.4 ± 10.2 ($p = 0.145$) | 0.72 |

Asteroids indicate significant differences, i.e., $p < 0.05$, when compared to 3T GRE.

TABLE 4 Comparison of CMR CINE functional quantities, using 3T bSSFP as reference.

| Sequence | LV EDV ($mm^3$) | LV ESV ($mm^3$) | LV Mass (g) | LV EF (%) | RV EDV ($mm^3$) | RV ESV ($mm^3$) | RV EF (%) |
|---|---|---|---|---|---|---|---|
| 3T bSSFP | 129.8 ± 18.5 | 45.1 ± 9.1 | 98.1 ± 21.2 | 65.3 ± 4.1 | 142.2 ± 20.5 | 63.0 ± 13.4 | 56.1 ± 4.7 |
| 3T GRE | 128.1 ± 20.2 | 43.3 ± 9.2 | 105.7 ± 20.7 | 66.4 ± 5.0 | 148.7 ± 21.4* | 62.3 ± 13.1 | 58.4 ± 4.9* |
| 5T GRE | 130.1 ± 19.2 | 44.0 ± 11.6 | 104.0 ± 20.2* | 66.8 ± 6.0 | 152.1 ± 21.3* | 66.5 ± 12.7 | 57.4 ± 4.7 |
| 5T GRE HR | 129.6 ± 18.0 | 45.2 ± 10.8 | 101.5 ± 19.5 | 65.4 ± 5.2 | 151.5 ± 20.2* | 65.8 ± 13.8 | 56.8 ± 6.5 |

Asteroids indicate significant differences, i.e., $p < 0.05$, when compared to 3T bSSFP.

functional measurements did not show statistically significant differences, except for RV EDV (all GRE), RV EF (3T GRE), and LV Mass (5T GRE).

Figures 4, 5 show the Bland-Altman plots for cardiac functional analyses on LV and RV, respectively. Both figures indicate good agreement of all GRE scans including 5T's to the reference 3T bSSFP scans.

## Discussion

In this pilot study, we performed an initial evaluation of CMR performance on a newly developed 5T whole body system (19). We used the 3T GRE CINE images as reference for image quality and SNR comparison, and used the 3T bSSFP images for the functional assessment accuracy comparison (23). The results not only demonstrated the feasibility of CMR imaging at 5T, but also suggested that 5T CMR may provide additional benefits compared to routine high field (e.g., 3T) by offering improved and balanced outcomes.

The 5T system provided excellent image quality and contrasts between myocardial muscles and blood, showing improved contrasts than the 3T GRE images. There are several factors that may contribute to such improvement in image quality.

First, the higher field creates a stronger time-of-flight inflow effect on the inflowing blood (10), thus increasing the myocardium-blood contrast and leading to visually sharper boundaries, even under the same resolution settings. This is true for all slice orientation settings (i.e., SAX, 4 ch, and 2 ch views), as evidenced in Figure 2. Such improved tissue contrast potentially offers more useful details for applications involving cardiac morphology (24), such as arrhythmogenic right ventricular dysplasia (ARVD) (25) where the trabeculae carneae may be obscured within relatively slower (than LV) flowing blood.

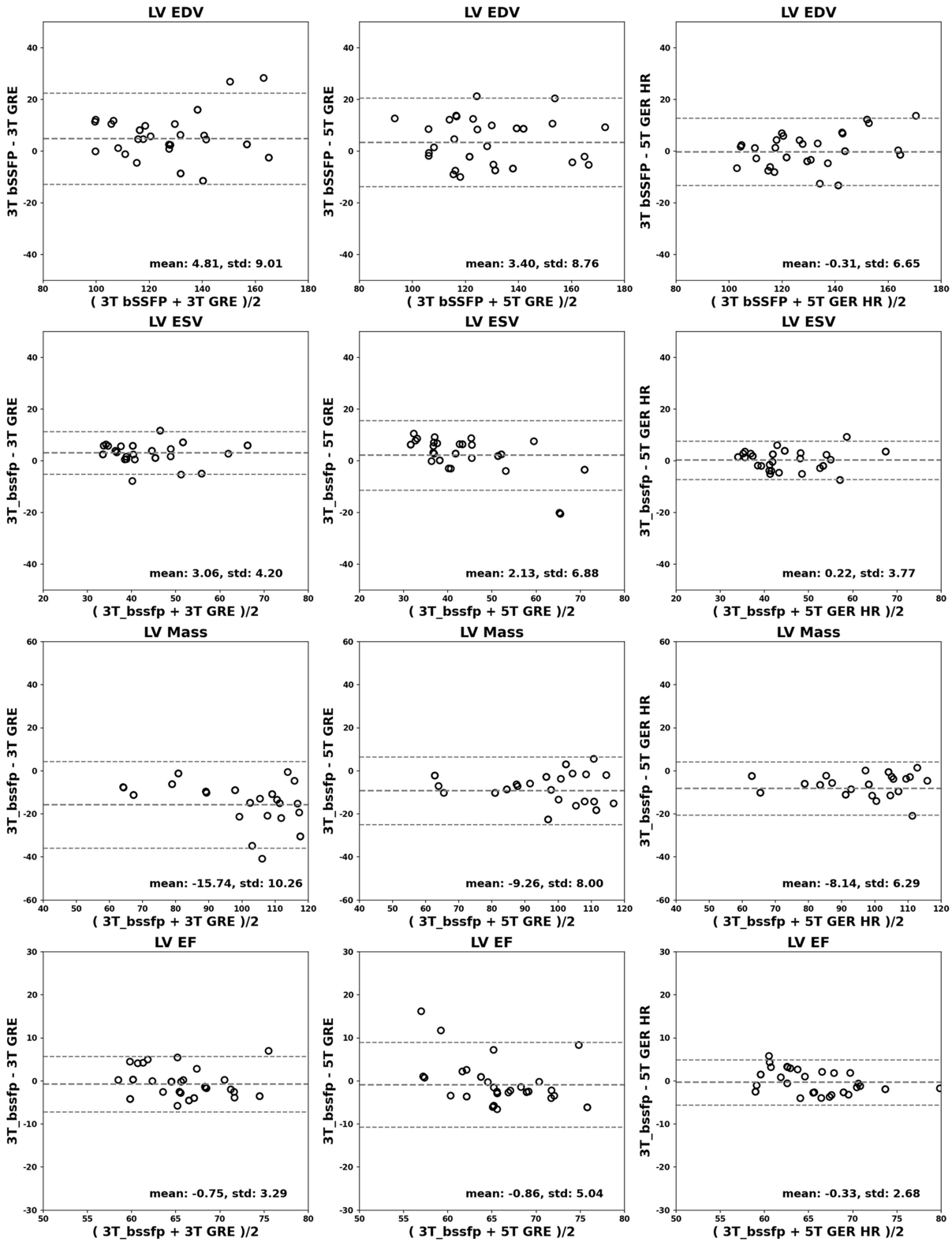


FIGURE 4
Bland-Altman analyses for LV. LV EDV (ml), ESV (ml), mass (g) and EF (%) are shown in rows. Comparisons of 3T GRE, 5T GRE, and 5T GRE HR to 3T bSSFP are shown in columns.

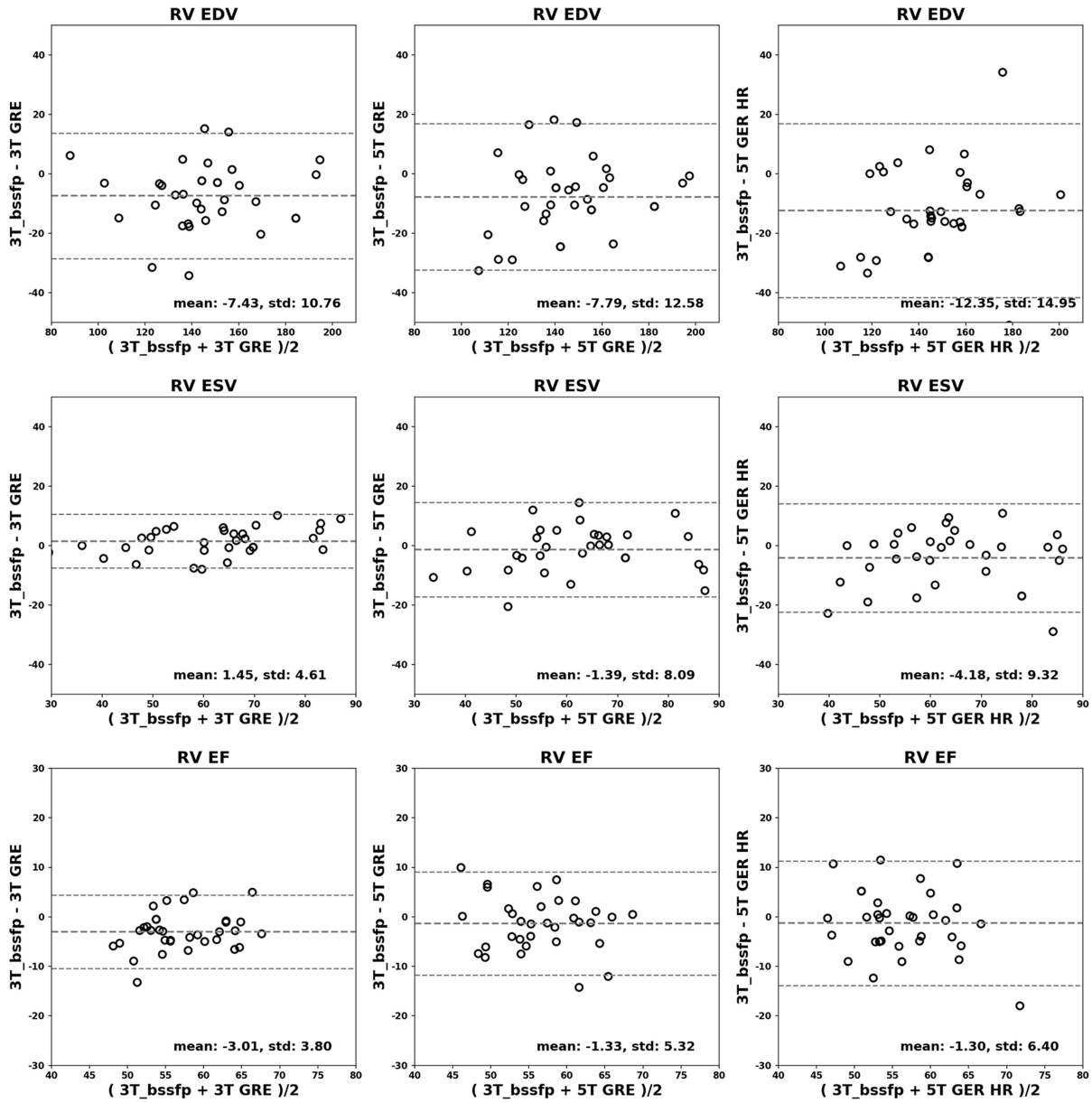


FIGURE 5
Bland-Altman analyses for RV. RV EDV (ml), ESV (ml) and EF (%) are shown in rows. Comparisons of 3T GRE, 5T GRE, and 5T GRE HR to 3T bSSFP are shown in columns.

Second, the gain in image quality at 5T was also evidenced by the increase in SNR and CNR. With regular resolution of 1.6 × 1.6 × 8.0 $mm^3$, the 5T GRE images showed significantly superior SNR and CNR than the GRE at 3T. Even with a much smaller voxel size (∼30% in voxel volume), the 5T GRE HR images still yielded sufficient SNR and CNR to support similar or even better visual quality than the routine 3T GRE. Unlike in most 7T CMR studies where local TX/RX coils (9, 11, 12, 18) were used, the 5T system employed a volumetric body coil for parallel RF transmission. With an 8-channel loop array design, the $B_{1+}$ field can be dynamically adjusted on a subject-by-subject basis. The advantage of using such a "global" parallel transmission over the "local" transceiver is that it can achieve more homogeneous excitation effects, especially on patients with larger girth sizes.

Third, the 5T system is capable of detecting almost distortion-free ECG signals for reliable gating during CMR scans, highly comparable to those from 3T (Figure 1) and much better than those from 7T (26). ECG signals originate

from the cardiac electrical activities associated with the cardiac rhythmic motions, which is field independent by itself. However, electrode-based ECG detection in MRI is usually overlaid with the so-called magneto-hydrodynamic (MHD) effects (27) originating from the conducting fluid (i.e., cardiac blood flow) under the influence of the external magnetic field and will become stronger at higher fields. Practically, the MHD effect is negligible at 3T and lower fields, but it has been determined to severely affect ECG readings at 7T (26) to the extent of non-usability. Therefore, alternative ECG gating techniques have been generally needed at UHF, such as acoustic cardiac triggering (28) or the finger-clipping pulse oximetry. However, these gating methods only provide an alternative form of the true ECG signals and have their own limitations (28). During our scanning process at 5T, the ECG quality of all subjects, both males and females, was sufficiently reliable to yield high quality images with minimal motion artifacts, while requiring no additional efforts than at 3T.

Finally, the combination of the high SNR and reliable ECG gating at 5T supports reliable high-resolution CMR scans. In this study, the high-resolution was set as $1.0 \times 1.0 \times 6.0\ mm^3$, which is <30% in voxel volume comparing to routine scan settings and has been rarely reported at 3T due to compromise in SNR. Nevertheless, the 5T GRE HR images still achieved satisfying SNR and CNR, suggesting the SNR benefit at UHF was indeed well utilized at 5T. On the other hand, the HR scans required a longer scan time by 5∼7 s, a reliable ECG gating is critical to containing the risks of motion artifacts. As revealed in the image results and visual rating statistics (Figure 2 and Table 2), the 5T GRE HR scans showed comparable or even better artifact control than 3T GRE, also demonstrating the traditional ECG method is well employed at 5T.

To briefly summarize, the improvement in imaging contrast and SNR/CNR, as well as the robust ECG gating capacity suggest the potential of the 5T UHF for reliable CMR imaging on cardiovascular anatomy and functionalities. Although 5T is midway between 3 and 7T, the 5T CMR setup, in terms of scanning parameters and the ECG gating scheme, was more similar to those at 3T, while its performance on SNR/CNR and imaging quality may be more 7T alike. Other challenges reported at 7T, such as $B_{1+}$ field inhomogeneity and high SAR levels, were also observed at 5T but with much milder effects, thus are expected to be coped with more easily.

Regarding the cardiac functional results, all scans from both systems yielded statistically comparable results, with only a few exceptions (Table 4). This was somewhat different from previous reports, where significant differences were observed for LV EDV/ESV/EF and RV EDV/ESV between bSSFP and GRE at 3T (5), or for LV mass between 7 (both regular- and high-resolution) and 1.5T GRE (10). The cause for such differences was previously attributed to the epicardial fat being differentiable in bSSFP images but not in GRE images (10), thus leading to large myocardium ROIs drawn on GRE images by including fatty tissues. In this study, by using out-of-phase echo times for GRE scans, visible myocardium-fat boundaries were created, which was clearly shown in all our pictorial figures. Therefore, with the automatic myocardium extraction by the CVI42 software followed by manual ROI adjustment, the cardiac functional quantities can be more reliably extracted even from GRE data, avoiding over-estimation by excluding most of the fatty tissues.

Several limitations of this study should be noted. In this pilot study, only a limited number of healthy volunteers without any cardiac conditions were included in the functional and statistical analyses. As has been demonstrated in a previous study (12) that HR CINE imaging at 7T can reveal myocardial crypts in hypertrophic cardiomyopathy patients, which were obscured at 3T. The benefits of imaging with better contrasts, SNR and resolution at 5T are yet to be demonstrated with a larger patient cohort with cardiovascular diseases. Second, this work only focused on CINE imaging, and other CMR techniques such as tissue characterization (29) and quantitative mapping (30, 31), should be further evaluated in future works. Third, only a normal flexible body coil was currently available on the 5T system, while further improvement in imaging quality can be expected with dedicated cardiac coils (32).

Since the 5T MRI system has become available only very recently, virtually any CMR techniques and applications can be revisited. Judging from the results of this study and from literatures, it is likely that CMR imaging at 5T can enjoy more of the pros from both sides while suffering from less of the cons. For instance, it is worth mentioning that in our preliminary tests on 5T bSSFP CINE scans, the SAR level (<13 W/kg) was well within the first level safety limit (i.e., 20 W/kg for body trunk), although the robustness of imaging quality against $B_0$ and $B_1$ effects still required improvement (thus data not shown). Since bSSFP CINE is generally considered the standard method (compared to GRE CINE) at 1.5 and 3T fields but is well-known to be unusable at 7T UHF (15, 17), its potential feasibility at 5T UHF will be highly desirable.

Moreover, with the stronger $T_1$ sensitivities, 5T may foreseeably have better performance on related applications such as quantitative perfusion or late gadolinium enhancement imaging, which can be of great interests for future works.

## Conclusion

In conclusion, this pilot study has presented the initial evaluation of CMR CINE imaging at 5T UHF. The image quality at 5T was generally superior or comparable to the 3T counterparts, while functional quantification results were statistically similar. Therefore, the new 5T UHF system has the potential to achieve a well-balanced performance for CMR CINE imaging to potentially meet the clinical and researching needs.

## Data availability statement

The raw data supporting the conclusions of this article will be made available by the authors, without undue reservation.

## Ethics statement

The studies involving human participants were reviewed and approved by the Institutional Review Board of Peking Union Medical College Hospital, Beijing, China. The patients/participants provided their written informed consent to participate in this study.

## Author contributions

LL and PL proposed the project and experimental designs and performed the subjective evaluation on imaging quality scoring and the post processing for subsequent quantitative analysis. YW, ZJ, DL, and HZ were involved in study set-up, interpretation of results, scientific, and clinical consultation. GS performed data acquisition and preparation. JW performed the statistical analysis. The manuscript was mainly prepared by LL and PL, with input and improvement from all other authors. All authors have read and approved the final manuscript.

## Funding

This work was partially supported by the National Key R&D Program of China (2017YFC0108800), the Major International (Regional) Joint Research Project of the National Natural Science Foundation of China (82020108018), and the National Natural Science Foundation of China (81873891).

## Conflict of interest

The authors declare that the research was conducted in the absence of any commercial or financial relationships that could be construed as a potential conflict of interest.

## Publisher's note

All claims expressed in this article are solely those of the authors and do not necessarily represent those of their affiliated organizations, or those of the publisher, the editors and the reviewers. Any product that may be evaluated in this article, or claim that may be made by its manufacturer, is not guaranteed or endorsed by the publisher.

## References

1. Thiele H, Nagel E, Paetsch I, Schnackenburg B, Bornstedt A, Kouwenhoven M, et al. Functional cardiac MR imaging with steady-state free precession (SSFP) significantly improves endocardial border delineation without contrast agents. *J Magn Reson Imag.* (2001) 14:362–7. doi: 10.1002/jmri.1195

2. Hunold P, Maderwald S, Ladd ME, Jellus V, Barkhausen J. Parallel acquisition techniques in cardiac cine magnetic resonance imaging using TrueFISP sequences: comparison of image quality and artifacts. *J Magn Reson Imag.* (2004) 20:506–11. doi: 10.1002/jmri.20125

3. Blankenberg F, Eisenberg S, Scheinman MN, Higgins CB. Use of cine gradient echo (GRE) MR in the imaging of cardiac hemochromatosis. *J Comput Assist Tomogr.* (1994) 18:136–8.

4. Curtis AD, Cheng HM. Primer and historical review on rapid cardiac CINE MRI. *J Magn Reson Imag.* (2022) 55:373–88. doi: 10.1002/jmri.27436

5. Grothues F, Boenigk H, Graessner J, Kanowski M, Klein HU. Balanced steady-state free precession vs. segmented fast low-angle shot for the evaluation of ventricular volumes, mass, and function at 3 Tesla. *J Magn Reson Imag.* (2007) 26:392–400. doi: 10.1002/jmri.20986

6. Moon JC, Lorenz CH, Francis JM, Smith GC, Pennell DJ. Breath-hold FLASH and FISP cardiovascular MR imaging: left ventricular volume differences and reproducibility. *Radiology.* (2002) 223:789–97. doi: 10.1148/radiol.2233011181

7. Malayeri AA, Johnson WC, Macedo R, Bathon J, Lima JA, Bluemke DA. Cardiac cine MRI: quantification of the relationship between fast gradient echo and steady-state free precession for determination of myocardial mass and volumes. *J Magn Reson Imag.* (2008) 28:60–6. doi: 10.1002/jmri.21405

8. Hudsmith LE, Petersen SE, Tyler DJ, Francis JM, Cheng AS, Clarke K. et al. Determination of cardiac volumes and mass with FLASH and SSFP cine sequences at 15 vs. 3 Tesla: a validation study. *J Magn Reson Imag.* (2006) 24:312–8. doi: 10.1002/jmri.20638

9. Brandts A, Westenberg JJ, Versluis MJ, Kroft LJ, Smith NB, Webb AG, et al. Quantitative assessment of left ventricular function in humans at 7T. *Magn Reson Med.* (2010) 64:1471–7. doi: 10.1002/mrm.22529

10. von Knobelsdorff-Brenkenhoff F, Frauenrath T, Prothmann M, Dieringer MA, Hezel F, Renz W, et al. Cardiac chamber quantification using magnetic resonance imaging at 7 Tesla: a pilot study. *Eur Radiol.* (2010) 20:2844–52. doi: 10.1007/s00330-010-1888-2

11. von Knobelsdorff-Brenkenhoff F, Tkachenko V, Winter L, Rieger J, Thalhammer C, Hezel F, et al. Assessment of the right ventricle with cardiovascular magnetic resonance at 7 Tesla. *J Cardiovasc Magn Reson.* (2013) 15:23. doi: 10.1186/1532-429X-15-23

12. Prothmann M, von Knobelsdorff-Brenkenhoff F, Topper A, Dieringer MA, Shahid E, Graessl A. et al. High spatial resolution cardiovascular magnetic resonance at 70 Tesla in patients with hypertrophic cardiomyopathy—first experiences: lesson learned from 70 Tesla. *PLoS ONE.* (2016) 11:e0148066. doi: 10.1371/journal.pone.0148066

13. Reiter T, Lohr D, Hock M, Ankenbrand MJ, Stefanescu MR, Kosmala A, et al. On the way to routine cardiac MRI at 7 Tesla: a pilot study on consecutive 84 examinations. *PLoS ONE.* (2021) 16:e0252797. doi: 10.1371/journal.pone.0252797

14. Barisano G, Sepehrband F, Ma S, Jann K, Cabeen R, Wang DJ, et al. Clinical 7T MRI: are we there yet? A review about magnetic resonance imaging at ultra-high field. *Br J Radiol.* (2019) 92:20180492. doi: 10.1259/bjr.20180492

15. Kraff O, Quick HH. 7T: Physics, safety, and potential clinical applications. *J Magn Reson Imag.* (2017) 46:1573–89. doi: 10.1002/jmri.25723

16. Kangarlu A, Burgess RE, Zhu H, Nakayama T, Hamlin RL, Abduljalil AM, et al. Cognitive, cardiac, and physiological safety studies in ultra high field magnetic resonance imaging. *Magn Reson Imag.* (1999) 17:1407–16.

17. Hansson B, Simic M, Olsrud J, Markenroth Bloch K, Owman T, Sundgren PC, et al. MR-safety in clinical practice at 7T: evaluation of a

multistep screening process in 1819 subjects. *Radiography.* (2021) 28:454–9. doi: 10.1016/j.radi.2021.12.007

18. Snyder CJ, DelaBarre L, Metzger GJ, van de Moortele PF, Akgun C, Ugurbil K, et al. Initial results of cardiac imaging at 7 Tesla. *Magn Reson Med.* (2009) 61:517–24. doi: 10.1002/mrm.21895

19. Shen Z, Zhu X, Han S, Fang F, Luo W, Che S, et al., editors. Initial experience of body imaging at 5T. In: *Proceedings 29th Scientific Meeting, International Society for Magnetic Resonance in Medicine* (2021).

20. Fang F, Luo W, Gong J, Zhang R, Wei Z, Li Y, editors. An 8-channel transmit loop array for body imaging 9 at 5T. In: *Proceedings 29th Scientific Meeting, International Society for Magnetic Resonance in Medicine* (2021).

21. Katscher U, Bornert P, Leussler C, van den Brink JS. Transmit SENSE. *Magn Reson Med.* (2003) 49:144–50. doi: 10.1002/mrm.10353

22. Cerqueira MD, Weissman NJ, Dilsizian V, Jacobs AK, Kaul S, Laskey WK, et al. Standardized myocardial segmentation and nomenclature for tomographic imaging of the heart. A statement for healthcare professionals from the cardiac imaging committee of the council on clinical cardiology of the American Heart Association. *Circulation.* (2002) 105:539–42. doi: 10.1161/hc0402.102975

23. Camargo GC, Erthal F, Sabioni L, Penna F, Strecker R, Schmidt M, et al. Real-time cardiac magnetic resonance cine imaging with sparse sampling and iterative reconstruction for left-ventricular measures: comparison with gold-standard segmented steady-state free precession. *Magn Reson Imag.* (2017) 38:138–44. doi: 10.1016/j.mri.2017.01.002

24. Ringenberg J, Deo M, Devabhaktuni V, Berenfeld O, Boyers P, Gold J. Fast, accurate, and fully automatic segmentation of the right ventricle in short-axis cardiac MRI. *Comput Med Imag Graph.* (2014) 38:190–201. doi: 10.1016/j.compmedimag.2013.12.011

25. Tandri H, Friedrich MG, Calkins H, Bluemke DA. MRI of arrhythmogenic right ventricular cardiomyopathy/dysplasia. *J Cardiovasc Magn Reson.* (2004) 6:557–63. doi: 10.1081/JCMR-120030583

26. Stab D, Roessler J, O'Brien K, Hamilton-Craig C, Barth M. ECG triggering in ultra-high field cardiovascular MRI. *Tomography.* (2016) 2:167–74. doi: 10.18383/j.tom.2016.00193

27. Gregory TS, Cheng R, Tang G, Mao L, Tse ZTH. The magnetohydrodynamic effect and its associated material designs for biomedical applications: a state-of-the-art review. *Adv Funct Mater.* (2016) 26:3942–52. doi: 10.1002/adfm.201504198

28. Frauenrath T, Hezel F, Renz W, d'Orth Tde G, Dieringer M, von Knobelsdorff-Brenkenhoff F, et al. Acoustic cardiac triggering: a practical solution for synchronization and gating of cardiovascular magnetic resonance at 7 Tesla. *J Cardiovasc Magn Reson.* (2010) 12:67. doi: 10.1186/1532-429X-12-67

29. Paddock S, Tsampasian V, Assadi H, Mota BC, Swift AJ, Chowdhary A, et al. Clinical translation of three-dimensional scar, diffusion tensor imaging, four-dimensional flow, and quantitative perfusion in cardiac MRI: a comprehensive review. *Front Cardiovasc Med.* (2021) 8:682027. doi: 10.3389/fcvm.2021.682027

30. Hamilton-Craig CR, Strudwick MW, Galloway GJ. T1 mapping for myocardial fibrosis by cardiac magnetic resonance relaxometry: a comprehensive technical review. *Front Cardiovasc Med.* (2016) 3:49. doi: 10.3389/fcvm.2016.00049

31. Hamlin SA, Henry TS, Little BP, Lerakis S, Stillman AE. Mapping the future of cardiac MR imaging: case-based review of T1 and T2 mapping techniques. *Radiographics.* (2014) 34:1594–611. doi: 10.1148/rg.346140030

32. Schmitt M, Potthast A, Sosnovik DE, Polimeni JR, Wiggins GC, Triantafyllou C, et al. A 128-channel receive-only cardiac coil for highly accelerated cardiac MRI at 3 Tesla. *Magn Reson Med.* (2008) 59:1431–9. doi: 10.1002/mrm.21598

frontiers | Frontiers in Cardiovascular Medicine

TYPE Original Research
PUBLISHED 15 September 2022
DOI 10.3389/fcvm.2022.840735



OPEN ACCESS

EDITED BY
Luca Saba,
Azienda Ospedaliero-Universitaria Cagliari, Italy

REVIEWED BY
Fu-Zong Wu,
Kaohsiung Veterans General Hospital, Taiwan
Yining Wang,
Peking Union Medical College Hospital (CAMS), China

*CORRESPONDENCE
Liang Jin
jin_liang@fudan.edu.cn
Ming Li
ming_li@fudan.edu.cn

†These authors have contributed equally to this work

SPECIALTY SECTION
This article was submitted to Cardiovascular Imaging, a section of the journal Frontiers in Cardiovascular Medicine

RECEIVED 21 December 2021
ACCEPTED 12 August 2022
PUBLISHED 15 September 2022

CITATION
Jin L, Gao P, Wang K, Li J and Li M (2022) Intraindividual evaluation of effects of image filter function on image quality in coronary computed tomography angiography. *Front. Cardiovasc. Med.* 9:840735. doi: 10.3389/fcvm.2022.840735



# Intraindividual evaluation of effects of image filter function on image quality in coronary computed tomography angiography

Liang Jin[1*†], Pan Gao[1†], Kun Wang[1], Jianying Li[2] and Ming Li[1,3*]

[1]Radiology Department, Huadong Hospital, Affiliated to Fudan University, Shanghai, China, [2]CT Research Center, GE Healthcare China, Beijing, China, [3]Institute of Functional and Molecular Medical Imaging, Fudan University, Shanghai, China

**Objectives:** To evaluate whether applying image filters (smooth 3D+ and edge-2) improves image quality in coronary CT angiography (CCTA).

**Methods:** Ninety patients (routine group) with suspected coronary artery diseases based on 16-cm wide coverage detector CT findings were retrospectively enrolled at a chest pain center from December 2019 to September 2021. Two image filters, smooth 3D+ and edge-2 available on the Advantage Workstation (AW) were subsequently applied to the images to generate the research group (SE group). Quantitative parameters, including CT value, signal-to-noise ratio (SNR) and contrast-to-noise ratio (CNR), image sharpness and image quality score, and diagnostic accuracy were compared between the two groups.

**Results:** A total of 900 segments from 270 coronary arteries in 90 patients were analyzed. SNR, CNR, and image sharpness for vessels and image quality scores in the SE group were significantly better than those in the routine group (all $p < 0.001$). The SE group showed a slightly higher negative predictive value (NPV) on the left anterior descending artery and right coronary artery (RCA) stenosis evaluations, as well as total NPV. The SE group also showed slightly higher sensitivity and accuracy than the routine group on RCA stenosis evaluation.

**Conclusion:** The use of an image filter combining smooth 3D+ and edge-2 on an AW could improve the image quality of CCTA and increase radiologists' diagnostic confidence.

KEYWORDS

**coronary artery disease, X-ray computed tomography, analysis, sharpness, image quality**

# Introduction

Coronary computed tomography angiography (CCTA) has been widely used for detecting coronary artery stenosis in patients with suspicious coronary artery disease (CAD) (1–3). However, motion artifacts and image noise decrease CCTA image quality (4–7), and thus affect the diagnosis, management, and treatment of CAD (8). Notably, 16-cm-wide coverage-detector CT with motion-corrected reconstruction algorithm Snapshot Freeze (SSF) has been shown to reduce respiratory movement and motion artifacts (9–16). However, the image noise due to insufficient photon quantity in low-dose CCTA still needs to be overcome (17). Common ways to reduce image noise without increasing radiation dose include the use of iterative reconstruction algorithms (IRs), deep learning-based image reconstruction algorithms, and low-pass reconstruction kernels (RKs) in CCTA (18).

On the other hand, image filters (19) operated in the image domain also provide several options that could be applied through the post-processing procedure to reduce image noises and enhance edges (edge sharpening). Image sharpness as a quantitative index is important to evaluate the image quality (20–23). However, the use of image filters has not been focused on and whether this application of image filters could improve image quality and diagnostic accuracy remains unknown and was not reported before. Therefore, we hypothesized the improved diagnostic image quality through image filters, and the purpose of this study was to compare quantitative measurements, qualitative image score, diagnostic accuracy through CAD-RADS report guideline (24), and image sharpness between CCTA images with the combination of image smoothing and edge-enhancement filters and those without.

Abbreviations: AO, aortic root; CAD, coronary artery disease; CAD-RADS, Coronary Artery Disease - Reporting and Data System; CCTA, Coronary computed tomography angiography; CNR, contrast-to-noise ratio; DICOM, Digital Imaging and Communications in Medicine; DLP, dose-length product; DSA, digital subtraction angiography; IRs, iterative reconstruction algorithms; LAD-D, distal left anterior descending artery; LAD-M, middle left anterior descending artery; LAD-P, proximal left anterior descending artery; LCX-D, distal left circumflex artery; LCX-M, middle left circumflex artery; LCX-P, proximal left circumflex artery; MTF, modulation transfer function; NPV, negative predictive value; PVAT, perivascular adipose tissue; RCA-D, distal-proximal right coronary artery; RCA-M, middle right coronary artery; RCA-P, proximal right coronary artery; SNR, signal-to-noise ratio; SSF, Snapshot Freeze; SD, standard deviation; RKs, reconstruction kernels; ROI, region of interest; WC/WW, window center-window width.

# Materials and methods

## Patients

This single-center, retrospective study was approved by the ethics committee of our hospital, and the requirement for written informed consent was waived owing to the retrospective nature of the study. Patients with suspected coronary heart disease due to chest pain who underwent CCTA at our center between December 2019 and September 2021 were consecutively selected from the hospital radiology information system. Inclusion criteria included CCTA imaging performed using the SSF technique with CT (GE Healthcare). Exclusion criteria included the image that does not meet the diagnostic requirements due to motion artifacts. A total of 90 patients (23 women; mean age: 67.1 ± 11.7 [range 38–90] years) were enrolled for image quality evaluation and 35 of the 90 patients who undergone digital subtraction angiography (DSA) were also used for diagnostic accuracy evaluation (Figure 1). Of these 35 patients, 28 patients' main lesion caused significant coronary stenosis is mixed plaque and 7 patients' is non-calcified plaque.

## Image acquisition and reconstruction

All patients underwent wide-coverage-detector CT (Revolution CT, GE Healthcare) with the following parameters: tube voltage, 100–120 kV; automatic tube current modulation, 300–800 mA; data acquisition window (R–R interval), 30–80%; and detector coverage, 100 mm, 120 mm, 140 mm, or 160 mm dependent on patient heart sizes. The gantry rotation speed was 0.28 s/rotation.

CCTA images with a slice thickness of 0.625 mm and increment of 0.625 mm were reconstructed using the 80% adaptive statistical iterative reconstruction-V [ASIR-V80%, GE Healthcare] with the STND kernel at the optimal reconstruction phase automatically selected by the SmartPhase technique (GE Healthcare), and the cardiac motion correction technique (snapshot freeze, SSF) was also applied (12, 15, 17). The generated images were assigned as the routine group. Subsequently, all the CCTA images of the routine group were sent to an Advantage Workstation (AW4.7, GE Healthcare) to undergo further image filtering. After our preliminary exploration and comparison with different combinations of smooth and edge enhancement filters that are readily available on the AW4.7, the filter combination was narrowed down to the combination of smooth 3D+ and edge-2. On the workstation, the volume rendering software was selected, and the Smooth 3D+ image filter option was selected for noise reduction. The resulting images were subsequently saved as a new group named Smooth 3D+. In a second pass, volume rendering software was once again selected, and the Edge-2 image filter option was chosen for edge sharpening of the Smooth 3D+ group. The

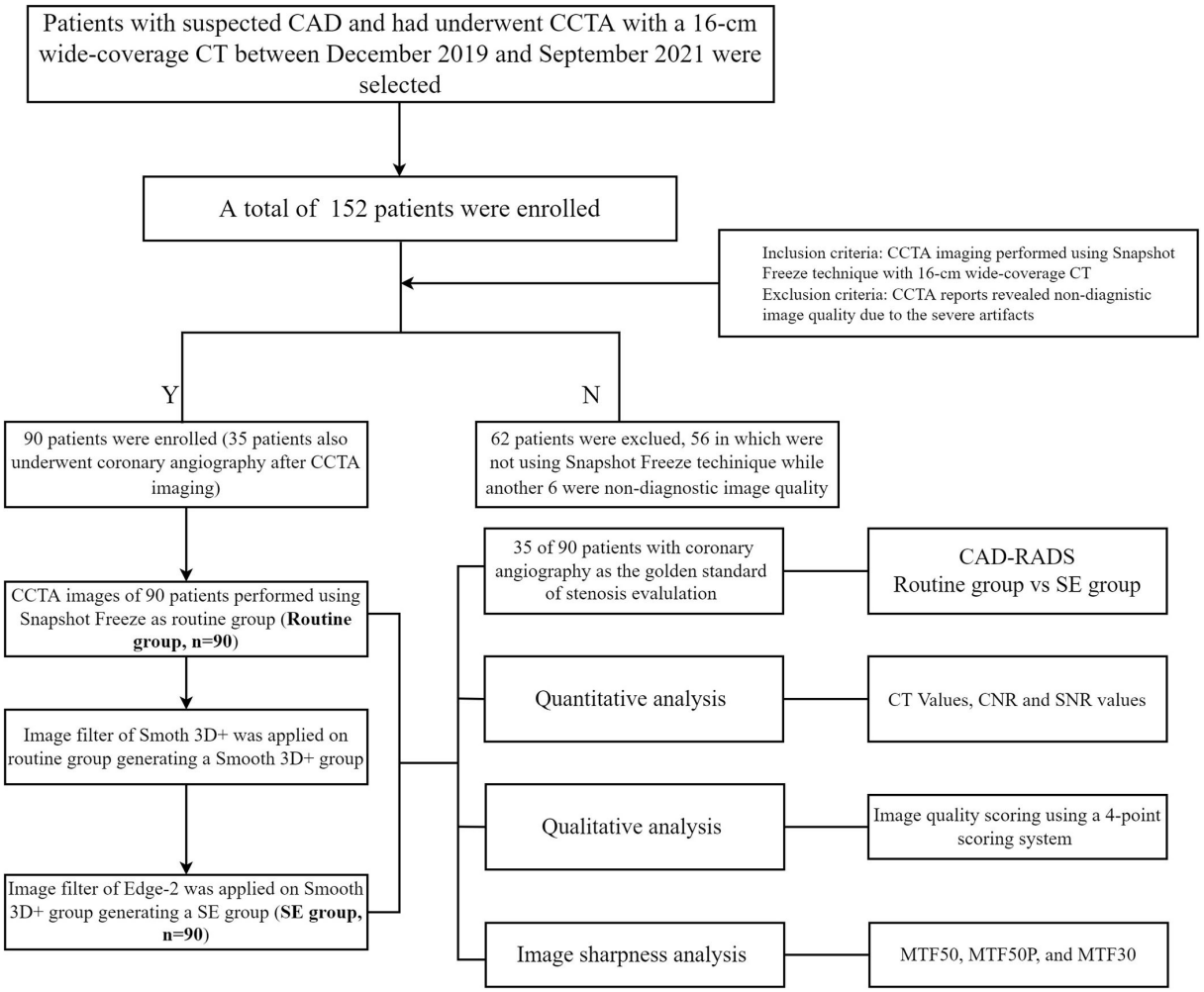


FIGURE 1
The flow chart of the patients' enrollment.

resulting images were saved as a new group named the smooth 3D+ and edge-2 group (SE group). The signal-to-noise ratio (SNR), contrast-to-noise ratio (CNR), and image quality scores were then compared between the original routine group and the SE group (Figure 2).

## Quantitative analysis

Quantitative measurements were performed including CT values and standard deviation (SD) of the lumen of the aortic root (AO), proximal left anterior descending artery (LAD-P), middle left anterior descending artery (LAD-M), distal left anterior descending artery (LAD-D), proximal left circumflex artery (LCX-P), middle left circumflex artery (LCX-M), distal left circumflex artery (LCX-D), proximal right coronary artery (RCA-P), middle right coronary artery (RCA-M), distal-proximal right coronary artery (RCA-D), and perivascular adipose tissue (PVAT). The region of interest (ROI) in the AO was set to 90 $mm^2$, and those in others were set to 1 $mm^2$. Image noise was classified as the SD of the attenuation within the ROI in the AO. Each ROI was measured three times by an independent reader, and the average of the three measurements was used for further analysis. The SNR was defined as CT value (vessel)/image noise, and the CNR was defined as [CT value (vessel) - CT value (PVAT)]/SD(PVAT).

## Qualitative analysis

Double-blinded image quality scoring was performed by two radiologists, one with 8 years of experience and the other with more than 15 years of experience in cardiovascular diagnosis, using the 18-segment model of the Society of Cardiovascular

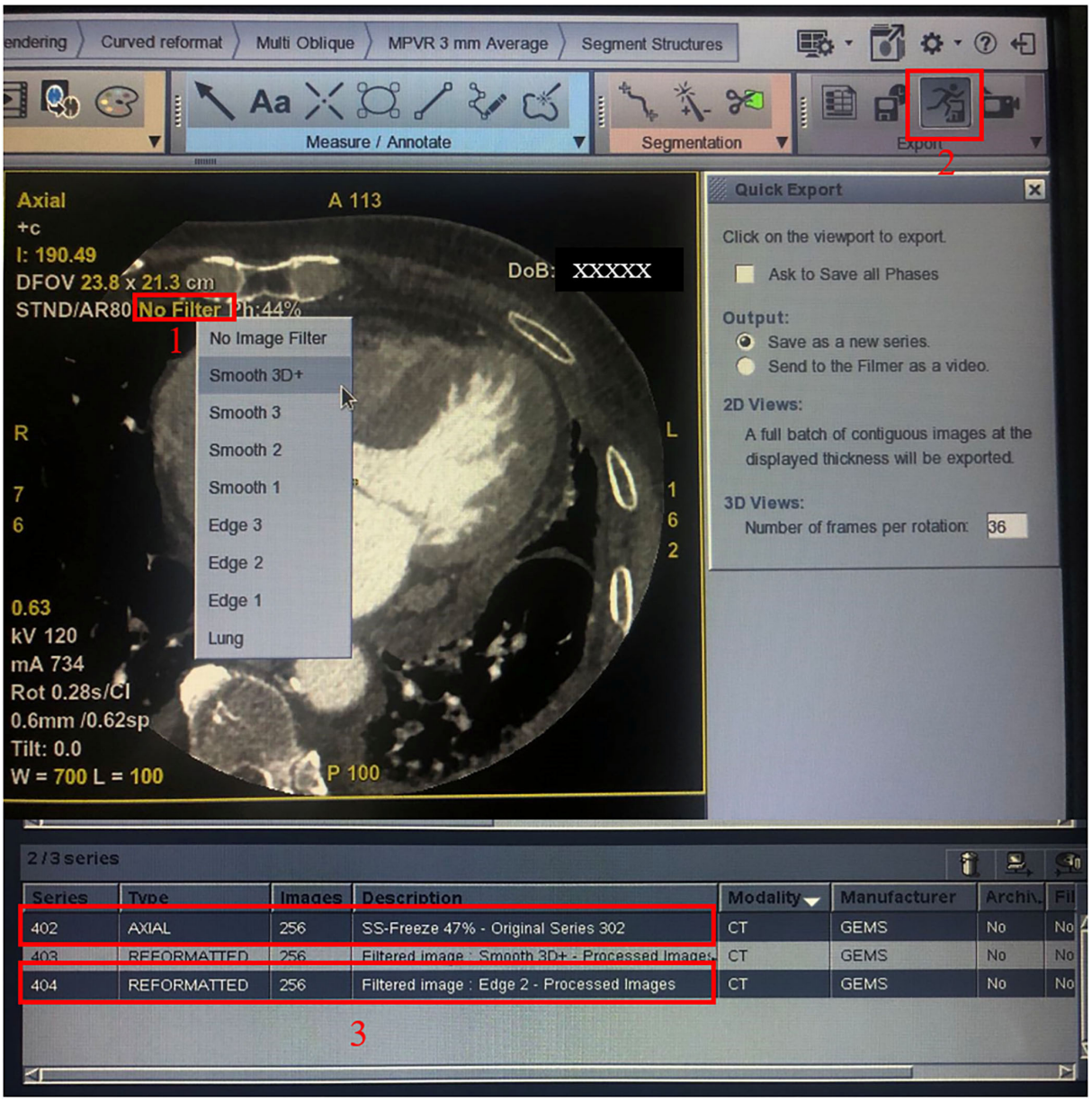


FIGURE 2
Procedure for generating the SE group. Step 1: Click the "No Filter" option in red frame 1 and select smooth 3D+; step 2: Click the button in red frame 2 to generate the smoothed 3D+ group. Then, quit the software program and start again, repeat step 1 but choose the edge-2 filter, and repeat step 2 and generate the SE group. Finally, the original series 402 and the SE group 404 were showed in two red frame 3.

Computed Tomography guidelines (25). Evaluations were conducted over 1 month to eliminate the observers' recall effects between routine and SE groups of the same patient. A 4-point scoring system was used for overall image quality analysis (26, 27) [(1) excellent, no artifacts; (2) good, minor artifacts; (3) moderate, artifacts, but diagnosis still possible; and 4: poor, non-diagnostic]. Each patient's CCTA was evaluated through the following 10 segments for the severity of stenosis: left main artery, LAD-P, LAD-M, LAD-D, LCX-P, LCX-D, RCA-P, RCA-M, RCA-D, and posterior descending artery. The stenosis degree was assessed using Coronary Artery Disease - Reporting and Data System (CAD-RADS) with a 7-grade scoring system (0–2: non-significant stenosis [luminal irregularities or lumen diameter narrowing <50%]; 3–5: significant stenosis [lumen diameter narrowing ≥50%]; 6: non-diagnostic situation) (Table 1). In cases of disagreement on the image quality score or stenosis assessment between the two radiologists, a third experienced observer (more than 15 years of experience) would

TABLE 1 Diagnostic criteria for coronary stenosis by CCTA and DSA.

| | Degree of maximal coronary stenosis | Interpretation |
|---|---|---|
| CAD-RADS 0 | 0% (No plaque or stenosis) | Documented absence of CAD |
| CAD-RADS 1 | 1–24% - Minimal stenosis or plaque | Minimal non-obstructive CAD |
| CAD-RADS 2 | 25–49% - Mild stenosis | Mild non-obstructive CAD |
| CAD-RADS 3 | 50–69% stenosis | Moderate stenosis |
| CAD-RADS 4 | 70–99% stenosis | Severe stenosis |
| CAD-RADS 5 | 100% (total occlusion) | Total coronary occlusion |
| CAD-RADS 6 | Non-diagnostic study | Obstructive CAD cannot be excluded |

CAD-RADS, Coronary Artery Disease - Reporting and Data System; CCTA, Coronary computed tomography angiography; DSA, digital subtraction angiography.

mediate to reach a final agreement. Individual adjustments of the window center and window width were allowed.

The results of digital subtraction angiography (DSA) were used as the reference standard to determine the significant stenosis independent of the CCTA results. Patients underwent DSA for diagnostic accuracy by two cardiologists (with more than 10 years of experience). The stenosis degree of each segment of coronary vessels (range: 0–100%) was quantitatively evaluated. Similar to CCTA, all segments were classified as being non-significant stenosis, significant stenosis, or non-diagnostic situation.

## Image sharpness analysis

An image quality testing software (Imatest, V5.2.21, USA) was used to evaluate the spatial frequency response reflecting the image sharpness through modulation transfer function (MTF) in the 2D image domain (28). One radiologist chose the same Digital Imaging and Communications in Medicine (DICOM) slices of the beginning of the coronary sinus of every patient in each group (one from the routine group and one from the SE group) and then exported this image as a 2D image (Portable Network Graphic, PNG) for further image sharpness evaluation. Using the Imatest software, the same ROI was set on the same position of two 2D images, including the heart, and the MTF50, MTF50P, and MTF30 were then calculated automatically by the software (Figure 3).

## Radiation dose

The radiation dose of CCTA imaging, including the dose-length product (DLP) and the volume CT dose index was recorded through the dose reports provided by the CT scanner. The effective dose was estimated by multiplying the DLP by a conversion factor of 0.014 mSv/(mGy·cm) (29).

## Statistical analysis

SPSS Statistics V22.0 (IBM, Chicago, IL, USA) was used for statistical analysis. Quantitative indices are presented as mean ± SD and medians (range: maximum to minimum). Data with non-normal distribution are expressed as medians (interquartile ranges). Quantitative data were analyzed using the independent samples t-test or the Wilcoxon signed rank-sum test. Counts were assessed using Pearson's chi-squared test, and Fisher's exact test was employed to examine the probability when the expected value was <5. A kappa value was calculated and defined as follows: < 0.20, almost inconsistent; 0.21–0.40, slightly consistent; 0.41–0.60, medium consistency; 0.61–0.80, good consistency; and 0.81–1.00, perfect consistency (27). The false-positive rate, false-negative rate, positive predictive value, negative predictive value (NPV), sensitivity, specificity, and accuracy were calculated for CCTA vs. DSA for each reconstruction on per-vessel and total levels and analyzed by the $\chi^2$ test, and differences were analyzed with ANOVA between three groups. The significance level was set at $p < 0.05$.

# Results

In total, we analyzed 90 patients, 900 vessel segments, and 270 images of coronary arteries with scoreable quality. The mean DLP was 345.18 ± 94.74 mGy·cm, and the mean effective dose was 4.83 ± 1.33 mSv. Patients' characteristics are presented in Table 2.

## Quantitative analysis, image quality scores, and image sharpness

The CT value of the AO ROI and the image noise in the routine group were higher than those in the SE group ($P < 0.001$). Moreover, the SNR and CNR were significantly higher in the SE group than in the routine group (all $Ps < 0.05$). The SE group had significantly higher MTF50 and MTF50P values than the routine group, while the MTF30 values were similar in these two groups (Table 3).

Due to individual differences in coronary artery anomalies, the image quality score was calculated based on three main coronary arteries (i.e., LAD, LCX, and RCA). The consistency of the two readers was good or perfect for each vessel (LAD, LCX, and RCA) and total vessels (kappa: 0.71–0.84), and the image quality scores in the SE group were significantly lower (i.e., better) than those in the routine group in each vessel and total vessels (all $Ps < 0.001$). Image quality scores of three main

10.3389/fcvm.2022.840735

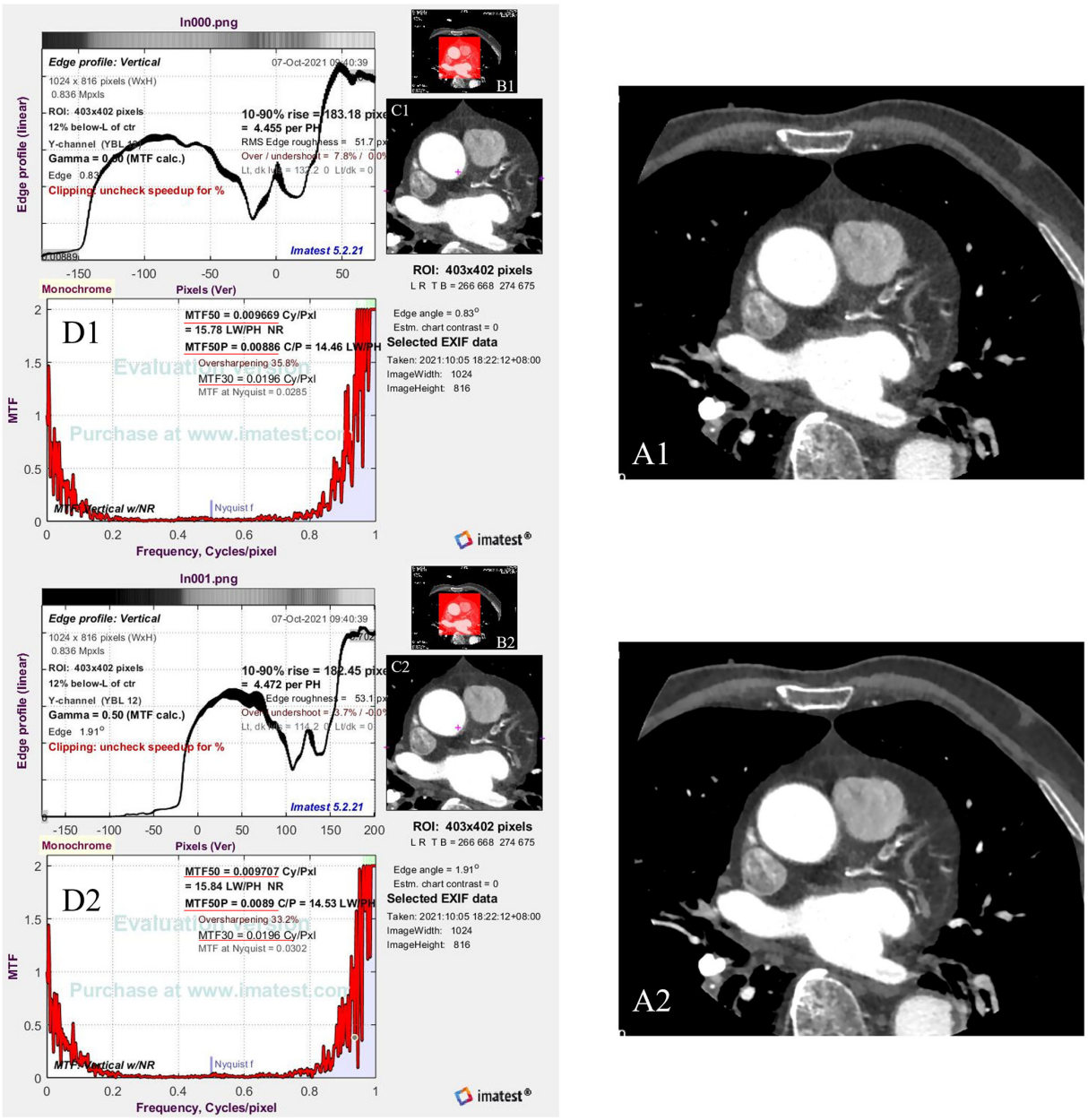


FIGURE 3
The flow chart shows how to calculate the image sharpness. **(A1,A2)** are the same Digital Imaging and Communications in Medicine (DICOM) slices of the beginning of the coronary sinus of one patient [**(A1)** from the routine group and **(A2)** from the SE group], which are exported to be a PNG format (Portable Network Graphic). Red frames in **(B1,B2)** are the setting of ROI (region of interest) **(C1,C2)**. Then, the software calculates the image sharpness through the ROI based on the MTF50, MTF50P, and MTF 30 [red underlines in **(D1,D2)**].

coronary arteries (LAD, LCX, and RCA) and total segments improved to different degrees after removing image quality score 1 of those segments (percent: 49–70%) (Table 4).

## Diagnostic accuracy

Among the 90 patients, 35 underwent DSA for stenosis evaluations after CCTA imaging. Based on the results of DSA, the accuracy of the findings related to stenosis in these 35 patients was compared among the three groups (routine group, SE group, and DSA group). The results showed no statistically significant difference in the accuracy of the stenosis evaluations between the SE and routine groups at the per-vessel and total levels (all *Ps* > 0.05). However, the SE group showed a slightly higher NPV on the LAD and RCA stenosis evaluations, as well as total NPV. The SE group also showed slightly higher sensitivity and accuracy than the routine group on the RCA

TABLE 2 Patients' information and radiation dose.

| | |
|---|---|
| Age | 67.1 ± 11.7 |
| Sex (F/M) | 23/67 |
| BMI (kg/m$^2$) | 27.4 ± 4.9 |
| Smoker | 56 (62%) |
| Hypertension | 70 (78%) |
| Diabetes | 61 (68) |
| Hyperlipemia | 39 (43%) |
| DLP, (mGy) | 344.69 ± 103.07 |
| ED, (mSv) | 4.8 ± 1.4 |

F/M, Female/Male; BMI, Body Mass Index; DLP, Dose-length Product; ED, Effective radiation dose.

stenosis evaluation. Moreover, eight segments were evaluated with CAD-RADS 6 (non-diagnostic situation) in the routine group, while two segments of RCA from these eight segments were improved to the diagnostic situation (Table 5).

## Discussion

Our study found that the application of a combination of image filters (smooth 3D+ and edge-2) on CCTA images significantly improved SNR and CNR values, due to ∼36% image noise reduction with the use of the smooth 3D+ image filter. Importantly, we showed that image sharpness was significantly better in the SE group than in the routine group in terms of MTF50 and MTF50P. Notably, image sharpness is usually considered a desirable image quality for evaluating vessel lesions on CCTA (23, 30, 31) (Figure 4). Moreover, previous studies have also reported additional edge rise distance as a quantitative measure for image sharpness evaluation (7, 31). However, in our study, similar MTF30 between the groups indicated that the image sharpening ability of the SE group was limited.

Image quality scores were significantly lower in the SE group than in the routine group, indicating better image quality in the SE group. Consistent with the image quality scores assigned by the observers for the three main coronary arteries, the better quantitative image quality and image sharpness enhanced the diagnostic confidence of observers. In the group-wise comparison of diagnostic accuracy against the DSA results, no significant differences were observed between these two groups. However, in the routine group, 8 out of 105 coronary arteries had a CAD-RADS of 6, indicating poor image quality. Moreover, obstructive CAD could not be excluded, and 2 of the 8 arteries changed from undiagnosable to diagnosable, consistent with the DSA stenosis degree (<50%), indicating that the diagnostic accuracy in the SE group was improved compared to that in the routine group.

A major strength of our study is that our intervention could be implemented using readily available post-processing

TABLE 3 Comparison of sharpness of image between the routine and SE groups.

| CT values | Routine group ($n = 90$) | SE group ($n = 90$) | $p$-value |
|---|---|---|---|
| AO (HU) | 409.55 ± 77.48 | 407.42 ± 77.86 | <0.001 |
| Image noise | 25.73 ± 7.12 | 16.34 ± 6.12 | <0.001 |
| **SNR** | | | |
| AO | 16.99 ± 5.16 | 28.34 ± 12.25 | <0.001 |
| LAD-P | 26.43 ± 15.06 | 46.51 ± 37.70 | <0.001 |
| LAD-M | 9.38 ± 5.74 | 12.48 ± 12.36 | 0.005 |
| LAD-D | 6.49 ± 5.20 | 7.80 ± 6.19 | 0.009 |
| LCX-P | 26.43 ± 15.06 | 46.51 ± 37.70 | <0.001 |
| LCX-M | 13.19 ± 7.43 | 18.04 ± 12.48 | <0.001 |
| LCX-D | 7.52 ± 4.95 | 9.74 ± 6.55 | <0.001 |
| RCA-P | 26.42 ± 15.30 | 32.29 ± 30.99 | <0.001 |
| RCA-M | 17.68 ± 11.92 | 25.75 ± 23.63 | <0.001 |
| RCA-D | 13.43 ± 9.43 | 18.28 ± 12.75 | <0.001 |
| **CNR** | | | |
| AO | 40.48 ± 32.74 | 80.65 ± 51.39 | <0.001 |
| LAD-P | 42.01 ± 31.30 | 76.30 ± 48.96 | <0.001 |
| LAD-M | 29.57 ± 23.41 | 52.60 ± 39.45 | <0.001 |
| LAD-D | 23.96 ± 18.87 | 48.83 ± 33.68 | <0.001 |
| LCX-P | 42.01 ± 31.30 | 76.30 ± 48.96 | <0.001 |
| LCX-M | 32.59 ± 27.49 | 64.91 ± 43.19 | <0.001 |
| LCX-D | 25.59 ± 22.75 | 51.92 ± 33.44 | <0.001 |
| RCA-P | 42.71 ± 29.89 | 76.80 ± 50.84 | <0.001 |
| RCA-M | 32.79 ± 27.09 | 68.40 ± 45.64 | <0.001 |
| RCA-D | 34.06 ± 22.97 | 60.73 ± 39.33 | <0.001 |
| **SHARPNESS** | | | |
| MTF50 | 0.0091 (0.0046, 0.0137) | 0.0093 (0.0051, 0.0164) | 0.036 |
| MTF50P | 0.0088 (0.0046, 0.0128) | 0.0090 (0.0059, 0.0136) | 0.049 |
| MTF30 | 0.0134 (0.0072, 0.0217) | 0.0211 (0.0146, 0.0258) (0.231,0.001) | 0.122 |

SE, smooth 3D+ combined with edge-2; CT, computed tomography; SNR, signal-to-noise ratio; CNR, contrast-to-noise ratio; HU, household; AO, lumen of the aortic root; LAD-P, M, D, left anterior descending artery, proximal, middle, and distal; LCX-P, M, D, left circumflex artery, proximal, middle, and distal; RCA-P, M, D, right coronary artery, proximal, middle, and distal; MTF, Modulation Transfer Function. Significance level, $P < 0.05$.

software on the workstation or console and will thus be easy to replicate because this technique is based on image domain processing instead of the raw data domain reconstruction. The image filter function on the AW4.7 workstation is convenient to use by any radiological worker whenever necessary. Moreover, this method improves image quality and increases radiologists' diagnostic confidence without increasing the cost or radiation dose to the patients. CCTA is a very mature imaging method in the evaluation of coronary stenosis and has relatively high diagnostic accuracy. Thus, improving the post-processing algorithms would not expect to dramatically improve the

TABLE 4 Comparison of image quality scores between the routine and SE groups.

| | | LAD | | | LCX | | | RCA | | | Total | | |
|---|---|---|---|---|---|---|---|---|---|---|---|---|---|
| | | R1 | R2 | ka. | R1 | R2 | ka. | R1 | R2 | ka. | R1 | R2 | ka. |
| Score (Median (25%,75%) | Routine group | 3 (2, 3) | 3 (2, 3) | 0.81 | 3 (3, 4) | 3 (3, 4) | 0.83 | 3 (2, 3) | 3 (2, 3) | 0.84 | 3(2, 4) | 3(2, 4) | 0.83 |
| | SE group | 2 (1, 3) | 2 (1, 3) | 0.78 | 2 (2, 3) | 3 (2, 3) | 0.80 | 2 (1, 3) | 2 (1, 2) | 0.71 | 2(1, 3) | 2(1, 3) | 0.77 |
| | *p* | <0.001 | <0.001 | <0.001 | <0.001 | <0.001 | <0.001 | <0.001 | <0.001 | | <0.001 | <0.001 | |
| Improved Vessels (Number, %) | | 48(57) | 59 (60) | | 51 (49) | 60 (56) | | 40 (69) | 57 (69) | | 139(70) | 176(69) | |

SE, smooth 3D+ combined with edge-2; LAD, left anterior descending artery; LCX, left circumflex artery; ka., Kappa; R, radiologist; RCA, right coronary artery.

TABLE 5 Comparison of diagnostic accuracy among the routine group, SE group, and the DSA group for coronary artery stenosis on per-segment and total levels.

| | LAD | | LCX | | RCA | | total | |
|---|---|---|---|---|---|---|---|---|
| | Routine | SE | Routine | SE | Routine | SE | Routine | SE |
| FPR, % | 0.36 | 0.39 | 0.43 | 0.43 | 0.41 | 0.41 | 0.39 | 0.40 |
| FNR, % | 0.04 | 0.03 | 0.02 | 0.02 | 0.01 | 0.00 | 0.02 | 0.02 |
| PPV, % | 0.85 | 0.84 | 0.84 | 0.84 | 0.91 | 0.89 | 0.87 | 0.87 |
| NPV, % | 0.88 | 0.90 | 0.92 | 0.92 | 0.94 | 1.00 | 0.90 | 0.93 |
| Se, % | 0.96 | 0.97 | 0.98 | 0.98 | 0.99 | 1.00 | 0.98 | 0.98 |
| Sp, % | 0.64 | 0.61 | 0.57 | 0.57 | 0.59 | 0.59 | 0.61 | 0.60 |
| Accuracy, % | 0.86 | 0.86 | 0.86 | 0.86 | 0.91 | 0.92 | 0.88 | 0.88 |
| *p* (routine vs. SE) | 0.839 | | 1.000 | | 0.418 | | 0.776 | |
| Non-diagnostic segment | 1 | 1 | 1 | 1 | 6 | 4 | 8 | 6 |

SE, smooth 3D+ combined with edge-2; FPR, False Positive Rate; FNR, False Negative Rate; PPV, Positive Predictive Value; NPV, Negative Predictive Value; Se, Sensitivity; Sp, Specificity; LAD, left anterior descending artery; LCX, left circumflex artery; RCA, right coronary artery; DSA, digital subtraction angiography.

diagnostic accuracy, unless the original images do not meet the diagnostic requirements. In our study, the original CCTA images were from routine examinations and already had relatively high diagnostic accuracy. Even though the use of image filters provided improvement in some of the diagnostic parameters, such as NPV, the main effect of this image filter combination was the improvement of image quality and readers' diagnostic confidence. Nevertheless, our concept and results could be helpful for future CCTA applications. For example, the ability to reduce image noise with the combined filters could be used to further reduce the required radiation dose for patients. The improved diagnostic confidence may be beneficial in speeding up the workflow and relieving the pressure on radiologists who need to read a lot of images every day.

Our study has several limitations. First, the study participants were retrospectively recruited from a single institution, and the sample size was small. And only one-third of the patients had undergone DSA due to the fact that if CCTA showed negative results, patients were less likely to undergo DSA. However, this intra-individual study with such a sample size clearly showed significant improvements in quantitative measurements, including image noise and sharpness and qualitative image evaluation. Second, we only used the combination of smooth 3D+ and edge-2 in the research group but did not compare this combination and other combinations. Smooth 3D+ was chosen as the highest level of reducing image noise and edge-2 was only the second highest level of edge sharpening because the highest level (edge-3) showed excessive sharpening with a severe "dark ring" around the edge (32, 33) (Figure 5). Therefore, the combination of image filters (smooth 3D+ and edge-2) was investigated in our study, and our results demonstrated that this combination balanced the image noise and spatial resolution and remarkably improved image quality. Third, the effect of the image filter was evaluated on CCTA images obtained by only GE CT. It remains unknown whether similar results will be observed if CT scanners from other vendors are used. However, conceptually our results clearly supported our hypothesis.

In conclusion, this study showed that the use of an additional image filter combining smooth 3D+ and edge-2 in the image domain on an AW could improve the image quality of CCTA and increase radiologists' diagnostic confidence.

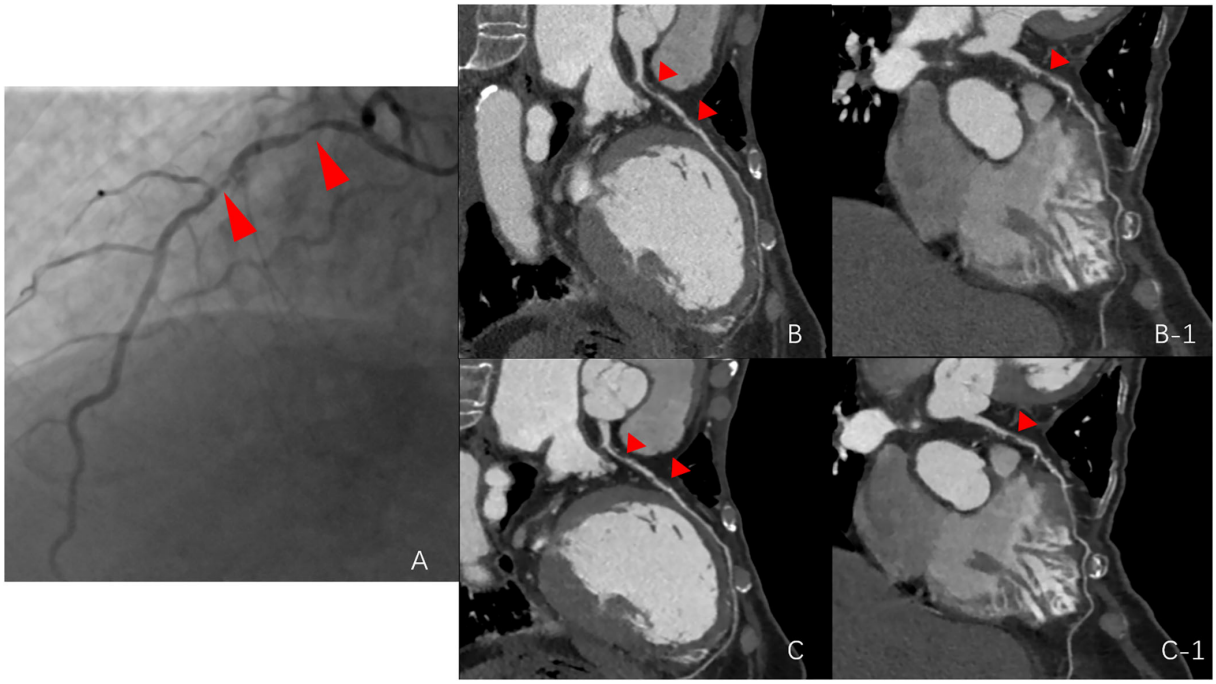


FIGURE 4
Comparison among the routine group, SE group, and digital subtraction angiography (DSA) group. **(A)** stenosis of the DSA group (red arrows point to the left anterior descending artery); **(B,B-1)**, stenosis of the routine group; and **(C,C-1)**, stenosis of the SE group.

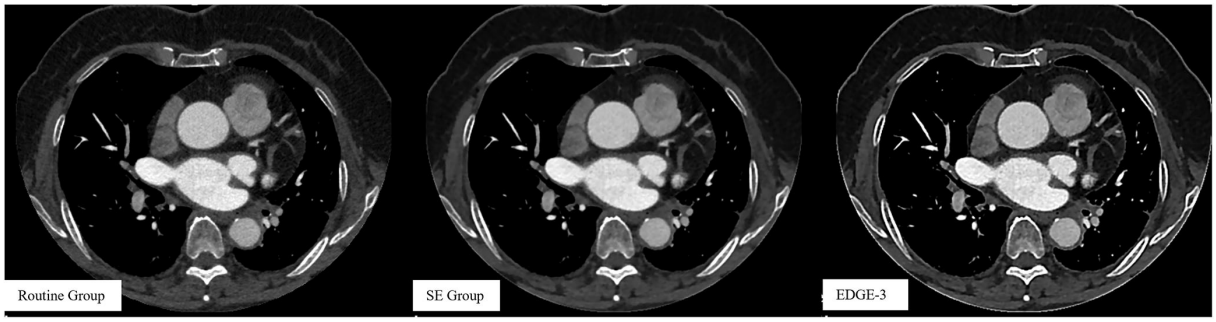


FIGURE 5
Images without using a combination of image filters in the routine group and images after using a combination of image filters in the SE (smooth 3D+ and edge-2) and Edge-3 (smooth 3D+ and edge-3) groups.

## Summary

Smoothing and edge-enhancement filters may be combined to improve the image quality and diagnostic confidence in CCTA. Image domain filters such as smooth 3D+ and edge-2 are readily available on an AW and are easy to be applied.

## Data availability statement

The raw data supporting the conclusions of this article will be made available by the authors, without undue reservation.

## Ethics statement

The studies involving human participants were reviewed and approved by Ethics Committee of Huadong Hospital. Written informed consent for participation was not required for this study in accordance with the national legislation and the institutional requirements.

## Author contributions

LJ and ML: conception, design, and study supervision. LJ and PG: development of methodology. LJ, PG, KW, and

ML: acquisition of data (provided animals, acquired and managed patients, and provided facilities, etc.). LJ, JL, and ML: analysis and interpretation of data (e.g., statistical analysis and computational analysis). LJ, PG, and ML: writing, review, and/or revision of the manuscript. All authors contributed to the article and approved the submitted version.

## Funding

This work was supported by the Youth Medical Talents—Medical Imaging Practitioner Program [Grant number, AB83030002019004], the Health Commission of Shanghai [Grant number, 2018ZHYL0103], the National Natural Science Foundation of China [Grant number, 61976238], and Fudan University.

## Conflict of interest

Author JL was employed by GE Healthcare China.

The remaining authors declare that the research was conducted in the absence of any commercial or financial relationships that could be construed as a potential conflict of interest.

## Publisher's note



## References

1. Stocker TJ, Deseive S, Leipsic J, Hadamitzky M, Chen MY, Rubinshtein R, et al. Reduction in radiation exposure in cardiovascular computed tomography imaging: results from the PROspective multicenter registry on radiaTion dose Estimates of cardiac CT angIOgraphy iN daily practice in 2017 (PROTECTION VI). *Eur Heart J.* (2018) 39:3715–23. doi: 10.1093/eurheartj/ehy546

2. Stocker TJ, Leipsic J, Hadamitzky M, Chen MY, Rubinshtein R, Deseive S, et al. Application of low tube potentials in CCTA: results from the PROTECTION VI Study. *JACC Cardiovasc Imaging.* (2020) 13:425–34. doi: 10.1016/j.jcmg.2019.03.030

3. Shen YW, Wu YJ, Hung YC, Hsiao CC, Chan SH, Mar GY, et al. Natural course of coronary artery calcium progression in Asian population with an initial score of zero. *BMC Cardiovasc Disord.* (2020) 20:212. doi: 10.1186/s12872-020-01498-x

4. Ghekiere O, Salgado R, Buls N, Leiner T, Mancini I, Vanhoenacker P, et al. Image quality in coronary CT angiography: challenges and technical solutions. *Br J Radiol.* (2017) 90:20160567. doi: 10.1259/bjr.20160567

5. Kalisz K, Buethe J, Saboo SS, Abbara S, Halliburton S, Rajiah P. Artifacts at cardiac CT: physics and solutions. *Radiographics.* (2016) 36:2064–83. doi: 10.1148/rg.2016160079

6. Kim S, Chang Y, Ra JB. Cardiac motion correction for helical CT scan with an ordinary pitch. *IEEE Trans Med Imaging.* (2018) 37:1587–96. doi: 10.1109/TMI.2018.2817594

7. Hong JH, Park EA, Lee W, Ahn C, Kim JH. Incremental image noise reduction in coronary CT angiography using a deep learning-based technique with iterative reconstruction. *Korean J Radiol.* (2020) 21:1165–77. doi: 10.3348/kjr.2020.0020

8. Abdelrahman KM, Chen MY, Dey AK, Virmani R, Finn AV, Khamis RY, et al. Coronary computed tomography angiography from clinical uses to emerging technologies: JACC state-of-the-art review. *J Am Coll Cardiol.* (2020) 76:1226–43. doi: 10.1016/j.jacc.2020.06.076

9. Andreini D, Pontone G, Mushtaq S, Conte E, Perchinunno M, Guglielmo M, et al. Atrial fibrillation: diagnostic accuracy of coronary CT angiography performed with a whole-heart 230-microm spatial resolution CT scanner. *Radiology.* (2017) 284:676–84. doi: 10.1148/radiol.2017161779

10. Li Q, Li P, Su Z, Yao X, Wang Y, Wang C, et al. Effect of a novel motion correction algorithm (SSF) on the image quality of coronary CTA with intermediate heart rates: segment-based and vessel-based analyses. *Eur J Radiol.* (2014) 83:2024–32. doi: 10.1016/j.ejrad.2014.08.002

11. Liang J, Wang H, Xu L, Dong L, Fan Z, Wang R, et al. Impact of SSF on diagnostic performance of coronary computed tomography angiography within 1 heart beat in patients with high heart rate using a 256-row detector computed tomography. *J Comput Assist Tomogr.* (2018) 42:54–61. doi: 10.1097/RCT.0000000000000641

12. Liang J, Wang H, Xu L, Yang L, Dong L, Fan Z, et al. Diagnostic performance of 256-row detector coronary CT angiography in patients with high heart rates within a single cardiac cycle: a preliminary study. *Clin Radiol.* (2017) 72:694 e7–694 e14. doi: 10.1016/j.crad.2017.03.004

13. Sheta HM, Egstrup K, Husic M, Heinsen LJ, Lambrechtsen J. Impact of a motion correction algorithm on quality and diagnostic utility in unselected patients undergoing coronary CT angiography. *Clin Imaging.* (2016) 40:217–21. doi: 10.1016/j.clinimag.2015.10.007

14. Sheta HM, Egstrup K, Husic M, Heinsen LJ, Nieman K, Lambrechtsen J. Impact of a motion correction algorithm on image quality in patients undergoing CT angiography: a randomized controlled trial. *Clin Imaging.* (2017) 42:1–6. doi: 10.1016/j.clinimag.2016.11.002

15. Shuai T, Deng L, Pan Y, Li W, Liao K, Li J, et al. Free-breathing coronary CT angiography using 16-cm wide-detector for challenging patients: comparison with invasive coronary angiography. *Clin Radiol.* (2018) 73:986 e1–986 e6. doi: 10.1016/j.crad.2018.06.023

16. Suh YJ, Kim YJ, Kim JY, Chang S, Im DJ, Hong YJ, et al. A whole-heart motion-correction algorithm: Effects on CT image quality and diagnostic accuracy of mechanical valve prosthesis abnormalities. *J Cardiovasc Comput Tomogr.* (2017) 11:474–81. doi: 10.1016/j.jcct.2017.09.011

17. Jin L, Gao Y, Shan Y, Sun Y, Li M, Wang Z. Qualitative and quantitative image analysis of 16 cm wide-coverage computed tomography compared to new-generation dual-source CT. *J Xray Sci Technol.* (2020) 28:527–39. doi: 10.3233/XST-190624

18. Wu YJ, Mar GY, Wu MT, Wu FZ. A LASSO-Derived Risk Model for Subclinical CAC Progression in Asian Population With an Initial Score of Zero. *Front Cardiovasc Med.* (2020) 7:619798. doi: 10.3389/fcvm.2020.619798

19. Wang ZY, Zhang JY. Classification Smoothing Filtering Algorithm Based on Edge Information. In: *2016 IEEE Information Technology, Networking, Electronic and Automation Control Conference(ITNEC 2016)*. Xi'an (2016).

20. Park C, Choo KS, Jung Y, Jeong HS, Hwang JY, Yun MS. CT iterative vs deep learning reconstruction: comparison of noise and sharpness. *Eur Radiol.* (2021) 31:3156–64. doi: 10.1007/s00330-020-07358-8

21. Lee KB, Goo HW. Comparison of quantitative image quality of cardiac computed tomography between raw-data-based and model-based iterative reconstruction algorithms with an emphasis on image sharpness. *Pediatr Radiol.* (2020) 50:1570–8. doi: 10.1007/s00247-020-04741-x

22. Euler A, Martini K, Baessler B, Eberhard M, Schoeck F, Alkadhi H, et al. 1024-pixel image matrix for chest CT - Impact on image quality of bronchial structures in phantoms and patients. *PLoS ONE.* (2020) 15:e0234644. doi: 10.1371/journal.pone.0234644

23. Araoz PA, Kirsch J, Primak AN, Braun NN, Saba O, Williamson EE, et al. Optimal image reconstruction phase at low and high heart rates in dual-source CT coronary angiography. *Int J Cardiovasc Imaging.* (2009) 25:837–45. doi: 10.1007/s10554-009-9489-3

24. Cury RC, Abbara S, Achenbach S, Agatston A, Berman DS, Budoff MJ, et al. CAD-RADS(TM) Coronary Artery Disease - Reporting and Data System. An expert consensus document of the Society of Cardiovascular Computed Tomography (SCCT), the American College of Radiology (ACR) and the North American Society for Cardiovascular Imaging (NASCI) Endorsed by the American College of Cardiology J Cardiovasc Comput Tomogr. (2016) 10:269–81. doi: 10.1016/j.jcct.2016.04.005

25. Leipsic J, Abbara S, Achenbach S, Cury R, Earls JP, Mancini GJ, et al. SCCT guidelines for the interpretation and reporting of coronary CT angiography: a report of the Society of Cardiovascular Computed Tomography Guidelines Committee. *J Cardiovasc Comput Tomogr.* (2014) 8:342–58. doi: 10.1016/j.jcct.2014.07.003

26. Achenbach S, Marwan M, Ropers D, Schepis T, Pflederer T, Anders K, et al. Coronary computed tomography angiography with a consistent dose below 1 mSv using prospectively electrocardiogram-triggered high-pitch spiral acquisition. *Eur Heart J.* (2010) 31:340–6. doi: 10.1093/eurheartj/ehp470

27. Yin WH, Lu B, Li N, Han L, Hou ZH, Wu RZ, et al. Iterative reconstruction to preserve image quality and diagnostic accuracy at reduced radiation dose in coronary CT angiography: an intraindividual comparison. *JACC Cardiovasc Imaging.* (2013) 6:1239–49. doi: 10.1016/j.jcmg.2013.08.008

28. Bayrakceken K, Hondur AM, Atalay HT, Aribas YK. Real-life comparison of the viewing angle and the image quality of two commonly used viewing systems for vitreoretinal surgery. *Turk J Med Sci.* (2020) 50:689–96. doi: 10.3906/sag-1910-11

29. Jia CF, Zhong J, Meng XY, Sun XX, Yang ZQ, Zou YJ, et al. Image quality and diagnostic value of ultra low-voltage, ultra low-contrast coronary CT angiography. *Eur Radiol.* (2019) 29:3678–85. doi: 10.1007/s00330-019-06111-0

30. Oda S, Weissman G, Vembar M, Weigold WG. Iterative model reconstruction: improved image quality of low-tube-voltage prospective ECG-gated coronary CT angiography images at 256-slice CT. *Eur J Radiol.* (2014) 83:1408–15. doi: 10.1016/j.ejrad.2014.04.027

31. Gordic S, Desbiolles L, Sedlmair M, Manka R, Plass A, Schmidt B, et al. Optimizing radiation dose by using advanced modelled iterative reconstruction in high-pitch coronary CT angiography. *Eur Radiol.* (2016) 26:459–68. doi: 10.1007/s00330-015-3862-5

32. Abou Zeid N, Pirko I, Erickson B, Weigand SD, Thomsen KM, Scheithauer B, et al. Diffusion-weighted imaging characteristics of biopsy-proven demyelinating brain lesions. *Neurology.* (2012) 78:1655–62. doi: 10.1212/WNL.0b013e3182574f66

33. Moreno R, Smedby O. Gradient-based enhancement of tubular structures in medical images. *Med Image Anal.* (2015) 26:19–29. doi: 10.1016/j.media.2015.07.001

# Advantages of publishing in Frontiers

**OPEN ACCESS**
Articles are free to read for greatest visibility and readership

**FAST PUBLICATION**
Around 90 days from submission to decision

**HIGH QUALITY PEER-REVIEW**
Rigorous, collaborative, and constructive peer-review

**TRANSPARENT PEER-REVIEW**
Editors and reviewers acknowledged by name on published articles

**Frontiers**
Avenue du Tribunal-Fédéral 34
1005 Lausanne | Switzerland

**Visit us:** www.frontiersin.org
**Contact us:** frontiersin.org/about/contact

**REPRODUCIBILITY OF RESEARCH**
Support open data and methods to enhance research reproducibility

**DIGITAL PUBLISHING**
Articles designed for optimal readership across devices

**FOLLOW US**
@frontiersin

**IMPACT METRICS**
Advanced article metrics track visibility across digital media

**EXTENSIVE PROMOTION**
Marketing and promotion of impactful research

**LOOP RESEARCH NETWORK**
Our network increases your article's readership